
Characterising the hot and dense fireball with virtual photons at HADES

Charakterisierung des heißen und dichten Feuerballs mit virtuellen Photonen bei HADES

Zur Erlangung des Grades eines Doktors der Naturwissenschaften (Dr. rer. nat.)

Genehmigte Dissertation im Fachbereich Physik von Niklas Schild

Tag der Einreichung: 19.01.2026, Tag der Prüfung: 18.02.2026

1. Gutachten: Prof. Dr. Tetyana Galatyuk

2. Gutachten: Prof. Dr. Claudia Höhne

Darmstadt, Technische Universität Darmstadt



TECHNISCHE
UNIVERSITÄT
DARMSTADT

Physics Department
Institut für Kernphysik
AG Galatyuk (ViP-QM)

Characterising the hot and dense fireball with virtual photons at HADES
Charakterisierung des heißen und dichten Feuerballs mit virtuellen Photonen bei HADES

Accepted doctoral thesis in the department of Physics by Niklas Schild

Date of submission: 19.01.2026

Date of thesis defense: 18.02.2026

Darmstadt, Technische Universität Darmstadt

Bitte zitieren Sie dieses Dokument als:

DOI: <https://doi.org/10.26083/tuda-7835>

Jahr der Veröffentlichung auf TUprints: 2026

Dieses Dokument wird bereitgestellt von tuprints,

E-Publishing-Service der TU Darmstadt

<https://tuprints.ulb.tu-darmstadt.de>

tuprints@ulb.tu-darmstadt.de

Die Veröffentlichung steht unter folgender Creative Commons Lizenz:

Namensnennung 4.0 International

<https://creativecommons.org/licenses/by/4.0/>

This work is licensed under a Creative Commons License:

Attribution 4.0 International

<https://creativecommons.org/licenses/by/4.0/>

Erklärungen laut Promotionsordnung

§ 8 Abs. 1 lit. d PromO

Ich versichere hiermit, dass zu einem vorherigen Zeitpunkt noch keine Promotion versucht wurde. In diesem Fall sind nähere Angaben über Zeitpunkt, Hochschule, Dissertationsthema und Ergebnis dieses Versuchs mitzuteilen.

§ 9 Abs. 1 PromO

Ich versichere hiermit, dass die vorliegende Dissertation – abgesehen von den in ihr ausdrücklich genannten Hilfen – selbstständig verfasst wurde und dass die „Grundsätze zur Sicherung guter wissenschaftlicher Praxis an der Technischen Universität Darmstadt“ und die „Leitlinien zum Umgang mit digitalen Forschungsdaten an der TU Darmstadt“ in den jeweils aktuellen Versionen bei der Verfassung der Dissertation beachtet wurden.

§ 9 Abs. 2 PromO

Die Arbeit hat bisher noch nicht zu Prüfungszwecken gedient.

Darmstadt, 19.01.2026

N. Schild

Abstract

Understanding the properties of strong interaction matter under extreme conditions of temperature and baryon density is a central objective of modern nuclear physics. While the phase structure of QCD at vanishing baryo-chemical potential is constrained by lattice QCD calculations and ultra-relativistic heavy-ion collision experiments at CERN and RHIC, its behaviour at higher net-baryon densities serves as an increasingly active area of experimental and theoretical study. In recent years, this interest is further driven by increasing efforts in the search for a potential first order deconfinement and chiral phase transition and QCD critical end point as well as by connections to astrophysical phenomena, such as neutron stars and neutron star mergers, which involve the equation-of-state in similar conditions.

In this setting, heavy-ion collisions at a few GeV per nucleon, as produced at the SIS18 accelerator at GSI, Darmstadt, provide essential baseline measurements for investigating the onset of critical phenomena and for benchmarking theoretical models in this baryon-rich regime. Electromagnetic probes, in particular virtual photons measured via their dilepton (e.g. e^+e^- , $\mu^+\mu^-$) decays, serve as unique and penetrating candidates for characterising QCD matter at highest temperature and density achieved in collisions, as they are emitted throughout the evolution of the system and traverse the medium with negligible final-state interactions.

This thesis exploits the sensitivity of dielectrons to investigate the properties and dynamics of the hot and dense fireball created in heavy-ion collisions via measurements with the High-Acceptance-Di-Electron-Spectrometer (HADES) at GSI. The main focus lies on Ag+Ag collisions at centre-of-mass energies of $\sqrt{s_{NN}} = 2.42$ GeV and 2.55 GeV. An independent reconstruction of dielectron spectra at $\sqrt{s_{NN}} = 2.55$ GeV is performed, serving as a validation and finalisation of previous HADES measurements, while the analysis at $\sqrt{s_{NN}} = 2.42$ GeV represents a new analysis, enabling a more systematic comparison of dielectron production at two closely spaced energies. The complete analysis chain is carried out, including advances in particle identification, pair selection, background subtraction, and efficiency and acceptance corrections.

After subtracting contributions from freeze-out as well as sources produced in initial first chance collisions, the thermal dielectron yield is isolated and studied as a function of invariant mass and collision centrality. From the invariant-mass spectra, an average fireball temperature of $T_{\text{Ag}2.55\text{Ag}} = 82.2 \pm 0.8_{\text{stat}} \pm 2.9_{\text{sys}}$ MeV at $\sqrt{s_{NN}} = 2.55$ GeV and $T_{\text{Ag}2.42\text{Ag}} = 73.5 \pm 1.8_{\text{stat}} \pm 3.0_{\text{sys}}$ MeV at $\sqrt{s_{NN}} = 2.42$ GeV is extracted for 0-40% centrality. These results are interpreted in conjunction with the measured excess yields, which exhibit a non-linear scaling with the number of participating nucleons. In combination, this provides first insights into the interplay between temperature, volume, and lifetime of the (locally) thermalised fireball.

The second focus of this thesis is the development and application of a complete analysis framework for the extraction of dielectron azimuthal anisotropies. Motivated by recent theoretical predictions of the sensitivity of dileptons to the time evolution of collective dynamics, direct and elliptic flow coefficients v_1 and v_2 are reconstructed for Au+Au and Ag+Ag collisions at $\sqrt{s_{NN}} = 2.42$ GeV and 2.55 GeV. While all measurements are compatible within their statistical and systematic uncertainties, the highest-statistics data set at $\sqrt{s_{NN}} = 2.55$ GeV provides the most stringent constraint, indicating a reduced elliptic flow

magnitude for thermal dielectron radiation compared to hadronic freeze-out sources. This observation is consistent with theoretical expectations that dileptons probe earlier stages of the collision, prior to the full build-up of collective flow, and demonstrates the feasibility and sensitivity of the analysis approach. Building on this, the framework developed in this thesis establishes the methodological foundation for future dielectron flow measurements at varying energies and for collision systems, not only in HADES, but future experiments such as, for example, the Compressed Baryonic Matter (CBM) experiment at FAIR.

In this context, a dedicated machine learning approach has also been developed to identify and suppress contamination from interactions with surrounding target material. The model demonstrates robust performance across all tested evaluation metrics and is successfully integrated into the data analysis, leading to a significant improvement in data quality of semi-central collisions.

The results presented in this thesis advance the quantitative characterisation of dielectron production and collective dynamics in heavy-ion collisions at high baryon density. They provide essential experimental benchmarks for theoretical descriptions of strong interaction matter in the region of the QCD phase diagram of high density and moderate temperatures.

Zusammenfassung

Das Verständnis der Eigenschaften von Materie der starken Wechselwirkung unter extremen Bedingungen von Temperatur und Baryondichte ist ein zentrales Ziel der modernen Kernphysik. Während die Phasenstruktur der QCD bei verschwindendem baryonischen chemischen Potential durch QCD Gitterrechnungen und ultra-relativistische Kollisionsexperimente am CERN und RHIC eingeschränkt wird, stellt ihr Verhalten bei höheren Netto-Baryondichten ein ebenso aktives Gebiet experimenteller und theoretischer Forschung dar. In den letzten Jahren wurde dieses Interesse durch verstärkte Bemühungen bei der Suche nach einem möglichen Dekonfinement erster Ordnung und einem chiralen Phasenübergang sowie einem kritischen Endpunkt der QCD weiter vorangetrieben. Hinzu kommen Verbindungen zu astrophysikalischen Phänomenen wie Neutronensternen und Neutronensternverschmelzungen, bei denen die Zustandsgleichung unter ähnlichen Bedingungen eine Rolle spielt.

In diesem Umfeld liefern Schwerionenkollisionen mit einigen GeV pro Nukleon, wie sie am SIS18-Beschleuniger der GSI in Darmstadt erzeugt werden, wichtige Basismessungen für die Untersuchung des Einsetzens kritischer Phänomene und für den Vergleich theoretischer Modelle in diesem baryonenreichen Bereich. Elektromagnetische Sonden, insbesondere virtuelle Photonen, die über ihre Dileptonen-Zerfälle (z.B. e^+e^- , $\mu^+\mu^-$) gemessen werden, dienen als einzigartige und durchdringende Beobachtungskandidaten, da sie während der gesamten Entwicklung des Systems emittiert werden und das Medium mit vernachlässigbaren Endzustandswechselwirkungen durchlaufen.

Diese Arbeit nutzt die Sensitivität von Dielektronen, um die Eigenschaften und Dynamik der heißen und dichten Feuerballs, die in Schwerionenkollisionen erzeugt wird, mittels Messungen mit dem High-Acceptance-Di-Electron-Spectrometer (HADES) zu untersuchen. Der allgemeine Fokus liegt auf Ag+Ag-Kollisionen bei Schwerpunktsenergien von $\sqrt{s_{NN}} = 2.42$ GeV und 2.55 GeV. Eine unabhängige Rekonstruktion der Dielektronenspektren bei $\sqrt{s_{NN}} = 2.55$ GeV wird durchgeführt, um frühere HADES-Messungen zu validieren und abzuschließen, während die Analyse bei $\sqrt{s_{NN}} = 2.42$ GeV eine neue Auswertung darstellt, die einen systematischeren Vergleich der Dielektronenproduktion bei zwei eng beieinander liegenden Energien ermöglicht. Die vollständige Analyseketten wird durchgeführt, einschließlich Fortschritten in der Teilchenidentifikation, Parselektion, Hintergrundsubtraktion sowie Effizienz- und Akzeptanzkorrekturen.

Nach Abzug der Beiträge aus dem Freeze-out sowie der Quellen, die bei den ersten Kollisionen entstanden sind, wird die thermische Dielektronenausbeute isoliert und als Funktion der invarianten Masse und Kollisionszentralität untersucht. Aus den invarianten Massenspektren wird eine durchschnittliche Feuerballtemperatur von $T_{\text{Ag}2.55\text{Ag}} = 82.2 \pm 0.8_{\text{stat}} \pm 2.9_{\text{sys}}$ MeV bei $\sqrt{s_{NN}} = 2.55$ GeV und $T_{\text{Ag}2.42\text{Ag}} = 73.5 \pm 1.8_{\text{stat}} \pm 3.0_{\text{sys}}$ MeV bei $\sqrt{s_{NN}} = 2.42$ GeV für 0–40% Zentralität extrahiert. Diese Ergebnisse werden im Zusammenhang mit den gemessenen Überschussausbeuten interpretiert, die eine nichtlineare Skalierung mit der Zahl der beteiligten Nukleonen aufweisen. In Kombination liefert dies erste Einblicke in das Zusammenspiel von Temperatur, Volumen und Lebensdauer der (lokal) thermalisierten Feuerballs.

Der zweite Schwerpunkt dieser Arbeit liegt auf der Entwicklung und Anwendung eines vollständigen Analyse-Frameworks zur Extraktion von dielektronischen Azimut-Anisotropien. Motiviert durch jüngste

theoretische Vorhersagen zur Sensitivität von Dileptonen auf die zeitliche Entwicklung kollektiver Dynamik, werden direkte und elliptische Flusskoeffizienten v_1 und v_2 für Au+Au- und Ag+Ag-Kollisionen bei $\sqrt{s_{NN}} = 2.42$ GeV und 2.55 GeV rekonstruiert. Während alle Messungen innerhalb ihrer statistischen und systematischen Unsicherheiten kompatibel sind, liefert der Datensatz mit der höchsten Statistik bei $\sqrt{s_{NN}} = 2.55$ GeV die strengste Einschränkung und deutet auf eine reduzierte elliptische Flussstärke für thermische Dielektronenstrahlung im Vergleich zu hadronischen Freeze-out-Quellen hin. Diese Beobachtung ist konsistent mit theoretischen Erwartungen, dass Dileptonen frühere Stadien der Kollision abbilden, bevor der kollektive Fluss vollständig aufgebaut ist, und demonstriert die Machbarkeit und Sensitivität des Analyseansatzes. Auf dieser Grundlage schafft das in dieser Arbeit entwickelte Rahmenwerk die methodische Grundlage für zukünftige Dielektronenflussmessungen bei unterschiedlichen Energien und für Kollisionssysteme, nicht nur in HADES, sondern auch in zukünftigen Experimenten wie beispielsweise dem Compressed Baryonic Matter (CBM)-Experiment bei FAIR.

In diesem Zusammenhang wurde auch ein spezieller maschineller Lernansatz entwickelt, um Kontaminationen durch Wechselwirkungen mit dem umgebenden Zielmaterial zu identifizieren und zu unterdrücken. Das Modell zeigt eine robuste Leistung über alle getesteten Evaluationsmetriken und wird erfolgreich in die Datenanalyse integriert, was zu einer signifikanten Verbesserung der Datenqualität bei semi-zentralen Kollisionen führt.

Insgesamt tragen die in dieser Arbeit präsentierten Ergebnisse zur quantitativen Charakterisierung der Dielektronenproduktion und der kollektiven Dynamik in Schwerionenkollisionen bei hoher Baryondichte bei. Sie liefern wesentliche experimentelle Referenzpunkte für theoretische Beschreibungen der Materie der starken Wechselwirkung in dem Bereich des QCD-Phasendiagramms bei hoher Dichte und moderaten Temperaturen.

Contents

1	Introduction	1
1.1	The Standard Model	1
1.2	Strong Interaction Matter	3
1.2.1	QCD Phase Diagram	4
1.2.2	Chiral Symmetry	6
1.3	Probing the QCD Phase Diagram with Heavy-Ion Collisions	8
1.4	Electromagnetic Probes	12
1.4.1	Experimental Results on Dilepton Production	13
1.4.2	Theoretical Description of Thermal Dileptons	16
1.5	Motivation and Outline of this Thesis	17
2	The HADES Experimental Setup	19
2.1	GSI Accelerator Facility	20
2.2	The Segmented Target	20
2.3	START and VETO Detector	21
2.4	Ring Imaging Cherenkov Detector	22
2.5	Multiwire Drift Chambers and Magnet	23
2.6	Time-of-Flight Detectors	23
2.7	Electromagnetic Calorimeter	24
2.8	The Forward Hodoscope Wall	24
2.9	Data Acquisition and Trigger System	25
3	General Data Processing and Selection in HADES	27
3.1	Creation of the Data Summary Tape	28
3.1.1	Simulations to Emulate the Detector Response	29
3.2	Event Selection Criteria	31
3.3	Centrality Determination	33
3.3.1	Glauber Monte Carlo Simulation	34
3.3.2	Resulting Centrality Classes	34
3.4	Event Plane Reconstruction	36
3.4.1	Event Plane Resolution	38
3.5	Identification of Ag+C contamination with Machine Learning	39
3.5.1	Neural Network-Based Identification of Ag+C Events	41
3.5.2	Model Evaluation	45
4	DiElectron Reconstruction and Analysis Procedure	49
4.1	Electron Identification at HADES	49
4.1.1	Electron Selection Criteria Using the RICH Detector	50

4.1.2	Electron Selection Criteria from Time-of-Flight	53
4.1.3	Evaluation of the Electron Identification	54
4.2	Reconstruction of the DiElectron Signal	55
4.2.1	Estimation of the Combinatorial Background	56
4.2.2	Optimising the Signal-To-Background Ratio with Conversion Rejection	59
4.3	Efficiency and Acceptance Corrections	61
4.3.1	Single Track Correction Matrices	61
4.3.2	Accounting for Momentum Smearing in Simulations	63
4.3.3	Estimation of the Pair Corrections	64
4.3.4	Self-Consistency Checks for the Corrections	66
4.4	Disentangling the Relative Yields in the DiElectron Cocktail	67
4.5	Systematic Uncertainties of the DiElectron Spectra	69
5	Reconstruction Procedure of the Azimuthal Anisotropy	71
5.1	Reconstruction of the Azimuthal DiElectron Distribution	71
5.2	Flow Coefficient Reconstruction Procedures	72
5.3	Efficiency and Acceptance Corrections in the Flow Reconstruction	74
5.4	Event-By-Event Efficiency Correction as a Function of the Event Plane	75
5.5	Disentangling the Flow Coefficients in the DiElectron Cocktail	78
5.6	Systematic Uncertainties of the Flow Coefficients	80
5.7	Adaptations in Au+Au Data Reanalysis	81
6	Evaluation and Interpretation of the Experimental Results	83
6.1	Characterising the Hot and Dense Fireball via the Invariant Mass Spectrum	83
6.1.1	System Size and Centrality Dependence of the Thermal Radiation	85
6.2	Integrated DiElectron Flow Coefficients	90
6.3	Isolation of the Thermal DiElectron Flow Coefficients	93
6.4	Ongoing Perspectives with Multi-Differential Measurements	98
7	Summary and Outlook	103

List of Figures

1.1	Summary of elementary particles in the Standard Model.	2
1.2	Summary of measurements of the coupling constant α_S in dependence of the momentum transfer Q	3
1.3	QCD phase diagram.	5
1.4	Comparison of simulations between a neutron star merger and a heavy-ion collision.	6
1.5	Comparison of vacuum ρ and a_1 spectral function.	7
1.6	Prediction of the evolution of chiral partners particle spectra with increasing temperature.	8
1.7	Visualisation of the evolution of a heavy-ion collision, based on a UrQMD simulation of Au+Au collisions at $\sqrt{s_{NN}} = 20$ GeV.	10
1.8	Illustration of the collision centrality.	11
1.9	Flow coefficients as a function of excess energy energies based on available world data.	12
1.10	Timeline of important dilepton experiments.	14
1.11	Dilepton spectra from CERES and NA60.	15
1.12	Dielectron excess yield measured in Au+Au collisions at $\sqrt{s_{NN}} = 2.42$ GeV.	16
2.1	Schematic Layout of the HADES experiment in the 2019 Ag+Ag campaign.	20
2.2	Photo of the segmented target for the Au+Au (left panel) and Ag+Ag (right panel) experiments in 2012 and 2019.	21
2.3	Left: Schematic layout of the RICH detector. Right: Photo of the MAPMT read out plane.	22
2.4	Illustration of the Forward Wall.	25
3.1	(Simplified) flow chart of the DST production process with and without simulations.	30
3.2	Percentage of accepted events after subsequent application of the event selection criteria for the Ag+Ag collisions at $\sqrt{s_{NN}} = 2.55$ GeV (left panel) and 2.42 GeV (right panel).	33
3.3	Distributions of impact parameter and number of participating nucleons from the Glauber Monte Carlo model.	35
3.4	Fitted Glauber Monte Carlo model with experimental data.	36
3.5	Illustration of the event plane reconstruction procedure.	37
3.6	Event plane resolution up to the third order for the Ag+Ag collisions, collected at HADES, at $\sqrt{s_{NN}} = 2.55$ GeV (left panel) and 2.42 GeV (right panel).	39
3.7	Illustration on the x-y geometry of a single target segment.	40
3.8	ERAT distribution as a function of the number of META hits N_{META}	41
3.9	Distribution of events, normalised in the region of $80 < N_{META} < 200$ for various segments.	42
3.10	Illustration of how pure Ag+Ag and Ag+C samples can be selected using START hit positions in the first target segment.	43
3.11	Output distribution of the trained classifier applied to Ag+Ag data at $\sqrt{s_{NN}} = 2.55$ GeV.	44
3.12	Comparison of experimental data with Glauber Monte Carlo simulation before and after Ag+Ag classifier application.	46

3.13	Directed flow v_1 of positrons before and after removal of Ag+C collisions for Ag+Ag collisions at $\sqrt{s_{NN}} = 2.55$ GeV.	47
4.1	Distribution of $\Delta\theta$ in experimental data (black) and simulation (blue) for Ag+Ag collisions at $\sqrt{s_{NN}} = 2.55$ GeV for three momentum bins in system 0, sector 1.	51
4.2	Example illustrating the determination of $\Delta\theta$ thresholds for particle identification in Ag+Ag collisions at $\sqrt{s_{NN}} = 2.55$ GeV, using multiple momentum bins in system 0, sector 1.	52
4.3	Example illustrating the determination of β thresholds for particle identification in Ag+Ag collisions at $\sqrt{s_{NN}} = 2.55$ GeV, using three momentum bins in system 0.	53
4.4	Velocity β in dependence of the charge q times momentum p before and after lepton selection for Ag+Ag collisions at $\sqrt{s_{NN}} = 2.55$ GeV and 2.42 GeV.	54
4.5	Pion suppression factor as a function of the momentum p after sequential application of the various electron/positron identification criteria.	55
4.6	Illustration of uncorrelated (red) and correlated (blue) combinatorial background in the example of neutral pion decays.	56
4.7	Ratio of same-event to mixed-event combinatorial background in dependence of the invariant mass for Ag+Ag collisions at $\sqrt{s_{NN}} = 2.55$ GeV (left panel) and $\sqrt{s_{NN}} = 2.42$ GeV (right panel).	57
4.8	Charge asymmetry factor k in dependence of the invariant mass for Ag+Ag collisions at $\sqrt{s_{NN}} = 2.55$ GeV (left panel) and $\sqrt{s_{NN}} = 2.42$ GeV (right panel).	58
4.9	Resulting signal after subtraction of the combinatorial background in dependence of the invariant mass for Ag+Ag collisions at $\sqrt{s_{NN}} = 2.55$ GeV (left panel) and $\sqrt{s_{NN}} = 2.42$ GeV (right panel).	59
4.10	Signal-to-background ratio (left panel) and significance (right panel) with the standard as well as improved, based on RICH, conversion rejection criteria for Ag+Ag collisions at $\sqrt{s_{NN}} = 2.55$ GeV and 2.42 GeV.	60
4.11	Single lepton efficiency in dependence of the polar angle θ and momentum p for electrons (left panel) and positrons (right panel) for Ag+Ag collisions at $\sqrt{s_{NN}} = 2.55$ GeV at 0-40% centrality.	62
4.12	Ideal vs. reconstructed momentum of electrons (left panel) and positrons (right panel) for Ag+Ag collisions at $\sqrt{s_{NN}} = 2.55$ GeV at a given θ interval.	63
4.13	Pair correction factors in dependence of the invariant mass for Ag+Ag collisions at $\sqrt{s_{NN}} = 2.55$ GeV and 2.42 GeV.	65
4.14	Ratio of true and estimated pair efficiency in the self-consistency check.	67
4.15	Efficiency-corrected dielectron invariant mass spectra compared to the Pluto cocktail for Ag+Ag collisions.	69
4.16	Systematic Uncertainties in the Dilepton Mass Spectra.	70
5.1	Azimuthal distribution of the dielectron spectrum with background in relation to the event plane.	72
5.2	Fourier fit on the azimuthal distribution of the dielectron signal in respect to the event plane.	73
5.3	Left panel: Local track density as a function of θ and $\Delta\phi$. Right panel: Corresponding efficiency due to occupancy effects.	75
5.4	Directed flow v_1 of positrons before and after the occupancy correction for Ag+Ag collisions at $\sqrt{s_{NN}} = 2.55$ GeV and 2.42 GeV.	78
5.5	Measured elliptic flow of positively charged pions (π^+) compared to predictions from several transport models for Ag+Ag collisions at $\sqrt{s_{NN}} = 2.55$ GeV.	79

6.1	Thermal dielectron excess as a function of invariant mass for Ag+Ag collisions at $\sqrt{s_{\text{NN}}} = 2.55$ GeV (left) and 2.42 GeV (right) at 0–40% centrality.	84
6.2	Thermal dielectron excess in dependence of the invariant mass for Ag+Ag collisions at $\sqrt{s_{\text{NN}}} = 2.55$ GeV in 10% centrality bins.	87
6.3	Thermal dielectron excess in dependence of the invariant mass for Ag+Ag collisions at $\sqrt{s_{\text{NN}}} = 2.42$ GeV in 10% centrality bins.	88
6.4	Thermal integrated excess yield (right panel) and fireball temperature (left panel) in dependence of the number of participants $\langle N_{\text{part}} \rangle$ for Ag+Ag collisions at $\sqrt{s_{\text{NN}}} = 2.55$ GeV and 2.42 GeV.	89
6.5	Thermal integrated excess yield, normalised by the number of pions, in dependence of the number of participants $\langle N_{\text{part}} \rangle$ for Ag+Ag collisions at $\sqrt{s_{\text{NN}}} = 2.55$ GeV and 2.42 GeV. . .	90
6.6	Inclusive dielectron v_1 for two collision systems and two energies.	91
6.7	Directed flow v_1 in 10% centrality bins.	92
6.8	Integrated dielectron v_2 for two collision systems and two energies.	93
6.9	Measurement of the integrated dielectron v_2 over centrality (left panel), transverse momentum (middle panel) and rapidity (right panel)	94
6.10	Estimated isolated dielectron v_2 after subtraction of the π^0 contribution	96
6.11	Estimated isolated dielectron v_2 after subtraction of the π^0 and η contribution	97
6.12	Dielectron spectrum as a function of transverse momentum p_t for various invariant-mass intervals in Ag+Ag collisions at $\sqrt{s_{\text{NN}}} = 2.55$ GeV. The left panel shows the integrated signal. The right panel displays the excess yield after subtraction of the freeze-out contributions from π^0 , η , and ω decays.	99
6.13	DiElectron spectrum in dependence of the invariant mass for various bins of rapidity for Ag+Ag collisions at $\sqrt{s_{\text{NN}}} = 2.55$ GeV. The left panel shows the integrated signal. The right panel shows the excess after subtraction of freeze-out contributions of π^0 , η and ω	100

List of Tables

1.1	Comparison of the four fundamental interactions.	1
1.2	Overview of heavy-ion collision experiments and their corresponding accelerators, facilities, and key characteristics.	9
1.3	Overview of dielectron (e^+e^-) sources at collision energies of 1–2A GeV, listing quantum numbers, masses, dominant decay channels and their branching ratios (BR), and rare dielectron decays.	13
3.1	Overview of past HADES production campaigns.	27
3.2	Classification performance on simulation data by centrality and model.	45
4.1	Summary of particle multiplicities and scaling for various centralities in Ag+Ag $\sqrt{s_{NN}} = 2.55$ GeV and 2.42 GeV collisions. The number of participants for each centrality class is based on the calculation of the Glauber Monte Carlo model discussed in section 3.3.	68
5.1	Final values of the occupancy correction parameter ϵ^{\min} for electrons and positrons.	76
6.1	Slope of directed flow dv_1/dy at midrapidity ($y = y_{cm}$), measured at HADES for Ag+Ag collisions at $\sqrt{s_{NN}} = 2.55$ GeV, of dielectrons and charged pions as a function of collision centrality.	92

List of Abbreviations

ADC	Analog-to-Digital Converters
BES	Beam energy scan
BR	Branching Ratio
CB	Combinatorial Background
CBM	Compressed-Baryonic-Matter
CEP	Critical End Point
CERES	CErenkov-Ring-Electron-Spectrometer
CTS	Central Trigger System
DAQ	Data Acquisition
DST	Data Summary Tape
ECAL	Electromagnetic Calorimeter
EoS	Equation of State
EM	Electromagnetic
FAIR	Facility for Antiproton and Ion Research
FEE	Front-End Electronics
FW	Forward Wall
GSI	Gesellschaft für Schwerionenforschung
HADES	High-Acceptance-Di-Electron-Spectrometer
HIC	Heavy-Ion Collision
HLD	HADES Listmode Data
HYDRA	HADES System for Data Reduction and Analysis
LHC	Large Hadron Collider
MC	Monte Carlo
MDC	Mini-Drift Cells
META	Multiplicity and Trigger Array

MMQ	META matching quality
NBD	Negative Binomial Probability Distribution
PID	Particle Identification
PT	Physics Trigger
QCD	Quantum Chromodynamics
QED	Quantum Electrodynamics
QFT	Quantum Field Theory
QGP	Quark-Gluon Plasma
RHIC	Relativistic Heavy Ion Collider
RICH	Ring Imaging CHerenkov (Detector)
RPC	Resistive Plate Chambers
RMQ	RICH matching quality
SIS18	Schwerionensynchrotron 18
SPS	Super-Proton-Synchrotron
TDC	Time-to-Digital Converters
TOF	Time-of-Flight (Detector)
TRD	Transition Radiation Detector
UNILAC	Universal Linear Accelerator
UrQMD	Ultra-relativistic Quantum Molecular Dynamics
VDM	Vector Dominance Model

1 Introduction

Physical matter is generally defined as anything that possesses mass and occupies space [1]. It forms the fundamental substance of all physical objects, ranging from galaxies and stars to planets, moons, and other celestial bodies, down to their constituents and all the way to living organisms. Naturally, this leads to one of the most profound questions and quests in philosophy and physics: understanding the origin and nature of this matter.

Beginning with the early concepts of fundamental building blocks in ancient Greece [2], and advancing through significant developments in quantum mechanics and relativity during the 20th century, the most established and comprehensive theory for this today is arguably the Standard Model of particle physics. Despite its limitations and inability to address certain fundamental questions [3], it remains a cornerstone of modern particle and nuclear physics, guiding ongoing research into the nature of elementary particles and fundamental forces.

This thesis aims to contribute to this exploration by studying heavy-ion collisions at relativistic energies at HADES, with a specific focus on electromagnetic probes, as outlined in section 1.5. Before delving into the detailed analysis, key concepts and theoretical foundations are introduced and defined. These serve to motivate this thesis and lay the groundwork for the methodologies and results presented in subsequent chapters.

1.1 The Standard Model

The Standard Model has a long and interesting history [4]. Driven by various theoretical as well as experimental developments in the 20th century, it can be summarised today by figure 1.1 and table 1.1. On its most basic level, it is assumed that everything in the visible universe is made from a small number of elementary particles which interact via four fundamental forces: Gravitation, electromagnetism, the weak and the strong interaction. Among these, gravity is treated separately via Einstein's General Relativity. As indicated in table 1.1, it is also the weakest of the four forces and therefore usually ignored in the context of particle physics.

Interaction	Exchange Particle	Coupling Constant	Range	Relative Strength
Gravitational	Graviton (hypothetical)	G_N	∞	10^{-39}
Electromagnetic	Photon (γ)	α	∞	10^{-2}
Weak	W and Z bosons (W^\pm, Z)	g_W	10^{-18} m	10^{-7}
Strong	Gluon (g)	α_s	10^{-15} m	1

Table 1.1: Comparison of the four fundamental interactions. Adapted from [5].

The other three forces, however, are all described within the Standard Model. More specifically, figure 1.1 shows all so-called fermions, acting as the essential building blocks of all visible matter in the universe. They are typically categorised into quarks, which carry colour charge and experience the strong interaction, as well as leptons, which carry no colour charge and are thereby "blind" to it. Every physical process can now be understood as the interaction between these matter particles through the exchange of virtual particles with spin one. These force carriers are known as gauge bosons: photons for electromagnetic interactions, W and Z bosons for weak interactions, and gluons for the strong force.

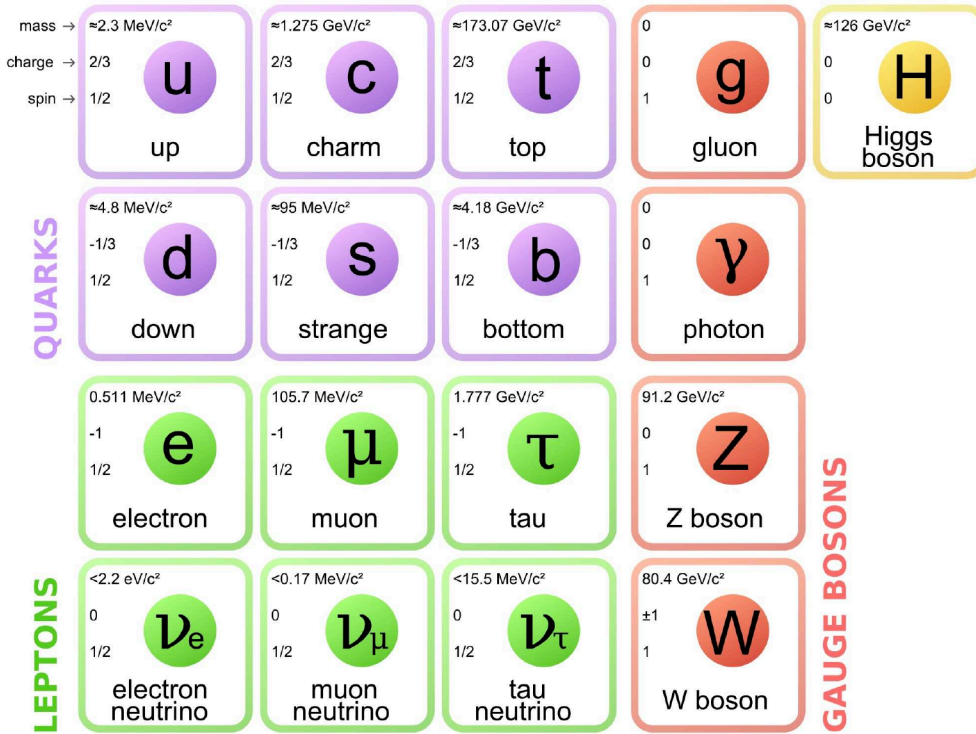


Figure 1.1: Summary of elementary particles in the Standard Model, together with their physical properties, e.g. mass, charge and spin. Figure taken from [6, 7].

Finally, the Higgs boson completes the current understanding of the Standard Model. Proposed by Peter W. Higgs along with François Englert and Robert Brout in 1964 [8], it is a scalar boson with spin zero, whose underlying quantum field is associated with mass generation. While a number of questions beyond the Standard Model remain unanswered [3], the experimental discovery of the Higgs boson in 2012 [9, 10] serves as one more confirmation of the described particle framework and led to the awarding of the Nobel Prize in Physics in 2013 [11].

Mathematically, the Standard Model is build upon relativistic quantum field theory (QFT). For instance, the Lagrangian of Quantum Electrodynamics (QED), describing the electromagnetic interaction, can be formulated as [6]:

$$\mathcal{L}_{QED} = \bar{\psi}(i\gamma^\mu \mathcal{D}_\mu - m)\psi - \frac{1}{4}F_{\mu\nu}F^{\mu\nu} \quad (1.1)$$

Where $F_{\mu\nu} = \partial_\mu A_\nu - \partial_\nu A_\mu$ is the electromagnetic field tensor and $D_\mu = \partial_\mu + ieA_\mu$ is the covariant derivative. In this case, one can identify e as the electric charge which serves as the essential property for

electromagnetic interactions.

Similarly, the strong force is described by the theory of Quantum Chromodynamics (QCD). Its Lagrangian can be written as [6]:

$$\mathcal{L}_{QCD} = \bar{\psi}_i (i(\gamma^\mu \mathcal{D}_\mu)_{ij} - m\delta_{ij}) \psi_j - \frac{1}{4} G_{\mu\nu}^a G_a^{\mu\nu} \quad (1.2)$$

Where, analogous to $F_{\mu\nu}$, one can identify the gluon field tensor $G_{\mu\nu}^a$:

$$G_{\mu\nu}^a = \partial_\mu A_\nu^a - \partial_\nu A_\mu^a + gf^{abc} A_{\mu c}^b A_{\nu c}^a \quad (1.3)$$

Initially, the Lagrangians between QCD and QED appear to have a similar mathematical structure. Upon closer examination, however, a crucial difference emerges in equation 1.3 from the additional term and its dependence on the f^{abc} . It describes the phenomenon that gluons, serving as gauge bosons, possess colour charge, enabling them to interact with other gluons. This is in contrast with QED, where photons cannot self-interact. This fact gives rise to a number of particular behaviours and characteristics unique to the strong interaction.

1.2 Strong Interaction Matter

As summarised in table 1.1, the strength of every interaction within the Standard Model is determined via a coupling constant. The magnitude of these constants varies with the energy scale, i.e. the momentum transfer Q between the interacting particles. It is illustrated in figure 1.2 for the strong interaction with α_s where the effect is particularly striking, a phenomenon typically referred to as running coupling constant.

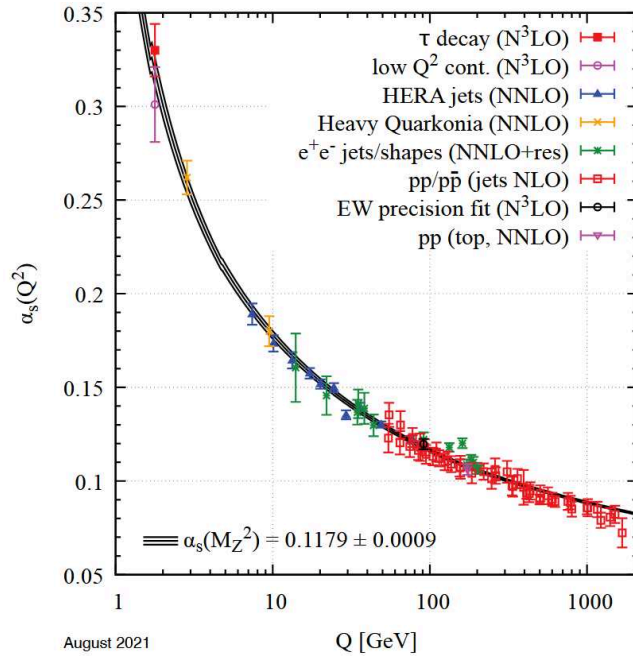


Figure 1.2: Summary of measurements of the coupling constant α_s of the strong interaction in dependence of the momentum transfer Q . Brackets indicate the respective degree of QCD perturbation theory used for the extraction of α_s . Figure taken from [12].

On the one side, at small momentum transfers, or equivalently at larger distances, the strong coupling constant α_S increases significantly. This behaviour leads to one of the defining features of the strong interaction: confinement. It dictates that colour-charged particles, such as quarks, cannot exist in isolation but are always bound together in colour-neutral configurations. These configurations manifest as hadrons which are further classified into mesons, e.g. pions, and baryons, e.g. protons. It can be understood intuitively because of the increasing force which would be required to separate a quark from such a system, eventually exceeding the energy needed for the production of a new quark - anti-quark pair. As such, the end result would again be two colourless hadrons.

However, on the other side, at high energies and short distances, the strong interaction becomes asymptotically weaker. This asymptotic freedom translates to weaker interactions at small distances. In this regime, the distinction between individual hadrons becomes less and less pronounced. Instead, the quarks and gluons act more freely and may form a more homogeneous "soup", called the Quark-Gluon-Plasma (QGP).

This transition between the confined phase of hadronic matter and the deconfined phase of quarks and gluons represents one of the key features of the strong interaction. Understanding this transition, and determining at what temperatures and densities such a transition occurs, is central to the study of QCD.

1.2.1 QCD Phase Diagram

The QCD phase diagram describes the behaviour of QCD matter under varying conditions. Most commonly, this entails the temperature T as well as the baryo-chemical potential μ_b , although other quantities like the isospin chemical potential μ_I , strangeness or electromagnetic fields may similarly impact the characteristics of matter [13]. The exploration of this phase diagram is the subject of various ongoing experimental and theoretical efforts [14, 15, 16, 17]. In particular, a large focus is set to find hallmarks of a potential first-order deconfinement and chiral phase transition, which would mark the existence of a potential QCD critical end point (CEP). Figure 1.3 shows a summary of a conjectured phase diagram and brings it into context with various measurements and theoretical predictions.

The area at vanishing μ_b and at high temperatures ($T \sim 155$ MeV) reflects conditions that were present in the early universe, i.e. a few microseconds after the Big Bang. Theoretically, this region of the phase diagram can be studied using perturbative methods or lattice QCD calculations. They predict a smooth crossover [19] region with a pseudo-critical temperature T_{pc} of around 150 MeV [20]. This is marked with the example of two such calculations as the yellow and blue band in figure 1.3.

Experimentally, such conditions can be induced in the laboratory with nuclear collisions with energies of a few TeV, such as at the Relativistic Heavy Ion Collider (RHIC) and CERN facility. Various observables, for example the nuclear modification factor or particle flow, seem to confirm that a new form of matter, e.g. the QGP, has been produced in such collisions [17]. The black symbols in figure 1.3 represent chemical freeze-out points as they are deduced via the statistical hadronisation model [21] fit to hadron yields as produced in the late stage heavy-ion collisions. A more direct measurement of the conditions, also during the hottest and high-density stage of the collisions, can be achieved through electromagnetic probes. The red triangles display such measurements and will be discussed in more detail in section 1.4.1.

With decreasing collision energies, the probed regions move towards higher μ_b and lower T . As indicated in figure 1.3, it is here where a conjectured critical endpoint is predicted. Unfortunately, predictions based on lattice QCD becomes less reliable for these higher μ_b due to the sign problem [16]. Instead, some guidance may come from other non-perturbative methods, e.g. functional renormalisation group approaches [22,

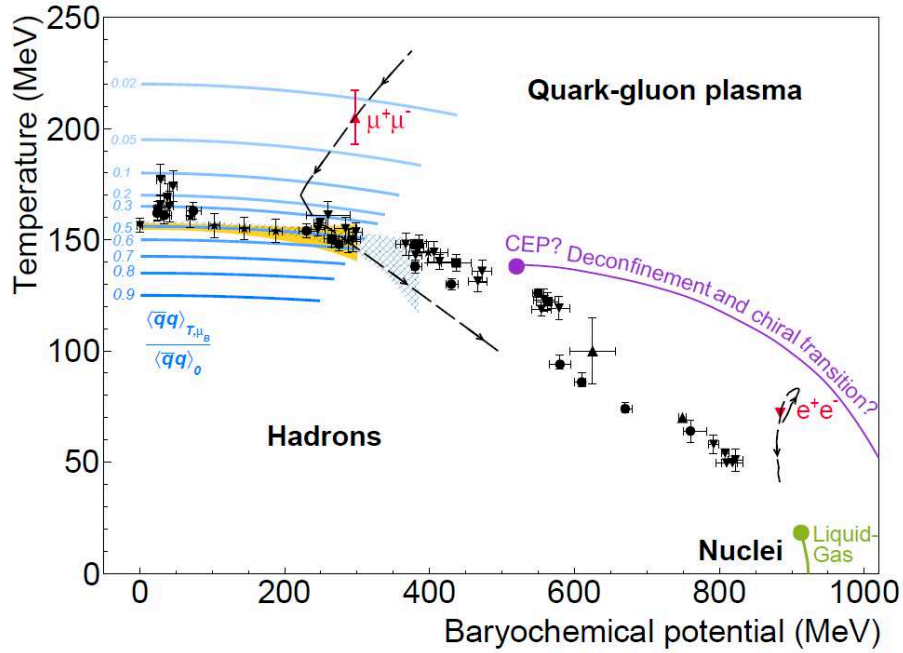


Figure 1.3: QCD phase diagram of strongly interacting matter. It shows experimental measurement points in black and red, along with theoretical prediction curves, both of which are discussed further in the text. Figure taken from [18].

23]. While no clear evidence of the CEP or a first-order phase transition has been established so far from lattice QCD calculations, various state-of-the-art theoretical approaches predict its location to be in a similar range of $T_{\text{CEP}} \sim 100\text{--}110$ MeV and $\mu_{\text{CEP}} \sim 420\text{--}650$ MeV [24].

Therefore, future experiments, in particular the CBM experiment [25] at the Facility for Antiproton and Ion Research (FAIR) [26] will be essential to experimentally study this particular energy range in more detail. Finally, the region of the highest μ_b and moderate temperatures in the right of figure 1.3 is probed by existing experiments, in particular the HADES experiment, which is essential for this work and described in detail in chapter 2.

While no QGP formation is expected to occur in nuclear collisions in this regime, the study of the equation of state (EoS) at such high densities is an equally active area of research in context of the QCD phase diagram. Among other aspects, it provides a baseline for theory and experimental data of higher collision energies. In addition, the resulting conditions of the QCD matter are particularly interesting in connection with astrophysics, namely neutron stars and neutron star mergers. Although the time and length scales differ by many orders of magnitude, the relevant densities and temperatures show remarkable similarities [18]. This is demonstrated in figure 1.4 which visually illustrates the comparability between neutron star mergers and heavy-ion collisions. In this way, the study of the EoS in the laboratory may directly constrain astrophysical observables [27]. Last but not least, the study of QCD matter at high temperatures, and even more so at high densities, is also fundamental for understanding chiral symmetry restoration.

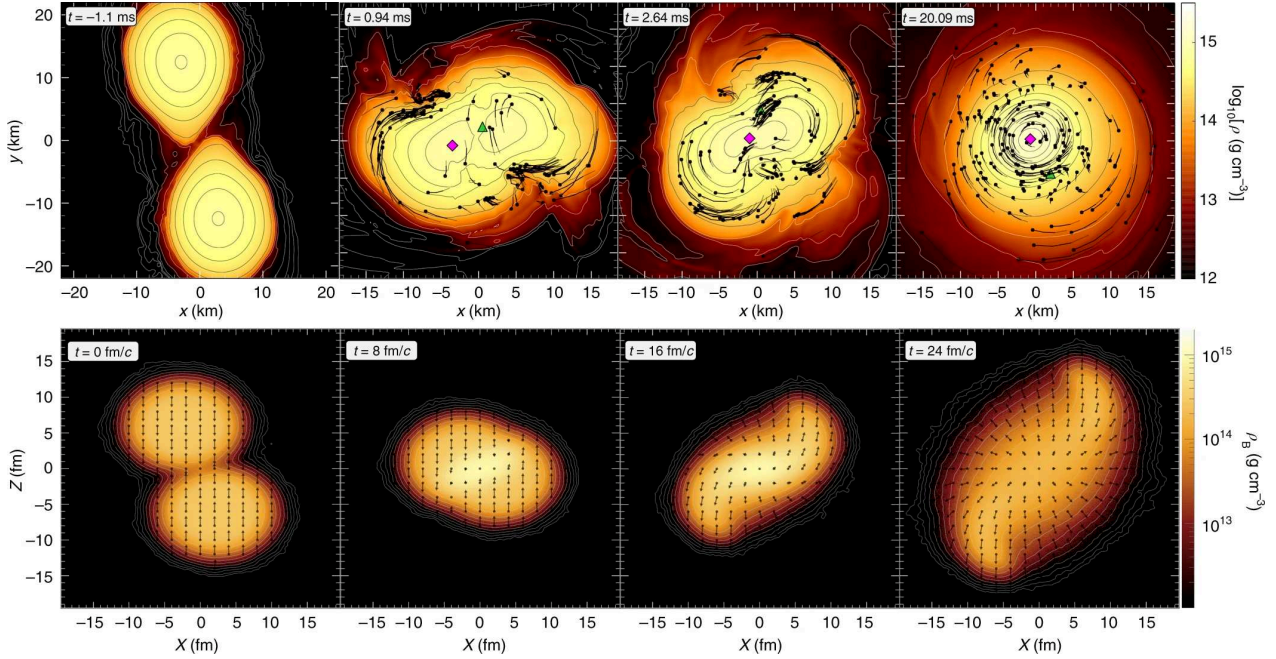


Figure 1.4: Comparison of simulations between a neutron star merger and a heavy-ion collision. Top row: Simulation of a $1.35 M_{\odot}$ binary neutron star merger, forming a compact object with temperatures up to 75 MeV and densities up to 5 times saturation. The green triangle marks the maximum temperature and the magenta diamond marks the maximum density. Bottom row: Energy density evolution in a non-central Au+Au collision at $\sqrt{s_{NN}} = 2.42$ GeV, with densities up to 3 times saturation and temperatures up to 80 MeV. Figure taken from [18].

1.2.2 Chiral Symmetry

Chiral symmetry in Quantum Chromodynamics refers to the invariance of the QCD Lagrangian under global transformations of left-handed and right-handed quark fields, mathematically described by the group $SU(N_f)_L \times SU(N_f)_R$ where N_f is the number of quark flavors [28]. It is known to be exact only for massless quarks ($m_q = 0$), and is therefore explicitly broken by QCD due to the non-vanishing masses exhibited in reality. Even so, it serves as a useful theoretical tool to explain a number of phenomena observed in nature. This includes the mass generation of hadrons, the emergence of pions with relatively small masses as well as the mass splitting of chiral partners in vacuum, e.g. the ρ meson at $775 \text{ MeV}/c^2$ compared to the a_1 meson at $1260 \text{ MeV}/c^2$ as seen in figure 1.5.

All of these effects can be related back to an approximate chiral symmetry which is true especially for the light quarks (up and down). With their small masses of only a few MeV/c [12], one may assume chiral symmetry to practically hold. The clear separation between chiral partners in vacuum, as seen in figure 1.5, is thus not a consequence of the explicit symmetry breaking. Instead, it is understood from spontaneous symmetry breaking.

A symmetry is spontaneously broken if the Hamiltonian generally fulfills the symmetry, except for the ground state. Such a scenario not only explains the observed mass splitting, but also further brings an intuition for the relatively, in comparison to other mesons, low masses seen in pions. Following the Goldstone theorem [20], one expects the emergence of massless Goldstone bosons, which is approximately fulfilled in nature by pions. In case of the chiral symmetry, this spontaneous breaking is induced by a

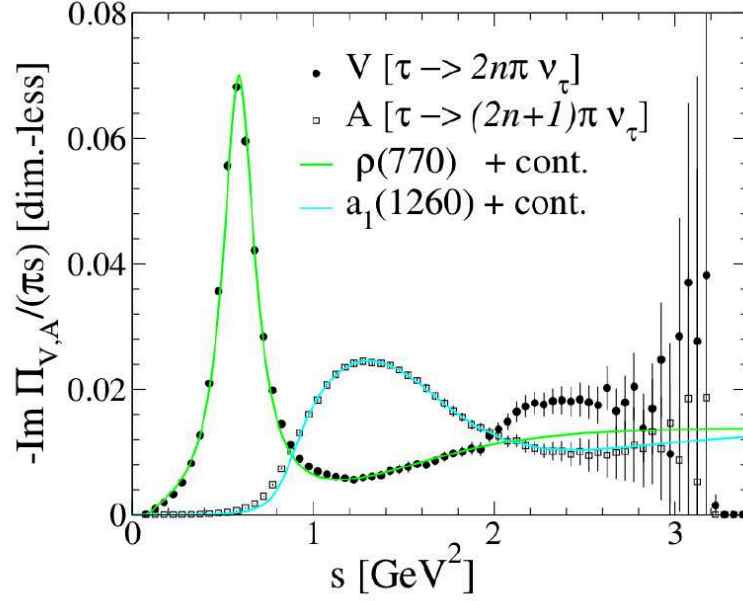


Figure 1.5: Comparison of vacuum ρ and a_1 spectral function. Black points indicate measurements made of the vector meson V and axial-vector meson A from τ decays [29], while the continuous lines represent fits using the spectral functions [30]. Figure taken from [31].

finite scalar quark-antiquark condensate $\langle q\bar{q} \rangle \neq 0$ in the vacuum state [31, 32]. Hence, the strength of the quark condensate directly translates to the degree of symmetry breaking. Although it cannot be measured directly, it may be inferred from the observed effects, most notably the mass splitting between chiral partners.

In the same vein, the restoration of the (approximate) chiral symmetry outside the vacuum state should be reflected in a degeneracy of the chiral partners once the finite expectation value of the quark condensate $\langle q\bar{q} \rangle$ decreases. This is demonstrated in figure 1.6. It shows one example which predicts a decrease of the quark condensate with increasing temperatures and densities. One can observe how this is encoded in the spectral functions of the two chiral partners, slowly approaching one another with the restoration of chiral symmetry.

Historically, two scenarios for this process are proposed. One approach, commonly referred to as Brown–Rho scaling, postulated a dropping mass of the ρ , as the medium approaches chiral restoration [33]. An alternative description, developed within hadronic many-body theory, predicts a strong broadening and eventual melting of the ρ spectral function due to interactions with the surrounding medium [34]. In general, however, current experimental evidence favours the broadening scenario as discussed in section 1.4.1.

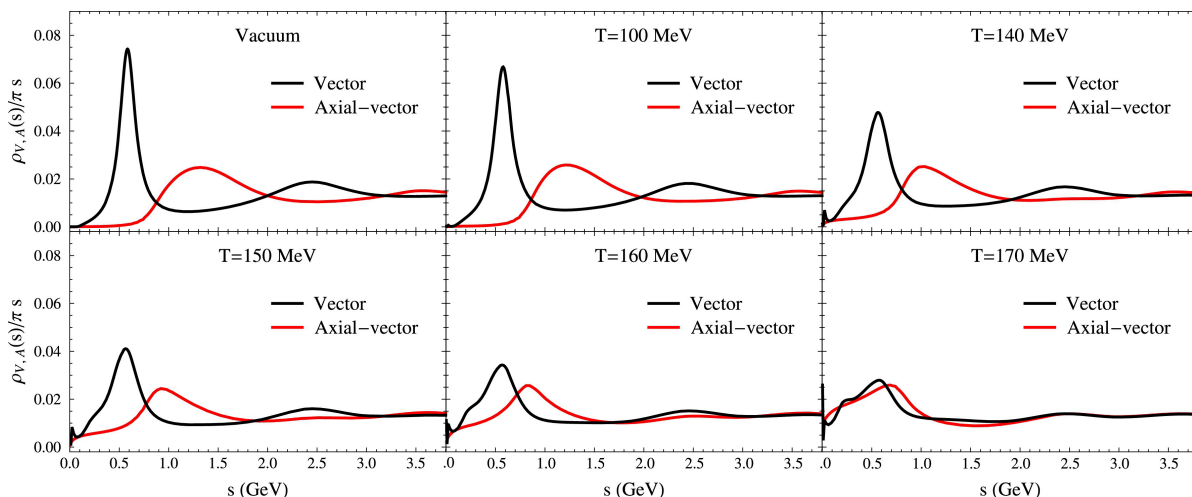


Figure 1.6: Prediction of the evolution of chiral partners particle spectra with increasing temperature. Figure taken from [35].

1.3 Probing the QCD Phase Diagram with Heavy-Ion Collisions

The essential tool to experimentally study the properties of QCD matter at higher densities and temperatures, i.e. to explore the QCD phase diagram and related effects like the chiral symmetry restoration, are nuclear collisions at relativistic energies. They are characterised by the acceleration of a nucleus with a particle accelerator and the subsequent collision with either a stationary target (fixed target experiment) or another particle beam (collider experiment).

While the resulting collision zone itself is too small and too short-lived for any direct observations, the measurement and analysis of the produced particles allows insights into the characteristics of the underlying matter. The collision energy, system size as well as centrality are thereby the crucial dials which govern the dynamics and properties in terms of probed densities and temperatures.

One major distinction is made by separating collisions into small systems (p+p or p+A) and heavy-ion systems (A+A), where the accelerated ions typically have mass numbers of $A \gtrsim 100$. Heavy-ion systems thus involve substantially more nucleons in the initial state, resulting in larger interaction volumes that enable the study of in-medium effects at high densities and temperatures. In this context, smaller systems serve mainly as a reference, while heavy-ion systems provide the primary environment for exploring strong interaction matter under extreme conditions.

An overview of key accelerator facilities and associated experiments is provided in table 1.2. It illustrates the rich history of nuclear collision research which began to gain momentum in the mid-20th century and continues to evolve through both ongoing and upcoming experiments today. Generally, every experiment serves a unique setup with distinct advantages and disadvantages. They are optimised for the specific energy range and may put special emphasis on selected aspects or observables of nuclear collisions. Consequently, the various experiments probe distinct regions of the QCD phase diagram and only by combination of the world data, a more complete picture of the entire QCD phase diagram may emerge. In every case, some overarching and general characteristics and properties of heavy-ion collisions can be identified.

Accelerator	Facility	Year	Projectile	max. Energy	Experiments
Bevalac	LBNL, Berkeley	1974–1993	C, Ne, Ar	2 AGeV	PlasticBall, Streamer Chamber DLS, EOS TPC
		1982–1984	Ca, Nb, La, Au	1 AGeV	
		1984–1993	Ca, Nb, La, Au	1 AGeV	
Synchrophasotron	JINR, Dubna	1974–1985	d, He	5 AGeV	
Saturne	Saclay	1978–1997	Ne, Ar	1 AGeV	DIOGENE
ISR	CERN, Geneva	1980–1983	d, He	15.7 AGeV	
SPS	CERN, Geneva	1986–today	O, S, In, Pb	200/158 AGeV	NA35, NA45, NA44, NA49 NA61, WA80, WA93, WA97 WA87, NA57, NA60, ...
AGS	BNL, Brookhaven	1986–1994	Si, Au	14.5/11.5 AGeV	E802, E810, E814, E859 E866, E877, E891, E895 E896, E910, E917, ...
SIS18	GSI, Darmstadt	1990–today	Au, Bi	2 AGeV	FOPI, KaoS, HADES ALADIN, INDRA, TAPS
RHIC	BNL, Brookhaven	2000–today	Cu, Au, U d, He, Zr, Ru	$\sqrt{s_{NN}} = 200$ GeV	STAR, PHENIX, BRAHMS PHOBOS
LHC	CERN, Geneva	2009–today	Xe, Pb	$\sqrt{s_{NN}} = 5.5$ GeV	ALICE, CMS, ATLAS, LHCb
SIS100	FAIR, Darmstadt	2028		11–14 AGeV	HADES, CBM

Table 1.2: Overview of heavy-ion collision experiments and their corresponding accelerators, facilities, and key characteristics. Table adapted from [5], based on information from [36, 37].

Evolution of a Heavy-Ion Collision: The conditions created in nuclear collisions are highly dynamic, short-lived, and rapidly changing over time. Any measurement captures the final-state particles which have emerged after all interactions within the original medium have seized. While there are some possibilities of more direct measurements via electromagnetic probes, which are discussed in section 1.4, useful interpretations of the collected data always requires knowledge of the initial conditions as well as an understanding of the hadronisation and freeze-out processes. A typical evolution of a heavy-ion collision is depicted in figure 1.7. Generally, the exact dynamics are heavily dependent on the collision energy and system size. Here, we focus on the stages typically identified for energies of a few GeV per nucleon:

- **Initial NN collisions:** At such energies, the colliding nuclei experience moderate Lorentz contraction along the beam axis. As the nuclei approach each other and begin to overlap, individual nucleons undergo first-chance binary collisions. It is accompanied by significant baryon stopping in which the incoming nucleons lose a substantial portion of their longitudinal momentum and deposit energy within the interaction zone.
- **Hot and dense fireball:** The initial stopping of the incoming nuclei leads to a rapid buildup of density and energy. Once the nuclei fully overlap, the system reaches its hottest and densest state. At sufficient collision energies, a QGP may be formed. At lower energies of a few GeV per nucleon, the system compresses into a dense, baryon-rich medium. In some ways the system acts as one (locally) thermalised fireball.
- **Freeze-out:** Subsequently, the whole system expands and cools down over time. Initial and newly created hadrons might scatter inelastically along themselves, creating further excited states and new particles. The end of inelastic scattering marks the point of chemical freeze-out. Once elastic

scattering seizes as well, the so-called kinetic freeze-out is reached. What remains are the final-state particles which can be measured by the detectors.

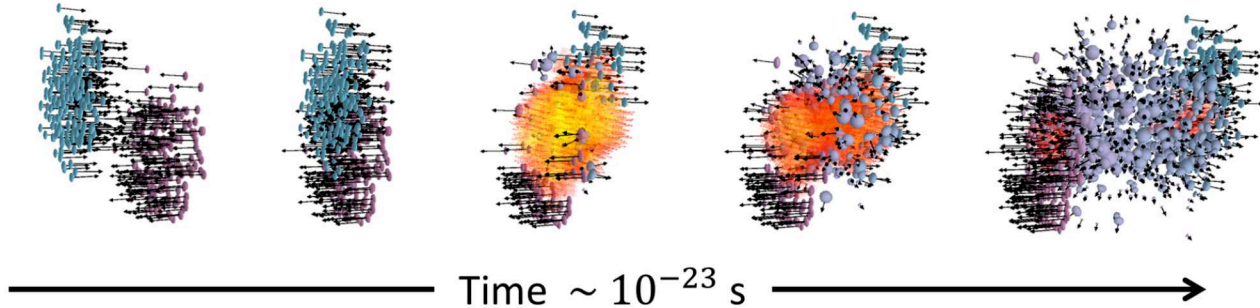


Figure 1.7: Visualisation of the evolution of a heavy-ion collision, based on a UrQMD simulation of Au+Au collisions at $\sqrt{s_{\text{NN}}} = 20$ GeV.

Collision Centrality: Due to the extremely small size of atomic nuclei, which is in the order of a few fermi, a direct controlled collision between selected individual ions is neither feasible nor practical. Instead, heavy-ion collisions are inherently statistical in nature. Ions are accelerated in bunches and brought to collide with a fixed or opposing beam target, leading to an overall collision probability. This is usually repeated millions of times in order to find and study the rare phenomena occurring in the resulting system. In this context, one major property that characterises every heavy-ion collision, is the collision centrality as demonstrated in figure 1.8.

If one assumes random collisions between two approximately circular nuclei, they will in all likelihood not collide fully, but with some impact parameter b which determines the size of the overlapping collision zone. All nucleons within this region are marked as participating nucleons N_{part} . All nucleons outside are referred to as spectators. In this way, the centrality is directly related to the size of the collision zone, as well as the amount of particles. Consequently, it directly impacts many observables and needs to be taken into account for most studies and comparisons to model predictions.

Mathematically, the centrality C can be defined as the fraction of the total nucleus-nucleus cross section σ_{AA} [38]:

$$C = \frac{1}{\sigma_{\text{AA}}} \int_0^b \frac{d\sigma}{db'} db' \quad (1.4)$$

A larger impact parameter b corresponds therefore to a larger centrality. These are referred to as peripheral collisions. Small impact parameters b refer to smaller centralities and are referred to as central collisions. Unfortunately, b is not directly accessible in experiment but can be estimated through the overall multiplicity in an event. The exact procedure for this work is described in more depth in section 3.3.

Collective Flow: Collective flow describes the bulk motion of particles produced in heavy-ion collisions, caused by the initial conditions and the subsequent compression and expansion of the interacting QCD matter. It is commonly separated into two phenomena. For one, radial flow describes the global expansion velocity β of the system. As the two colliding nuclei are compressed, large pressures and pressure gradients are formed, leading to the rapid expansion and cooling of the system. This rapid expansion is reflected

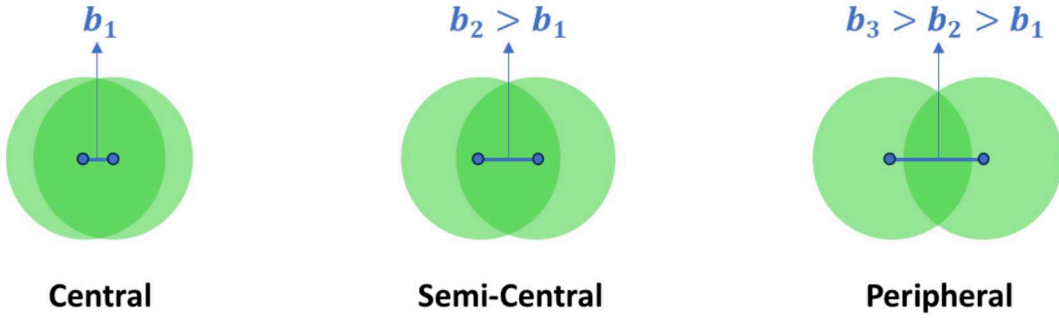


Figure 1.8: Illustration of the collision centrality, from central over semi-central to peripheral collisions with increasing impact parameter b , which spans between the centre of the two circular nuclei. The overlapping region in dark green defines the participating nucleons. The remaining light area corresponds to the spectators.

in a blue shift in the measured momentum spectra. The exact extent of this expansion depends crucially on how much pressure builds up from the energy density, i.e. how stiff or soft the medium is. Therefore, radial flow is directly related to the equation of state.

For another, there is anisotropic flow. It stems from initial spatial anisotropies of the participating nucleons, which translate into an anisotropy in the momentum distribution of the final-state particles. It is usually defined via the Fourier expansion [39]:

$$\frac{dN}{d\Delta\phi} \propto 1 + 2 \sum_{n=1}^{\infty} v_n \cos n(\phi - \Psi_{\text{RP}}) \quad (1.5)$$

where Ψ_{RP} is the azimuthal angle of the reaction plane, spanned by the impact parameter b and the beam axis. The azimuthal distribution is then fully characterised by the so-called flow coefficients v_n . They entail the directed flow v_1 and elliptic flow v_2 but also higher-order flow harmonics. The efficiency with which any initial spatial anisotropy is converted into momentum anisotropy similarly depends on the pressure-to-energy-density relation defined by the EoS. A stiffer EoS, which corresponds to higher pressure for a given energy density, produces stronger pressure gradients. This, in turn, is reflected in the magnitude of the flow coefficients, making them uniquely sensitive to the EoS [27, 40]. At sufficiently high collision energies, where the system is thought to be thermalised, flow coefficients may also provide access to various thermodynamic transport properties such as the bulk viscosity to entropy density ratio ζ/s and shear viscosity to entropy density ratio η/s [40, 41, 42].

Figure 1.9 shows available measurements with protons of the slope of the directed flow v_1 as well as elliptic flow v_2 for various collision energies. One can note a positive v_2 , representing an in-plane emission, at higher energies of dozens of GeV and above. This aligns with the naive expectation from the almond shape of the initial collision zone and can be described theoretically by hydrodynamic simulations [43, 44]. However, at collision energies of a few GeV, this picture becomes more complex. The measured freeze-out hadrons exhibit a negative v_2 , representing an out-of-plane emission due to the so-called squeeze-out effect. It stems from the interplay with spectators, which can partially block the emission of particles in-plane. Extracting meaningful information about the equation of state under these conditions therefore requires a detailed understanding of the time evolution of anisotropic flow. This generally necessitates microscopic

simulations of the collision dynamics using transport models [45] which are discussed further in sections 1.4.2 and 3.1.1.

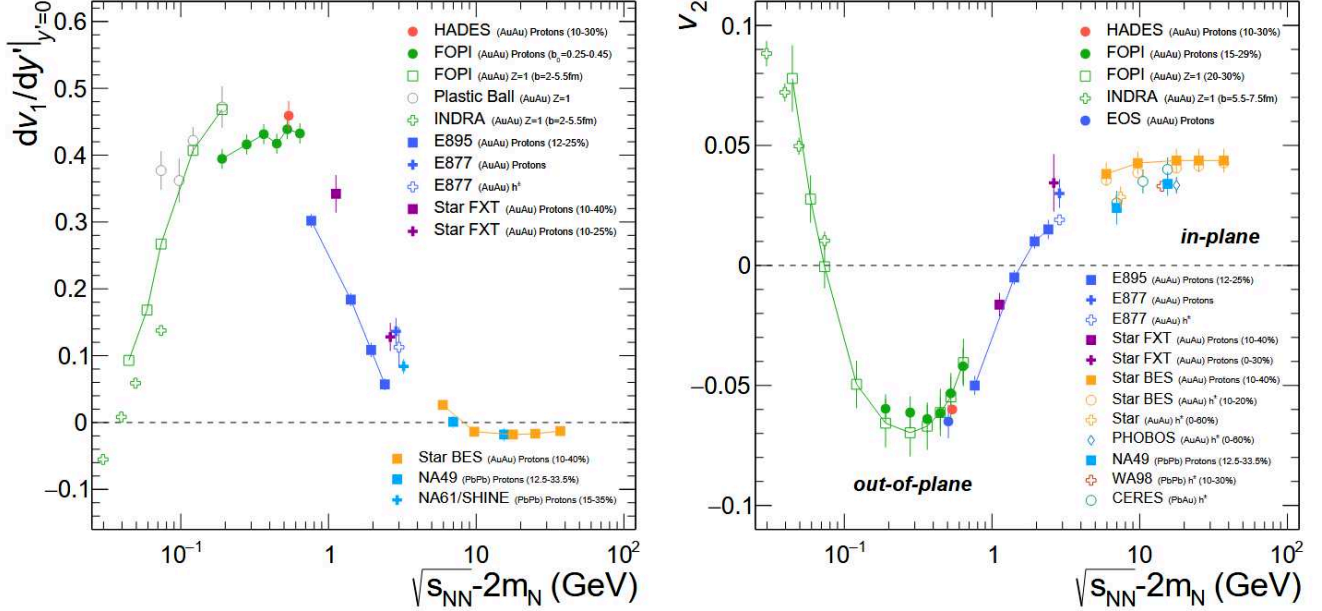


Figure 1.9: Flow coefficients as a function of excess energy energies based on available world data.. Figure taken from [46].

1.4 Electromagnetic Probes

One of the main challenges in the study of heavy-ion collisions, is the interpretation of how the measured final-state particles relate back to the early stages of the collision of highest temperature and density. Any strong interacting particle will be heavily impacted by the inelastic scatterings during the freeze-out stages. This makes direct conclusions about their origin and the nature of the matter during the fireball stage difficult. In this respect, electromagnetic probes, i.e. real and virtual photons (γ, γ^*), offer a unique perspective. Due to their lack of colour charge, they do not interact strongly and escape the medium without further scatterings, carrying immediate information from the moment of their creation to moment they are measured at detectors. Virtual photons, decaying into dilepton (l^+l^-) pairs, are particularly powerful, as the reconstruction of their invariant mass brings an additional observable. It encodes valuable information as will be demonstrated in chapter 6.

The possible dilepton sources are plentiful and depend on the available energy. Table 1.3 shows an overview of the most relevant contributions in heavy-ion collisions with energies of about 1-2A GeV.

One can note how the branching ratios (BR) for these electromagnetic decays are relatively small, in comparison to the dominant hadronic decays. This can be naively understood from from the presence of electromagnetic vertices in the decay processes. Each electromagnetic vertex contributes a factor of the fine-structure constant α to the transition amplitude, such that dilepton production via a virtual photon is suppressed by α^2 relative to strong decays. This is what allows electromagnetic probes to escape the medium largely undistorted, but also makes them more rare.

Source	J^P	I	Mass (MeV/ c^2)	Dominant Decay		Dielectron Decay	
				Channel	BR	Channel	BR
π^0	0^-	1	135	$\gamma\gamma$	98.8%	γe^+e^-	1.2%
η	0^-	0	547	$\gamma\gamma$	39.4%	γe^+e^-	0.5%
ρ	1^-	1	771	$\pi^+\pi^-$	100%	e^+e^-	4.7×10^{-5}
ω	1^-	0	782	$\pi^+\pi^-\pi^0$	89%	e^+e^- $\pi^0 e^+e^-$	7.3×10^{-5} 7.7×10^{-4}
ϕ	1^-	0	1019	K^+K^-	49%	e^+e^-	3×10^{-4}
Δ	$3/2^+$	3/2	1232	$N\pi$	>99%	pe^+e^-	4×10^{-3}
pn Brems.						pne^+e^-	
pp Brems.						ppe^+e^-	

Table 1.3: Overview of dielectron (e^+e^-) sources at collision energies of 1–2A GeV, listing quantum numbers, masses, dominant decay channels and their branching ratios (BR), and rare dielectron decays. Inspired by a similar table in [47]. Branching ratios are taken from [12].

Table 1.3 further demonstrates the numerous possibilities for the emission of virtual photons. On the one hand, this benefits the experimentalists. On account of the various decay channels, electromagnetic probes are emitted at all times during the collision. In the very early stages of initial nucleon-nucleon interactions, Bremsstrahlung and Δ Dalitz-decays are most dominant. During the hot and dense fireball, the vector mesons (ρ, ω, ϕ) can describe the dilepton emission, as will be discussed in section 1.4.2. Most importantly is the ρ meson, which is most likely to decay within the fireball stage due to its short lifetime. Finally, later decays of the vector mesons, as well as the decays of η and π^0 occur during and after the freeze-out stages. In this way, one could probe the full evolution of the system via direct measurement of electromagnetic probes. In practice, however, the origin of individual measurements is hard to determine. Any dilepton measurement initially represents an integral from all possible sources, and thereby from all stages of the collision. Therefore, on the other hand, the contribution of interest needs to be isolated from the overall dilepton spectra.

All in all, the main appeal as well as the challenges become apparent. While the reconstruction of virtual photons allows unique insights and direct measurements of the earlier stages, a careful estimation of the full dilepton cocktail is necessary. On top of this, dileptons are rare probes. As a consequence from the small branching ratios, a large number of collision events needs to be recorded, in order to differentially interpret the results. In combination, this makes the experimental measurement challenging, yet highly desirable.

1.4.1 Experimental Results on Dilepton Production

The possibility to directly measure signatures of the hot and dense matter with electromagnetic probes has been explored with different collisions systems and various collision energies. Figure 1.10 shows an overview of some of the essential past, current and future experimental facilities in this regard. As they have been established as a powerful probe, one can also highlight how various collaborations include a dilepton program in future planned operations.

Among the many important measurements, one famous example at higher collision energies comes from the Cerenkov Ring Electron Spectrometer (CERES) collaboration at the Super Proton Synchrotron (SPS). It

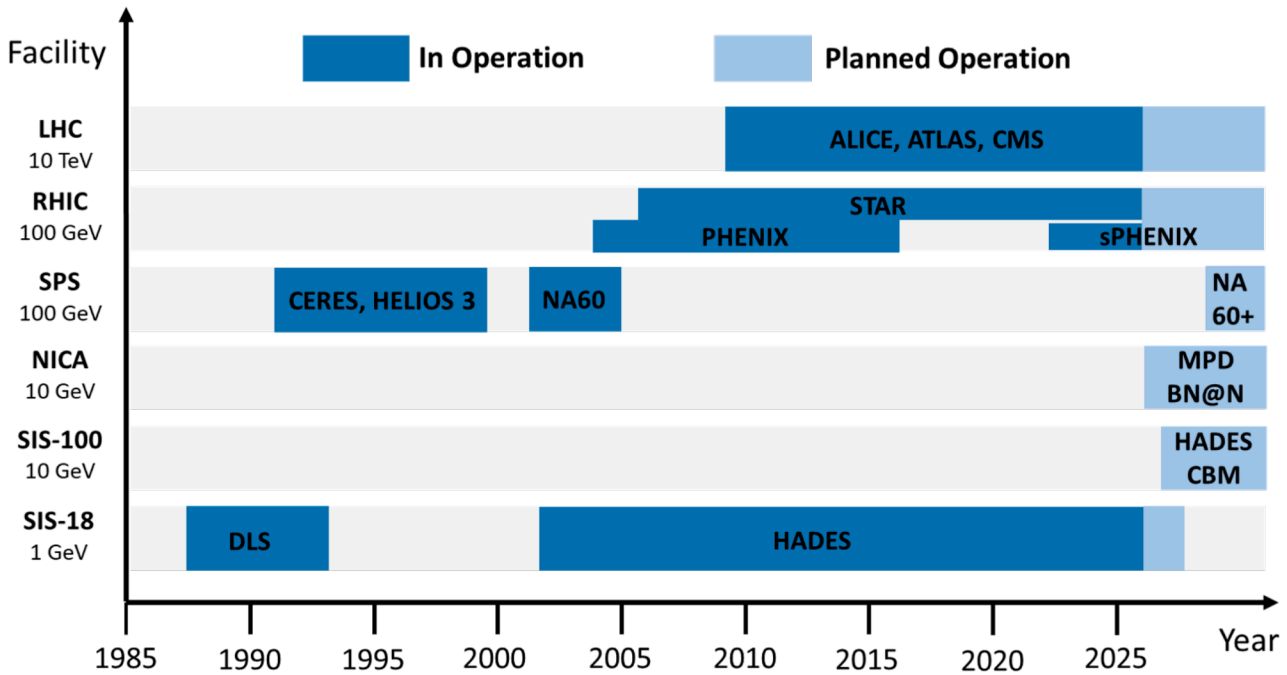


Figure 1.10: Timeline of key dilepton experiments illustrating the development of the field. Based on a similar figure in [31], with additional updates. The list is representative but not exhaustive.

was found that the reconstructed e^+e^- dielectron spectrum for proton induced p+Be and p+Au collisions at 450A GeV could be described fully by a simulated cocktail with electron pairs from hadron decays [48]. However, a larger system of S+Au at 200A GeV showed an enhancement by a factor of 5. This was reproduced for other heavy-ion collision systems, i.e. Pb+Au at 158A GeV and 40A GeV with an enhancement factor of 2.45 [49] and 5.9 [50] respectively. This clearly demonstrates the importance of the system size. Typically, any heavy-ion collision measurement needs to be compared with an elementary reference, namely p+p, p+n or p+A. It is this comparison and the subsequent analysis of the excess which brings information about the in-medium modifications. In this vein, the same Pb+Au data at 158A GeV allowed for the isolation of the ρ spectrum by subtraction of the remaining hadronic cocktail. The resulting spectrum is shown in the left panel of figure 1.11. For one, this allowed for first insights into the mechanism of chiral restoration. By comparison of the data with a mass-dropping against a broadening scenario, the restoration via broadening was found to be more likely. For another, the influence of the ρ -baryon interactions to the modifications was investigated. It showed how baryonic effects are essential to describe the measured data.

This was further underlined by measurements from the NA60 Collaboration in In+In collisions at 158A GeV via the dimuon ($\mu^+\mu^-$) channel [51, 55], which offers the unique advantage of reduced combinatorial background from conversion pairs, as well as the possibility to apply a trigger to collect higher statistics. The right panel of figure 1.11 shows the excess spectrum in comparison with several model predictions [52, 53, 54]. The best descriptions are again given by many-body calculations which take into account ρ -baryon interactions. Similarly, the broadening scenario is once more heavily favoured over a mass-dropping scenario [56, 57]. Finally, a Boltzman fit of the form $dN/dM \propto M^{3/2} \exp(-M/T)$ to the intermediate mass region from $1.2 < M < 2.0 \text{ GeV}/c^2$ was performed in order to extract a temperature. A value of $T = 205 \pm 12 \text{ MeV}$ [51] is found. This measurement is shown in figure 1.3 and noticeably higher than

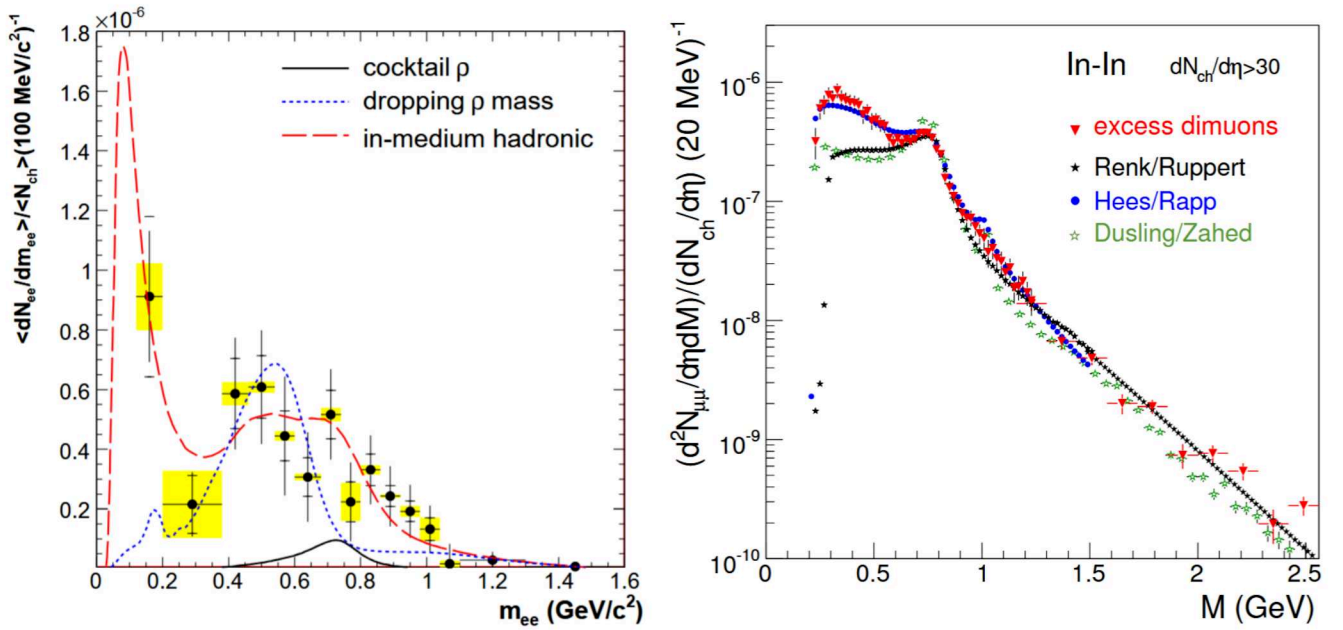


Figure 1.11: Left: Invariant mass spectrum of dileptons measured in Pb+Au at 158A GeV beam kinetic energy by the CERES Collaboration [49], together with model calculations of the ρ_0 spectral function. Right: invariant mass of excess dimuons measured at the same energy in In+In by the NA60 Collaboration [51] compared to the model calculations of Ruppert et al. [52], van Hees and Rapp [53] and Dusling and Zahed [54].

any temperature estimations from hadrons at freeze-out. It can be interpreted as the average temperature during the hottest and densest stage, demonstrating the penetrating nature of dileptons.

As one might expect, these and more effects are therefore studied further at other experiments with higher as well as lower collision energies. Within this group are recent measurement from the High-Acceptance-Di-Electron-Spectrometer (HADES) experiment of Au+Au collisions at $\sqrt{s_{NN}} = 2.42$ GeV [18]. As discussed in section 1.2.1, these energies probe the higher baryochemical-potential regime. As such, this region is particularly important for chiral symmetry restoration and the study of in-medium modifications induced by hadrons. The reconstructed dielectron excess is shown in figure 1.12. Similarly to the NA60 measurement, it is compared with various model calculations. A coarse-grained approach [58], utilising a heavily medium modified ρ spectral function, describes the data best. This is consistent with the findings from higher collision energies and strengthens the evidence for the importance of the in-medium collisional broadening due to the ρ coupling to baryons. In addition, a temperature T could be extracted from an analogous fit to the lower mass regions of $0.2 < M < 0.7$ GeV/c². It is found to be at $T = 71.8 \pm 2.1$ MeV and serves as the second dilepton temperature measurement shown in figure 1.3.

It is noteworthy that beyond these examples, a multitude of other aspects and observables are examined through electromagnetic probes [59]. Yet, it already becomes clear how the central advantages of electromagnetic probes are invariant across different collision systems and energies. Currently, active research is performed on bridging the gap between the measurements of NA60 and HADES, utilising the beam energy scan (BES) conducted with the Solenoidal Tracker at RHIC (STAR) experiment [60]. Finally, figure 1.10 indicates that future facilities plan to continue with new and updated dilepton programs. The CBM experiment will feature both a Ring Imaging Cherenkov (RICH) detector as well as a Transition Radiation

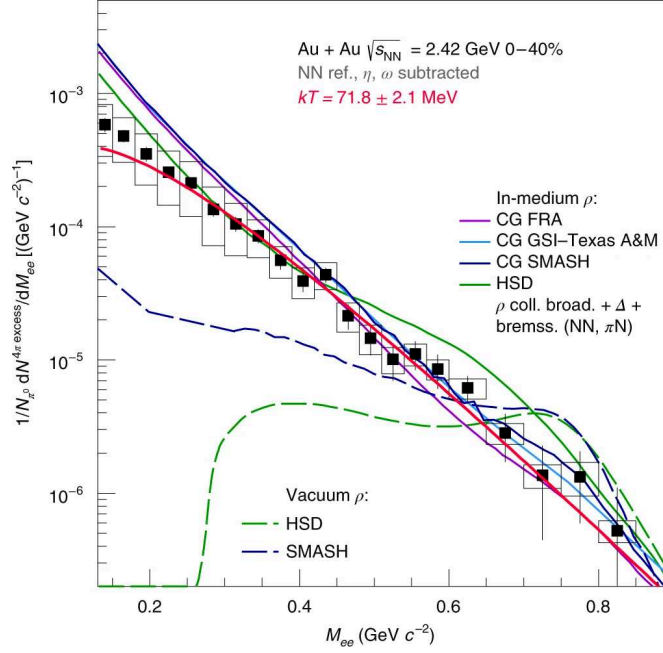


Figure 1.12: Dielectron excess yield measured in Au+Au collisions at $\sqrt{s_{\text{NN}}} = 2.42$ GeV. Various model comparisons as well as a fit to determine the temperature T are shown.

Detector (TRD) for electron identification and a muon chamber for precise muon detection, paired with high data acquisition rates of up to 10 MHz. These capabilities position CBM as a promising candidate for a new era of precision dilepton measurements. This is particularly significant, as it will probe collision energies near the expected critical end point which serves as a region of considerable theoretical and experimental interest as discussed in section 1.2.1.

1.4.2 Theoretical Description of Thermal Dileptons

In addition to the experimental dilepton measurements, several developments in their theoretical description have been made over the years. In general, the thermal dilepton emission rate per unit four-volume d^4x and four-momentum d^4q is given by the McLerran-Toimela-formula [61, 62]:

$$\frac{dN}{d^4x d^4q} = -\frac{\alpha_{em}^2}{M^2 \pi^3} f_B(q_0, T) \frac{L(M)}{M^2} \text{Im} \Pi_{em}^\mu(M, q; T, \mu_B) \quad (1.6)$$

where $f_B(q_0, T)$ is the thermal Bose function, $L(M)$ is the lepton phase space factor, $\text{Im} \Pi_{em}^\mu$ is the electromagnetic spectral function, and $M = M_{ll}$ is the invariant mass. This relationship enables the connection between measurements of dileptons in experiment to calculations of the electromagnetic (em) spectral function [62]. Furthermore, in the region of low masses ($M_{ee} < 1.1$ GeV/ c^2) one may assume the dilepton production to be powered by the vector mesons ρ , ω and ϕ , reducing the spectral function to the sum of the vector meson propagators [23, 31]:

$$\text{Im} \Pi_{em} \sim \text{Im} D_\rho + \frac{1}{2} \text{Im} D_\omega + \frac{2}{9} \text{Im} D_\phi \quad (1.7)$$

This is known as the vector meson dominance model (VDM) which has been successful in the description and prediction of experimental data [48, 55, 63], including the results highlighted in the previous section.

In the case of lower collision energies of 1-2A GeV one may note an additional challenge in the modeling. In contrast to the ultra-relativistic collisions at LHC/RHIC, one may not assume the fireball to act as a single isotropically expanding system in equilibrium and rely on hydrodynamic models. Instead, a coarse grained approach is applied [58, 64, 65]. Here, one simulates collisions using a microscopic transport model and separates the phase space into a finite 4-dimensional grid with the three spatial and one time dimension. For every cell within the grid, a thermalisation criterion is applied. Only if it is found to be thermalised and a temperature T can be determined, the thermal dilepton yield can be calculated via equation 1.6. In this way, it combines a microscopic transport and many-body approach to calculate the in-medium spectral function and suitably describe the available dilepton data [18]. In the end, it is the combination of experimental results with these theory predictions that enables precise interpretation of the data.

1.5 Motivation and Outline of this Thesis

The previous sections have introduced the QCD phase diagram and outlined how heavy-ion collisions provide a tool to explore strong interaction matter under extreme conditions. In particular, electromagnetic probes, and dielectrons in particular, offer a unique and direct window into the time evolution of the collision system, as they escape the medium largely unscathed and carry information from the hottest and densest stages of the fireball.

With this motivation, this thesis aims to reconstruct key dielectron observables from data collected at the HADES experiment. Building on previous studies of Ag+Ag collisions at $\sqrt{s_{NN}} = 2.55$ GeV [66], this work seeks to serve as an independent analysis at the same energy, and to extend the investigation to include multidifferential studies of Ag+Ag collisions at $\sqrt{s_{NN}} = 2.42$ GeV. This is intended to enable a more systematic characterisation of fireball properties, such as temperature, lifetime, and volume, from the measured dielectron spectra. Furthermore, inspired by an exploratory flow analysis in Au+Au collisions [67], this thesis aims to develop a complete analysis procedure to extract dilepton flow coefficients for Au+Au and Ag+Ag collisions at $\sqrt{s_{NN}} = 2.55$ GeV and $\sqrt{s_{NN}} = 2.42$ GeV. Recent theoretical studies [68, 69] highlight the sensitivity of dileptons to collective behaviour, motivating the development and application of such an analysis, which is expected to provide new insight into the complex time evolution of collectivity in this energy regime.

The thesis is organised as follows. Chapter 2 provides an overview of the experimental setup, focusing on the HADES detector components and the surrounding experimental facilities. Chapter 3 presents the general data processing and selection procedures employed in HADES. One particular emphasis is put on the development and application of a newly trained machine learning model to identify and remove contamination from collisions with surrounding target material. Chapter 4 focuses on the reconstruction and analysis procedures specific to dielectron spectra, including particle identification, background subtraction, and necessary corrections. Chapter 5 describes the additional challenges and procedures required for reconstructing the azimuthal anisotropy of dielectrons. Chapter 6 presents the evaluation and interpretation of the experimental results, including the extraction of fireball properties and collective observables, and places these findings in the context of previous experimental and theoretical studies, while also discussing future perspectives. Finally, Chapter 7 summarizes the main conclusions of the thesis and outlines potential directions for future research.

2 The HADES Experimental Setup

The High-Acceptance-Di-Electron-Spectrometer (HADES) has first been proposed in the 1990s. From the time of its construction around the 2000s, through its first production run in 2002, and continuing with several upgrades over the ensuing years, it has served as a unique experimental setup for exploring QCD matter through nuclear collisions. HADES is located at the Helmholtzzentrum für Schwerionenforschung (GSI) in Darmstadt. There, heavy-ions and hadrons beams are pre-accelerated in the adjacent Universal Linear Accelerator (UNILAC), injected to the Schwerionensynchrotron 18 (SIS18), and finally guided toward the fixed target located at the centre of the spectrometer. The physics program involves experiments with proton, deuteron and heavy-ion as well induced reactions, typically with energies around 1 to 2A GeV. On this basis, a wide range of physics questions can be addressed. Generally, this entails the exploration of the QCD phase diagram at high densities of a few times the saturation density, and moderate temperatures. For this purpose, a variety of probes and observables are investigated. Some examples include the study of hadron production [70, 71], fluctuations [72], flow [46] or strangeness [73]. Another central pillar of HADES is the study of electromagnetic probes. In fact, one of the original goals has been to study the medium modifications of the light vector mesons ρ , ω and ϕ through their leptonic decay channel [74]. This is reflected in the design of the experiment which demonstrates a number of key features which make it uniquely suitable to study dielectrons:

- **Geometrical acceptance:** The HADES is divided into 6 detector segments, also called sectors, which are fitted in a ring structure behind the target. The region between the sectors is kept as small as possible, thereby leading to an symmetric acceptance in the azimuthal angle ϕ of almost 360° . In addition, the main detector covers a polar angle θ from 18° - 85° . This coverage is particularly important at the designated collision energies of a few GeV per nucleon and allows reconstruction of dielectrons in the relevant phase space region with high efficiency and acceptance.
- **Rate capabilities:** In order to study the rare electromagnetic probes, a large number of collision events need to be collected to allow for the necessary statistics. Given the limited beam time allocated by the accelerator facility, high data-taking rates are highly desirable. After a key upgrade of the data acquisition (DAQ) system around 2011 [75], HADES is capable of recording heavy-ion collisions at rates up to 20 kHz. For more elementary beams of protons and pions, where measured multiplicities are smaller, this rate increases further up to 50 kHz.
- **Low material budget:** The full spectrometer is designed to minimize the amount of material that particles need to cross. This limitation of the material budget is especially helpful for dielectron analyses as it minimizes the background from pair conversion of real photons in the surrounding material.

A schematic layout of the HADES setup is shown in figure 2.1. It shows the various detector components, which come together to allow for an efficient detection of hadrons, leptons and photons. If not otherwise stated, the following descriptions focus on the setup as it was present during the 2019 Ag+Ag campaign.

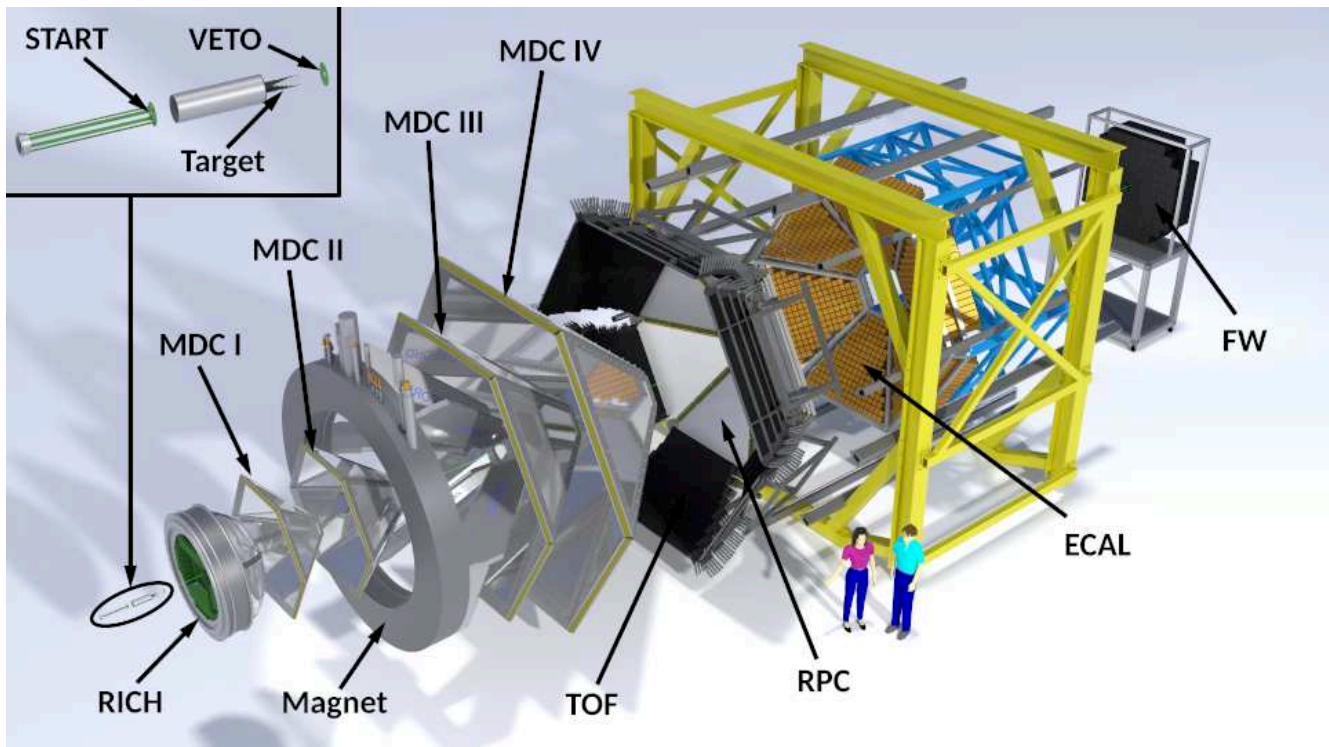


Figure 2.1: Schematic Layout of the HADES experiment in the 2019 Ag+Ag campaign.

2.1 GSI Accelerator Facility

The foundation of any collision experiment lies in the accelerator facilities that provide the desired beams at a given energy. For the HADES experiment at GSI, the acceleration process is divided into two main stages. The **UNILAC** serves as the initial accelerator. It is capable of delivering a wide range of ion species, from protons to uranium, at energies of up to 11.4 MeV per nucleon [76]. Ions are extracted from dedicated sources and accelerated in linear stages before being prepared for further acceleration. Depending on the required beam characteristics, different ion sources and charge states are employed. In many cases, the ions pass through a thin gas target to increase their charge state before final acceleration. The **SIS18** then further accelerates the ions to relativistic energies. This synchrotron has a maximum magnetic rigidity of 18 Tm. This translates to a final beam energy of up to several GeV per nucleon, depending on the ion species and charge state. For example, uranium ions can reach approximately 1A GeV, while protons can be accelerated up to 4.5 GeV. After acceleration, the beam is extracted and transported via dedicated beamlines to the HADES fixed-target setup. The facility supports high repetition rates necessary for dielectrons and similarly rare probes.

2.2 The Segmented Target

Depending on the experiment, various targets have been employed at HADES. The segmented targets for the heavy-ion campaigns of Ag+Ag (2019) and Au+Au (2012) are shown in figure 2.2. They are designed, first and foremost, to reduce the material budget and thereby the conversion probability of photons from

the collision [77]. Hence, it is segmented into 15 thin circular disks, each stationed at 4 mm distance. Each disk has a diameter of 2.2 mm and a thickness of 25 μm in the gold target of 2012 and 42 μm in the silver target of 2019, chosen in both cases to achieve an interaction probability of 1%. They are held in place by kapton strips with a thickness of 7 μm .

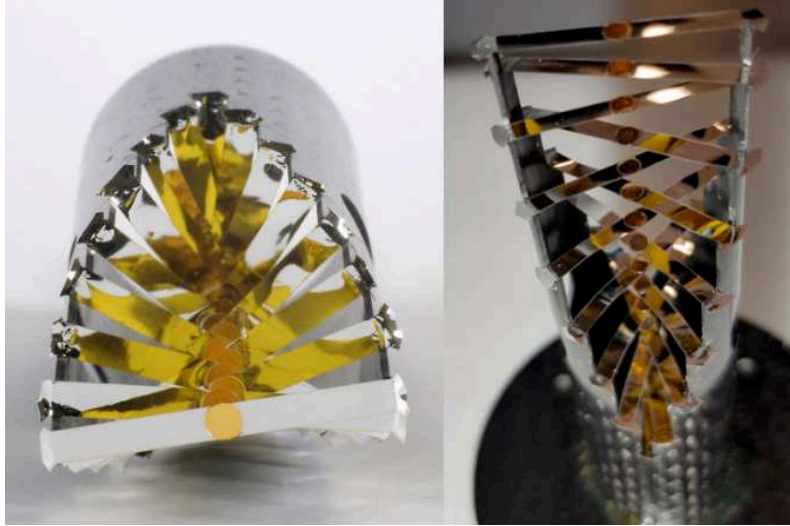


Figure 2.2: Photo of the segmented target for the Au+Au (left panel) and Ag+Ag (right panel) experiments in 2012 and 2019.

In order to avoid any contamination of beam collisions with the surrounding kapton structure material, as discussed in detail in section 3.5, more recent heavy-ion campaigns of 2024 and 2025 have employed an updated gold target. The kapton has been replaced by gold as the structure material, ensuring that every collision from the target zone is a true Au+Au collision.

2.3 START and VETO Detector

As seen in figure 2.1, there are two detectors placed right inside the beamline. The START detector is 2 cm in front of the target, and the VETO detector 70 cm behind the START. They are both single-crystal Chemical Vapor Deposition (scCVD) diamond-based detectors which demonstrate a high-radiation hardness, low interaction probability, due to their narrow thickness, as well as a good timing precision of the order of 50 ps [78], allowing precise determination of the reaction start time. The START detector consists of 16 strips in X and Y direction with a width of 300 μm . In this way, it provides a fine position measurement of the incoming beam, which is utilised for beam alignment and beam monitoring. As is discussed in section 3.5, it has also proven useful to assist in the rejection of potential Ag+C or Au+C events from collisions occurring with some probability with the kapton structure material around the target. Moreover, the signals from the START serve as the initial start times T_0 needed to calculate the time-of-flight. Further down the beamline, the VETO detector has lower spatial resolution, but can be used to suppress pile-up events by measurement of non-interacting beam ions. It thereby serves as a useful tool for the event selection criteria discussed in section 3.2.

2.4 Ring Imaging Cherenkov Detector

The Ring Imaging Cherenkov Detector (RICH) serves as one of the central components to identify and separate electrons and positrons from hadrons. Its underlying mechanism is the exploitation of the Cherenkov Radiation. It is emitted by particles travelling with a velocity β through a medium with refractive index n faster than the speed of light c_0 . This condition can be formulated as:

$$c = \frac{c_0}{n} \leq \beta c_0 \implies p_{th} = \frac{mc^2}{\sqrt{1 - \frac{1}{n^2}}} \quad (2.1)$$

In this way, the threshold momentum p_{th} needed to produce Cherenkov radiation, grows proportionally with the rest mass m of the traversing particle. A suitable choice of n thereby makes it possible to build a hadron blind detector in which only electrons and positrons emit radiation.

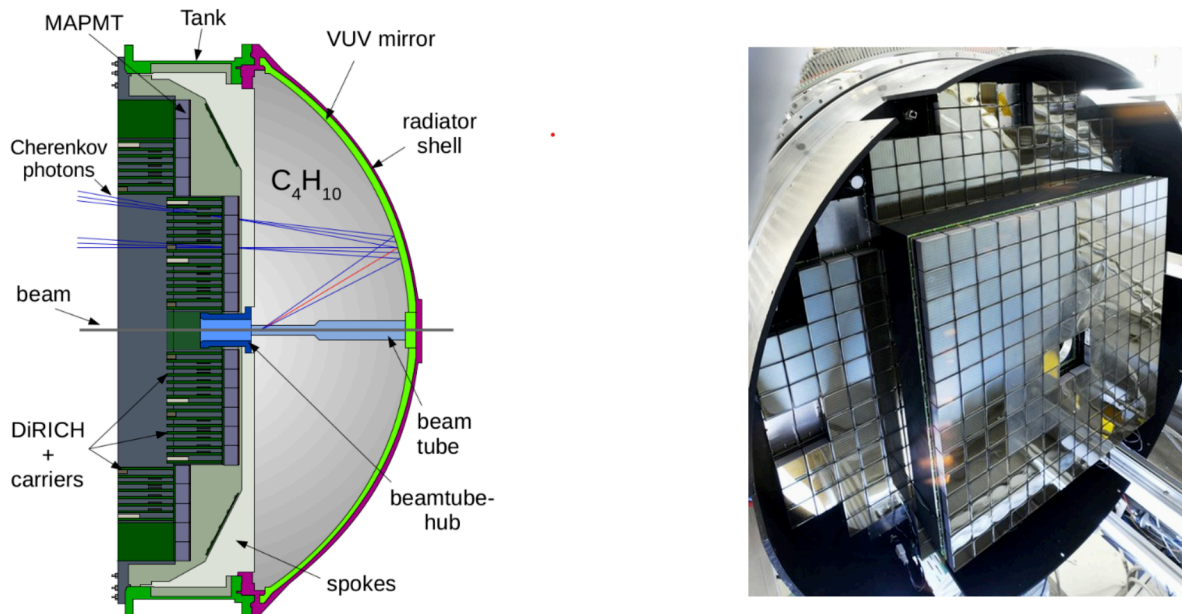


Figure 2.3: Left: Schematic layout of the RICH detector. Right: Photo of the MAPMT read out plane. Figures taken from [79, 80].

The RICH detector at HADES is depicted in figure 2.3. The central chamber is filled with C₄H₁₀ with a refractive index of $n = 1.0014$, which relates to a minimum momentum of electrons of $p_{th} = 9.65 \text{ MeV}/c$, according to equation 2.1. The next heavier particle, charged pions, requires a momentum of at least $p_{th} = 2630 \text{ MeV}/c$ to generate Cherenkov photons. Consequently, this makes the RICH essentially hadron blind at typical SIS18 collision energies.

In order to see any Cherenkov photons, they are reflected and focused by a Vacuum Ultra-Violet (VUV) mirror. They can then be measured by the PhotoMultiMultiplier (PMT) plane. Since 2018, the HADES RICH has been upgraded by replacing the old CsI+MWPC based detection system with H12700 MAPMTs [80]. This resulted in a significant improvement in the detection efficiency and separation of close rings, which is utilised in the dielectron reconstruction procedures discussed in chapter 4.

2.5 Multiwire Drift Chambers and Magnet

HADES is a magnetic spectrometer. By combination of a superconducting toroidal magnet with two pairs of multiwire drift chambers, one in front of and one behind the magnetic field, it is possible to reconstruct the trajectories and momenta of the traversing charged particles. This is discussed in section 3.1 from the data processing perspective. In terms of hardware, the two major components for this task include:

Multiwire Drift Chambers: A total of 24 multiwire drift chambers, four per sector, make up the central HADES tracking system. The central unit inside each of them are small gas-filled mini-drift cells (MDCs) which are interspersed with sense, field and cathode wires. Because of the applied field in the order of around 1800-2400V [81], any charged particle traversing a chamber leaves a trail of ionised gas atoms which drift to the surrounding anode wires, thereby giving an electric signal. Through six layers of MDCs, each stacked upon each other with different orientation angles ($0^\circ, \pm 20^\circ, \pm 40^\circ$), this allows for a precise reconstruction of a particles trajectory in the order of $85 - 125 \mu\text{m}$, while maintaining minimal material budget. The employed counting gas is Ar/CO₂ (70:30%).

Superconducting Magnet: The HADES magnet provides a kick to any charged particle flying through the detector, thereby allowing the reconstruction of the momentum via measurement of the strength of deflection. Ideally, the magnetic field should be constrained to the space between the two pairs of multiwire drift chambers. In particular, the identification of electrons within the RICH is designed to have a magnetic field free region around the target. Thus a toroidal field geometry, based on six coils around the beams axis, is utilised. In order to achieve the required field strength of up to 3.6 T, while maintaining a compact design, superconductivity is essential. The necessary temperatures are reached with liquid nitrogen and helium, cooling the system down to temperatures of about 4.7 K [82]. With this setup, a momentum resolution for electrons of $\sigma_p/p = 1.5 - 2\%$ is accomplished [83]. At the same time large solid angle ($\theta = 18^\circ - 85^\circ$) and large momentum range of $0.1 - 2 \text{ GeV}/c$ is covered. Generally, the two planes of MDCs in front of the magnet are referred to as the inner planes, the two planes of MDCs behind the magnetic field as outer planes.

2.6 Time-of-Flight Detectors

Behind the outer two planes of multiwire drift chambers are the time-of-flight detectors. They are referred to as the Multiplicity and Trigger Array (META) and are composed out of two systems covering different polar angles θ :

- **Resistive Plate Chamber Wall:** Resistive plate chambers (RPC) cover polar regions of $18^\circ < \theta < 45^\circ$. In the analysis, they are frequently referred to as system 0. They consist of two partially overlapping layers with three columns of 31 individually shielded RPC cells which are filled with an admixture of SF₆/C₂H₂F₄ (10:90%) [84]. In addition, build-in electrodes are used, in combination with a high voltage up to 6 kV [85], to create a strong electric field. Any charged particle crossing the cell will therefore ionize the gas and lead to an electric signal in the anode. This results in a time resolution of $\sigma_t \simeq 70 \text{ ps}$ with a positional resolution of about 8 mm. More importantly, this system can handle the high rates seen at these polar angles during experiments with heavy nuclei collisions. Quantitatively, rates of up to $1 \text{ kHz}/\text{cm}^2$ while maintaining a detection efficiency of 95% have been found in Au+Au collisions [84].

- **Time-of-Flight Wall:** The polar regions of $45^\circ < \theta < 85^\circ$ are covered by another time-of-flight (TOF) detector. In the analysis, it is referred to as system 1. In contrast to the RPC wall, the TOF wall is based on scintillator technology. More specifically, it consists of a total of 344 polyvinyltoluene-based plastic scintillator rods (Bicron BC-408) [86], arranged in the typical six sector fashion of HADES. Particles traversing the scintillating material transfer energy into it, thereby creating excited atomic states which emit light when falling back to their ground state. This light is measured at each side of the rod via photomultiplier tubes. This gives two arrival times and two signal amplitudes which can be used to estimate not only the time-of-flight of the particle, but also its position within the rod, as well as the energy loss. This setup achieves a measurement of the time-of-flight with a resolution $\sigma_t \approx 150$ ps [86], as well as of the position with a resolution of about 25 mm [5].

Together with the start time t_0 , these detectors allow for a reconstruction of the time-of-flight for every reconstructed charged particle. Combining this information with the trajectories, and thereby with the path lengths, enables the reconstruction of the velocity β , which finally serves as a major tool for particle identification as discussed in section 4.1.

2.7 Electromagnetic Calorimeter

Starting in 2018, HADES has been upgraded with an electromagnetic calorimeter (ECAL) [87, 88]. It covers polar angles of 12° to 45° and enables energy measurements of charged particles as well as neutral particles. The underlying detection mechanism is based on Cherenkov radiation. More specifically, the full ECAL wall consists of a total 978 lead glass elements. Any energetic probes traversing one such element deposits energy. For photons, the central interaction process is pair production, creating new dielectron pairs. For electrons, it is Bremsstrahlung, creating high energy photons. In this way, there is a reciprocal effect, resulting in the generation of a so-called electromagnetic shower. Due to the large refraction index of $n = 1.708$ in lead, the newly produced dielectrons travel faster than light inside the medium. This generates Cherenkov radiation which is finally measured at an adjacent photomultiplier. The number of Cherenkov photons is expected to be approximately proportional to the deposited energy. Assuming a sufficient module length, the full energy of the initial particle can be transferred into the medium. Therefore, the ECAL allows for an energy measurement and is the only detector at HADES capable of identifying photons as well as neutrons. In addition, ECAL serves as an important electron identification detector and provides a additional hadron suppression fraction for particle momenta above 400 Mev/ c . In the experiment of Ag+Ag in 2019, the ECAL has been operational in only two of the six sectors. The full installation was completed in 2023, which raises the possibility for a number of new measurements and makes additional decay channels, e.g. $\pi^0 \rightarrow \gamma\gamma$, experimentally accessible.

2.8 The Forward Hodoscope Wall

The Forward Wall (FW) is placed 6.8 m downstream the target, covering a polar angle of $0.3^\circ < \theta < 7.3^\circ$. It consists of 288 cells arranged around the beam axis as illustrated in figure 2.4. The changing granularity reflects the expected track density, i.e. considerably higher closer to the beam axis. Each cell is made up of a scintillator and photomultiplier tube, thereby delivering information about the deposited energy as well time-of-flight. This allows for a simple particle identification, in particular the charge Z of the nuclear fragments through the measurement of the energy loss. In this way, the detector is particularly valuable for

the reconstruction of projectile spectators which are used for the determination of the event plane, see section 3.4, as well as the centrality, see section 3.3.

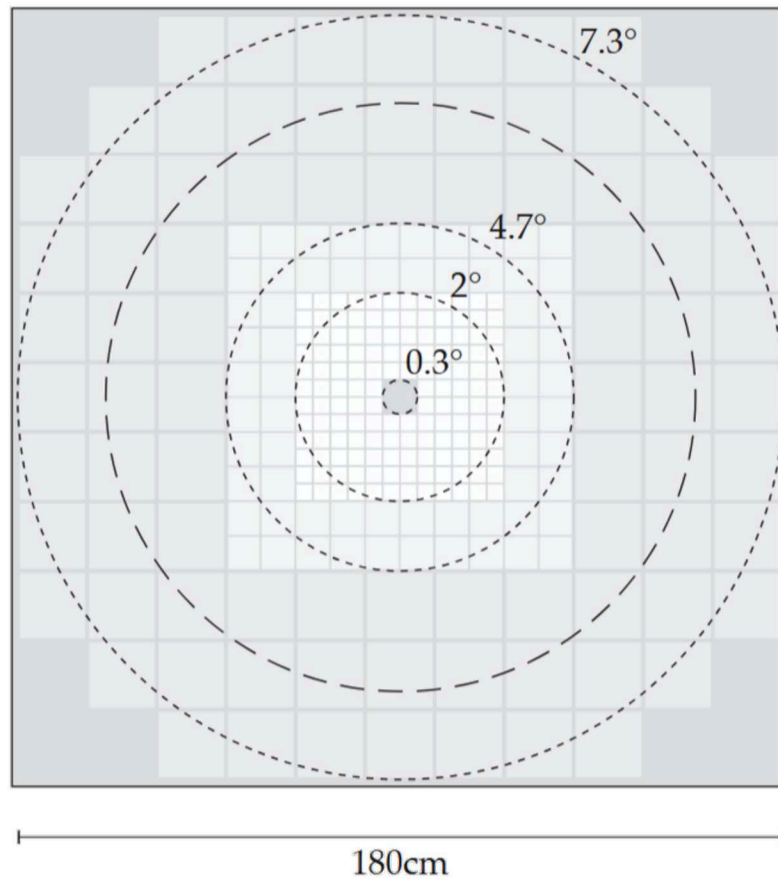


Figure 2.4: Illustration of the Forward Wall, demonstrating the increasing granularity closer to the beam axis. Figures taken from [5].

2.9 Data Acquisition and Trigger System

The sheer volume of data produced in heavy-ion experiments necessitates a selective data acquisition strategy. Consequently, a finely tuned data acquisition system (DAQ) [75] is employed to efficiently record only those events that are most relevant for the underlying physics goals, thereby maximising bandwidth usage and minimising unnecessary data storage.

At the heart of the DAQ system lies the Central Trigger System (CTS), which coordinates the readout process. First, signals from the detectors are processed by their respective front-end electronics (FEE), where they are digitised and timestamped. During the Ag+Ag beam time, the trigger logic mainly relied on the total number of hits recorded in the META detectors described in section 2.6. Two trigger conditions were defined. Physics Trigger 2 (PT2) required a minimum of 5 META hits. Physics Trigger 3 (PT3) required at least 20 META hits. As can be seen in section 3.3.2, the PT3 condition is fulfilled approximately by the 50% most central events, which were the main focus of this campaign. In order to study also some more peripheral events, e.g. for the centrality determination, a subset of PT2 events are also stored. In the

Ag+Ag beam time, only every 32nd PT2 event without a corresponding PT3 condition was accepted for recording. This significantly reduced the data load while maintaining a representative sample of peripheral interactions.

For all events passing the trigger conditions, the CTS distributes a global reference time and initiates the readout process. All FEEs transfer their data to the central DAQ infrastructure, where a set of event builders assembles complete events. The data are written to disk in the HADES Listmode Data (HLD) format which forms the basis for later analysis discussed in chapter 3. This architecture ensures a scalable and reliable acquisition system capable of operating under high interaction rates, while efficiently selecting and storing the most relevant events for further analysis.

3 General Data Processing and Selection in HADES

The HADES collaboration, over the course of more than 20 years of operation, has conducted a wide range of experimental campaigns across various collision systems, including proton, deuteron as well as pion induced reactions and heavy-ion collisions. They are summarised in table 3.1 with a compilation of the recorded number of events and total data volume. It illustrates the versatility of the experiment in terms of the diversity of beam species and energies. Moreover, one can note that there have been additional variations in internal settings within many campaigns, such as adjustments to the magnetic field to optimize the sensitivity to different observables across a wide momentum range.

Year	System	Energy [A GeV]	Recorded events [10^9]	Data [TB]
2002	C + C	2.00	0.25	1.2
2004	p + p	2.20	0.44	0.9
2004	C + C	1.00	0.495	1.1
2005	Ar + KCl	1.765	0.925	8.3
2006	d(n) + p	1.25	0.85	1.9
2007	p + p	1.25	1.70	5.3
2007	p + p	3.50	1.18	3.1
2008	p + Nb	3.50	4.21	13.6
2012	Au + Au	1.23	7.31	138.0
2014	π^- + A	0.5–1.57	0.38	2.1
2014	π^- + p	0.5–1.57	1.23	6.6
2019	Ag + Ag	1.58	13.64	333.6
2019	Ag + Ag	1.23	1.56	34.8
2022	p + p	4.50	40.2	662.0
2022	p + p	1.58	1.17	21.8
2024	Au + Au	0.2–0.8	5.57	122.3
2025	Au + Au	0.2–0.8	6.16	273.1

Table 3.1: Overview of past HADES production campaigns with the year, collision system, beam energy, number of recorded events, and total data volume. The horizontal line marks a major upgrade of the data acquisition system, enabling significantly higher recording rates. The bold rows indicate the Ag+Ag collisions which constitute the main focus of this work. Adapted from [5].

In general, the principles and core methods employed in the analysis of the collected data remain consistent across all experimental campaigns. However, it is important to emphasize how each of these systems introduces unique experimental challenges in terms of detector setup, beam energy, particle flux and event rates, all of which require tailored strategies for data acquisition, detector calibration, and analysis

procedures. As a result, each experimental run, or "beam time" is treated individually, with careful consideration given to the specific conditions of the experiment at hand.

Unless otherwise indicated, the focus of this work is primarily on the analysis of Ag+Ag collisions collected in 2019 at incident energies of $\sqrt{s_{NN}} = 2.55$ and 2.42 GeV. In particular, the high statistics measurement at 2.55 GeV represents one of the most statistically significant datasets available, providing a unique opportunity to study rare dielectron observables. The central software environment for all HADES analyses is the HADES System for Data Reduction and Analysis (HYDRA). Built on the ROOT framework [89] and written in C++, HYDRA extends ROOT functionalities with HADES specific classes, thereby forming the technical basis for handling and analysing the large datasets.

In every case, general data processing and preselection is required at the outset. This involves translating raw detector signals into physical observables, identifying track candidates, and determining global event characteristics. These initial steps form the foundation for higher-level physics analyses shown in chapter 4 and 5.

3.1 Creation of the Data Summary Tape

As indicated in section 2.9, the data acquisition system collects and stores relevant experimental data in uncalibrated HLD files during a data-taking campaign. They contain the raw data transmitted by the readout electronics from the various detectors, including measurements of the signal strength and amplitude obtained via Analog-to-Digital Converters (ADC) as well as timing information from Time-to-Digital Converters (TDC), along with hardware addresses that identify the module from which the signal originates. The first step in the analysis chain is to convert these raw signals into more easily interpretable quantities, thereby making them more suitable for higher-level physics analyses. At HADES, this is done centrally, and the processed data is saved into so-called data summary tape (DST) files. The essential steps in their production include [90]:

1. **Unpacking:** In order to save bandwidth during transmission as well as disk space during storage, the information from the detectors is sent in a compact, binary format. The first step entails the unpacking and decoding of the data.
2. **Calibration:** Raw data, such as ADC values, are initially in arbitrary units and must be calibrated to physical quantities, i.e. charge, energy etc. The calibration procedure also corrects for systematic effects, such as time walk [91], which can distort measurements. Calibration parameters are determined individually for each channel and detector module, accounting for both module-to-module variations and performance changes over time. These parameters are stored in an Oracle database and applied during DST production to ensure consistent and accurate data sets for both, experimental and simulated data.
3. **Hit Reconstruction:** After calibration, the next step is hit reconstruction, in which the calibrated data are used to create hits that represent a particle's interaction with the detector. This includes, for example, the reconstruction of RICH rings [92] or the determination of position and time of crossing points in the drift chambers or time of flight detectors. As a consequence of the large number of wires in the MDCs, a particular effort needs to be done to avoid ghost clusters. Therefore, a number of procedures to reduce ghost tracks are employed.

4. **Track Segment Reconstruction:** Based on the reconstructed hits, the first part of the track reconstruction focuses on the MDCs. In an initial approximation, the magnetic field is assumed to act purely like a kick plane between the inner and outer chambers. Accordingly, two straight-line segments may be constructed, one from the two inner chambers (inner segment) in respect to target, and one from the two outer chambers (outer segment) in respect to the kick plane.
5. **Full Track Reconstruction:** The resulting track segments are subsequently extrapolated and matched with the other detectors of the spectrometer. To quantify how close an inner track segment aligns with a RICH hit, the RICH matching quality (RMQ) is defined:

$$RMQ = \sqrt{(\theta_{ring} - \theta_{track})^2 + ((\phi_{ring} - \phi_{track}) \cdot \sin(\theta_{track}))^2} \quad (3.1)$$

Similarly, the META matching quality (MMQ) quantifies how well an outer track segment aligns with a hit in one of the two META detectors [93]:

$$MMQ = \sqrt{\frac{dx^2}{\sigma_x^2} + \frac{dy^2}{\sigma_y^2}} \quad (3.2)$$

Here, dx and dy correspond to the distance between the track intersection point and the measured hit in the coordinate system of the plane of the META detector. σ_x and σ_y are the spacial resolutions of the META detector at the hit position. Finally, the momentum is reconstructed on the basis of a full magnetic field map and Runge Kutta procedure. While this is computationally expensive, it offers the best momentum resolution. The resulting χ^2 may be used as an order parameter to asses the quality of a track.

It can be noted that the described track reconstruction process is an iterative procedure which also employs a number of rejection criteria to avoid fake-tracks. In the end, the essential information is compiled into the data summary tape (DST) files. They list all recorded events and include global information such as the reconstructed event vertex, trigger type, and global multiplicities. Additionally, each event is associated with a list of track candidates, each identified by reconstructed physical properties such as velocity, momentum, and charge.

As calibrations improve or software updates are made, the DST production is repeated, resulting in new and significantly improved data sets. The Ag+Ag data in this work was initially analysed using generation 5, but all final plots have been updated to generation 6, following its production in early 2025.

3.1.1 Simulations to Emulate the Detector Response

Beyond the experimental data, a number of simulation tools are utilised to interpret and supplement the analysis. Examples include, but are not limited to, basic consistency and cross-checks of assumptions and observables, as well as the estimation of a baseline for comparisons. Most importantly, they are necessary to reconstruct and understand the detector response, i.e. to estimate the efficiency and acceptance, as discussed in section 4.3.

In general, two types of event generators are employed at HADES. For one, microscopic transport models allow for the full simulation of heavy-ion collisions between two nuclei at a given energy. Several such

models exist, each with its own capabilities and limitations [94]. At HADES, version 3.3p2 of the Ultra-relativistic Quantum Molecular Dynamics (UrQMD) model [95, 96] was utilised for this purpose up to generation 5 of the Ag+Ag collision data from 2019. With generation 6 of early 2025, the simulation model has been changed to SMASH v3.1 [97]. The primary motivation for this transition was the inclusion of a coalescence afterburner, which improves the description of light nuclei production [98].

Moreover, it can be useful to study specific decay channels in isolation. This is especially relevant for rare probes, such as dielectron decays, where full event simulations predominantly generate unrelated processes, resulting in excessive disk usage and unnecessary computational overhead. To address this and ensure sufficient statistics for rare decays, the Pluto particle generator [99] is employed to simulate only the channel of interest. Pluto assumes the emission of particles from a thermal source and, based on input parameters such as temperature, radial expansion velocity and polarisation, generates the kinematic distributions of the final-state particles.

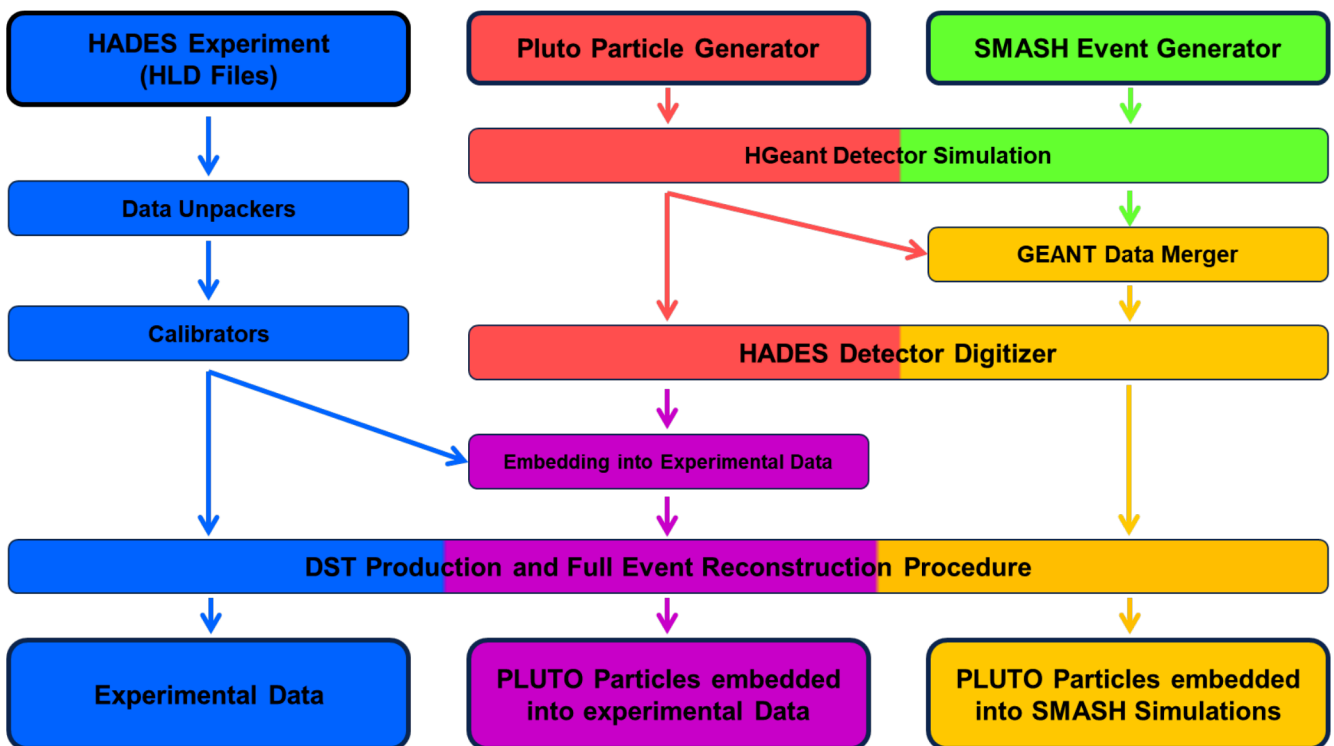


Figure 3.1: (Simplified) flow chart of the DST production process with and without simulations. The diagram shows how experimental data (blue), simulated Pluto particles (red), and UrQMD events (green) are processed into final DSTs: purely experimental data (blue), experimental data embedded with Pluto (purple), and embedded SMASH simulations (yellow). Figure inspired from a similar chart in [93].

Figure 3.1 illustrates how these simulation tools are then combined in practice. First, purely experimental data is processed according to the DST production procedure outlined in the previous section. Second, this experimental data can be supplemented with simulated particles from the Pluto event generator. In this case, the experimental data serves purely as background for the decay channel of interest, while the embedded simulation enables an estimation of the detectors ability to identify the decay products within this environment. Finally, a complete SMASH simulation may be employed to fully trace how specific particles contribute to observed detector signals. For example, this allows for an estimation of the purity, i.e.

the fraction of correctly identified particles relative to all identified candidates. Similar to the experimental data, these full-event simulations can also be embedded with rarer decay channels generated by Pluto to study their detectability. In all cases, the interaction of simulated particles with the detector material and magnetic field is modelled using the HGeant package, which is based on GEANT version 3.21 [100]. It includes the full three-dimensional geometry of the spectrometer, incorporating all detector subsystems and relevant structural components, along with their respective materials and physical properties. Based on the resulting interactions, digitizers simulate the detectors electronic response, generating signals equivalent to what would be recorded in a real experiment. The final production of DSTs is then performed analogously to the real data workflow, treating the simulated detector signals in exactly the same way. In the end, the inclusion of these simulations serves as an important tool for the analyses in chapters 4 and 5.

3.2 Event Selection Criteria

Not all triggered collision events collected during the experiment are of equal relevance for the analysis. Some events originate from reactions occurring outside the designated target region, while others suffer from incomplete or corrupted detector information. A particular class of problematic events are so-called pile-up events, where multiple collisions occur within a short time interval and are recorded as a single event. This results in overlapping detector signals which can severely distort the reconstruction of physical observables. In particular, pile-up complicates the track reconstruction procedure, causes incorrect vertex determination, affects time-of-flight measurements, and ultimately biases the efficiency corrections, thereby compromising the overall quality and interpretability of the data.

To ensure consistent data quality and minimize background or misreconstructed events, a series of event selection criteria are applied. These criteria aim to isolate well-defined, target-centred collisions with reliable detector responses. For the Ag+Ag experiment, the applied selection criteria are listed below [93], along with the corresponding flag names used in the HYDRA framework (version 2-7.0) where applicable.

- **Physics Trigger 3:** By default, only central and semi-central collision events are included in the analysis by requiring a positive PT3 decision. It takes at least 20 META hits in case of the Ag+Ag collisions from 2019, as discussed in section 2.9, corresponding to around 55% of the most central collisions. (`kGoodTrigger`)
- **Good Vertex:** Using the reconstructed event vertex from the track reconstruction, see section 3.1, events with a vertex position outside the range of -70 to 0 mm along the beam axis (z-direction) are rejected. This removes most reactions occurring in the START and VETO detectors and ensures that the reaction took place within the target region. (`kGoodVertexCand` and `kGoodVertexClust`)
- **No Flash MDC:** Events exhibiting an unphysically large number of hits in one or more MDC chambers are rejected. Specifically, the number of activated sense wires with a time-over-threshold below 30 ns and occurring earlier than 5 ns before the trigger are counted in each chamber. If this count exceeds 20 in any chamber, the event is removed to eliminate noise-induced false clusters. (`kNoFlashMDC`)
- **Good START hit:** The event must have a well-defined start time, as measured by the START detector. This is essential because it serves as a prerequisite for all time-of-flight measurements performed with the META detectors. (`kGoodStart`)

- **No additional START hit:** One of the criteria to suppress pile-up is to reject events containing a second START hit within a ± 15 ns time window. This helps to ensure a correct time-of-flight determination and minimizes the likelihood of signal overlap from multiple collisions. (kNoSTART)
- **No VETO hit:** A similar condition removes events with a VETO hit within the same ± 15 ns time window around the selected START hit. This is based on the assumption that the VETO detector primarily registers beam ions which did not interact in the target. Therefore, the presence of a VETO hit alongside a triggered event suggests that at least two beam ions passed through the START detector in quick succession. As a result, the START time may originate from either ion and is no longer reliable for time-of-flight measurements. (kNoVETO)
- **Good START-VETO:** The VETO detector is further used to reduce the likelihood of pile-up by verifying that no secondary reaction occurred within a time window of 15–350 ns after the selected START hit. Specifically, every additional START hit in this interval must be correlated with a VETO detector hit within ± 2 ns. Only under this condition can all subsequent START signals in this time frame be attributed to beam ions that did not interact in the target. (kGoodSTARTVETO)
- **Good START-META:** In a similar vein, all additional START hits occurring within the time window of 80–350 ns after the selected one are checked for correlations with META detector hits in a time-of-flight window of 7–12 ns. If more than four correlated hits are found, it may indicate a secondary interaction that produced additional META activity. Such events are therefore excluded to reduce the risk of pile-up. (kGoodSTARTMETA)
- **Good START Clusters:** A final START criterion is imposed on the total number of START hits occurring around the time of the event. For the Ag+Ag beamtime, this time window is around -450 ns to 550 ns. This requirement is motivated by the observation that a higher number of beam ions increases the probability of producing δ -electrons. These secondary electrons may interact with cells in the MDC, temporarily rendering them inactive until they reset. As a result, affected cells are unable to properly register particles originating from the event of interest, thereby reducing the overall tracking efficiency. Although this effect is, in principle, accounted for in the simulations used for efficiency corrections, see section 3.1.1, the impact becomes more pronounced as the number of δ -electrons increases. To minimize any large losses of tracking efficiency, only events with fewer than five additional START hits are retained in the analysis. (IsGoodSTARTCluster)
- **Good Sector:** To ensure consistent detector performance, each of the six sectors is evaluated run-by-run using the average yields of identified particle tracks (protons, π^+ , π^- , e^+ , e^-). Runs where any sector shows deviations beyond $\pm 7\%$ for hadrons or $\pm 10\%$ for leptons compared to daily averages are rejected. This procedure helps exclude periods with significant detector inefficiencies or instabilities that may not be accounted for in simulations, thereby improving the reliability of track reconstruction and efficiency corrections. (IsGoodSector)
- **Good Event Plane:** For analyses involving the azimuthal distribution of particles, a reliably reconstructed event plane, as discussed in 3.4, is essential. Thus, events in which the event plane could not be accurately determined, as is the case in some of the most central events with few to none spectators, are omitted from the azimuthal analyses described in chapter 5. (IsGoodEventPlane)

The sequential application of the event selection criteria is summarised in figure 3.2. It is based on a subsample of the full dataset. Approximately 50% of the initial global event sample remains after all criteria have been enforced. The proportion is slightly higher in the energy of $\sqrt{s_{\text{NN}}} = 2.42$ GeV, most likely because of differences in the intensity and fine-tuning of the beam. The remaining dataset represents a

balanced compromise between maintaining sufficient statistics and ensuring high data quality, forming the foundation for the subsequent analysis.

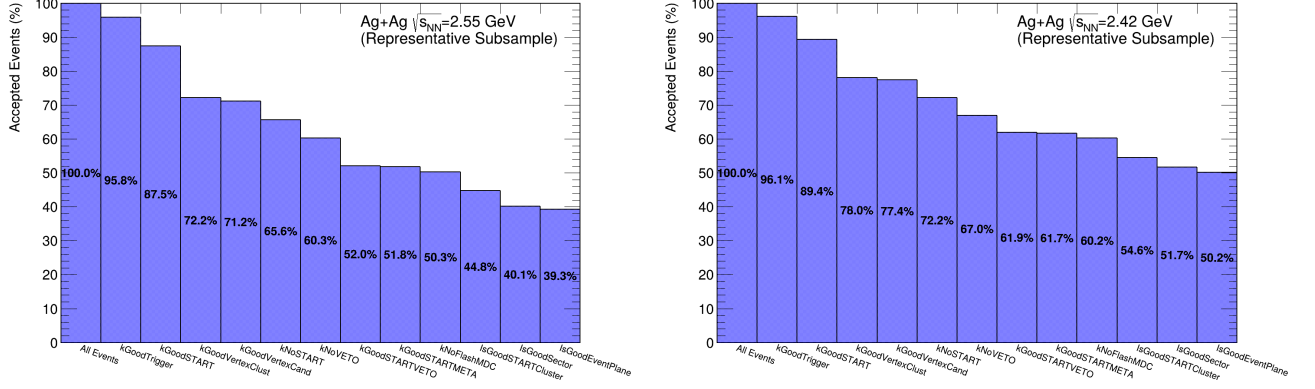


Figure 3.2: Percentage of accepted events after subsequent application of the event selection criteria for the Ag+Ag collisions at $\sqrt{s_{NN}} = 2.55$ GeV (left panel) and 2.42 GeV (right panel).

3.3 Centrality Determination

As introduced in section 1.3, an essential event characteristic that significantly influences many observables in heavy-ion collisions is the collision centrality. While the relevant impact parameter b cannot be directly measured in experiment, there are two general strategies to infer it from experimentally accessible observables. One method involves detecting the spectator nucleons, which can be achieved at HADES using the Forward Wall detector. The alternative approach is based on estimating the multiplicity of particles produced in the interaction zone. In the HADES experiment, this can be realised either by counting the number of reconstructed charged particle tracks N_{tracks} , or the number of hits in the META system N_{META} . All of these options have been explored and compared in previous works [101]. In the end, the latter, based on N_{META} , serves as the default estimator in this analysis. It provides a fast and inclusive measure of event activity with stable acceptance over the entire data-taking period.

The reconstruction of centrality relies on the assumption that the impact parameter b is, on average, proportional to the number of participating nucleons N_{part} . Furthermore, N_{part} is assumed to be proportional to the observed multiplicity, in this case measured via N_{META} . Based on these assumptions, the original definition of centrality, given in equation 1.4, can be reformulated in terms of the measured multiplicity, yielding the following expression [38]:

$$C \approx \frac{1}{\sigma_{AA}} \int_{N^{\text{thr}}}^{\infty} \frac{d\sigma}{dN'} dN' \quad (3.3)$$

where N^{thr} is the lower multiplicity threshold of a given centrality class, and σ_{AA} is the total nucleus-nucleus cross-section.

3.3.1 Glauber Monte Carlo Simulation

In order to estimate the nucleus-nucleus cross-section σ_{AA} and understand how the average number of participating nucleons $\langle N_{\text{part}} \rangle$ relates to the impact parameter b , a Glauber Monte Carlo simulation [102] is employed. Assuming that the motion of individual nucleons is independent, and that their large momenta allow them to travel nearly undeflected, the Glauber model serves as a relatively simple, yet effective, description for the centrality of heavy-ion collisions [103]. This approximation, known as the eikonal approximation, is well established for high energies, typically for collision energies of $\sqrt{s_{\text{NN}}} \geq 10$ GeV [38, 104, 105]. However, it has also been demonstrated to provide a useful description at lower energies [106]. As a result, the heavy-ion collision is modeled as the collection of independent binary nucleon-nucleon collisions. In the first step, the positions of the nucleons within the colliding nuclei are generated according to a realistic density profile. In this case, a two-parameter Fermi distribution is employed [38]:

$$\rho(r) = \frac{1 + w \left(\frac{r}{R}\right)^2}{1 + \exp\left(\frac{r-R}{a}\right)} \quad (3.4)$$

Based on [107], the parameters are set to $R = 5.301$ fm, $a_{\text{Ag}} = 0.523$ fm and $w = 0$ for silver. An additional hard constraint is imposed to ensure that nucleons are not positioned closer than 0.9 fm, accounting for the physical size of nucleons and their repulsive forces at short distances. Once the nucleon positions are generated, the two nuclei are placed relative to each other based on a randomly chosen impact parameter b . The collision simulation then involves calculating the closest approach between nucleons from the projectile and target nuclei. If the distance between two nucleons falls below a critical value determined by the inelastic nucleon-nucleon cross-section $\sigma_{\text{inel}}^{NN}$, the nucleons are considered to have interacted. This condition is mathematically expressed as [38]:

$$b_{NN} \leq \sqrt{\frac{\sigma_{\text{inel}}^{NN}}{\pi}} \quad (3.5)$$

The inelastic nucleon-nucleon cross-sections are taken from [108, 109] and set to $\sigma_{\text{inel}}^{NN} = 27.23$ mb for pp or nn collisions and $\sigma_{\text{inel}}^{NN} = 24.26$ mb for pn or np collisions for an energy of $\sqrt{s_{\text{NN}}} = 2.55$ GeV, or $\sigma_{\text{inel}}^{pp} = 26.4$ mb and $\sigma_{\text{inel}}^{np} = 21.0$ mb for the energy of $\sqrt{s_{\text{NN}}} = 2.42$ GeV. In the end, nucleons that satisfy this condition are classified as participants. By repeating the Monte Carlo simulation multiple times, the statistical relationship between the impact parameter b and the number of participants N_{part} can be accurately established. It is shown in figure 3.3.

3.3.2 Resulting Centrality Classes

The resulting distribution of N_{part} is subsequently related to an experimentally measured multiplicity N_{ch} based on the wounded nucleon model [110]:

$$\langle N_{\text{ch}} \rangle = \mu \langle N_{\text{part}} \rangle \quad (3.6)$$

The central idea is that the average number of charged particles produced is directly proportional to the average number of participating nucleons, with μ acting as the proportionality constant. Crucially,

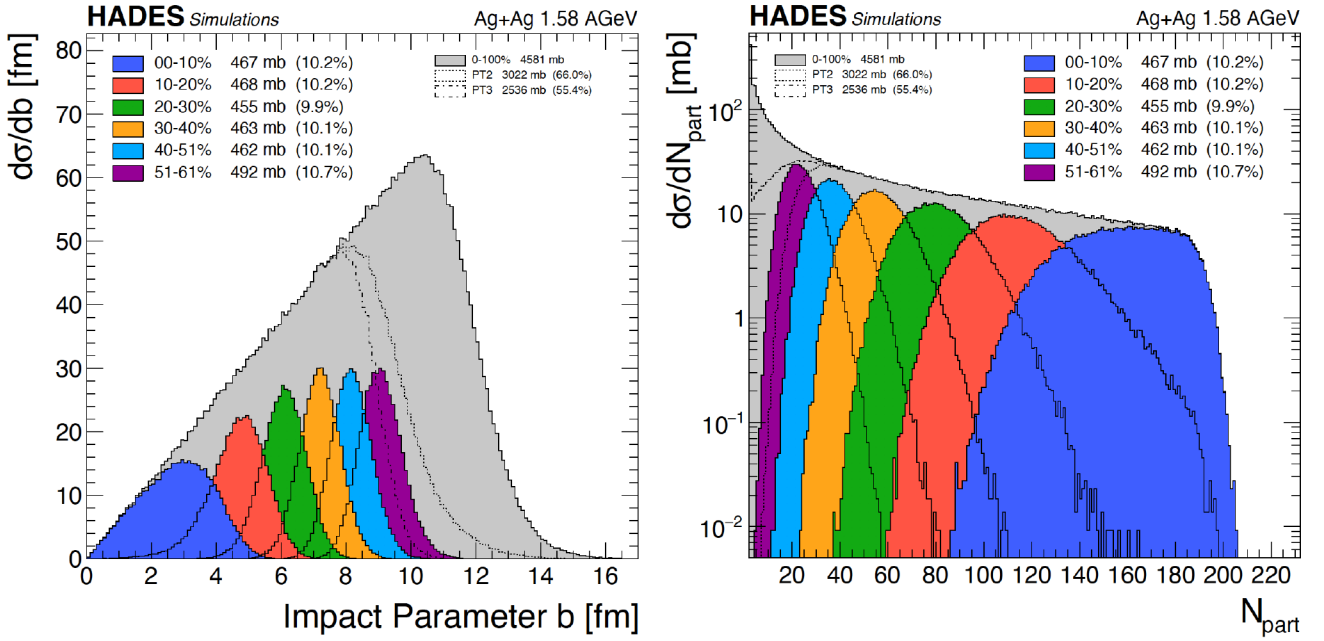


Figure 3.3: Illustration of cross-sections from a Glauber Monte Carlo simulation. The left panel shows the distribution of the impact parameter b , while the right panel shows the number of participating nucleons N_{part} . The full Ag+Ag interaction cross section is indicated by the grey area. Dotted and dashed lines denote the approximate trigger thresholds for PT2 and PT3. Centrality classes in 10% binning are highlighted in color and are derived from the multiplicity of hits in the META system, i.e. the number of hits in the TOF and RPC detectors.

this assumption must be extended to account for event-by-event fluctuations to accurately reflect the realistic behaviour of the system. Therefore, an additional sampling using a negative binomial probability distribution (NBD) is applied [38]:

$$P_{\mu,k}(n) = \frac{\Gamma(n+k)}{\Gamma(n+1)\Gamma(k)} \cdot \frac{(\mu/k)^n}{(\mu/k+1)^{n+k}} \quad (3.7)$$

where Γ is the gamma function and k a dispersion parameter. A final refinement to equation 3.6 is introduced with an efficiency term $\epsilon(\alpha)$, which accounts for non-linear multiplicity dependent reconstruction inefficiencies as well as secondary particle production [38]:

$$\epsilon(\alpha) = 1 - \alpha N_{\text{part}}^2 \quad (3.8)$$

Together, these components allow for a fit of the simulated Glauber Monte Carlo results to the experimental data, as shown in figure 3.4. To minimize any selection biases, only minimal event selection criteria are applied, specifically `kGoodStart` and `kGoodVertexCand`.

For the most part, the Glauber Monte Carlo model describes the data well, with a small undershoot observed at low $N_{\text{hits}}^{\text{TOF RPC}}$. This deviation is likely due to Ag+C contamination, which is discussed in more detail in section 3.5.2. As a result, the fitted Glauber Monte Carlo model is used to define centrality classes based

on equation 3.3. The resulting centrality class boundaries, in 10% intervals, are shown as vertical lines. The colored regions in figure 3.3 illustrate how this is reflected in the distributions of N_{part} and b . The effect of event-by-event fluctuations is clearly visible, leading to an overlap of the distributions.

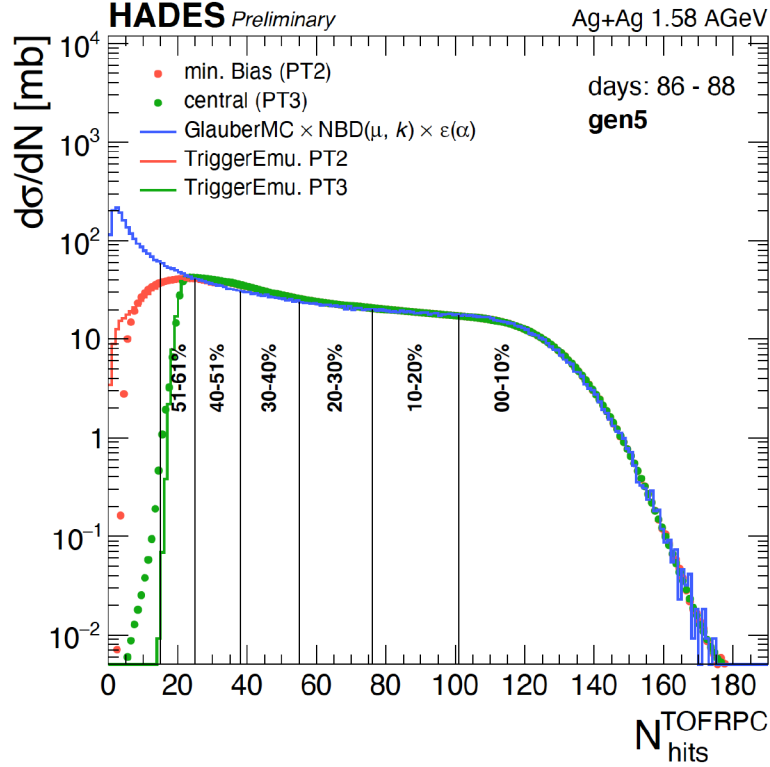


Figure 3.4: Cross-section as a function of $N_{\text{hits}}^{\text{TOFRPC}}$ for minimum bias (PT2 trigger, red symbols) and central (PT3 trigger, green symbols) data, compared with the fitted Glauber Monte Carlo model (blue line). Vertical lines visually indicate the boundaries of the 10% centrality classes.

3.4 Event Plane Reconstruction

Any analysis involving collective behaviours in terms of azimuthal anisotropies, see section 5, further requires information about the reaction plane Ψ_{RP} . Similarly to the impact parameter b , however, the exact orientation of Ψ_{RP} cannot be directly measured. Nevertheless, an experimental estimate can be made by, for example, by analysing the azimuthal distribution of the spectators projectiles. This approximation is referred to as the event plane Ψ_{EP} , which serves as a proxy for Ψ_{RP} in the analysis.

At HADES, the general reconstruction procedure, as illustrated in figure 3.5, relies on a Q-vector analysis [111, 112] of the spectators detected by the HADES Forward Wall.

The components of the Q-vector are defined as the averages over the hit positions X_{FW} and Y_{FW} in the Forward Wall [113]:

$$\begin{aligned}
Q_{n,x} &= \frac{1}{N_{FW}} \sum_{i=0}^{N_{FW}} \omega_i X_{i,FW} = \sum_{i=0}^{N_{FW}} \omega_i \cos(n\phi_{i,FW}) \\
Q_{n,y} &= \frac{1}{N_{FW}} \sum_{i=0}^{N_{FW}} \omega_i Y_{i,FW} = \sum_{i=0}^{N_{FW}} \omega_i \sin(n\phi_{i,FW})
\end{aligned} \tag{3.9}$$

where n represents the order of the Q-vector, and ω_i are the potential weights. Using these components, the n -th order event plane can be estimated as:

$$\Psi_{EP,n} = \arctan\left(\frac{Q_{n,y}}{Q_{n,x}}\right) \tag{3.10}$$

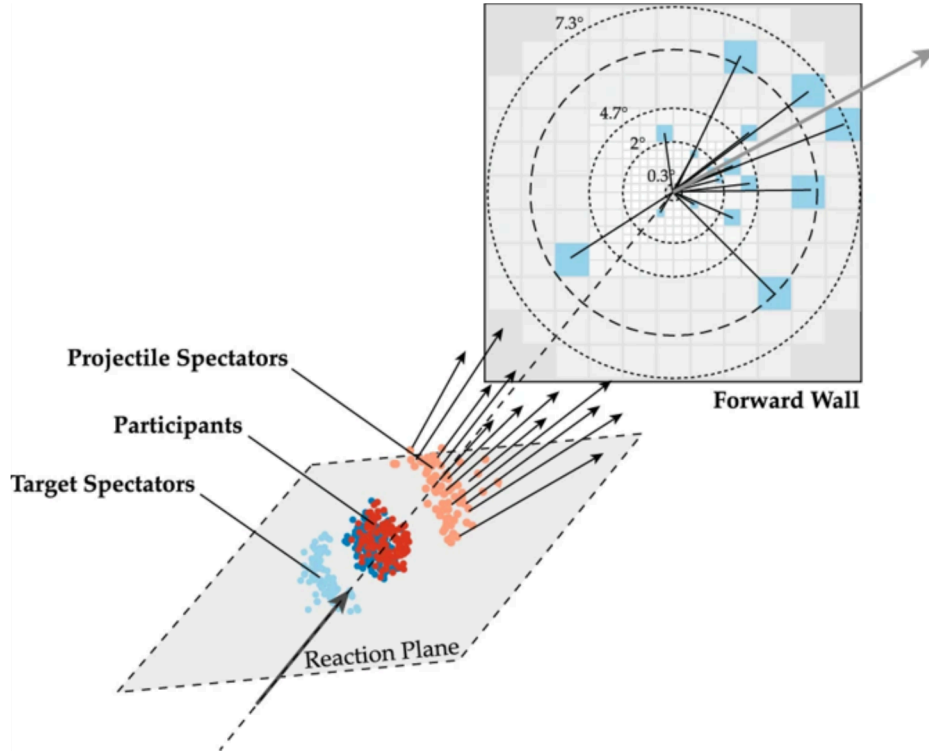


Figure 3.5: Illustration of the event plane reconstruction procedure. It shows how the reaction plane is defined by the impact parameter and the beam axis, and how its orientation is reflected in the distribution of spectator projectiles in the Forward Wall. Taken from [46].

In this work, we utilize the first order event plane ($n = 1$) as the reference for the flow reconstruction procedure outlined in chapter 5. In principle, the orientation of the reaction plane is expected to be uniformly distributed across all angles in the laboratory frame. However, the initial estimation of Ψ_{EP} based on equation 3.10 reveals anisotropies due to the detector acceptance, reconstruction efficiencies, contamination of participating nuclei in the Q-vectors and other similar factors. Consequently, several corrections must be applied:

- **Weighting:** To mitigate noise and remove contributions from participating nucleons, a velocity cut of $0.85 < \beta < 1.2$ [113] is applied, along with a minimum charge deposit threshold in the detector cells. This ensures that the remaining sample primarily consists of signals from projectile spectators. Furthermore, to account for the varying sizes of the fragments, the weights in equation 3.9 are assigned according to the charge Z , as it is determined via the signal amplitude.
- **Recentering:** The selected hits are recentered by shifting them to their mean and normalising their variances. Both are computed separately for each day of data taking and for each centrality class. This correction compensates for variations in the acceptance of the Forward Wall, which may arise due to dead cells or deviations in the beam position.
- **Rotation:** Any remaining non-uniformities are corrected using a final flattening procedure [114]. This procedure involves adding a correction angle to the event plane, $\Psi'_{EP} = \Psi_{EP} + \Delta\Psi$ which rotates the event planes to flatten the angular distribution.

3.4.1 Event Plane Resolution

The reconstructed event plane Ψ_{EP} fluctuates around the true reaction plane Ψ_{RP} by a dispersion $\Delta\Psi = \Psi_{EP} - \Psi_{RP}$. The average of this dispersion over all selected events defines the event plane resolution \mathfrak{R} [112]:

$$\mathfrak{R}_n = \langle \cos(n\Delta\Psi) \rangle \quad (3.11)$$

This resolution quantifies how well the reconstructed event plane approximates the true reaction plane. It also provides the correction factor relating the true flow coefficient v_n to the coefficient v_n^{rec} measured with respect to the event plane:

$$v_n^{\text{rec}} = v_n \cdot \mathfrak{R}_n \quad (3.12)$$

Since the average value of the cosine always has a magnitude less or equal to one, the reconstructed flow will be systematically smaller. This can be understood intuitively as this reflects the smearing of the azimuthal particle distribution caused by event plane fluctuations around the true reaction plane. Consequently, these effects need to be corrected for experimentally. The most common framework for this purpose is the (two) sub-event method. The central idea is to divide all hits in the Q-vector into two statistically independent subgroups of equal size, denoted as group A and B. In the limit of infinite multiplicity and perfect resolution, both sub-events should yield the same event plane angle, i.e. $\Psi_{EP,A} = \Psi_{EP,B}$. If this is not the case, any observed difference $\Delta\Psi_{EP} = |\Psi_{EP,A} - \Psi_{EP,B}|$ can be used to deduce the event plane resolution. Specifically, the relative number of events with $\Delta\Psi_{EP} > 90^\circ$ in comparison to all events can be related back to a resolution parameter χ [5, 112]:

$$\frac{N(\Delta\Psi_{EP} > \pi/2)}{N_{\text{total}}} = \frac{1}{2} e^{-\chi^2/2} \quad (3.13)$$

This parameter χ is, in turn, related to the event plane resolution \mathfrak{R}_n [115, 116]:

$$\mathfrak{R}_n(\chi) = \sqrt{\frac{\pi}{2}} e^{-\frac{\chi^2}{2}} \chi \left[I_{\frac{n-1}{2}} \left(\frac{\chi^2}{2} \right) + I_{\frac{n+1}{2}} \left(\frac{\chi^2}{2} \right) \right] \quad (3.14)$$

where I_n are the modified Bessel functions. This expression holds under the assumption that the Q-vector distribution around the reaction plane is Gaussian and that possible correlations from non-flow effects are negligible.

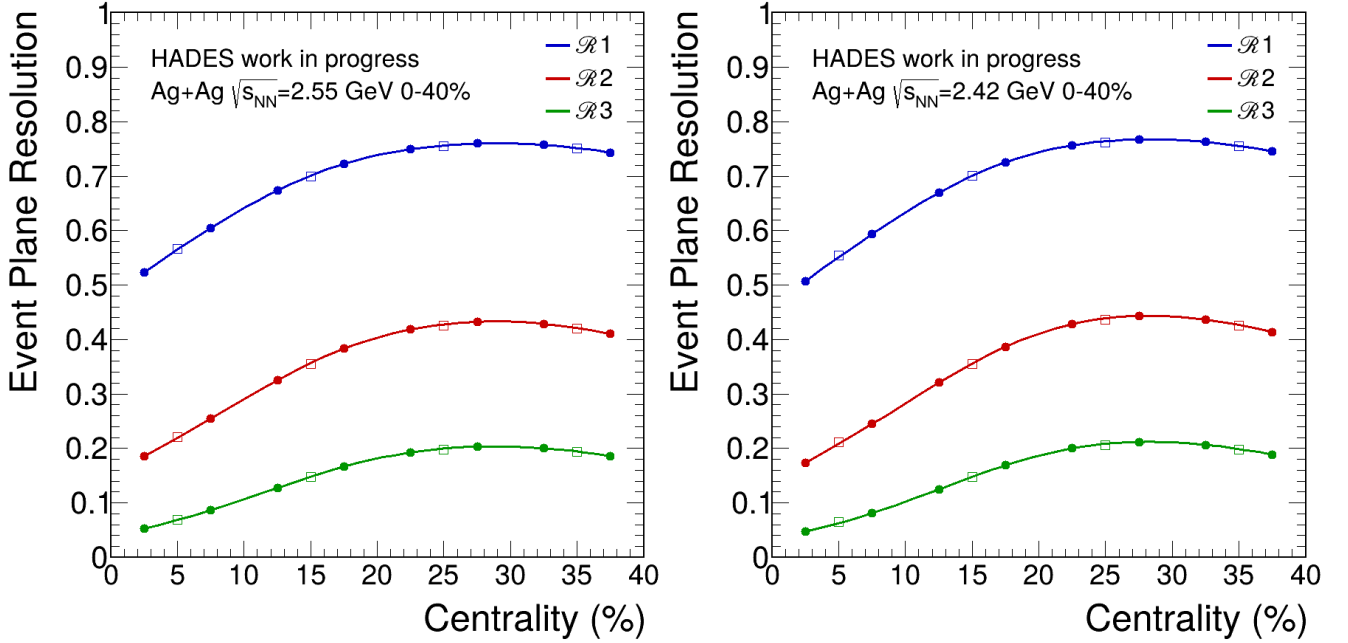


Figure 3.6: Event plane resolution up to the third order for the Ag+Ag collisions, collected at HADES, at $\sqrt{s_{NN}} = 2.55$ GeV (left panel) and $\sqrt{s_{NN}} = 2.42$ GeV (right panel). Full circles mark 5% centrality bins, open boxes represent 10% centrality classes.

On this basis, the event plane resolution \mathfrak{R}_n is evaluated for each centrality class and up to third order of $n = 3$. The results are summarised in figure 3.6. As expected, the resolution is lowest in the most central collisions due to the small number of surviving spectator nucleons. The resolution improves significantly in semi-central collision where more spectators contribute to the Q-vector. Only minor differences are seen between the two collected energies of $\sqrt{s_{NN}} = 2.55$ GeV and $\sqrt{s_{NN}} = 2.42$ GeV.

3.5 Identification of Ag+C contamination with Machine Learning

The general event selection criteria described in section 3.2 provide the baseline data sample for this and most HADES analyses. Within this sample, however, an additional contamination from Ag+C interactions is observed in more peripheral events with lower multiplicities. The origin of this effect is illustrated in figure 3.7. As mentioned in section 2.2, the heavy-ion campaigns of Ag+Ag in 2019 and Au+Au in 2012 employed a segmented target design. Each segment consists of a rectangular kapton strip with a thickness of $7 \mu\text{m}$. A hole of 1.4 mm diameter is laser-cut into the strip, onto which the actual silver (or gold) foil is glued. Consequently, collisions occurring within the hole region involve purely Ag+Ag (or Au+Au)

interactions. In the overlap region and beyond, however, the beam can interact with the underlying kapton support, leading to a non-negligible probability of Ag+C collisions. Unfortunately, the reconstructed event vertex resolution based on the measured particle tracks is in the order of a 2-3 mm and is therefore not enough to straightforwardly select purely center Ag+Ag collisions only.

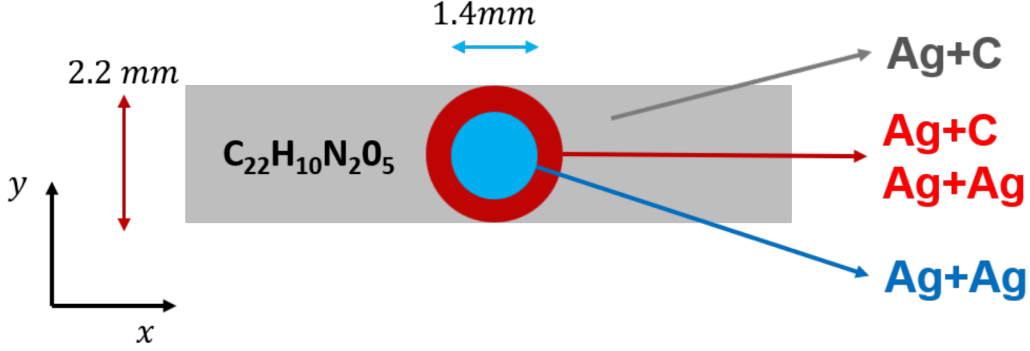


Figure 3.7: Geometry of a single target segment in the x - y plane. The round silver foil is mounted over a 1.4 mm hole (blue) in the kapton support material (grey). Outside of the hole, there is an area (red) where both Ag+C and Ag+Ag interactions can occur.

In contrast to the symmetric Ag+Ag system, Ag+C collisions exhibit a pronounced asymmetry and lead to shifts in the average rapidity of the produced particles. One observable sensitive to this difference is ERAT, defined as the ratio of the total transverse to longitudinal energy, summed over all particles i in the event:

$$\text{ERAT} = \frac{\sum_{i=1}^N E_i \sin(\phi)}{\sum_{i=1}^N E_i \cos(\phi)} \quad (3.15)$$

This effect is illustrated in figure 3.8, which compares the ERAT distributions from UrQMD simulations of pure Ag+Ag and Ag+C collisions to the experimental data. The data show a distinct enhancement at lower multiplicities, starting around $N_{\text{META}} < 70$, which is not reproduced by the Ag+Ag simulation alone. This excess can be attributed to contamination from Ag+C interactions in the surrounding target structure. It is important to note that this contamination is only relevant for semi-central and peripheral events. Due to the smaller system size and correspondingly lower multiplicities of Ag+C collisions, they do not contribute significantly to the more central Ag+Ag centrality classes. For this reason, the effect has been treated differently depending on the analysis goals and the observable under investigation. The most straightforward approach is to restrict the analysis to more central events, typically within the 0–30% centrality class [93]. This is particularly useful for multiplicity measurements, which focus on particle production under the hottest and densest conditions, as they are present in central collisions.

Other studies have applied a selection on the ERAT observable to suppress carbon contamination in semi-central events [72, 117]. This allows for the inclusion of a broader centrality range, which is important for flow measurements where the expected anisotropies, and consequently the flow signal, are stronger in semi-central collisions. Since the measurement of anisotropies via dileptons is a central focus of this work, additional effort has been made to develop a new procedure for the identification and removal of Ag+C events. This will also enable the extension of other dilepton measurements, i.e. of the excess spectra, to more peripheral collisions. As will be discussed in chapter 6, this is particularly valuable for studying the dependence on the number of participating nucleons N_{part} and system size in greater detail.

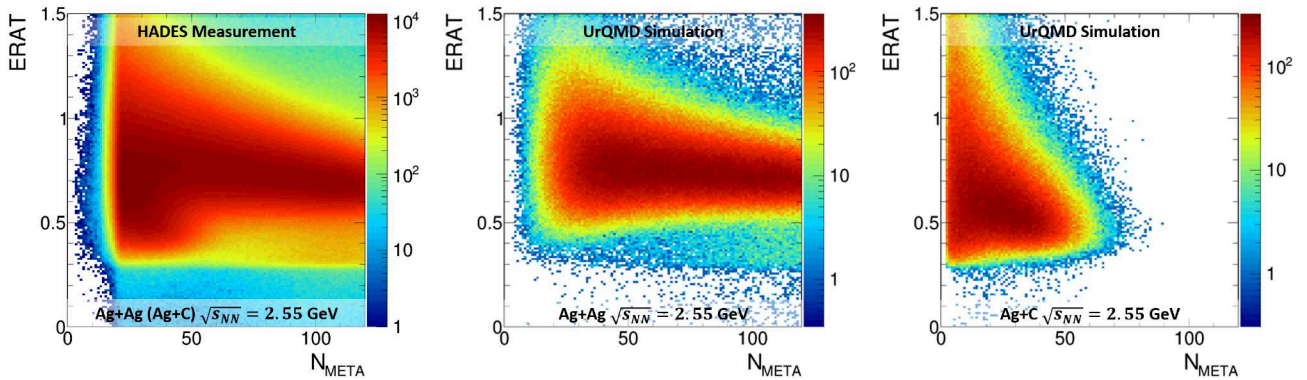


Figure 3.8: ERAT distribution as a function of the number of META hits N_{META} . The data and Ag+Ag simulation include only events with PT3 trigger. The excess at low multiplicities in the experimental data, compared to the pure Ag+Ag simulation, is consistent with additional Ag+C contamination.

3.5.1 Neural Network-Based Identification of Ag+C Events

Due to the statistical nature of heavy-ion collisions, which is characterised by significant event-by-event fluctuations, a clean separation of Ag+C and Ag+Ag events cannot be achieved using a single observable. While simple selection criteria, such as a cut on ERAT, can effectively suppress a large fraction of Ag+C events, all individually investigated features still exhibit substantial overlap in the distributions between the two collision systems. This necessitates a more sophisticated approach that can simultaneously account for multiple features and their correlations. Given their growing success in the context of heavy-ion physics [118], including applications within the HADES experiment, e.g. [119, 120], machine learning algorithms present a promising tool for this classification task.

Several strategies for identifying Ag+C collisions have already been explored [121, 122] at HADES. Early work on the Au+Au dataset from 2012, which combined an unsupervised clustering algorithm with a supervised neural network trained on simulated data, yielded promising results [121, 123]. This approach served as the basis for an analogous model trained for the Ag+Ag system. In this work, the goal was to extend these models towards a more data-driven procedure in order to reduce reliance on simulated data, which inherently introduce an unquantifiable degree of model dependence.

Initially, the focus was placed solely on the neural network, as the inclusion of the clustering algorithm did not yield a significant improvement in overall performance. The training procedure was structured in two stages. In the first stage, a neural network was trained on fully simulated data with known Ag+Ag and Ag+C labels. This preliminary model, combined with additional selection information, was then used to construct a dataset from experimental data containing predominantly pure Ag+Ag or Ag+C events. This curated dataset served as input for training a second model directly on experimental data. This two-stage procedure represented a first attempt at applying a semi-supervised learning approach [124, 125], where a small amount of labelled data is used to extract structure from a largely unlabelled dataset.

One observable, that has proven useful in the construction of the experimental training sample, is the target segment. As shown in figure 3.9, the distribution of the number of META hits N_{META} varies significantly across different target segments. Later segments tend to exhibit a higher rate of low-multiplicity events. This variation is not an acceptance effect, as confirmed by simulation studies, but is attributed to an

increased contribution of Ag+C collisions in those segments. It is likely caused by slight misalignments of the target segments relative to the beam axis, a divergent beam profile, or beam inclination, all of which can increase the probability of the beam interacting with the surrounding target material.

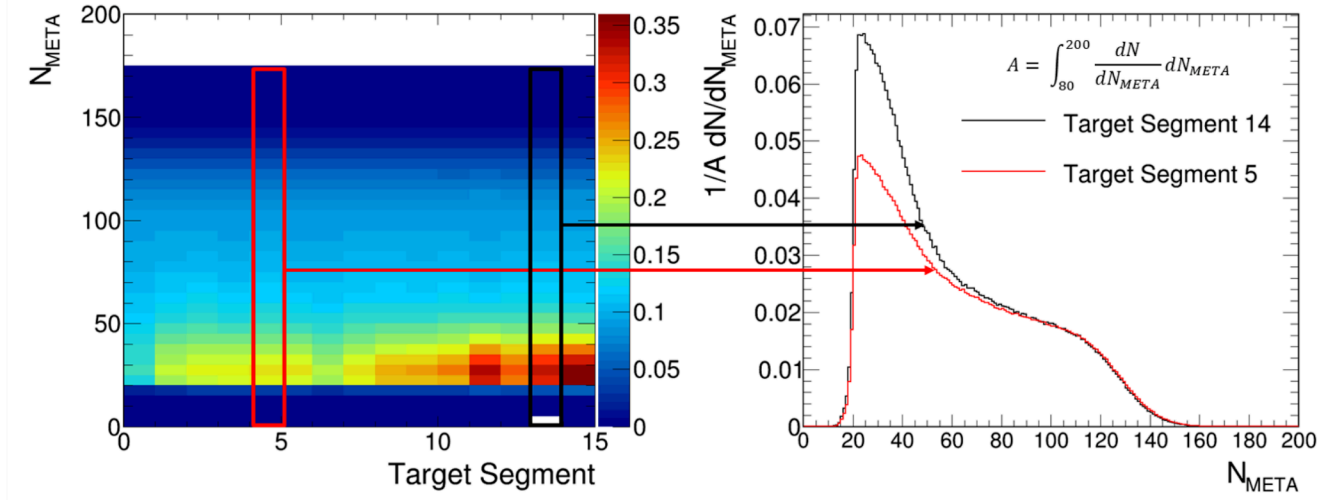


Figure 3.9: Distribution of events, normalised in the region of $80 < N_{META} < 200$ for various segments. The left panel shows the two-dimensional distribution for all segments, with a visible increase of low-multiplicity events at later target segments. The right panel shows the one-dimensional projection, in this example of target segment 5 and 14. The difference in the shape of the distributions is expected to come from carbon contamination.

This target-segment dependence has served as an additional criterion for constructing Ag+Ag- and Ag+C-enriched data samples for the semi-supervised training strategy. However, despite the initial success of the semi-supervised approach, the purity of the experimentally constructed training samples remained difficult to quantify, and simulated labels were still required to achieve reasonable training performance. For the final model used in this analysis, we therefore move beyond the semi-supervised strategy and employ a fully data-driven training procedure. A key observation is that the correlation between the beam position, reconstructed from the START detector, and the first target segments enables the identification of clean Ag+Ag and Ag+C events directly from experimental data. Each strip in the START detector has a width of approximately $300 \mu\text{m}$, which allows for a precise reconstruction of the transverse beam position. Although some degree of beam divergence or inclination may be present, the first target segments are located only about 2 cm downstream of the START module, as described in section 2.3. Over this short distance, the beam path remains sufficiently aligned with the beam axis to allow for accurate spatial correlation.

This effect is illustrated in figure 3.10, which shows the distribution of ERAT versus N_{META} for events in the first target segment, resolved by individual START strip positions. The overall beam profile is visible in the hit distribution, with certain regions showing little or no activity. Beyond this fact, some ERAT distributions reveal a characteristic enhancement for lower multiplicity events. This serves as the same indicator of Ag+C contamination as previously discussed in figure 3.8. In addition, it can be noted how these low-multiplicity events are localised at the edges of the beam spot. In contrast, events corresponding to more central beam positions exhibit the smooth distribution expected of pure Ag+Ag collisions. On this basis, one can estimate the location of the target. The blue circle in figure 3.10 indicates the estimated location of the central silver target foil, while the red region corresponds to the surrounding area where

the foil is mounted on the kapton support. Events outside the red zone are consequently attributed to pure Ag+C interactions.

It is important to note that this positional correlation degrades for later target segments. Nevertheless, it has been found to be very successful for the first few segments, and therefore chosen as the central criteria to select a pure Ag+Ag and Ag+C sample solely on experimental observables. This sample then forms the basis for training a final classification model entirely on real data. The applied selection is not expected to introduce a significant bias.

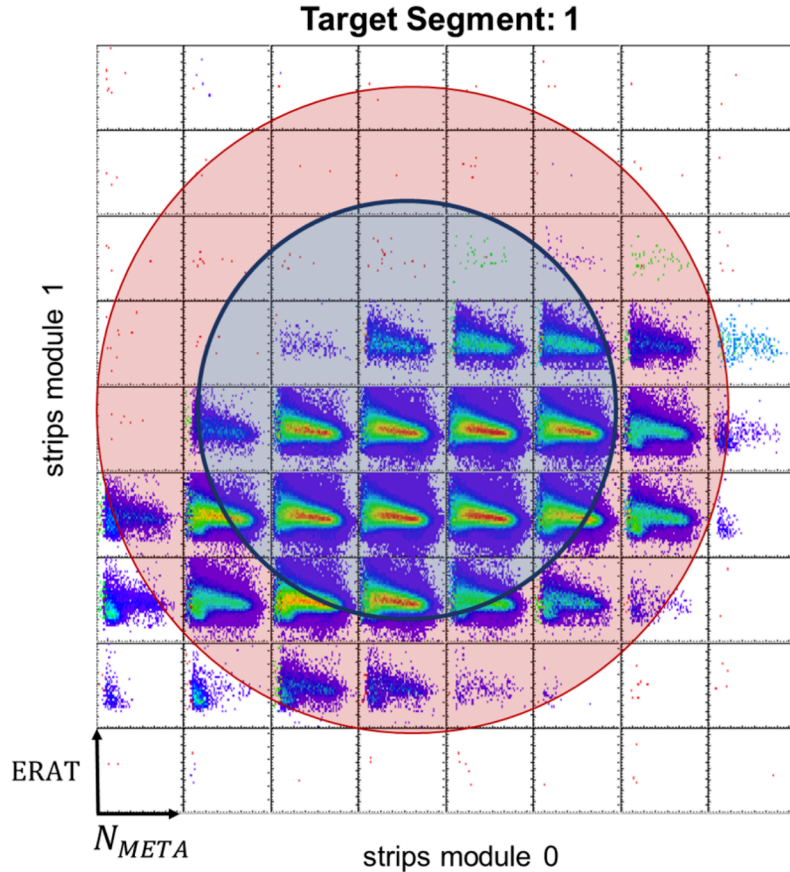


Figure 3.10: Illustration of how pure Ag+Ag and Ag+C samples can be selected using START hit positions in the first target segment. The blue circle indicates the central silver target foil, while the red region marks the surrounding area where the foil is glued to the kapton backing.

The selection of the final model architecture builds upon insights gained during the semi-supervised development phase. The following event-level observables serve as input features to the final neural network classifier:

- N_{TOF} : Number of hits in the TOF detector.
- N_{RPC} : Number of hits in the RPC detector.
- N_{Tracks} : Number of reconstructed tracks after the standard track selection.
- **Average Particle Rapidity**: Mean rapidity of all reconstructed particles within the event.

- **Average Transverse Momentum:** Mean transverse momentum of all reconstructed particles.
- **Average Rapidity:** Event-wise average rapidity of all detected particles.
- **Total Mass:** Sum of the reconstructed particle masses.
- **ERAT:** Ratio of total transverse to longitudinal energy, as defined in equation 3.15.
- **Sector Correction ID:** Integer identifier encoding the number of active sectors contributing to the event.
- **IsRejected:** Boolean flag indicating whether the event failed any of the standard event selection criteria described in section 3.2.

It can be noted that some of these features, particularly N_{TOF} , N_{RPC} , and N_{Tracks} , correlate strongly with one another, as they are all related to overall event multiplicity. In principle, a combination into one feature is possible, but has not shown an improvement in the model's performance.

The final model architecture consists of a fully connected feed-forward neural network with three hidden layers comprising 148, 148 and 138 neurons respectively. The hyperbolic tangent (tanh) was chosen as the activation function for all hidden layers. While alternative loss functions, such as the generalised cross-entropy loss [126], were considered, the final model employs the standard categorical cross-entropy loss function [127]. Optimisation during training was performed using the Adam optimizer [128]. The model was implemented in the Python programming language using the Keras API, which is built on top of TensorFlow. The final classifier output represents the confidence of the model p to classify a given event as purely Ag+Ag or Ag+C, see figure 3.11. This gives the end user the freedom to choose which level of certainty is desired in the analysis by choosing a decision threshold p between 0 and 1. The default is $p = 0.5$. Predictions are prepared for the the full dataset and stored in ROOT TTree structures to enable efficient access in subsequent physics analyses.

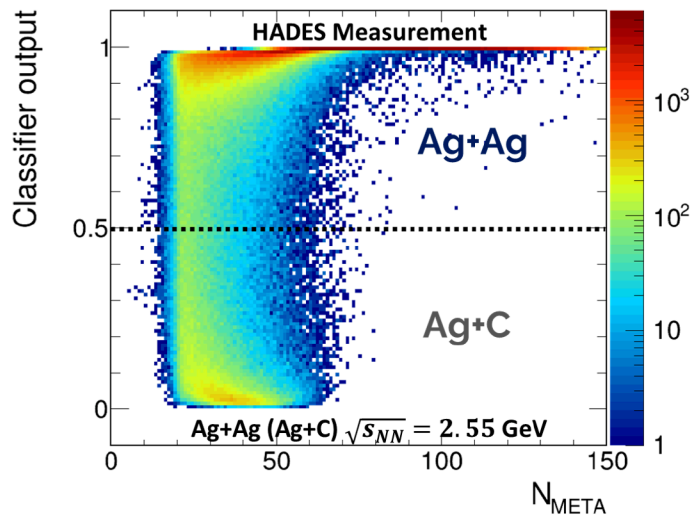


Figure 3.11: Output distribution of the trained classifier applied to Ag+Ag data at $\sqrt{s_{\text{NN}}} = 2.55$ GeV. The output value p represents the model's estimated probability that an event corresponds to an Ag+Ag collision. The default classification threshold is set to $p = 0.5$ as indicated by the dotted horizontal line.

3.5.2 Model Evaluation

After the successful training and validation of the model based on the selected data sample, a number of additional evaluations have been performed.

Evaluation on simulated data from transport models: While transport model simulations are inherently model dependent and are not yet expected to provide a perfect description of experimental data, they offer a first practical means for evaluating the performance of the classifier under controlled conditions. Most importantly, these simulations provide ground-truth labels for the collision system (Ag+Ag or Ag+C), which allows for a direct computation of standard classification metrics. In this work, three key metrics are

Centrality	Model	Accuracy (%)	Recall (%)	Precision (%)
30–40%	UrQMD	90.6	95.1	83.5
	DCM-QGSM	89.3	96.9	81.8
40–50%	UrQMD	87.2	96.1	85.5
	DCM-QGSM	82.7	97.4	80.3

Table 3.2: Classification performance (in %) of the final model on simulated data for two centrality classes, evaluated using UrQMD and DCM-QGSM transport models.

used to evaluate model performance: *accuracy*, *recall*, and *precision*. Accuracy is defined as the fraction of correctly classified events among all events. Recall quantifies the fraction of true Ag+C events correctly identified by the model. Precision measures the fraction of events classified as Ag+C that are indeed Ag+C. The employed models are UrQMD, also introduced in section 3.1.1, and DCM-QGSM [129, 130]. The resulting performance is summarised in table 3.2.

Overall, the model appears to successfully capture the distinguishing characteristics between Ag+C and Ag+Ag collisions and generalizes well from experimental training data to two independent transport simulations. As indicated by the precision values, the classifier tends to slightly favour purity over efficiency, occasionally misclassifying Ag+Ag events as Ag+C in order to minimize contamination of the Ag+Ag sample.

Comparison to Glauber Monte Carlo simulation: A further validation of the model can be performed through the comparison with the Glauber Monte Carlo (Glauber MC) simulation introduced in section 3.3. Figure 3.12 shows the fitted Glauber MC to the standard experimental data with minimum bias criteria, i.e. with the inclusion of PT2 events and minimal event selection of only `kGoodStart` and `kGoodVertexCand`. A clear excess of low-multiplicity events is observed in the data, as indicated in the black curve in figure 3.12. This is attributed to Ag+C contamination. After applying the trained classifier to select only events predicted as "pure" Ag+Ag, the agreement between the experimental data and Glauber MC improves noticeably. This is also reflected in the right panel of figure 3.12, which shows the ratio between the Glauber MC and the Ag+Ag data before and after application of the model. As in the previous evaluation, the model appears to apply a somewhat conservative selection, rejecting a small fraction of genuine Ag+Ag events in favor of improved sample purity. In this context, one may also note that the centrality class definitions introduced in section 3.3.2 remain unaffected by the removal of low-multiplicity events [123].

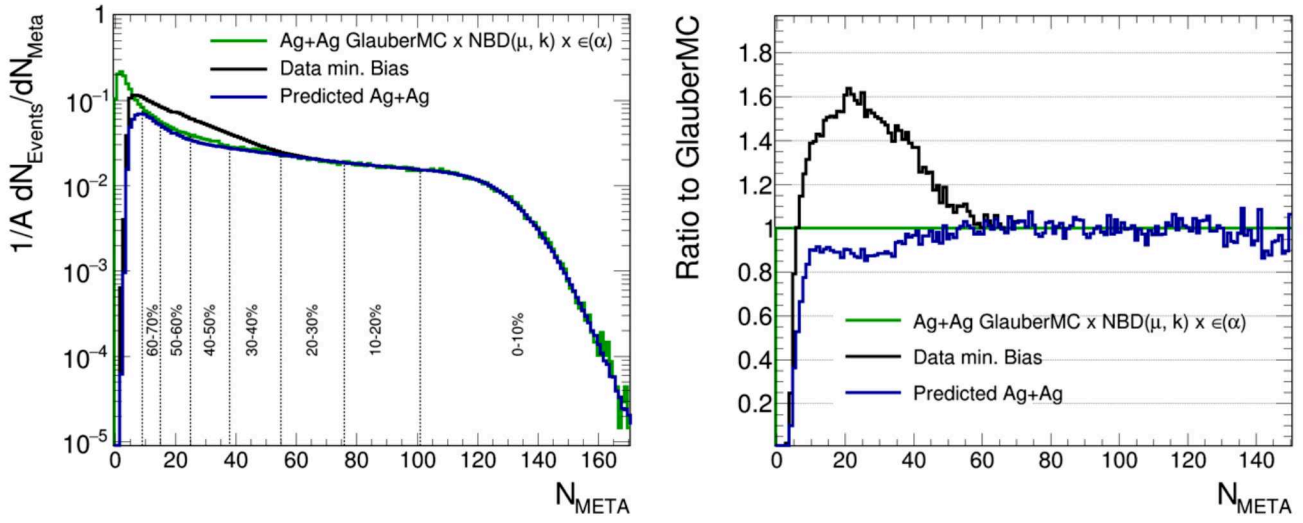


Figure 3.12: Comparison of experimental data with a Glauber Monte Carlo simulation, shown before and after applying the Ag+Ag classifier. Left: Multiplicity distribution compared to the fitted Glauber MC. Right: Ratio of experimental data to simulation.

Evaluation based on experimental observables: Finally, arguably the most important evaluations are based purely on experimental observables. Due to the symmetric nature of Ag+Ag collisions, one would generally expect symmetric distributions around midrapidity for various observables. Figure 3.13 shows an example in the directed flow v_1 of positrons as a function of rapidity. In the left panel, the default data set reveals a non-vanishing v_1 at midrapidity. After applying the classifier and selecting only events identified as Ag+Ag (right panel), the distribution becomes notably more symmetric. Similar checks have been performed based on the multiplicity measurement of charged pions and protons as a function of rapidity, particularly in the 30-50% centrality range. While some residual asymmetries remain, the model appears to generally correctly identify Ag+C and Ag+Ag events.

The performance of the classifier has been found to be satisfactory. Given the observed improvements in rapidity symmetry, it will be applied by default for the reconstruction of the dilepton azimuthal anisotropies discussed in chapter 5 where more peripheral collisions are especially important. In the case of the analysis of dilepton yields, discussed in chapter 4, the dominant contribution comes from more central collisions such that the potential contamination of carbon collisions is minimal and assumed to be negligible. Possible (unseen) biases could be introduced by the model, for example by consistently removing Ag+Ag events with higher average particle rapidity. In order to assess such effects, the classifier output is evaluated at various decision thresholds, and the resulting variations are used to estimate systematic uncertainties. This is also discussed in section 5.6. Lastly, although this discussion has focused on Ag+Ag collisions at $\sqrt{s_{\text{NN}}} = 2.55$ GeV, analogous classifiers based on the same architecture and selection strategy have been trained and applied for both Au+Au and Ag+Ag datasets at $\sqrt{s_{\text{NN}}} = 2.42$ GeV. In the remainder of this work, this model is referred to as the purifier.

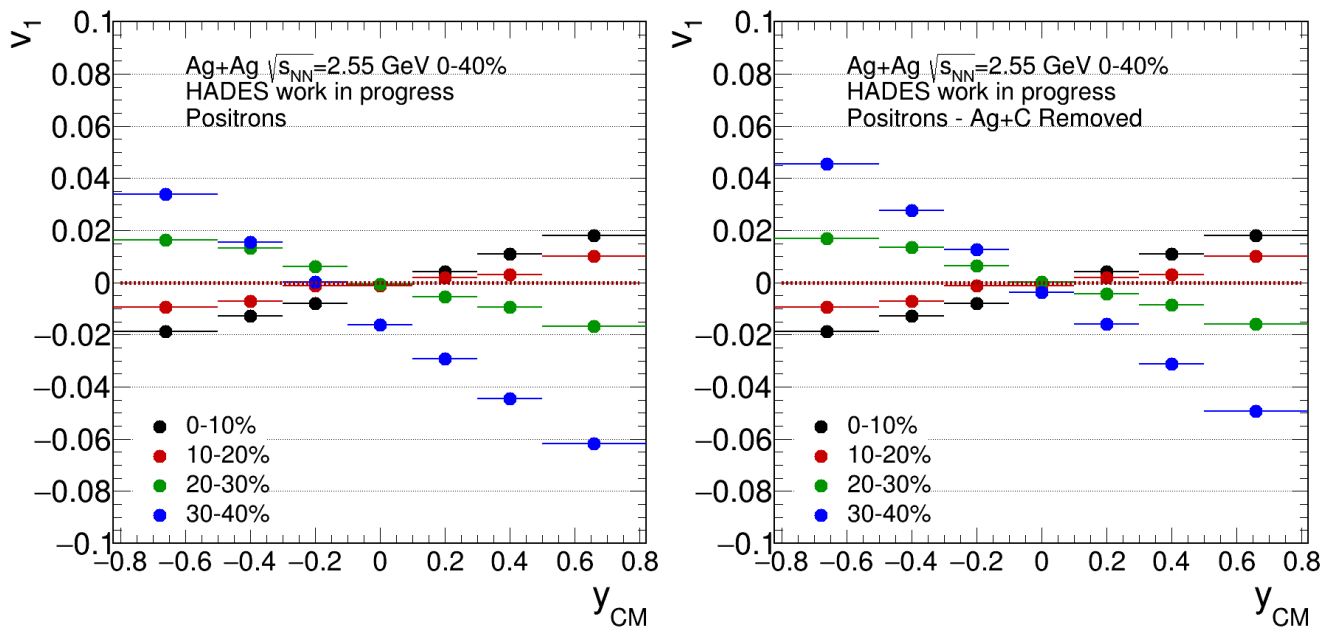


Figure 3.13: Directed flow v_1 of positrons before and after removal of Ag+C collisions for Ag+Ag collisions at $\sqrt{s_{NN}} = 2.55$ GeV. Details on the reconstruction of this observable are given in chapter 5.



4 DiElectron Reconstruction and Analysis Procedure

After the application of the general data processing and selection procedures, presented in the previous chapter, the higher-level physics analyses can follow. One goal of this work is the differential reconstruction of the dielectron signal, which entails a number of analysis steps, namely the identification of electrons and positrons, their combination into dielectron pairs and the application of various corrections. These steps constitute the framework for the final experimental spectra presented in chapter 6.

4.1 Electron Identification at HADES

The track candidates reconstructed in the DST production, see section 3.1, are based on loose criteria and allow for matching of multiple track segments with META and RICH hits as well as the usage of a single MDC segment for multiple track candidates. As a consequence, not all reconstructed candidates correspond to true particle trajectories. The first step of the analysis, therefore, consists of filtering the most plausible tracks corresponding to the particles of interest, namely electrons and positrons.

This filtering is performed using the so-called track sorter, which selects all candidates that meet a set of minimal quality requirements. In this work, only the most general criteria are applied:

- The Runge-Kutta fit quality is required to satisfy $\chi_{\text{RK}}^2 < 1000$.
- The track must include both a fitted inner and outer MDC segment.
- A matching hit in the META system must be present.
- A matching RICH ring must be associated with the track.

The resulting pool of track candidates is then sorted along their χ_{RK}^2 . In cases where two or more candidates share hits or track segments, the candidate with the best fit quality, i.e. lowest χ_{RK}^2 , is retained, while the others are discarded. In the end, this results in a list of unique tracks with a high probability of corresponding to genuine particle trajectories. This condition is referred to as **kIsLepton**.

Although the requirement of a RICH ring already introduces a sample of track enriched by electrons and positrons, additional and refined particle identification (PID) criteria are necessary to achieve the purity required for this analysis. The principal discriminant exploited is the small rest mass of the electron. This translates to velocities near the speed of light across the entire relevant momentum range, which can either be directly measured via the time-of-flight or indirectly via the distinctive detector response in the RICH detector. Information from the ECAL could provide additional information and thereby separating power. However, it is not used in this work because only two sectors were fully installed in 2019 at the time of the Ag+Ag campaign.

4.1.1 Electron Selection Criteria Using the RICH Detector

One of the central tools for separating individual leptons from the hadronic bulk of emitted particles is the RICH detector. As introduced in section 2.4, every electron, with sufficient momentum, passing through the RICH emits Cherenkov radiation, which results in the formation of a distinct ring around the particle's trajectory. By matching the centre of the reconstructed ring to the corresponding particle track, this feature serves as a key criterion for selecting electrons and positrons.

Each reconstructed ring is characterised by several observables, including the ring radius R_{ring} , the number of associated Cherenkov photons that were detected by the MAPMTs, called N_{cals} , and the rings position on the detector plane. In order to maximize the purity of the selected lepton sample, while minimising the probability of rejecting true electrons, careful consideration is given to study the distributions of these RICH observables and thereby define appropriate selection criteria accordingly.

The first selection criterion is based on the reconstructed ring radius R_{ring} . Significant effort has been invested in optimising the ring reconstruction algorithm to reduce the contamination from falsely reconstructed rings, primarily caused by noise [92]. This work introduces an additional cut to remove rings with atypically small or large radii. A detailed study conducted in [66] found a mean value of $\bar{R} = 23.24$ mm with a Gaussian fit. Rings beyond the 3σ threshold, specifically $R_{\text{min}} = 18.96$ mm and $R_{\text{max}} = 27.52$ mm, are excluded from the sample. Additionally, rings associated with fewer than eight detected photons in the MAPMTs, i.e. $N_{\text{cals}} < 8$, are discarded. It has been shown that, in this case, the ring radius does not scale with N_{cals} , suggesting that these rings are primarily background events [66].

Finally, the RICH matching quality of the track to the ring is scrutinised in greater detail. The default matching criterion from the track sorter is relatively loose, allowing for up to 4° of variation. However, since the majority of emitted particles are hadrons, this loose condition still results in a significant contamination from pions and protons, which are randomly and falsely associated with the Cherenkov ring. Therefore, tighter constraints on the matching quality are constructed for the final analysis. In this case, it is performed independently for $\Delta\theta = \theta_{\text{ring}} - \theta_{\text{track}}$ and $\Delta\phi = (\phi_{\text{ring}} - \phi_{\text{track}}) \cdot \sin(\theta_{\text{track}})$. Figure 4.1 shows the distribution of particles over $\Delta\theta$ for experimental data in black and white leptons embedded into experimental data in blue. The white leptons are sampled uniformly in momentum, θ and ϕ , without using a particle generator or realistic kinematic distributions. They serve as an important tool for efficiency corrections, as detailed in section 4.3. One can note, how the two distributions show variations in their mean and general shape which cannot be explained by the hadronic contamination in the experimental data. Naively, one would expect any random matches to hadrons to be more or less constant over all $\Delta\theta$, which means that the mean of the distribution would stay the same.

Another factor could come from multiple scattering of the leptons in the detectors' material. This can lead to changes in their flight path and vary the reconstructed ϕ and θ from their true original emission angle. A partial correction for this effect is possible by assuming that most of the multiple scattering occurs on the RICH mirror. In this scenario, the reconstructed ϕ and θ of the track are used to determine the collision point on the mirror. From there, the trajectory leading to the global event vertex should approximate the original flight path of the lepton. By replacing the reconstructed angles with those corresponding to the corrected trajectory, the matching quality improves significantly [66, 92]. It is done analogously for simulation and experimental data.

Despite these improvements, small discrepancies between the simulated and measured distributions remain. The challenge, therefore, lies in developing a selection criterion that acts consistently on both data and simulation. In this work, this is realised by fitting both the experimental data and the simulated data with

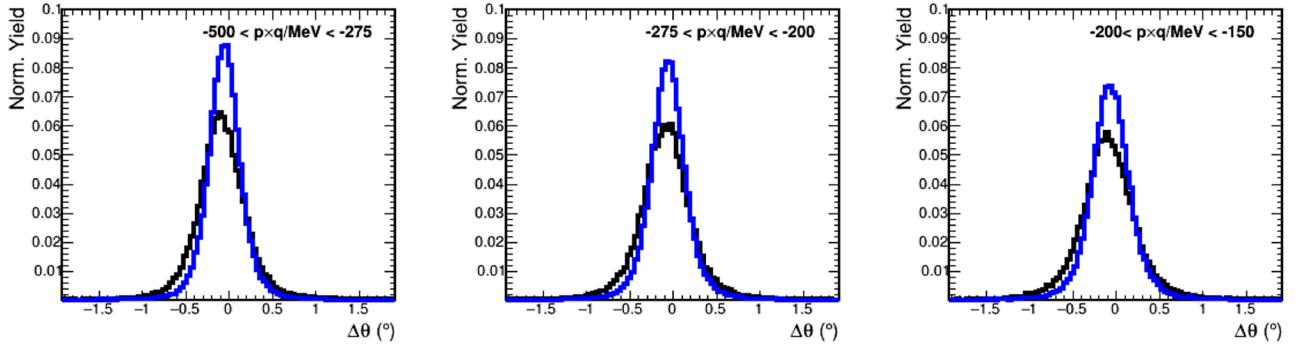


Figure 4.1: Distribution of $\Delta\theta$ in experimental data (black) and simulation (blue) for Ag+Ag collisions at $\sqrt{s_{\text{NN}}} = 2.55$ GeV for three momentum bins in system 0, sector 1.

the same functional form. The fit results are then used to select a specific percentage, e.g. 95%, of the full distribution in both domains. For this purpose, considerable effort has been invested in choosing an appropriate fit function, selecting a suitable fit range, and preselecting the data to ensure an accurate description.

The final procedure for deriving the selection criterion is outlined as follows. First, the distributions are reconstructed as a function of momentum for both simulated and experimental data. In order to minimize the hadronic contamination, tight constraints are applied on the velocity β , as well as $\Delta\phi$ and $\Delta\theta$. Only the observable under investigation is allowed to vary. The resulting distributions are then fitted with a custom fitting function shown in equation 4.1. Originally, it was expected that they can be describe by purely Gaussian distributions, but closer studies reveal that the tails cannot be described this way, as already be seen in figure 4.2. A normal distribution would represent a parabola in logarithmic scale which cannot capture the widening tails appearing as almost straight lines. This might be understood as a product of many normal distributions which underlie the data with varying means and standard deviations, cumulating into a more general distribution in the end. To account for this, an additional parameter m is introduced. It is empirically motivated and transforms the normal distribution towards a Laplace distribution when moving away from the mean towards the tails.

$$\propto \exp\left(-\left|\frac{1}{2}\left(\frac{x-\mu}{\sigma}\right)^{2-\tanh\left(m\frac{x-\mu}{\sigma}\right)}\right|\right) \quad (4.1)$$

After testing various functional forms, this function has been found to provide the most accurate and stable description of the data. The resulting fit is shown in figure 4.2. Because the tails of the experimental data are more prone to hadronic contamination, the fit parameter m is fixed using simulated data only. The free fit parameters on the experimental data are therefore the mean μ and standard deviation σ . The fit range is selected to be between -0.5° and 0.5° for both $\Delta\phi$ and $\Delta\theta$. Based on these fits, a final selection criteria is made by selecting 98% of particles around the mean. The corresponding thresholds are also shown in figure 4.2. These thresholds are determined as a function of momentum, and are applied separately to electrons and positrons, and individually for each sector as well as both META systems.

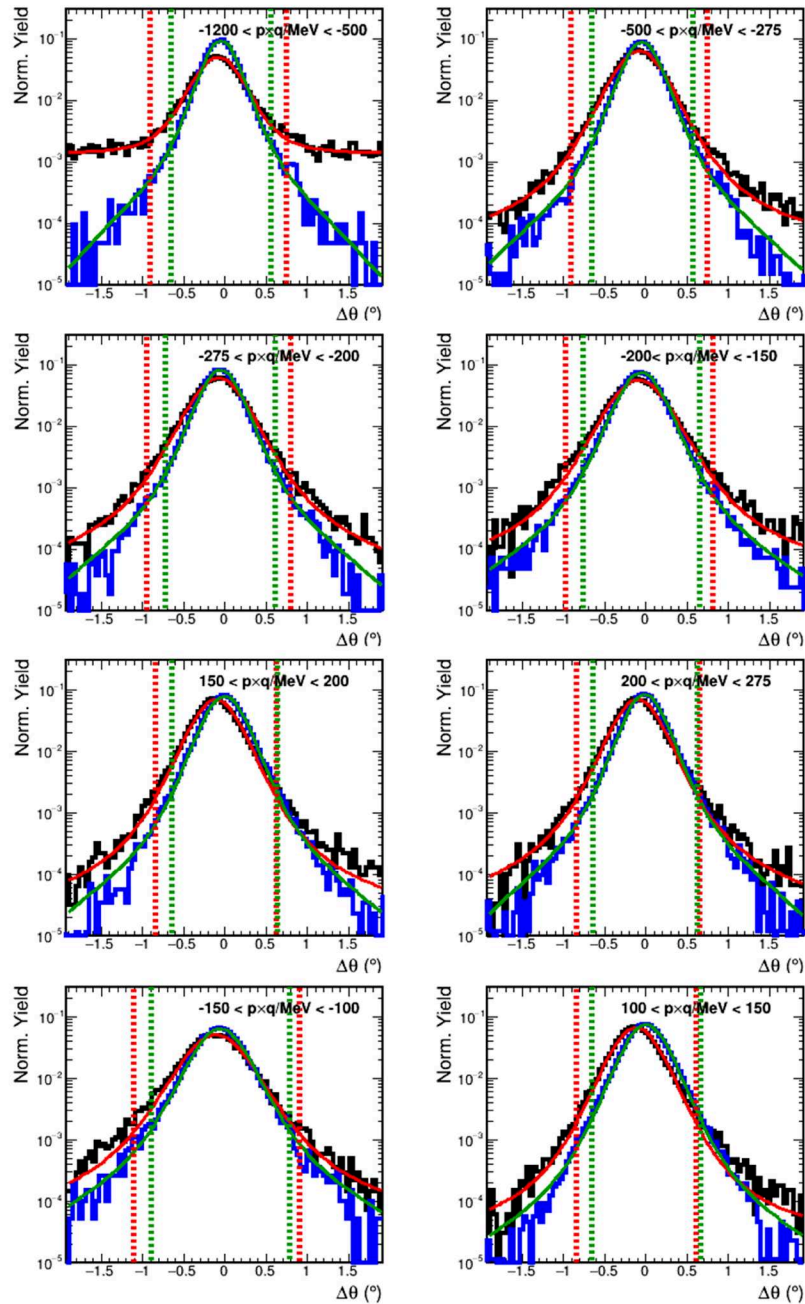


Figure 4.2: Example illustrating the determination of $\Delta\theta$ thresholds for particle identification in Ag+Ag collisions at $\sqrt{s_{NN}} = 2.55$ GeV, using multiple momentum bins in system 0, sector 1. Black represents the experimental data, blue shows white leptons embedded into the data. Red is the fit to the experimental data, while green is the fit to the simulated leptons. The vertical lines indicate the cut thresholds for the experimental data (red) and the white leptons embedded into the experimental data (green). Within the two lines lie 98% of the selected particles.

4.1.2 Electron Selection Criteria from Time-of-Flight

In addition to the RICH observables, a further selection criteria can be established based on the measured time-of-flight of the particles, which is directly related to the velocity β . Similar to the procedure used for selecting lepton candidates via $\Delta\phi$ and $\Delta\theta$, the distributions from simulations of white leptons embedded into experimental data show slight discrepancies compared to the measurements. As a result, an analogous procedure involving fitting and subsequent selection within a chosen confidence interval is applied. In this case, the data is first preselected with stringent cuts on the RICH matching quality, allowing for deviations of no more than 0.1° . The fit is performed in the same finite momentum bins, separately for positrons and electrons as well as system 0 (RPC) and system 1 (TOF). An example can be seen in figure 4.3 for system 0. This time, a normal distribution adequately describes the data, including the lepton tails. The additional structure coming from lower β at higher momenta is associated with pion contamination. Therefore, the introduction of an additional parameter as in equation 4.1 is not necessary. The fit range is set between $0.95 < \beta < 1.05$.

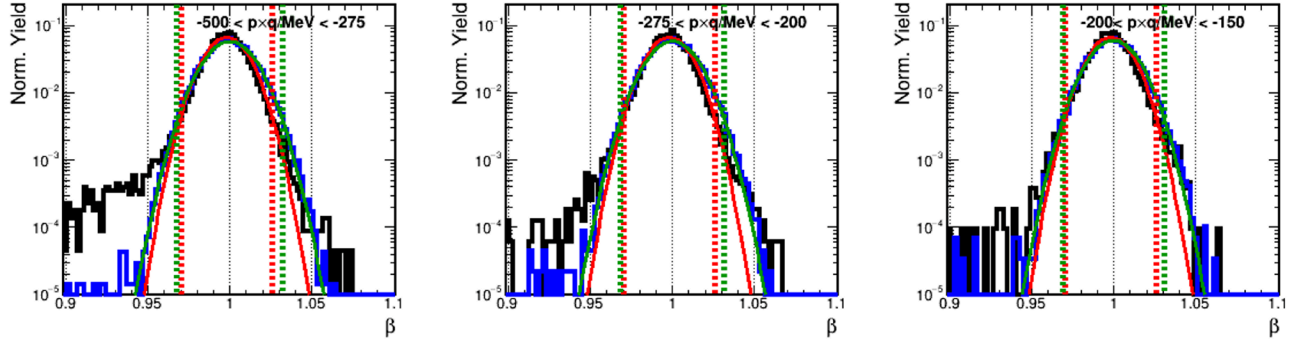


Figure 4.3: Example illustrating the determination of β thresholds for particle identification in Ag+Ag collisions at $\sqrt{s_{NN}} = 2.55$ GeV, using three momentum bins in system 0. Black represents the experimental data, blue shows white leptons embedded into the data. Red is the fit to the experimental data, while green is the fit to the simulated leptons. The vertical lines indicate the cut thresholds for the experimental data (red) and the white leptons embedded into the experimental data (green). Within the two lines lie 98% of the selected particles.

The resulting mean μ and standard deviation σ from the fit are used to select only the particles around the lepton peak. As shown in figure 4.3, there is a noticeable increase in contamination from pions at higher momenta, when the pion velocity approaches the speed of light. Conversely, in order to maximize the purity of the selected lepton sample, the sigma window n_σ around the mean is reduced exponentially as the momentum p increases. The specific relation used in this work is empirically motivated and set to:

$$n_\sigma = \exp(2 - 0.0017 \cdot p) \quad (4.2)$$

This ensures the inclusion of practically 100% of all leptons at lower momenta, where hadronic contamination is minimal, and gradually decreases down to about a 1σ window, selecting around 68% of the full distribution, at $p = 1200$ MeV/ c . In this way, it minimizes pion contributions while maintaining the highest possible statistics.

4.1.3 Evaluation of the Electron Identification

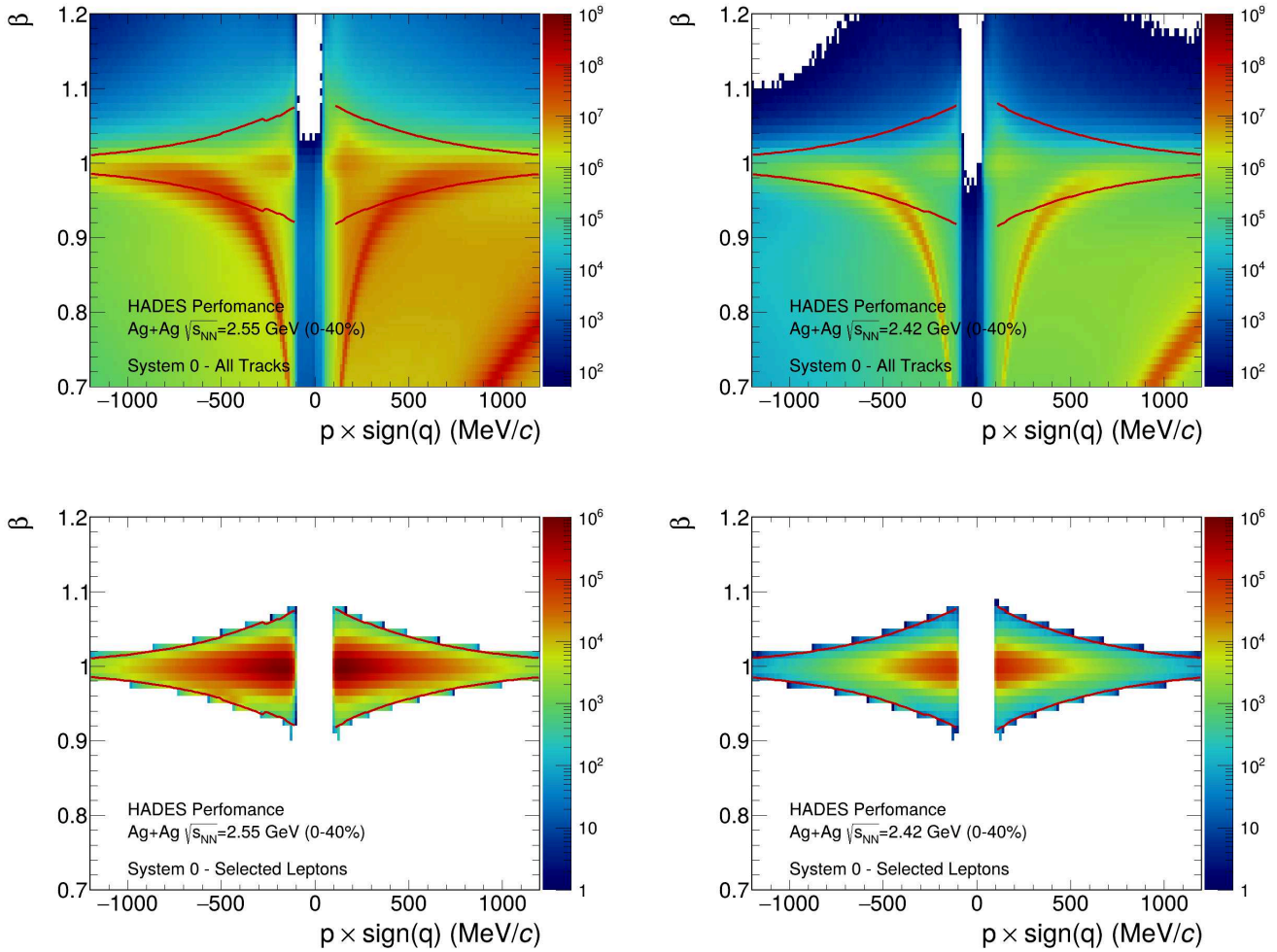


Figure 4.4: Velocity β in dependence of the charge q times momentum p before (top row) and after (bottom row) lepton selection for Ag+Ag collisions at $\sqrt{s_{NN}} = 2.55$ GeV (left panel) and $\sqrt{s_{NN}} = 2.42$ GeV (right panel). The red line indicates the selection condition defined in equation 4.2.

The effects of the lepton identification can most easily be seen in the β -momentum plots presented in figure 4.4. In this case, the top row shows all reconstructed particle tracks. The bottom row shows the remaining sample after application of the particle identification criteria outlined above, namely a cut on the velocity β , the RICH matching quality with $\Delta\phi$ and $\Delta\theta$, as well as the RICH ring radius. The drawn red line shows the empirically relation 4.2 used in the β selection. It can be observed how some pions could still contribute to the selected β -momentum region. However, their presence is strongly suppressed by the RICH-based selection. Overall, the lepton identification procedure performs as intended. In absolute terms, the Ag+Ag collisions at $\sqrt{s_{NN}} = 2.55$ GeV exhibit higher overall statistics due to a longer measurement period and consequently larger event sample, see table 3.1. In both energy settings, the majority of identified electrons and positrons are found at lower momenta, with only a small fraction of high-momentum leptons being observed. This observation motivates the use of a more stringent β cut, which effectively reduces residual pion contamination while removing only a negligible number of true leptons.

Further validation of the lepton identification can be obtained from simulations. The dominant source of potential contamination arises from charged pions. Figure 4.5 illustrates the pion suppression factor as a function of momentum. It is determined using pions embedded into real data and quantifying the fraction that survive after each successive application of the lepton identification criteria. Starting from the basic track sorter condition `kIsLepton`, roughly one in one hundred pions is misidentified as a lepton. With the additional RICH and velocity selections, the suppression improves to approximately 10^{-4} across the full momentum range, reaching values as low as 10^{-6} around $p \approx 100$ MeV/c. Despite the relatively low production rate of electromagnetic probes compared to the abundance of pions, this level of suppression guarantees a highly pure lepton sample while maintaining a satisfactory efficiency, as will be seen in section 4.3. All in all, these results demonstrate the robustness and reliability of the applied PID procedure.

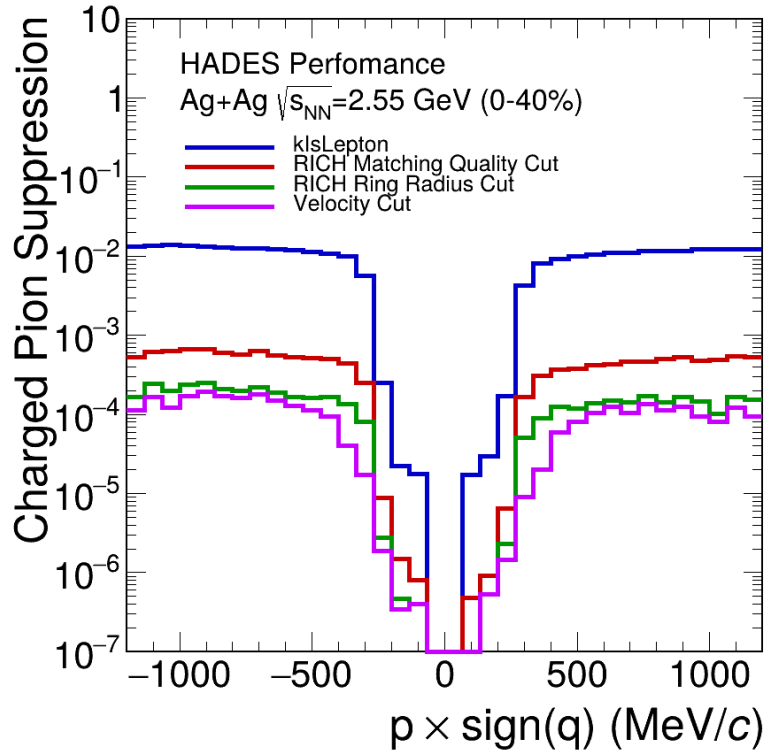


Figure 4.5: Pion suppression factor in dependence of the momentum p after sequential application of the various electron/positron identification criteria.

4.2 Reconstruction of the DiElectron Signal

After the identification of individual electrons and positrons, they are combined with their antiparticle partners to reconstruct the dielectron signal. In experiment, it is generally not possible to directly determine which single leptons belong together as a true pair. In principle, such a matching would require a reconstruction of the decay vertex with spatial resolution comparable to the size of the collision zone, which is on the order of a few femtometers. As this is far below any conceivable experimental vertex resolution, a different approach is taken. All possible combinations of e^+e^- pairs within one event N_{SE}^{+-}

are counted. This will include false matches, referred to as the combinatorial background (CB), which must be subtracted in order to extract the true signal pairs N^{Signal} :

$$N^{\text{Signal}} = N_{\text{SE}}^{+-} - N^{\text{CB}} \quad (4.3)$$

In general, two types of combinatorial background can be distinguished, as illustrated in figure 4.6. On the one hand, uncorrelated background consists out of an e^- and e^+ produced in decays of different particles. These can be viewed as independent of one another. Correlated background, on the other hand, can emerge from two-photon or Dalitz decays, which are most common for the π^0 and η mesons. If the real photon undergoes conversion in some material, i.e. the target or surrounding detector materials, it is possible to form leptons with different parent particles but a common grandparent. Such pairs can be correlated with the signal pair and need to be treated accordingly in the estimation of the combinatorial background.

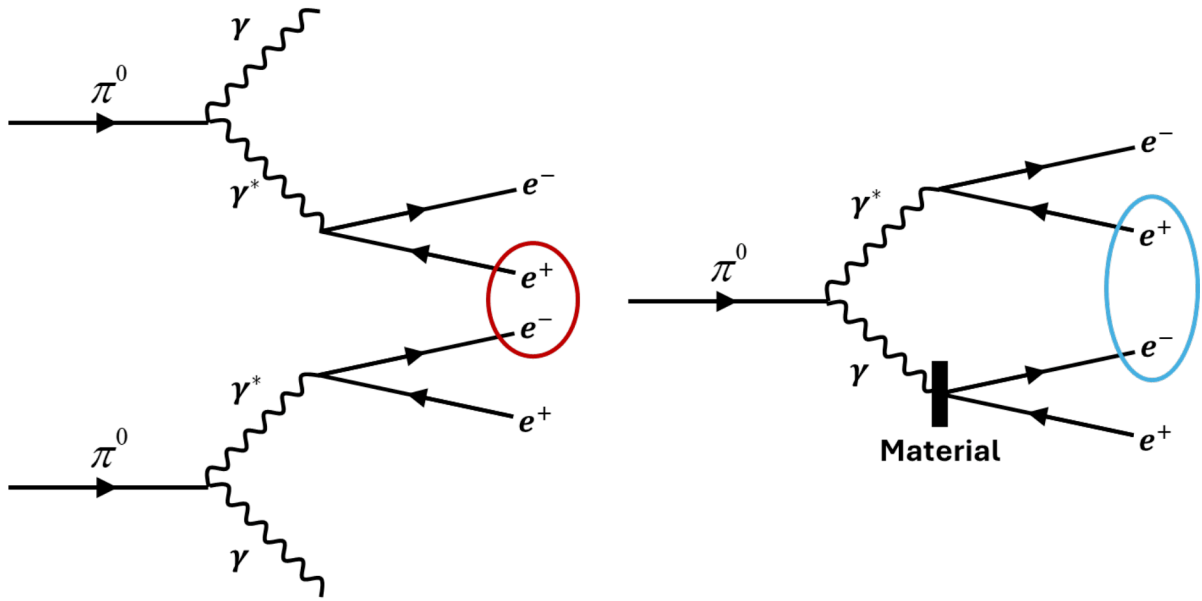


Figure 4.6: Illustration of uncorrelated (red) and correlated (blue) combinatorial background in the example of neutral pion decays.

4.2.1 Estimation of the Combinatorial Background

The most common approach to estimate the combinatorial background for dileptons is based on like-sign pairs in the same event [131, 132, 133]. By counting the number of positron–positron pairs N_{SE}^{++} and electron–electron pairs N_{SE}^{--} , the combinatorial background $N_{\text{SE}}^{\text{CB}}$ can be estimated via their geometric mean [90]:

$$N_{\text{SE}}^{\text{CB}} = 2k\sqrt{N_{\text{SE}}^{++} \cdot N_{\text{SE}}^{--}} \quad (4.4)$$

where the additional factor k accounts for any asymmetry in the spectrometer’s acceptance and reconstruction efficiency between negative and positive charges. It can be determined either via simulations or using event-mixing methods, discussed later in this section.

The big advantage of the same-event like-sign method is its mathematically well founded derivation, which ensures that both the correlated as well as uncorrelated backgrounds are properly described [132]. However, it is noticeably limited by the number of measured leptons within an event. Due to the rarity of electromagnetic probes, this can lead to significant statistical uncertainties, especially in the higher invariant mass regions where fewer dileptons are produced.

Therefore, a second approach based on event-mixing methods is also employed in this work. The principal idea is to match individual electrons and/or positrons with partners from separate events. This ensures that no true signal pairs can be included, and the resulting distribution of unlike-sign mixed-event pairs N_{ME}^{+-} should describe the shape of the combinatorial background arising from random matches of electrons and positrons. It also allows for a substantially larger number of events to be mixed, thereby minimising statistical uncertainties. The main constrain is given by the similarities that events need to fulfil in order to be combined. For this work, the following characteristics are included:

- **Same day:** While conditions during data-taking campaigns should ideally remain stable over time, only events from the same day are combined to minimize the impact of potential changes in efficiency.
- **Same target segment:** Because acceptance depends on the z -vertex of the collisions, only events originating from the same target segment, as reconstructed through the global event vertex, are mixed.
- **Same multiplicity class:** Only events from the same centrality class are mixed together.
- **Same event selection:** Only events passing the same event selection criteria are combined. This is especially important when selection criteria are varied, for example, by application of the purifier discussed in section 3.5.1.

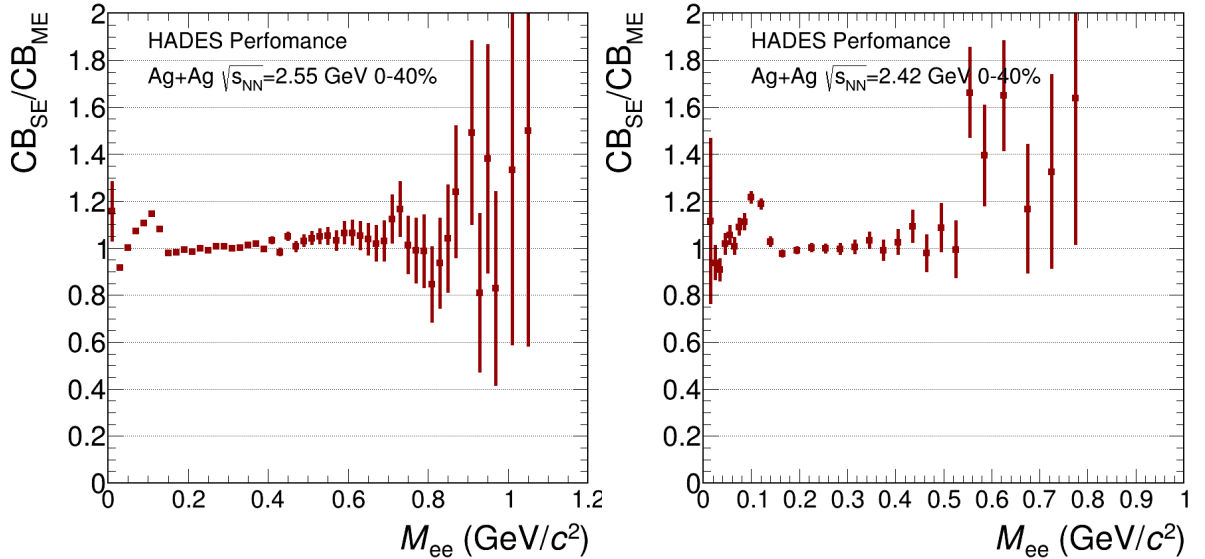


Figure 4.7: Ratio of same-event to mixed-event combinatorial background in dependence of the invariant mass for Ag+Ag collisions at $\sqrt{s_{NN}} = 2.55$ GeV (left panel) and $\sqrt{s_{NN}} = 2.42$ GeV (right panel). Vertical bars represent statistical uncertainties.

These criteria ensure that the combinatorial background calculated via event-mixing $N_{\text{ME}}^{\text{CB}}$ approximates the shape of the same-event background. This can be verified by comparing the same-event background $N_{\text{SE}}^{\text{CB}}$ with the mixed-event background $N_{\text{ME}}^{\text{CB}}$, as shown in figure 4.7 plotted as a function of invariant mass M_{ee} . At lower masses, below about $M_{ee} < 0.2 \text{ GeV}/c^2$, some fluctuations and deviations can be observed. These can be attributed to correlated background contributions, which are not described by event mixing. With increasing masses, however, the ratio of same-event to mixed-event background remains constant within statistical uncertainties. In this region, both methods appear to be generally suitable for estimating the combinatorial background.

The event-mixing technique further allows for an estimation of the charge asymmetry factor k , purely based on the experimental data [90]:

$$k = \frac{N_{\text{mix}}^{+-}}{2\sqrt{N_{\text{mix}}^{++} \cdot N_{\text{mix}}^{--}}} \quad (4.5)$$

This ratio describes how the like-sign combinations compare to the unlike-sign combinations. If positrons and electrons are equally likely to be detected, this factor approaches unity. This is indeed observed at higher masses, as seen in figure 4.8. At lower masses of about $M_{ee} < 0.3 \text{ GeV}/c^2$, a bump appears in the distribution, most likely caused by low-momentum leptons that may be bent out of the experimental acceptance in a charge-dependent manner. The effect of charge asymmetry also appears to be more pronounced at the higher collision energy of $\sqrt{s_{\text{NN}}} = 2.55 \text{ GeV}$. This can be attributed to the stronger magnetic field applied in this measurement, as the HADES superconducting magnet was operated at 3200 A for $\sqrt{s_{\text{NN}}} = 2.55 \text{ GeV}$, compared to 2500 A for $\sqrt{s_{\text{NN}}} = 2.42 \text{ GeV}$. Similar effects have been observed in analogous analyses by PHENIX [132], STAR [134], and ALICE [135].

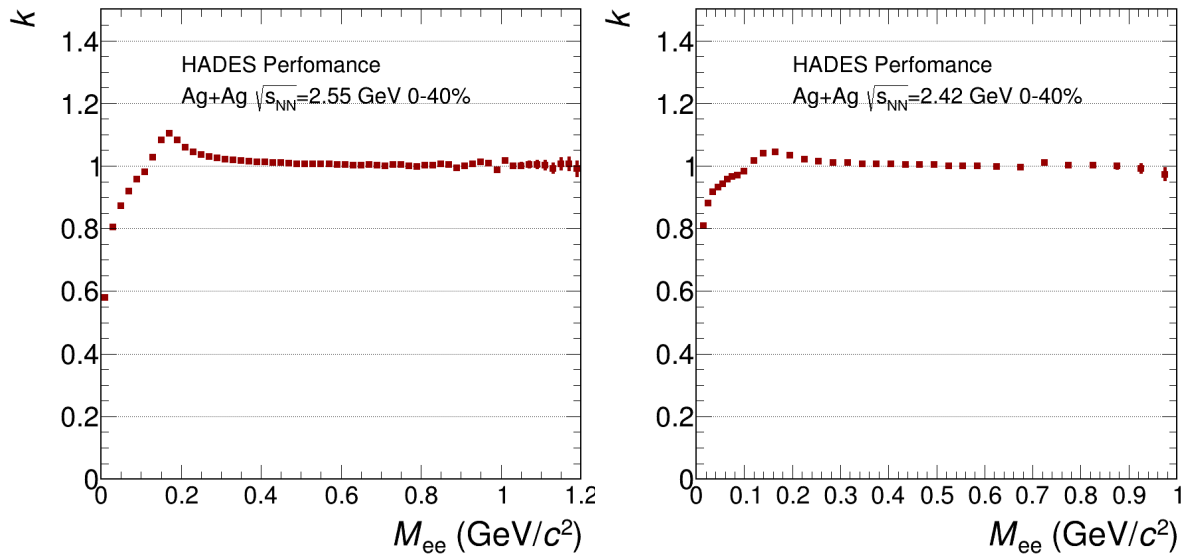


Figure 4.8: Charge asymmetry factor k in dependence of the invariant mass for Ag+Ag collisions at $\sqrt{s_{\text{NN}}} = 2.55 \text{ GeV}$ (left panel) and $\sqrt{s_{\text{NN}}} = 2.42 \text{ GeV}$ (right panel). Vertical bars represent statistical uncertainties.

Ultimately, the choice between the two methods depends on the observable under investigation. The same-event like-sign method accounts for both correlated and uncorrelated background but suffers from increasing statistical uncertainties in regions with fewer counts. The event-mixing method, on the other hand, does not suffer from such statistical limitations but cannot describe correlated background. In case of the reconstruction of the invariant mass spectrum, a combined approach is applied. Up to $M_{ee} = 0.4 \text{ GeV}/c^2$, the same-event method is used to capture the correlated background present in this mass range. For $M_{ee} > 0.4 \text{ GeV}/c^2$, the mixed-event spectrum is applied to reduce statistical uncertainties at higher masses. The mixed-event CB is normalised to the same-event spectrum in the region $M_{ee} = 0.2\text{--}0.3 \text{ GeV}/c^2$. The resulting signal is shown in figure 4.9 for the Ag+Ag data.

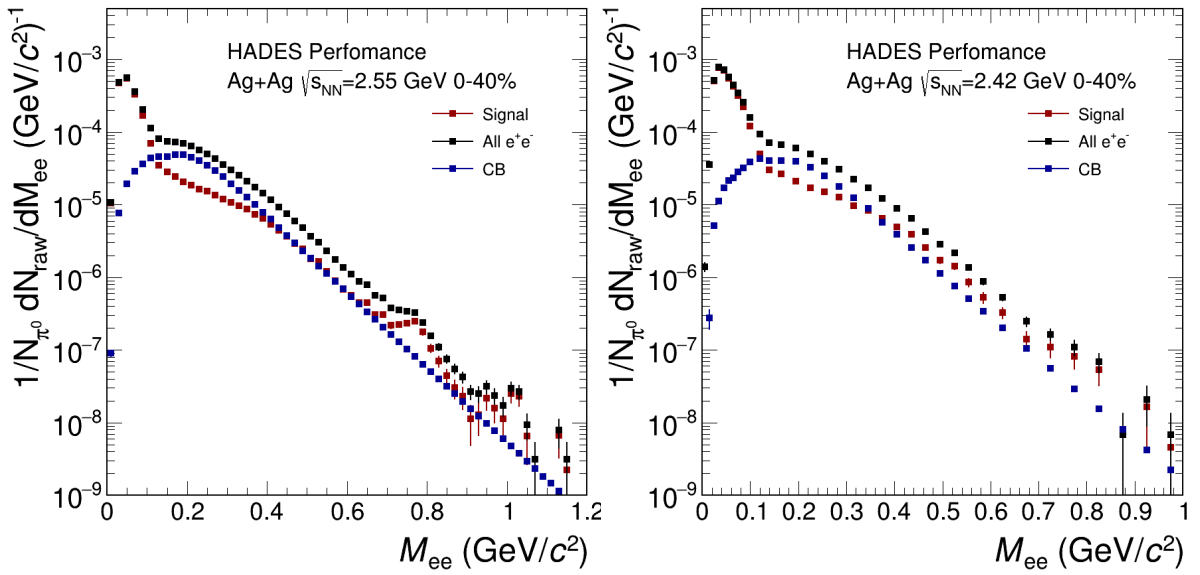


Figure 4.9: Resulting signal after subtraction of the combinatorial background factor k in dependence of the invariant mass for Ag+Ag collisions at $\sqrt{s_{NN}} = 2.55 \text{ GeV}$ (left panel) and $\sqrt{s_{NN}} = 2.42 \text{ GeV}$ (right panel). Black points indicate all possible e^+e^- pairs, blue shows the estimated combinatorial background, and red points display the final signal. Vertical bars represent statistical uncertainties.

4.2.2 Optimising the Signal-To-Background Ratio with Conversion Rejection

It is intuitive, that the combinatorial background can be reduced by removing electrons and positrons from the sample which do not contribute to the signal. While this is hardly possible in a general sense, one distinction can be made in analyses focusing on the reconstruction of virtual photons. In this case, the dominant physical background comes from real photons undergoing conversion in the target or detector materials, particularly in connection with π^0 Dalitz decays. These real photons produce additional electrons and positrons which contribute to the combinatorics. In particular, they are the major reason for correlated background. Such contributions can be partially suppressed by applying a few conversion rejection criteria, developed in detail in [66]. They exploit one of the characteristic features of photon conversion pairs, namely the small values of the e^+e^- opening angle in comparison to most dielectron sources.

- **Restriction on Maximum Number of RICH Cals:** A first requirement is set on the number of Cherenkov photons N_{cals} , detected around a RICH ring, as they can indicate the presence of close tracks. If N_{cals} exceeds a threshold of approximately 25 [66], it suggests that more than a single lepton contributed to the RICH signal. Crucially, this holds true even if only a single ring is reconstructed in cases of very close trajectories.
- **Restriction on Opening Angle:** Similarly, a second requirement is placed on the opening angle between two particle candidates. Historically, this is done based on the MDCs track candidates [31, 90]. With the upgrade RICH capabilities, this is extended by checking for the opening angles between RICH rings [66]. If two rings with an angle of less than 9° are found, the corresponding particle candidates are removed, improving upon the previous selection methods purely based on MDCs as seen in figure 4.10.
- **Restriction on the Single Track Vertex:** A final requirement is placed on the vertex of the particle candidate, ensuring it is close to the target region. This criterion aims to exclude conversion pairs originating from material outside the target. Due to the substantial multiple scattering, particularly pronounced for electrons and positrons at low momenta, the cut is kept relatively loose, removing approximately 1.71% of off-vertex tracks [66].

The effects of the conversion rejection are demonstrated in figure 4.10. It shows the signal-to-background ratio as well as the significance before and after application of the described criteria. An improvement of about a factor of 5 was achieved, in comparison to a standard 9° opening angle cut based on MDC tracks. Therefore, they are applied by default in this work, including the figures shown in the previous sections. One may also note that the performance between the two collected energies, i.e. $\sqrt{s_{NN}} = 2.55$ GeV and 2.42 GeV, appears to be very similar in terms of signal-to-background ratio and significance. A minor increase in the signal-to-background ratio at $\sqrt{s_{NN}} = 2.42$ GeV can be understood from the slightly smaller particle production rates at the lower energies, which reduces combinatorics.

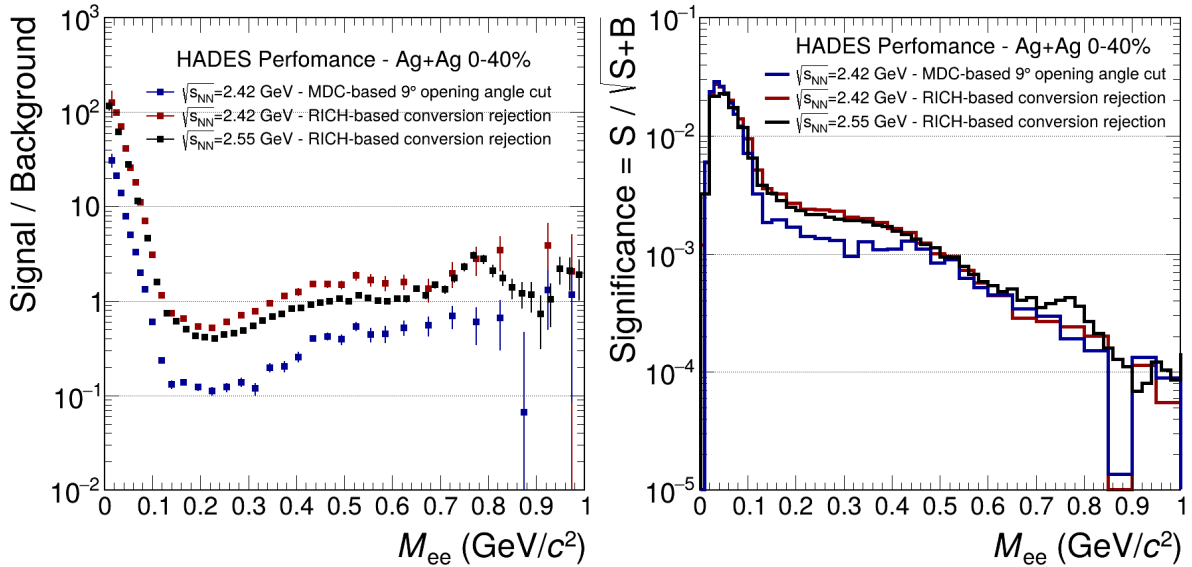


Figure 4.10: Signal-to-background ratio (left panel) and significance (right panel) with the standard as well as improved, based on RICH, conversion rejection criteria for Ag+Ag collisions at $\sqrt{s_{NN}} = 2.55$ GeV and 2.42 GeV.

4.3 Efficiency and Acceptance Corrections

The dielectron signal shown in figure 4.9 does not yet describe all dielectrons produced in the heavy-ion collisions. This is because of two factors inherent to the detector setup and reconstruction process. First, the detector only covers a finite region of the solid angle around the interaction point. Leptons emitted outside the active detector area remain undetected. This geometric constraint is known as acceptance. To compensate for this partial coverage, any multiplicity measurement must be extrapolated to the region of unmeasured phase space beyond the detector's field of view. Second, even for particles that pass through the sensitive volume of the detector, reconstruction and identification are not guaranteed. Due to inefficiencies in track reconstruction algorithms or strict selection criteria in the particle identification, some true leptons may not be correctly recognised or may be excluded from the analysis. This introduces a further loss in the efficiency. Because both acceptance and efficiency are specific to the detector system and the analysis procedure, uncorrected results cannot be directly compared to theoretical predictions or results from other experiments. Thus, appropriate correction factors should be applied to the measured data.

The acceptance ϵ_{Acc} is defined as the ratio of the number of leptons within the detector's geometrical and kinematic coverage N_{Acc} to the total number of leptons generated in the collision N_{Total} :

$$\epsilon_{\text{Acc}} = \frac{N_{\text{Acc}}}{N_{\text{Total}}} \quad (4.6)$$

The efficiency ϵ_{Eff} quantifies the performance of the reconstruction and identification procedures. It is given by the ratio of successfully reconstructed leptons N_{Reco} to the number of leptons within the accepted region:

$$\epsilon_{\text{Eff}} = \frac{N_{\text{Reco}}}{N_{\text{Acc}}} \quad (4.7)$$

In this work, the efficiency and acceptance are initially assessed at the level of individual electrons and positrons. This information, combined with a realistic dilepton cocktail simulation, enables the calculation of the global pair correction factors presented in section 4.3.3.

4.3.1 Single Track Correction Matrices

The estimation of the detector response is primarily based on the simulation described in section 3.1.1. In this case, the simulation utilizes a set of white leptons, characterised by isotropic momentum values ranging from 0 to 2 GeV/ c , as well as polar and azimuthal angles spanning 0° to 90° and 0° to 360° respectively. These leptons are embedded into real data to ensure a realistic representation of the background and event activity. Using this setup, the numbers of reconstructed N_{Reco} , accepted N_{Acc} , and total leptons N_{Total} can be determined. The selection criteria generated in section 4.1 are used for this process. Further, a lepton is defined as accepted if it passes the condition of having at least four hit wires in each MDC layer. In order to minimize fluctuations from regions with low acceptance and efficiencies, a geometrical acceptance condition is imposed. This criterion, based on [66], includes the following requirements:

- $16^\circ < \theta < 83^\circ$
- $100 \text{ MeV}/c < p < 1200 \text{ MeV}/c$

For positrons, an additional lower momentum cut is applied due to their tendency to be bend away from the spectrometer at low momenta and low polar angles:

- $p > \exp(-0.135 \theta + 8.3) + 100 \text{ MeV}/c$ (Ag+Ag at $\sqrt{s_{NN}} = 2.55 \text{ GeV}$)
- $p > \exp(-0.25 \theta + 10) + 100 \text{ MeV}/c$ (Ag+Ag at $\sqrt{s_{NN}} = 2.42 \text{ GeV}$)

Where the exponential terms are empirical parametrisations that yield the momentum p in units of MeV/c as a function of the polar angle θ . The momentum cut varies between the two energies due to differences in the magnetic field settings at each energy.

The counts of accepted, reconstructed, and total leptons are stored in 3D histograms, with fine binning based on momentum p , polar angle θ , and azimuthal angle ϕ . Alternatively, two-dimensional matrices of transverse momentum p_t and rapidity y can also be used to describe the phase space. Based on Equations 4.6 and 4.7, these histograms enable the calculation of the efficiency and acceptance for individual electrons and positrons. Thanks to the fine binning, the resulting matrices can be considered effectively model-independent, which justifies the use of white leptons and provides a direct estimate of the efficiency and acceptance at specific phase-space points. An example is shown in figure 4.11, illustrating the projected efficiency as a function of θ and momentum. The lines in the plot indicate the geometrical acceptance conditions described above. A slight decrease in efficiency with increasing momentum is observed, which is directly related to the stricter β cuts from equation 4.2. In contrast, no noticeable dependence of the efficiency on the polar angle θ is observed. Overall, the efficiency remains around 60% across most of the accepted phase space, with a visible drop only at the edges of the acceptance. This behaviour motivates the geometrical conditions highlighted in red.

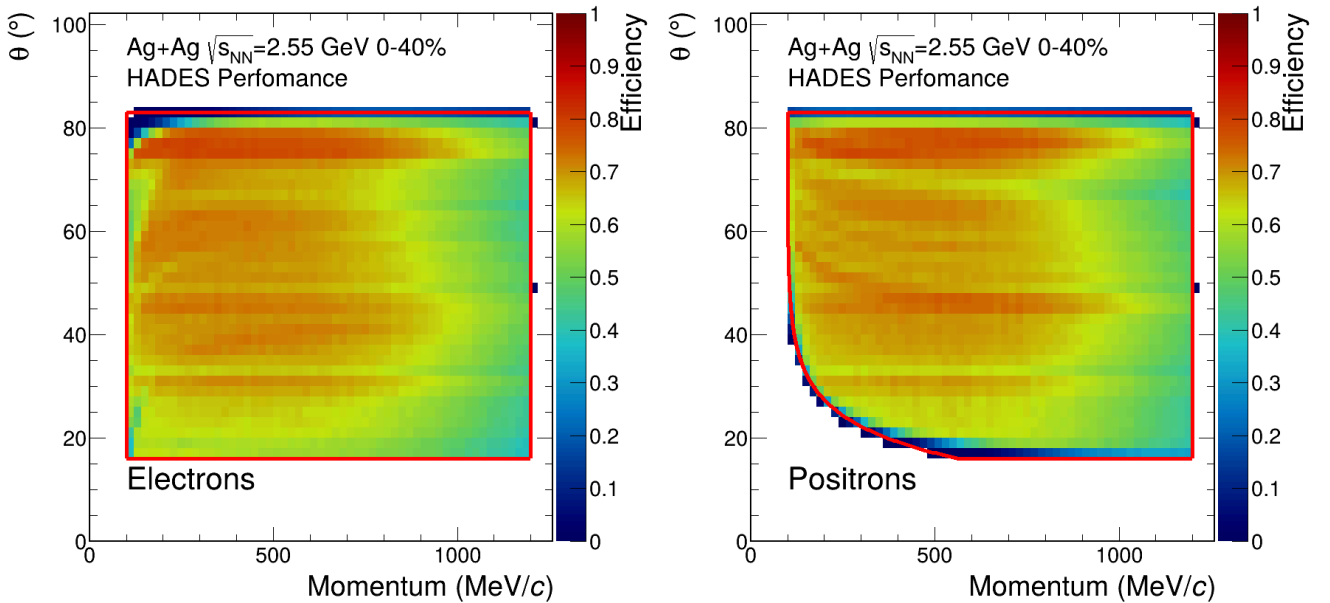


Figure 4.11: Single lepton efficiency in dependence of the polar angle θ and momentum p for electrons (left panel) and positrons (right panel) for Ag+Ag collisions at $\sqrt{s_{NN}} = 2.55 \text{ GeV}$ at 0-40% centrality. The red boxes outline the geometrical acceptance condition outlined above.

4.3.2 Accounting for Momentum Smearing in Simulations

An additional challenge when working with simulations is the difference between the reconstructed momentum p_{rec} and the initial momentum of the particle at the time of emission p_{ideal} . Through the interaction of the particle with the surrounding structure and detector material, every charged particle will experience some energy loss, reducing the momentum measured eventually at the MDCs. In principle, this is taken into account in the analysis procedure by application of a standard momentum correction. However, the electrons and positrons show additional losses due to Bremsstrahlung effects. This is demonstrated in figure 4.12, which shows the ideal momentum of electrons and positrons in comparison to the reconstructed, also called smeared, momentum in a given polar angle interval. It is based on white lepton simulation embedded into experimental data and should have all essential momentum loss procedures incorporated in the GEANT simulation. Two effects are visible. For one, the limited momentum resolution leads to symmetric fluctuations of p_{rec} around p_{ideal} , meaning that the reconstructed momentum can be either overestimated or underestimated with equal probability. For another, an additional tail towards smaller p_{rec} is evident. It can be identified as the effect from Bremsstrahlung, systematically lowering the measured momenta. Because of the stochastic nature of this process, it is only experienced noticeably by some electrons, while others remain largely unaffected. This makes an individual correction unfeasible. Nevertheless, this effect must be considered in any dielectron analysis. It necessitates a clear distinction between ideal and reconstructed momenta and to ensure they are not mixed in any calculations of correction factors. For consistency and to avoid any potential biases, this work defaults to show final observables using the reconstructed momentum, unless otherwise stated. For simulations that do not explicitly employ GEANT to model the momentum smearing, the two-dimensional distributions shown in figure 4.12 can be used to sample the corresponding effects. The distributions have been reconstructed in four θ bins: 0° – 35° , 35° – 55° , 55° – 70° , and 70° – 90° . Separate sets have been generated for positrons and electrons, although figure 4.12 already shows that the differences between the two are minor. The main deviations occur at the edges of the detector's acceptance, i.e. low or high θ , where particles may be bent outside the detector depending on their charge.

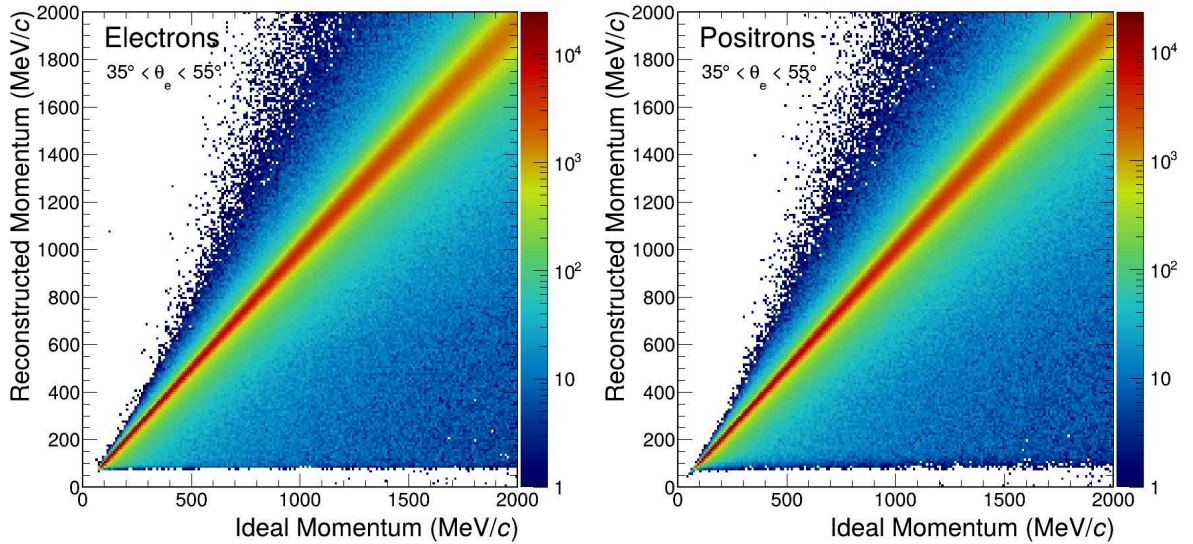


Figure 4.12: Ideal vs. reconstructed momentum of electrons (left panel) and positrons (right panel) for Ag+Ag collisions at $\sqrt{s_{\text{NN}}} = 2.55$ GeV at a given θ interval of 35° – 55° .

4.3.3 Estimation of the Pair Corrections

The impact of the individual corrections, denoted as ϵ_1 and ϵ_2 , on the total pair correction can be estimated via their product:

$$\epsilon_{\text{Pair}} = \epsilon_1 \cdot \epsilon_2 \quad (4.8)$$

While this approximation neglects potential correlations between the individual leptons, it will be shown in section 4.3.4 how it serves as a reasonable estimate. Based on this relation, a direct correction of the experimental data is possible. By filling a histogram of a given experimental observable with a weight of $1/\epsilon_{\text{Pair}}$, the final spectrum can, on average, be corrected. The key advantage of this method is that it avoids introducing additional model dependencies, relying solely on the distribution observed in the experimental data. Depending on the specific observable under investigation, however, there are limitations to this approach.

If the correction is applied individually to each dielectron pair on an event-by-event basis, the magnitude of the correction can vary significantly depending on the phase space of the underlying leptons. While this variation tends to average out when a sufficient number of pairs contribute to a data point, it may lead to large point-to-point fluctuations in cases where only a small number of counts add to a given bin in the final spectrum. This effect becomes more pronounced if the correction factor varies strongly within the region of phase space underlying the specific data point. Moreover, in regions of phase space where no particles are measured, the correction factor approaches infinity, making this correction procedure completely inapplicable in such areas. To circumvent these limitations, a different approach is employed in this analysis. Using a realistic dielectron cocktail simulation, the efficiency is determined as a function of dielectron observables, such as the invariant mass M_{ee} . This is referred to as a pair correction. This method suppresses bin-to-bin fluctuations and enables extrapolation into unmeasured regions of phase space by estimating the number of leptons which have been completely missed by the detector.

This could be achieved by embedding a realistic dielectron cocktail into experimental data or full event simulations, and evaluating the acceptance and efficiency according to equations 4.6 and 4.7. However, due to the low yield of electromagnetic probes compared to the hadronic background, this approach is limited by the high statistics required to achieve meaningful estimates for $\epsilon_{\text{acc,Pair}}$ and $\epsilon_{\text{eff,Pair}}$. It would demand substantial computing resources and disk space. Instead, it is much more efficient to utilize the calculated single lepton correction matrices. They already encode the detector performance for individual electrons and positrons for a given momentum p , polar angle θ and azimuthal angle ϕ , while accounting for event multiplicities and track densities, independent of the lepton origin. Based on this, the cocktail simulation in this work is restricted to dilepton sources and their decays into e^+e^- pairs. For each simulated event, the two leptons are first filtered by the HADES acceptance using the single particle acceptance matrices. A uniform random number between 0 and 1 is generated for each lepton. If it is less than the corresponding matrix value, the lepton is flagged as accepted. If this is true for both leptons, the pair adds to the spectrum within the HADES acceptance. Furthermore, a reconstructed spectrum can be estimated by weighting the accepted pairs using the product of their individual efficiency factors, as given in equation 4.8. To account for the momentum smearing discussed in the previous section, the reconstructed momentum can be sampled from the ideal momentum via the two-dimensional distributions shown in figure 4.12.

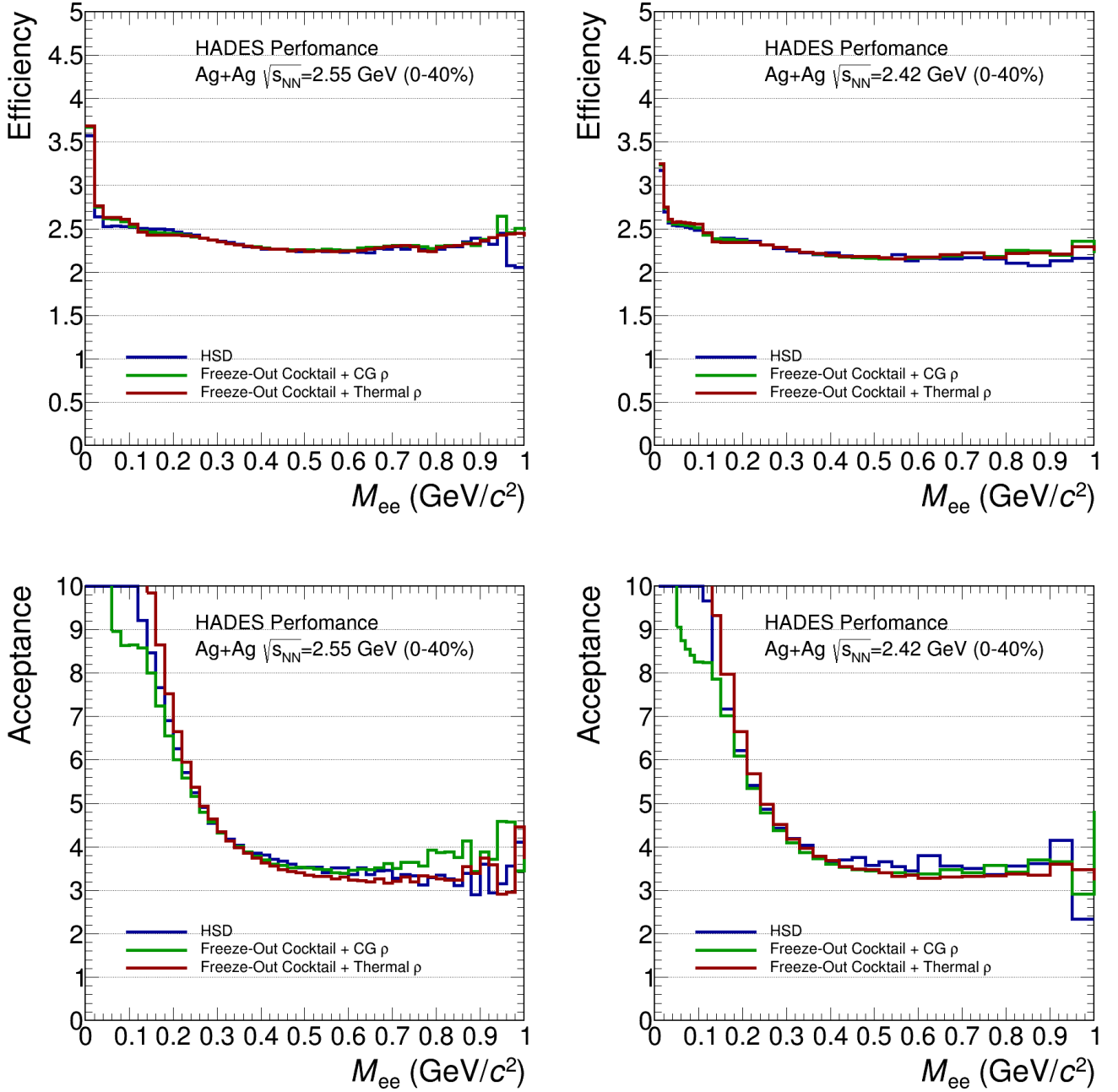


Figure 4.13: Pair correction factors in dependence of the the invariant mass for Ag+Ag collisions at 0-40% centrality. Top row: Efficiency for $\sqrt{s_{NN}} = 2.55$ GeV (left panel) and 2.42 GeV (right panel). Bottom row: Acceptance for $\sqrt{s_{NN}} = 2.55$ GeV (left panel) and 2.42 GeV (right panel).

This procedure yields three spectra: (i) the true dielectron distribution in the full phase space, (ii) the distribution within the HADES acceptance, and (iii) the reconstructed spectrum as it would appear in real data. The pair correction factor, as a function of the observable under investigation, is then obtained by dividing these spectra following the definitions in equations 4.6 and 4.7. They are shown in figure 4.13 in dependence of the invariant mass M_{ee} with three models that have been used to estimate the dielectron cocktail.

To ensure a realistic cocktail, the major dielectron sources, introduced in table 1.3, should be included in the simulation. Specifically, this entails contributions from π^0 , η , and ω Dalitz decays, along with direct decays from the vector mesons ρ , ω , and ϕ . The Pluto event generator [99] serves as the central tool to simulate each decay. They are then combined into one cocktail by weighting each contribution according to their measured yields and branching ratios. Details regarding the applied multiplicities are discussed in section 4.4. A special procedure is required for the treatment of in-medium modifications, which are particularly important for the ρ meson. It is known to exhibit a significant broadening, see section 1.4. This is not fully captured by the Pluto simulation. Therefore, the cocktail (π^0, η, ω) is also supplemented with coarse-grained in-medium predictions [58] in an effort to improve the description of the ρ meson. Finally, a further simulation based on Hadron-String-Dynamics (HSD) [136] serves as an independent alternative in the modelling of the dielectron cocktail.

As illustrated in figure 4.13, all three models yield comparable results. Only slight model dependencies are visible for the acceptance correction. For the final analysis, the mean of these models is used as the default pair correction factor. The spread among them is included in the systematic uncertainty. In general, the efficiency correction factor is found to be approximately constant across the entire mass range. Conversely, the acceptance correction factor shows a stronger dependence on invariant mass. While it remains in the range of 3–4 for $M_{ee} > 0.4 \text{ GeV}/c^2$, it increases sharply, exceeding a factor of 10, in the π^0 mass region. This behaviour is largely attributed to the opening angle cut discussed in section 4.2.2, which removes a substantial fraction of low-mass dielectrons and is corrected for in the extrapolation to the full phase space. Lastly, one can note that the estimated efficiency as well as the acceptance are found to be quite similar between the two energies of $\sqrt{s_{NN}} = 2.55 \text{ GeV}$ (left panel) and 2.42 GeV (right panel).

4.3.4 Self-Consistency Checks for the Corrections

The corrections for dielectron pairs are based on equation 4.8. Since this approach assumes no correlations between the individual leptons, its validity needs to be verified. Similarly, the overall implementation of the correction and simulation procedures should be thoroughly checked. Both questions are addressed by performing a self-consistency check. Dalitz decays from η and π^0 mesons are simulated using the Pluto event generator and embedded into real data. The embedded events undergo the full analysis chain, with the dielectron signal being reconstructed and corrected in the same manner as experimental data. The resulting reconstructed signal is then compared with the true expectations from the input simulations in order to validate the full correction procedure.

The ratio of the true pair efficiency $\epsilon_{\text{Pair,eff}}^{\text{Nominal}}$ to the estimated efficiency $\epsilon_{\text{Pair,eff}}^{\text{Estimated}}$, is illustrated in figure 4.14. It is found to be close to unity across most of the mass range. The key exception are significant discrepancies at very low masses ($M_{ee} < 30 \text{ MeV}/c^2$). These deviations are most likely due to unaccounted close-pair correlation effects. As such, they would need to be taken into account in studies relating to very low mass dielectrons. Since the primary focus of this work lies on masses above this threshold, the overall agreement is deemed excellent. The maximum deviations of about 8% in the higher mass range are incorporated into the systematic uncertainties.

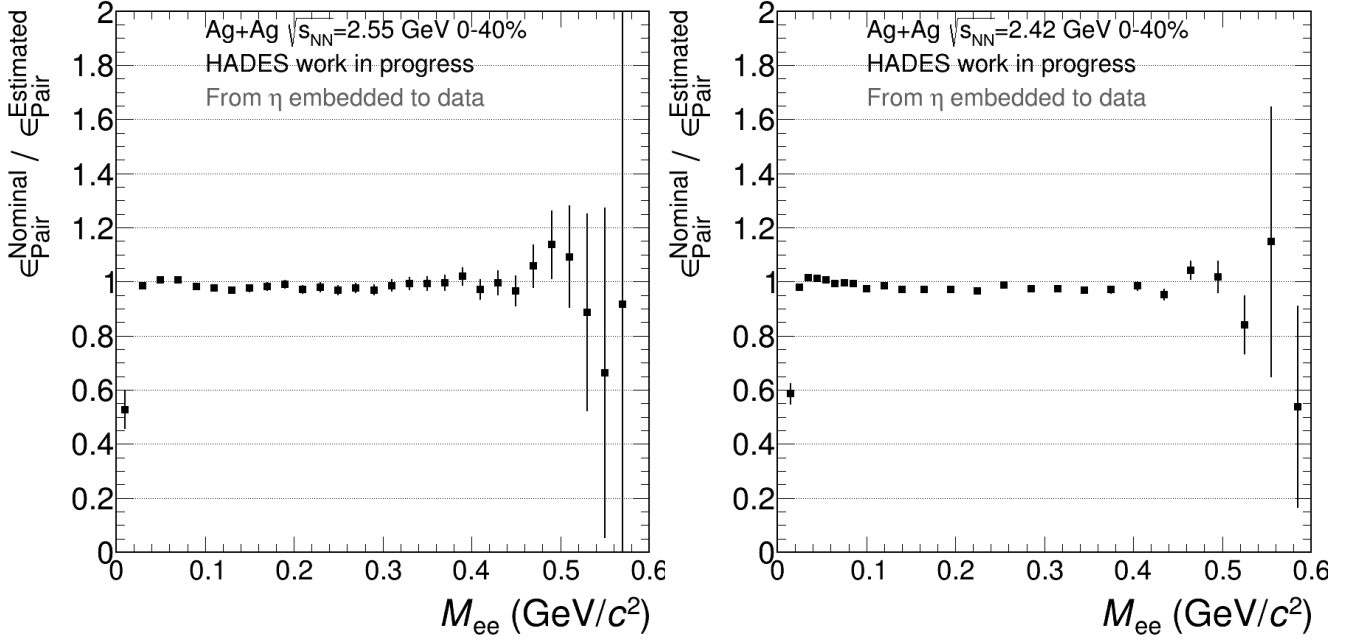


Figure 4.14: Ratio of true $\epsilon_{\text{Pair,eff}}^{\text{Nominal}}$ to the estimated efficiency $\epsilon_{\text{Pair,eff}}^{\text{Estimated}}$ in order to assess the consistency of the correction procedure. Vertical bars represent statistical uncertainties.

4.4 Disentangling the Relative Yields in the DiElectron Cocktail

As discussed in section 1.4, the reconstructed signal represents an integral over all dielectron contributions accumulated throughout the full evolution of the collision. To isolate the thermal radiation and investigate the properties of the hot and dense fireball, a detailed understanding of both the sources from initial, e.g. first chance nucleon-nucleon collisions, as well as freeze-out sources is essential. In this work, the decay channels listed in table 1.3 are considered. Each contribution is estimated individually to account for the distinct production mechanisms and the specific experimental methods used to quantify them.

- **π^0 Contribution:** The neutral pion multiplicity N_{π^0} is estimated by assuming isospin symmetry, taking the average of the charged pions N_{π^-} and N_{π^+} , measured in the same experiment [70], according to $N_{\pi^0} = \frac{N_{\pi^-} + N_{\pi^+}}{2}$. This method was validated in simulations [90] as well as experimentally through the measurement of the pion multiplicity using the $\pi^0 \rightarrow \gamma\gamma$ channel. When both photons undergo conversion, the reconstruction of the π^0 in the $4e$ channel provides an independent experimental estimate of N_{π^0} [66, 137]. In this case, the partial installation of the electromagnetic calorimeter (ECAL) also enabled, for the first time, a direct reconstruction of photons from π^0 decays at HADES [138]. All three approaches yield consistent results within the uncertainties.
- **η Contribution:** The η meson multiplicity is taken from independent measurements from the TAPS collaboration [123, 139]. Efforts are being done to similarly establish the η multiplicity directly at HADES. This includes detection of the η two-photon decay channel either directly with the ECAL [138] or indirectly through photon conversion and reconstruction in the four-electron ($4e$) channel [66, 137].

- **ω Contribution:** Direct measurements of the ω meson multiplicity are not available for the exact collision systems and energies studied here. Instead, estimates are inferred from previous Ar+KCl collision data [140], which provide guidance on the expected yield. These empirical results have been compared with predictions from the statistical hadronisation model [141] and are found to be consistent.
- **ϕ Contribution:** The ϕ meson multiplicity is estimated from its dominant decay channel $\phi \rightarrow K^+ K^-$ [142] for the Ag+Ag collisions at $\sqrt{s_{\text{NN}}} = 2.55$ GeV. Due to its strong suppression at lower energies, the ϕ contribution is considered negligible and therefore omitted for the Ag+Ag dataset at $\sqrt{s_{\text{NN}}} = 2.42$ GeV.
- **Initial-State Contributions:** The dielectron sources from first-chance NN collisions considered in this analysis primarily comprise Bremsstrahlung processes and the Dalitz decay of the Δ resonance, i.e. $\Delta \rightarrow Ne^+e^-$. These contributions serve as a baseline reference for heavy-ion collisions, derived from proton-proton ($p+p$) and proton-(quasi-free)neutron ($p+n$) reactions. At the beam energy $\sqrt{s_{\text{NN}}} = 2.42$ GeV, the relevant $p+p$ and $p+n$ data have been measured and reconstructed during a previous experimental campaign [143]. For the higher energy of $\sqrt{s_{\text{NN}}} = 2.55$ GeV, elementary reaction data have also been recorded, although their analysis is still in progress. Preliminary results show good agreement between the measured elementary collisions and theoretical predictions from the GiBUU transport model [144]. Consequently, for the current analysis at $\sqrt{s_{\text{NN}}} = 2.55$ GeV, the initial contributions are modelled using GiBUU simulations (GiBUU Release 2023, patch 2), while the experimentally measured reference is directly employed at $\sqrt{s_{\text{NN}}} = 2.42$ GeV.

The final particle multiplicities used in this work are summarised in table 4.1. They are determined separately for each centrality class. In cases where direct measurements are not available for a given class, the multiplicities are extrapolated based on participant scaling. Specifically, a linear scaling with N_{part} is assumed for pions as well as for the η mesons, as has been studied in [70] and [123] respectively. The vector mesons are scaled according to $\propto \langle N_{\text{part}} \rangle^{\frac{4}{3}}$ [31].

Centrality	Ag+Ag $\sqrt{s} = 2.55$ GeV					Ag+Ag $\sqrt{s} = 2.42$ GeV			
	$\langle N_{\text{part}} \rangle$	π^0	η	ω	ϕ	$\langle N_{\text{part}} \rangle$	π^0	η	ω
0-40%	103	8.04	0.2	3.6e-3	3.1e-5	102	5.67	8.1e-2	7.1e-4
0-10%	161	12.65	0.31	6.5e-3	5.5e-5	159	9.09	0.12	1.2e-3
10-20%	115	8.85	0.22	4.1e-3	3.5e-5	113	6.23	9e-2	8.1e-4
20-30%	81	6.3	0.16	2.5e-3	2.2e-5	80	4.38	6.4e-2	5.1e-4
30-40%	57	4.35	0.11	1.6e-3	1.4e-5	55	3.0	4.4e-2	3.1e-4
Scaling		linear	linear	$\langle N_{\text{part}} \rangle^{\frac{4}{3}}$	$\langle N_{\text{part}} \rangle^{\frac{4}{3}}$		linear	linear	$\langle N_{\text{part}} \rangle^{\frac{4}{3}}$
Mult/N_{part}		0.08	2e-3	3.5e-5	3e-7		0.055	8e-4	6.9e-6

Table 4.1: Summary of particle multiplicities and scaling for various centralities in Ag+Ag $\sqrt{s_{\text{NN}}} = 2.55$ GeV and 2.42 GeV collisions. The number of participants for each centrality class is based on the calculation of the Glauber Monte Carlo model discussed in section 3.3.

Figure 4.15 shows the measured dielectron mass spectra in comparison to the estimated cocktail contributions. One can observe an overshoot of the experimental data to the cocktail sum, which is attributed to the thermal radiation. Subtraction of the reference and freeze-out sources leads to the isolation of thermal spectra discussed in chapter 6.

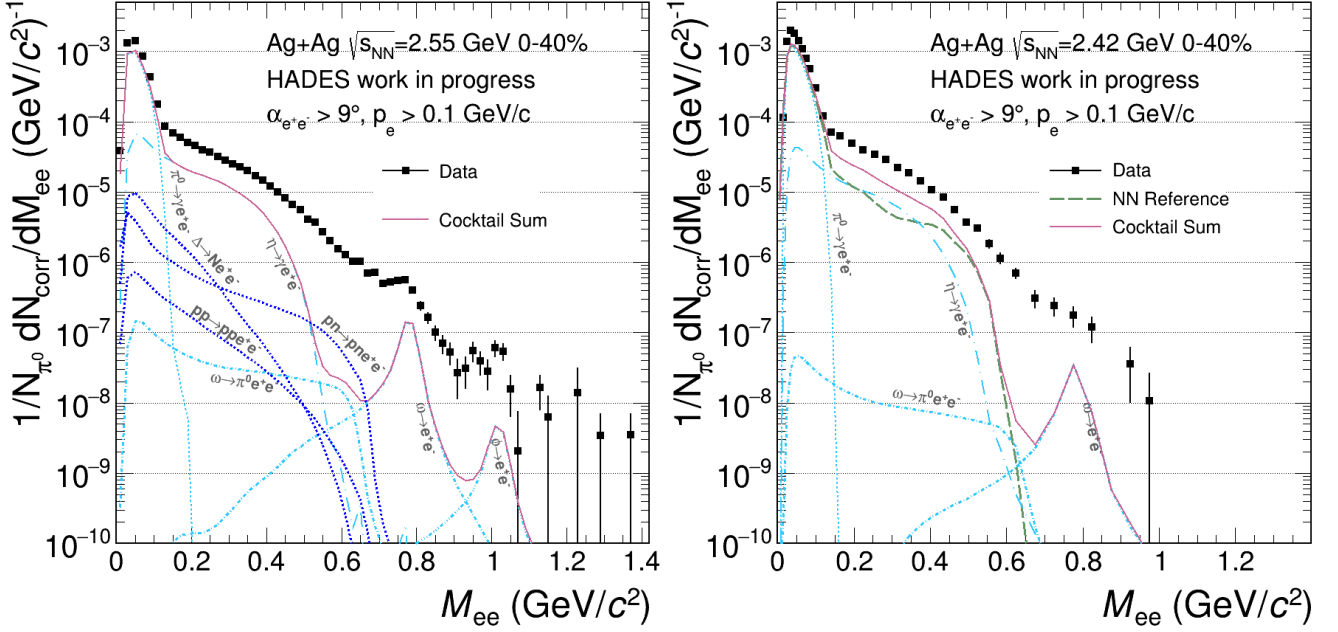


Figure 4.15: Efficiency-corrected dielectron invariant mass spectra compared to the Pluto cocktail for Ag+Ag collisions. The cocktail includes contributions from η , ω , and ρ mesons, based on experimental multiplicity measurements and Pluto simulations as discussed in the text, as well as from elementary $p + p$ and $p + n$ collisions. The elementary contributions have been measured at 1.25A GeV for $\sqrt{s_{\text{NN}}} = 2.42$ GeV, and simulated with GiBUU for $\sqrt{s_{\text{NN}}} = 2.55$ GeV. Vertical bars represent statistical uncertainties.

4.5 Systematic Uncertainties of the DiElectron Spectra

To quantify the systematic uncertainties affecting the final dilepton spectra, the various stages of the analysis, such as background subtraction or efficiency and acceptance correction, discussed in the previous sections, have been evaluated individually. The following sources of systematic uncertainty are considered for dielectron spectra:

- **Normalisation to the number of neutral pions:** A conservative estimate of 10% is assigned to account for uncertainties in the π^0 normalisation. This value is motivated by general uncertainties in the production cross-section and scaling assumptions.
- **Combinatorial Background:** The uncertainty arising from the subtraction of combinatorial background is estimated using the empirical relation $\text{Signal/Background} \times 0.02$, as determined in previous analyses [66, 90]. It relies on full event simulations to estimate how much the true signal diverges from the calculated signal after subtraction the combinatorial background.
- **Efficiency Correction:** The correction for reconstruction efficiency is based on consistency checks using embedded mesons into experimental data, see section 4.3.4. Deviations from unity in these checks indicate small residual differences. Based on the maximal deviation observed, a conservatively estimated global uncertainty of 8% is assigned independently of invariant mass.

- **Acceptance Correction:** Acceptance corrections are derived from simulations as discussed in section 4.3.3. To estimate the corresponding systematic uncertainty, results obtained using HSD and Pluto cocktails with thermal ρ , as well as ρ from coarse-grained transport models, are compared. The observed differences between these three simulations are taken as a measure of the systematic uncertainty in the pair acceptance factor.
- **Reference Subtraction:** The contribution of the simulated reference spectrum for Ag+Ag collisions at $\sqrt{s_{NN}} = 2.55$ GeV introduces a systematic uncertainty, for which a generous estimate of 30% is assumed. Given the relatively small size of the reference contribution to the overall yield, its impact on the final spectrum remains small. The systematic uncertainties for 2.42 GeV come from the measured reference spectrum.
- **Eta Subtraction:** An uncertainty of 10% is assigned to the η yield, which is taken into account when this contribution is subtracted from the dielectron signal.

Notably, the systematic uncertainty coming from the particle identification is found to be minimal and therefore not taken into account for the dielectron spectra. The total systematic uncertainty is obtained by summing all listed individual contributions in quadrature, assuming statistical independence. The relative size of each source and their cumulative contribution are illustrated in figure 4.16. Notably, the systematic uncertainties are the highest in the π^0 mass region, dominated by the acceptance correction. The total relative uncertainties are in the order of 20%.

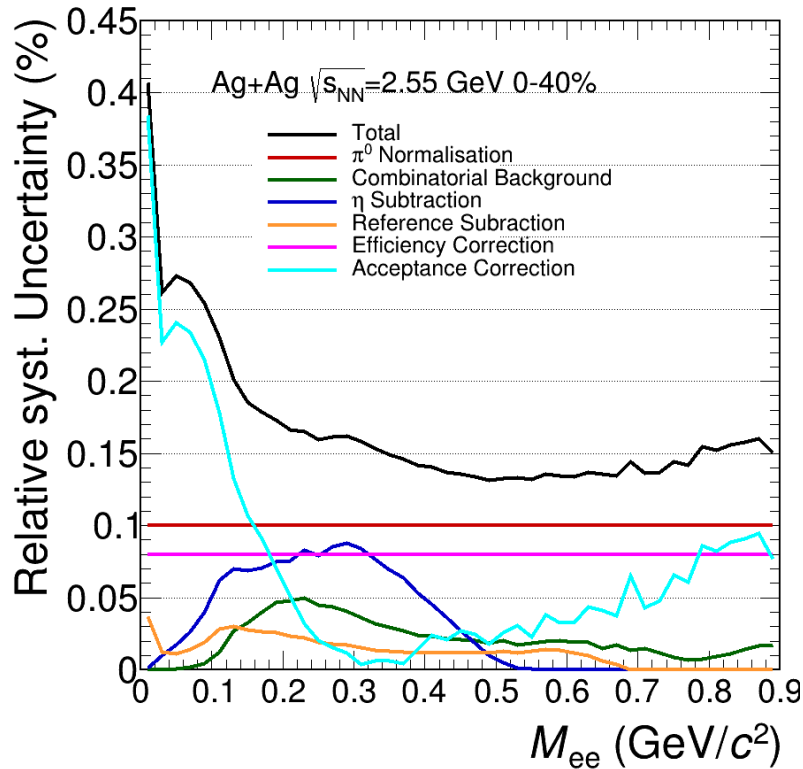


Figure 4.16: Relative systematic uncertainty of various sources, as well as their sum, as a function of the dilepton invariant mass.

5 Reconstruction Procedure of the Azimuthal Anisotropy

The reconstruction of the dielectron signal, as detailed in the preceding chapter, provides the foundation for probing the properties of the medium created in heavy-ion collisions with dielectrons. This work aims to further extend this analysis to investigate collective phenomena, focusing in particular on azimuthal anisotropy. As discussed in section 1.4, dileptons, with their sensitivity to the entire time evolution of the system, offer unique insights to the equation of state and the dynamical evolution of the collision. While the core criteria for particle identification and background subtraction remain largely unchanged, the analysis of azimuthal distributions requires the development of additional procedures and corrections. Specifically, the reconstruction framework is augmented with procedures to extract the flow coefficients and to correct for effects relevant in the studies of the azimuthal distribution. These refinements form the basis for the final, corrected anisotropy measurements presented in chapter 6.

5.1 Reconstruction of the Azimuthal Dielectron Distribution

The initial selection criteria of events and particle identification remain consistent with those presented in the previous chapter for the analysis of azimuthal anisotropy. Individual electron and positron candidates are selected based on the particle identification criteria outlined in section 4.1, which includes cuts on the velocity β , the RICH ring radius, and the RICH ring matching quality. Additionally, the conversion rejection criteria discussed in section 4.2.2 are applied. The central principle in the flow reconstruction in this work is then given by the reaction plane method. Specifically, the foundation for the anisotropy analysis is the dielectron signal as a function of the azimuthal angle relative to the event plane. Its estimation was discussed in section 3.4. As with any dielectron spectrum, the signal is calculated by combining all possible electron-positron pairs, followed by the subtraction of the combinatorial background. For this purpose, both same-event and mixed-event techniques are employed, analogously to what has been described in section 4.2.1. An important modification is introduced for the event-mixing procedure, where an additional event characteristic needs to be included, namely a condition on the **same event plane angle**: Only events with similar event plane angles Ψ_{EP} within 10° are mixed.

With these settings, the azimuthal dielectron distribution relative to the event plane is reconstructed, as shown in figure 5.1. In contrast to the reconstruction of the invariant mass spectrum, the event-mixing procedure is normalised not only in the region of $M_{ee} = 0.2 - 0.3 \text{ GeV}/c^2$, but across the entire mass range. While the event-mixing method is known not to describe correlated background, the resulting distributions show agreement within 1% between the same-event and mixed-event distributions in the azimuthal angle. For one, this could suggest that the correlations may be integrated out when looking at the $\Delta\Phi$ distribution. For another, it shows how the analysis benefits significantly from the improved conversion rejection criteria, which remove a substantial fraction of the correlated background. This leads to both

an enhanced signal-to-background ratio and better agreement between the same-event and mixed-event descriptions of the combinatorial background.

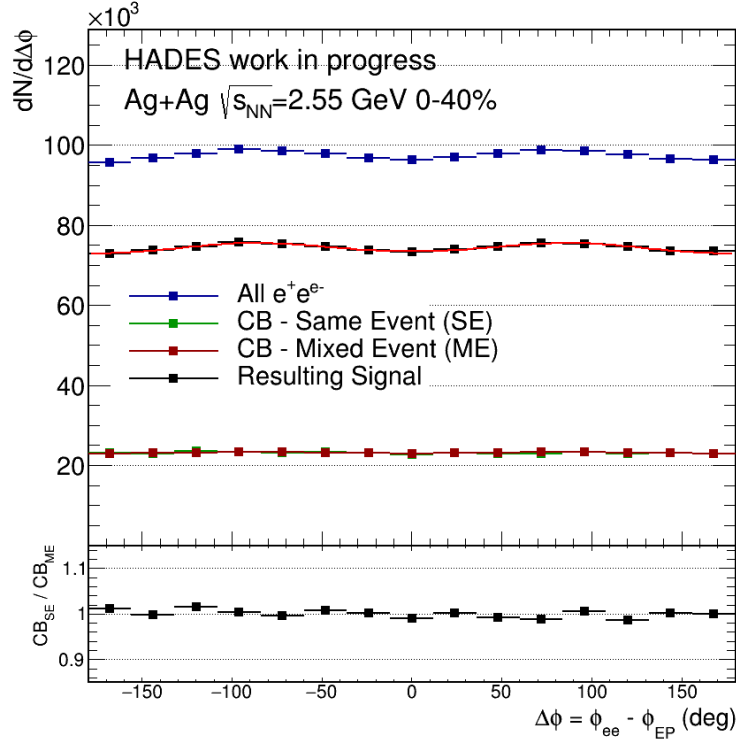


Figure 5.1: Top panel: Azimuthal distribution of the dielectron spectrum with background in relation to the event plane. Bottom panel: Ratio of the same-event (SE) and mixed-event (ME) backgrounds. Vertical lines represent statistical uncertainties.

5.2 Flow Coefficient Reconstruction Procedures

The dielectron signal shown in Figure 5.1 exhibits visible azimuthal anisotropy. In the next step, this is quantified through the calculation of the flow coefficients v_n . Two distinct approaches are utilised in this work.

Fitting Method: In the first approach, the azimuthal distribution of the reconstructed dielectron signal is fitted using the Fourier expansion described by equation 1.5. It is illustrated in figure 5.2. While this gives a straightforward estimate of the flow coefficients, it is important to note that this approach requires a sufficient number of histogram bins to adequately represent the shape of the azimuthal distribution. Previous studies [67] have shown that an insufficient binning can lead to a systematic underestimation of the flow coefficients. Furthermore, the fitting procedure cannot include an infinite number of Fourier coefficients, which necessitates the introduction of a truncation at some order. In this analysis, the procedure was tested up to the fourth order, although no significant contributions from v_3 or v_4 have been found due to the limited statistics. Hence, on the assumption that the first two contributions are overwhelmingly dominant, the fit for this analysis is restricted to include only the directed flow v_1 and elliptic flow v_2 .

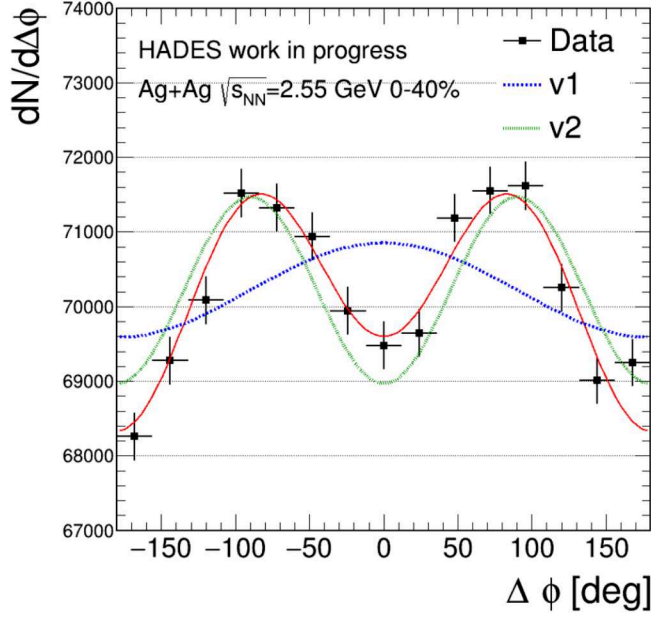


Figure 5.2: Fourier fit (red) on the azimuthal distribution of the dielectron signal in respect to the event plane. The blue line shows the magnitude of the resulting directed flow v_1 component. The green line marks the magnitude of the elliptic flow v_2 . Vertical lines represent statistical uncertainties.

Direct Calculation: In an alternative approach, the flow coefficients are computed directly from the average cosine[5]:

$$v_n^{\text{obs}} = \langle \cos n(\phi - \Psi_{\text{EP}}) \rangle \quad (5.1)$$

Here, it is assumed that the sine terms vanish due to the symmetry of the distribution. The direct calculation offers several advantages over the fitting method, as it is free from potential binning effects and is exact for all orders of n . In the practical code, it can be easily implemented with TProfile objects in the ROOT framework. However, as is the case for all dielectron observables, it is necessary to first estimate a total flow coefficients v_n^{tot} , based on all possible e^+e^- combinations. To isolate the signal contribution, the combinatorial background is then subtracted with the signal-to-background ratio r following [67]:

$$v_n^{\text{sig}} = \frac{1}{r} [(r + 1)v_n^{\text{tot}} - v_n^{\text{bg}}] \quad (5.2)$$

In the case of same-event combinatorial background, $v_{\text{SE},n}^{\text{bg}}$ needs to be estimated from the like-sign contributions $v_{\text{SE},n}^{++}$ and $v_{\text{SE},n}^{--}$. However, equation 4.4, has been derived for counts and cannot be directly applied for the flow coefficients in the same way. In order to estimate v_n^{bg} in such a case, equation 4.4 is rewritten in its product form:

$$N_{\text{SE}}^{\text{bg}} = (N_{\text{mix}}^{+-})^1 (N_{\text{SE}}^{++})^{1/2} (N_{\text{SE}}^{--})^{1/2} (N_{\text{mix}}^{++})^{-1/2} (N_{\text{mix}}^{--})^{-1/2} \quad (5.3)$$

Taking the derivative with respect to $\Delta\phi$ gives:

$$\begin{aligned} \frac{1}{N_{SE}^{bg}} \frac{dN_{SE}^{bg}}{d\Delta\phi} &= \frac{1}{N_{mix}^{+-}} \frac{dN_{mix}^{+-}}{d\Delta\phi} + \frac{1}{2} \frac{1}{N_{SE}^{++}} \frac{dN_{SE}^{++}}{d\Delta\phi} + \frac{1}{2} \frac{1}{N_{SE}^{--}} \frac{dN_{SE}^{--}}{d\Delta\phi} \\ &\quad - \frac{1}{2} \frac{1}{N_{mix}^{++}} \frac{dN_{mix}^{++}}{d\Delta\phi} - \frac{1}{2} \frac{1}{N_{mix}^{--}} \frac{dN_{mix}^{--}}{d\Delta\phi} \end{aligned}$$

Using the Fourier expansion from equation 1.5 and comparing the coefficients of each harmonic n yields:

$$v_{SE,n}^{bg} = v_{mix,n}^{+-} + \frac{1}{2}v_{SE,n}^{++} + \frac{1}{2}v_{SE,n}^{--} - \frac{1}{2}v_{mix,n}^{++} - \frac{1}{2}v_{mix,n}^{--} \quad (5.4)$$

The resulting equation 5.4 describes correlated and uncorrelated background and serves as the equivalent of equation 4.4 in terms of flow coefficients. One can also note how the introduction of the charge asymmetry factor k directly impacts the dependence of $v_{SE,n}^{bg}$ to the mixed-event combinatorial background. In this case, k could be identified as:

$$k_n = v_{mix,n}^{+-} - \frac{1}{2}v_{mix,n}^{++} - \frac{1}{2}v_{mix,n}^{--} \quad (5.5)$$

Motivated by small correlated background contributions seen in figure 5.1, one may alternatively assume a satisfactory description of v_n^{bg} purely based on the mixed-event description. Specifically, one may then assume that $v_n^{bg} = v_{mix,n}^{bg} = v_{mix,n}^{+-}$. Because the mixed-event method can only describe the relative shape of the background and not absolute yields, the signal-to-background ratio r is always determined via the same-event background.

In all methods, the resulting flow coefficients v_n are corrected for event plane resolution based on equation 3.12. They all give consistent values of v_n and are utilised for the evaluation of the systematic uncertainties as described in section 5.6.

5.3 Efficiency and Acceptance Corrections in the Flow Reconstruction

The measurement of azimuthal anisotropy is inherently a relative one, focused on evaluating variations in the signal as a function of the azimuthal angle with respect to the event plane. Within a given region of phase space defined by transverse momentum p_T , rapidity y , and invariant mass M_{ee} , such measurements are independent of detector inefficiencies and acceptance effects, provided they are stable over time. Due to the uniform distribution of the event plane angle, any such inefficiencies contribute equally to all azimuthal angles, thereby cancelling out in the final distribution. That being said, one central challenge in this analysis arises from the rarity of the dielectron probe. Even in the largest dataset analysed, the number of reconstructed signal pairs is in the order of $\sim 10^6$. This statistical limitation makes a fully multi-differential extraction of flow coefficients in (y, p_T, M_{ee}) space infeasible. Instead, certain regions of the phase space must be integrated to achieve sufficient statistical significance. In such integrated analyses, efficiency and acceptance corrections become essential. As the flow coefficients are expected to vary across phase space, each bin must be weighted according to its corrected yield to avoid introducing biases due to non-uniform acceptance or detector inefficiencies. Accordingly, the efficiency and acceptance correction

procedures described in section 4.3 are also applied here. In this case, the analysis is restricted to the single-lepton acceptance region defined in section 4.3.1. Within this region, a combined efficiency and acceptance correction factor is calculated. These correction factors are derived using the simulations introduced in section 4.3.3, employing the full Pluto freeze-out cocktail in conjunction with a coarse-grained ρ as the default. Additional model variations, based on a thermal ρ simulation and HSD, are used to estimate systematic uncertainties, see section 5.6. These corrections account for both the finite detector efficiency and geometric acceptance in terms of small gaps in detector coverage within the selected phase space region. Technically, the pair-level correction factor is stored in a three-dimensional matrix as a function of (y, p_T, M_{ee}) , using the same binning as the final spectra. During the analysis, these factors are applied as weights when populating histograms and TProfiles. Importantly, the measurement is not extrapolated into unmeasured regions of phase space, as doing so would increase the model dependence of the results. Instead, only interpolation across small acceptance gaps within the defined single-lepton acceptance region is performed. This approach not only minimizes model bias but also facilitates direct comparison with theoretical predictions, which can be easily constrained to the same single-lepton acceptance region.

5.4 Event-By-Event Efficiency Correction as a Function of the Event Plane

In addition to the global efficiency and acceptance corrections discussed in the previous section, the reconstruction of azimuthal distributions requires an additional event-by-event correction to account for variations in detector response as a function of the event plane angle Ψ_{EP} . This correction becomes necessary due to anisotropies in the distribution of reconstructed tracks, which lead to local variations in detector activity and thus affect reconstruction efficiency in an azimuthally dependent manner. This effect is illustrated in the left panel of figure 5.3, which shows the local track density D_{track} as a function of the polar angle θ and the relative azimuthal angle $\Delta\phi = \phi_{\text{track}} - \Psi_{EP}$. The majority of tracks originate from protons and pions, which are known to exhibit anisotropic out-of-plane emission [46]. This anisotropy is reflected in the track density distribution, which exhibits a clear modulation with respect to $\Delta\phi$. Higher

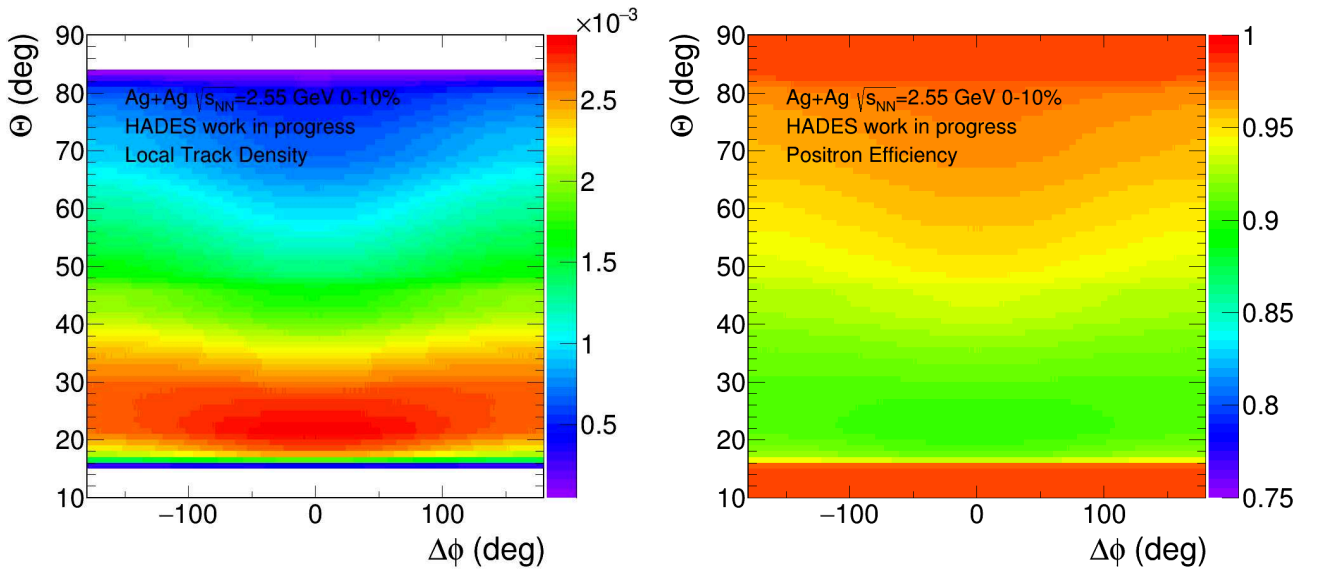


Figure 5.3: Left panel: Local track density as a function of θ and $\Delta\phi$. Right panel: Corresponding efficiency due to occupancy effects.

local track densities correspond to increased detector activity in a given region. The number of hits recorded within an active detector volume is referred to as occupancy, and it plays a key role in determining the reconstruction efficiency. At high occupancy, individual tracks are more difficult to resolve, leading to a degradation in tracking performance. While the global corrections discussed previously account for this effect on average, flow measurements, by their nature, require sensitivity to azimuthal variations tied to the event plane, and thus demand a more differential correction applied on an event-by-event basis. Based on previous studies [5, 145], the dependence of the tracking efficiency ϵ_D on the local track density $D_{\text{track}}(\theta, \Delta\phi, \text{cent})$ can be parametrised as:

$$\epsilon_D = \epsilon^{\text{max}} - c \cdot D_{\text{track}}(\theta, \Delta\phi, \text{cent})^n \quad (5.6)$$

where ϵ^{max} denotes the maximum achievable efficiency in the limit of minimal occupancy, c is an adjustable parameter controlling the strength of the correction, and n defines the functional form of the dependence of D_{track} . It is usually taken to be linear or quadratic with $n = 1$ or $n = 2$. All parameters are specific to the particle species under consideration. For practical purposes, it is convenient to express the parameter c explicitly in terms of efficiencies at the maximum and minimum track density $D_{\text{track}}^{\text{max}}$ and $D_{\text{track}}^{\text{min}}$. Denoting ϵ^{min} as the minimum efficiency, the parameter c can be written as [5]:

$$c = \frac{\epsilon^{\text{max}} - \epsilon^{\text{min}}}{(D_{\text{track}}^{\text{max}} - D_{\text{track}}^{\text{min}})^2} \quad (5.7)$$

For this analysis of electrons and positrons, ϵ^{max} is fixed to 0.98, based on simulation studies [5, 145]. This value corresponds to the efficiency observed in the lowest-density regions within the most peripheral centrality class. Further, a linear dependence ($n = 1$) is assumed. Finally, the proportionality constant c is determined through a data-driven approach. Specifically, ϵ^{min} is adjusted such that the directed flow v_1 at mid-rapidity vanishes ($y - y_{\text{cm}} = 0$), as is required by the symmetry of the Ag+Ag collision system. This tuning is performed independently for electrons and positrons. The results are summarised in table 5.1. Generally, the correction is observed to be stronger for electrons, suggesting that their reconstruction is more significantly affected by occupancy-related effects.

Particle Type	Centrality Class	ϵ^{min}	
		$\sqrt{s_{\text{NN}}} = 2.55 \text{ GeV}$	$\sqrt{s_{\text{NN}}} = 2.42 \text{ GeV}$
Electrons	0–40%	0.84	0.90
	0–10%	0.84	0.80
	10–20%	0.84	0.90
	20–30%	0.86	0.90
	30–40%	0.96	–
Positrons	0–40%	0.96	–
	0–10%	0.94	0.98
	10–20%	0.94	0.98
	20–30%	–	–
	30–40%	–	–

Table 5.1: Final values of the occupancy correction parameter ϵ^{min} for electrons and positrons in each centrality class for Ag+Ag collisions at $\sqrt{s_{\text{NN}}} = 2.55 \text{ GeV}$ and 2.42 GeV . A dash indicates that no correction was applied as it did not improve the symmetry around mid-rapidity.

The effectiveness of the correction is demonstrated in figure 5.4, which shows the directed flow in the example of positrons before and after applying the occupancy correction. As expected, the correction primarily affects the most central collisions, where track densities, and hence occupancy, are highest. For more semi-central events in the centrality class above 20-30% , the effect is negligible. It should be noted that the event selection procedure to remove potential Ag+C collisions, described in section 3.5, is also applied because this contamination also strongly effects the rapidity symmetry of the distributions. Residual asymmetries are still observed and may arise from higher-order effects not yet taken into account in this correction. An example of the resulting efficiency map derived via equation 5.6 is shown in the right panel of figure 5.3.

In the last step, the occupancy correction is propagated to the dielectron level. As is standard, the pair-level correction factor is assumed to factorize into the product of the single-lepton corrections:

$$\epsilon_{D_{\text{track}}}^{\text{pair}} = \epsilon_{D_{\text{track}}}^{(1)} \cdot \epsilon_{D_{\text{track}}}^{(2)} \quad (5.8)$$

These pair efficiencies are applied on an event-by-event basis as weights when filling the relevant histograms and profile distributions for the flow analysis.

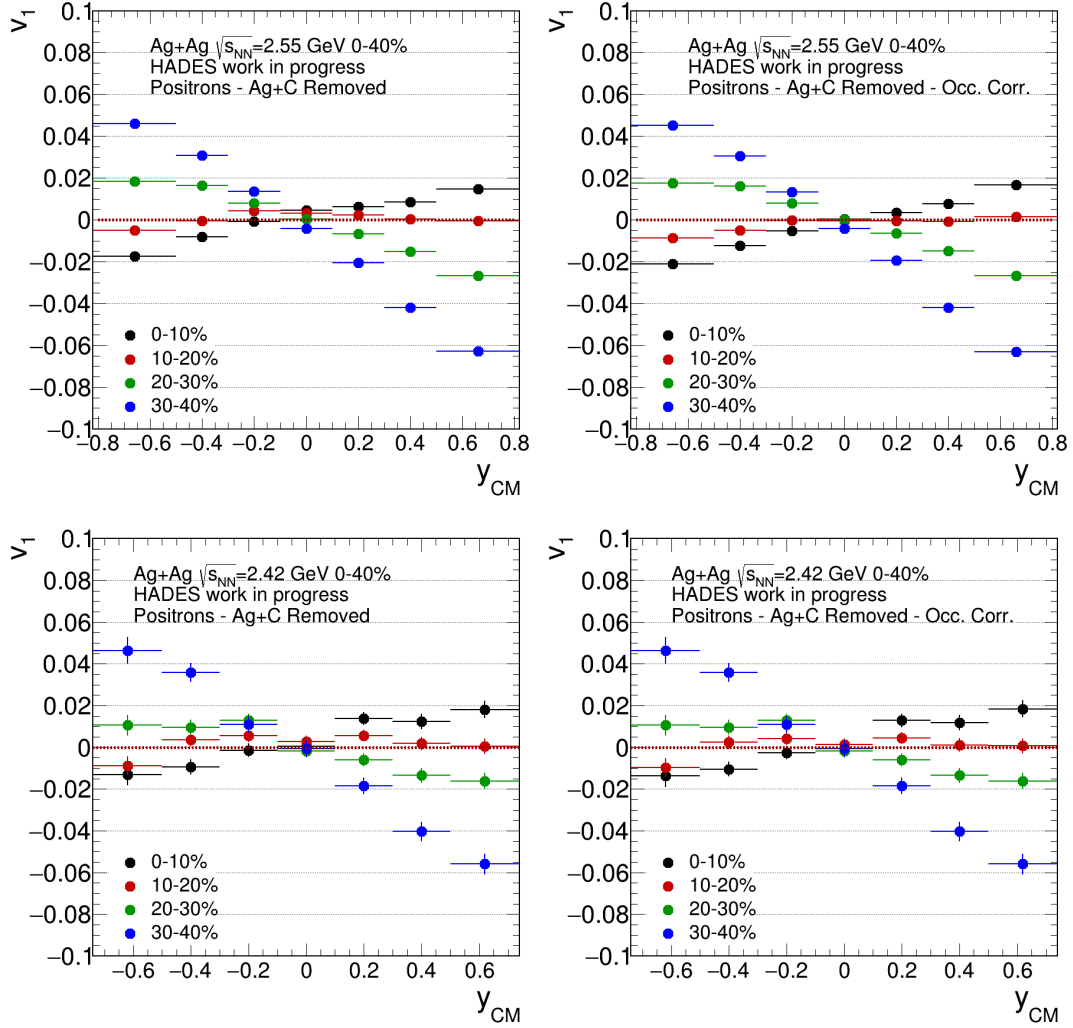


Figure 5.4: Directed flow v_1 of positrons before (left panels) and after (right panels) applying the occupancy correction for Ag+Ag collisions at 0–40% centrality. The top row shows results at $\sqrt{s_{NN}} = 2.55$ GeV, and the bottom row shows results at $\sqrt{s_{NN}} = 2.42$ GeV. Events likely originating from Ag+C collisions are removed using the procedure described in section 3.5.

5.5 Disentangling the Flow Coefficients in the DiElectron Cocktail

The particle yields for the various components of the dilepton cocktail have already been discussed in section 4.4. For the analysis of azimuthal anisotropies, however, knowledge of the anisotropic flow coefficients, in particular of the directed v_1 and elliptic flow v_2 , of the virtual photons associated with each decay channel is also needed.

The same individual hadronic sources described previously can be used to determine their respective flow contributions. However, experimental data on anisotropic flow for the most relevant cocktail sources, such as π^0 and η mesons, is limited. Some measurements are available from the TAPS collaboration [146, 147], which reports v_2 values for π^0 and η mesons at beam energies of 1–2A GeV. More recently, efforts have been made to reconstruct the π^0 flow using the HADES ECAL [138]. However, all of these results

suffer from significant uncertainties and are typically restricted to specific regions in phase space and centrality. An additional challenge arises from the nature of Dalitz decays. In decays such as $\pi^0 \rightarrow \gamma e^+ e^-$ and $\eta \rightarrow \gamma e^+ e^-$, only the virtual photon is reconstructed via the dielectron pair, while the accompanying real photon remains undetected. As a result, the anisotropy of the virtual photon is smeared relative to that of the parent meson. The magnitude of this smearing depends on several factors, including the momentum of the parent particle, the applied PID cuts, and the selected phase space. It has not been quantified experimentally.

Taken together, these limitations make a purely data-driven isolation of the thermal dielectron flow coefficients with existing measurements not yet possible. Instead, transport model simulations are employed to estimate the anisotropic flow of the relevant freeze-out sources. As a benchmark, their predictions are compared to measured charged pion flow, which is well established experimentally. It is likely that π^0 flow is of similar origin as the one of charged pions and therefore of a similar magnitude. Figure 5.5 shows the comparison between the measured elliptic flow of π^+ and various model predictions. While direct measurements of π^0 flow remains challenging in HADES, charged pions are abundant and serve as a suitable proxy for evaluating the model's ability to reproduce pion flow. Among the various models tested, UrQMD v3.4 [95, 96, 148], implemented with a hard equation of state [149], with $\alpha = -124$ MeV, $\beta = 71$ MeV and $\gamma = 2.00$ in a Skyrme-potential, was found to be the best in reproducing the experimental v_2 of charged pions at the energies studied by HADES.

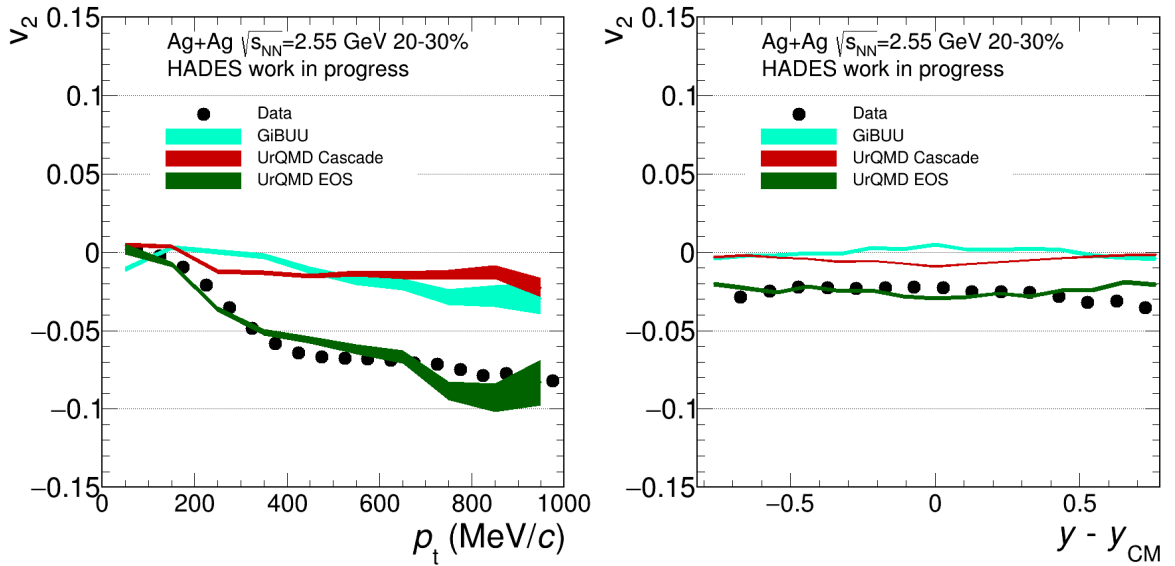


Figure 5.5: Measured elliptic flow of positively charged pions (π^+) compared to predictions from several transport models for Ag+Ag collisions at $\sqrt{s_{NN}} = 2.55$ GeV.

In contrast to the fine-binned mass spectra shown in figure 4.15, the final flow coefficients are calculated integrated over large mass regions. In this total signal, some contributions are minimal and can be ignored. Specifically, the treatment of the individual sources is outlined below:

- **π^0 Contribution:** The elliptic flow of virtual photons from π^0 Dalitz decays is taken from the UrQMD simulations with a hard equation of state shown in figure 5.5. Importantly, the simulated flow is extracted for the virtual photon (i.e. the e^+e^- pair), rather than the parent π^0 , to account for the smearing effect due to the unconsidered real photon. The same particle identification and acceptance

definitions as used in the experimental data are applied in the simulation. It is important to note that only the final flow coefficients are taken from the simulations. The yields remain based on experimental measurements as discussed in section 4.4.

- **η Contribution:** The flow contribution from η mesons is treated in a manner analogous to the π^0 . The virtual photon v_2 is extracted from UrQMD under the same conditions, including the application of particle identification and phase space cuts. The yields remain based on experimental data as discussed in section 4.4.
- **ω Contribution:** The ω meson can be handled in the same manner as the π^0 and η mesons, with its flow coefficients derived from UrQMD simulations. However, the contribution of the ω meson to the total dielectron yield in the integrated mass range is very small. The broad mass bins used in the anisotropy analysis result in an integrated contribution from ω decays that is estimated to be less than 1%. As such, it can be neglected in the isolation of the thermal flow coefficients as seen in section 6.3.
- **ϕ Contribution:** The treatment of the ϕ meson is analogous to that of the ω meson. In general, the contribution of the ϕ to the dielectron spectrum is even more suppressed, and it does not significantly influence the extracted flow coefficients. For this reason, the ϕ meson is excluded from further consideration in the flow analysis.
- **Initial Contributions:** Contributions from early-stage processes, such as Δ Dalitz decays and nucleon-nucleon Bremsstrahlung, are more difficult to quantify reliably in transport simulations. The precise definition of what constitutes as an "initial" source is essential and under investigation [150]. However, it is expected that minimal anisotropy is present at this early stage and no flow for the initial state sources is assumed. Furthermore, these sources contribute only a few percent to the total integrated dielectron yield and are not expected to significantly affect the observed anisotropies.

5.6 Systematic Uncertainties of the Flow Coefficients

In order to estimate systematic uncertainties for the flow coefficients, the analysis has been performed not only once, but each step in the analysis has been varied to study its effect on the final results.

- **Particle Identification:** The key observables for selecting electron and positron tracks are the RICH ring matching quality, RICH ring radius and velocity β . In the nominal run a selection window of 98% around each of these observables is applied for particle identification. A tighter cut of 95% is applied as a variation for systematics.
- **Flow Reconstruction Method:** Two methods, described in the previous sections, are used to calculate the flow coefficients v_n . Fitting the azimuthal distribution as in figure 5.2 is selected as the nominal run, the direct calculation via equation 5.1 as variation.
- **Combinatorial Background:** For both flow reconstructions methods, both the same-event like-sign as well as event-mixing method can be employed to estimate the combinatorial background. In order to take into account potential correlated background the same-event CB serves as the nominal run. The mixed-event CB serves as a variation when assuming a negligible contribution from correlated background.

- **Single lepton correction matrices:** For the nominal run, the single lepton matrices are estimated as a function of (p, θ, ϕ) . Matrices in dependence of (p_t, y) bring another variation.
- **Pair corrections:** In the nominal run, the Pluto cocktail in combination with the coarse-grained ρ serve as the simulated cocktail with which the pair correction factors are estimated. Pluto with a thermal ρ as well as an independent HSD simulation serve as variations.
- **Local-track density (occupancy) correction:** The occupancy correction, shortly described in the previous section, is employed in the nominal run. It is entirely left out in a variational run, serving as the maximum uncertainty to be expected from this effect.
- **Target material:** In the nominal run, the purifier model discussed in section 3.5 is employed to remove carbon contamination with a standard decision threshold of $p = 0.5$. To estimate its effect, the decision threshold of the model may be set to a looser setting in a variational run. For this thesis, the purifier model is left out in a variational run to ensure that no hidden biases within the model affect the final results.

This totals 192 variations, including the nominal one, which are being considered for the final results. The systematic uncertainty for each data point is finally calculated from the standard deviation around the nominal. As to not artificially shrink the estimated uncertainty, only variations with significant deviations are included. It can be noted that the treatment of the combinatorial background shows the largest influence on the final values. Therefore, regions with the highest signal-to-background ratio often demonstrate smaller systematic uncertainties. Finally, we assume an additional 5% global systematic uncertainty for the event plane resolution. It has been estimated using the three-subevent method [151].

5.7 Adaptations in Au+Au Data Reanalysis

Although not the primary focus of this work, some efforts have also been done to repeat and improve a previous analysis of the dielectron azimuthal distributions [63] in Au+Au collisions at $\sqrt{s_{NN}} = 2.42$ GeV, collected at HADES in 2012. The motivation for this reanalysis is twofold. First, several new and more refined procedures have been developed and implemented as part of this study. Notably, this includes the development of the Au+C removal model, described in section 3.5.1, as well as the global and event-by-event corrections, as outlined in sections 5.3 and 5.4. These improvements are crucial for a realistic measurement of the final azimuthal distributions. Second, a new set of DSTs corresponding to the 2012 beam time has been generated in early 2025 (generation 10), which motivates a rerun of all experimental analyses. To include the Au+Au azimuthal anisotropy analysis in the evaluation presented in chapter 6 and facilitate a fair comparison between all systems, the 2012 Au+Au dataset is reanalysed. While the majority of analysis steps are treated in the same manner as in Ag+Ag measurement, two important steps are adapted due to changes of the experimental setup and analysis over the years:

- **Particle Identification:** To enhance the statistical significance and maximize the efficiency of electron identification, a sophisticated machine learning model is employed to identify electrons and positrons in the Au+Au dataset from 2012 [90].
- **Global Efficiency Correction:** Instead of various models and coordinates for the single-lepton correction matrices, this correction is performed solely with the HSD model.

6 Evaluation and Interpretation of the Experimental Results

Building upon the reconstruction and analysis framework outlined in the previous chapters, the main experimental results obtained in this work are presented and discussed in the following.

The discussion can generally be divided into three main parts. The first focuses on the invariant-mass spectrum and the extraction of the thermal dielectron excess, which serves as a key observable for studying the properties of the hot and dense medium.

The second part is dedicated to the study of the azimuthal distributions of dielectrons, quantified through the measurement of the flow coefficients, both inclusively and with an attempt to isolate the thermal contribution.

The final section examines ongoing perspectives. In particular, this includes the study of the thermal excess in a more differential manner in terms of transverse momentum and rapidity.

Overall, these results aim to provide comprehensive insights into the dielectron radiation, emitted throughout the evolution of the system created in heavy-ion collisions, as motivated in section 1.5. As such, they will be part of several manuscripts currently planned for publication at HADES, one of which is drafted and focuses on the measurements of the dielectron azimuthal anisotropy.

6.1 Characterising the Hot and Dense Fireball via the Invariant Mass Spectrum

In order to isolate the thermal dielectron contribution, the analysis first focuses on the invariant mass spectrum. Figure 4.15 has shown the measured spectrum within the HADES acceptance, together with an estimate of all known non-thermal sources. The thermal component can then be extracted by subtracting contributions associated with freeze-out and initial-state processes. These include the nucleon–nucleon (NN) reference, consisting primarily of Bremsstrahlung and Δ -Dalitz decays, as well as the freeze-out decays of the π^0 , η , ω and ϕ mesons. After removal of these sources, the remaining signal is attributed to thermal radiation from the hot and dense medium, which is expected to be dominated by ρ -meson decays.

The resulting excess yield is subsequently extrapolated to the full 4π phase space using the pair-acceptance correction factors derived in section 4.3.3. The fully corrected invariant mass spectrum is displayed in figure 6.1. Because of the large acceptance factors at the lowest masses below $M_{ee} \lesssim 0.15 \text{ GeV}/c^2$, compare figure 4.13, the focus in figure 6.1 is set on the masses beyond $M_{ee} > 0.15 \text{ GeV}/c^2$. Additional studies, systematically studying this lowest mass range in order to extract information on the electrical conductivity, are ongoing with a dedicated run of low magnetic field that substantially increases the acceptance of low momentum tracks [152].

For the mass range investigated here, a pronounced broadening of the ρ spectral function is observed, which is consistent with the previous experimental observations discussed in section 1.4.1. This broadening leads to a largely smooth invariant mass distribution, which exhibits an approximately exponential decrease as a function of mass. Such a behaviour is characteristic of thermal radiation emitted from a (locally) thermalised medium, referred to as the fireball, at temperature T . This motivates a fit of the excess spectrum using a Boltzmann-like function of the form:

$$\frac{dN}{dM} \propto M^{\frac{3}{2}} \exp(-M/T) \quad (6.1)$$

The fit, presented by the red curve in figure 6.1, provides a good description of the data within the investigated mass range. It is performed in the interval $M_{ee} = 0.2\text{--}0.7 \text{ GeV}/c^2$, where the thermal ρ contribution is expected to dominate and where the spectrum is more sensitive to the temperature rather than details of the spectral function. For Ag+Ag collisions at $\sqrt{s_{NN}} = 2.55 \text{ GeV}$ and 0-40% centrality, an average fireball temperature of $T_{\text{Ag}2.55\text{Ag}} = 82.2 \pm 0.8_{\text{stat}} \pm 2.9_{\text{sys}} \text{ MeV}$ is extracted. The slightly lower energy of $\sqrt{s_{NN}} = 2.42 \text{ GeV}$ shows a somewhat smaller temperature of $T_{\text{Ag}2.42\text{Ag}} = 73.5 \pm 1.8_{\text{stat}} \pm 3.0_{\text{sys}} \text{ MeV}$. The latter is consistent with the previous measurement from Au+Au collisions at the same energy [18]. As mentioned in section 1.4.1, this temperature reflects the average fireball temperature throughout the evolution of the system and found to be substantially higher in comparison to the temperature extracted from hadron yield at freeze-out. This demonstrates the penetrating nature of the electromagnetic probes.

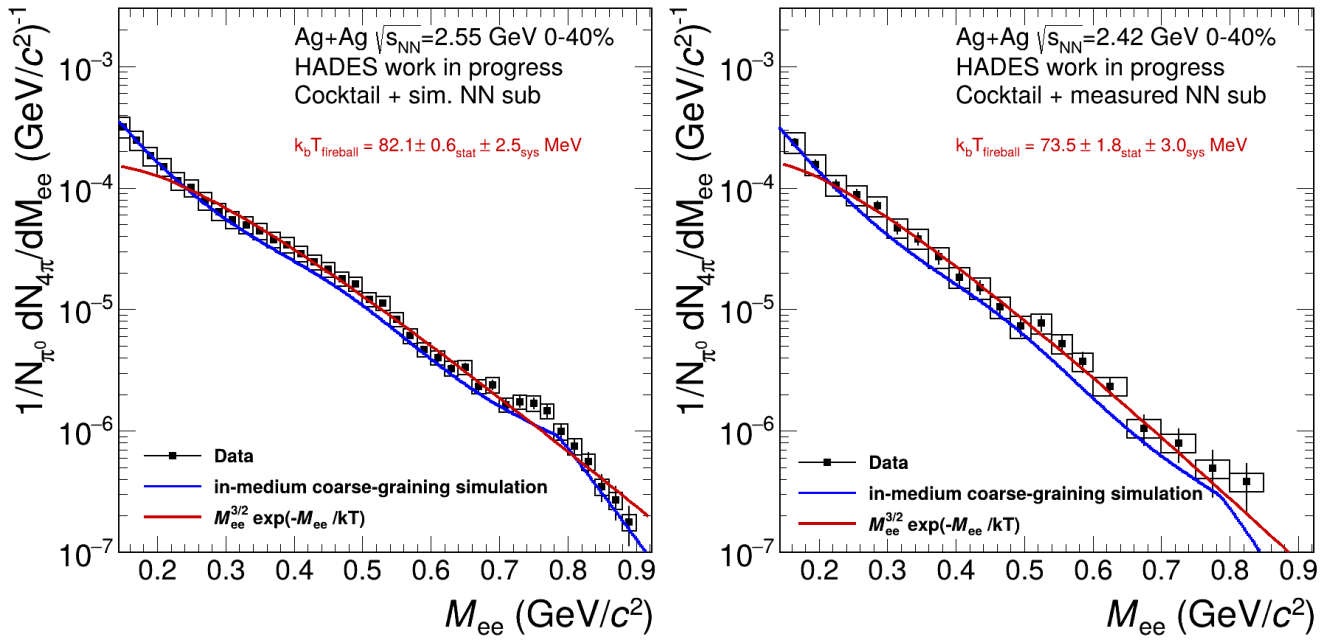


Figure 6.1: Thermal dielectron excess as a function of invariant mass for Ag+Ag collisions at $\sqrt{s_{NN}} = 2.55 \text{ GeV}$ (left) and 2.42 GeV (right) at 0–40% centrality. Vertical bars indicate statistical uncertainties, while boxes represent systematic uncertainties. The red curve shows the Boltzmann fit used to extract the average fireball temperature. The blue curve corresponds to the predicted thermal dielectron excess from coarse-grained UrQMD simulations employing in-medium spectral functions.

Beyond the spectral shape, additional information on the properties of the hot and dense medium can be obtained from the integrated excess yield N_{excess} . While the shape of the invariant mass distribution is primarily sensitive to the temperature, the absolute yield reflects the total amount of thermal radiation emitted over the systems evolution. For quantitative comparisons, the excess yield is defined as the number of excess dielectron pairs in the invariant mass interval from $0.3 \text{ GeV}/c^2$ to $0.7 \text{ GeV}/c^2$:

$$N^{\text{excess}} = \int_{0.3 \text{ GeV}/c^2}^{0.7 \text{ GeV}/c^2} \frac{dN^{\text{excess}}}{dM} dM \quad (6.2)$$

Similarly to the temperature fit, this mass range is chosen to maximise sensitivity to the ρ -meson contribution. From the spectra shown in figure 6.1 for the 0-40% centrality class, the excess yield is determined to be $N_{\text{Ag}2.42\text{Ag}}^{\text{excess}} = (3.16 \pm 0.17_{\text{stat}} \pm 0.24_{\text{syst}}) \times 10^{-5}$ for Ag+Ag collisions at $\sqrt{s_{NN}} = 2.42 \text{ GeV}$, and $N_{\text{Ag}2.55\text{Ag}}^{\text{excess}} = (6.22 \pm 0.10_{\text{stat}} \pm 0.28_{\text{syst}}) \times 10^{-5}$ at $\sqrt{s_{NN}} = 2.55 \text{ GeV}$.

Assuming that the observed dielectron excess indeed originates from thermal radiation, the integrated yield is expected to correlate with the temperature of the emitting medium. One might naively anticipate a power-law dependence, analogous to the Stefan–Boltzmann law where the radiated energy P scales as $P \propto T^4$. However, the hot and dense medium created in heavy-ion collisions does not correspond to a static, globally thermalised black body. Instead, the extracted temperature represents an average over a dynamically evolving system. After reaching a maximum temperature, the fireball undergoes continuous cooling and this time dependence plays a crucial role in determining the emitted radiation. Consequently, a simple T^4 scaling should be regarded only as an initial approximation. In the same vein, the excess yield is expected to depend on the volume V and lifetime τ of the radiating medium. A larger fireball emits more thermal radiation, and a longer-lived system accumulates a greater number of emitted dielectron pairs. All in all, these considerations can be summarised schematically as:

$$N^{\text{excess}} \sim T^4 \times V \times \tau \quad (6.3)$$

While this estimation neglects the complex space-time evolution of the system and oversimplifies the temperature dependence, it nevertheless captures the essential principles underlying the characterisation of the hot and dense fireball through thermal dielectrons. It illustrates the wealth of information encoded in the excess spectra. At the same time, it also indicates that a precise interpretation of any excess measurement requires disentangling the combined effects of the fireball's temperature, volume, and lifetime, which all influence the observed yield. One way to achieve this is by comparison with model predictions. Figure 6.1 shows such a comparison with coarse-grained UrQMD simulations utilising in-medium spectral functions, see section 1.4.2. The simulations exhibit reasonable agreement with the data and may thus be utilised to guide more detailed investigations about the origin of the thermal dielectron radiation. Further refinements of these models may even improve the distinction between thermal and non-thermal contributions [150].

6.1.1 System Size and Centrality Dependence of the Thermal Radiation

The considerations in equation 6.3 also highlight the importance of extending the analysis beyond the integrated 0–40% centrality range. By examining the excess spectra differentially in centrality, one can systematically explore how thermal radiation varies with the system size. In this way, it serves as a handle to experimentally disentangle the effects of volume V , lifetime τ and temperature T on the measured excess spectra.

Figure 6.2 and 6.3 show the thermal dielectron excess in 10% centrality bins for the Ag+Ag collisions at $\sqrt{s_{NN}} = 2.55$ GeV and $\sqrt{s_{NN}} = 2.42$ GeV, respectively. In every case, the excess spectra exhibit an approximately exponential shape. Accordingly, they can be described by the Boltzman fit as in equation 6.1, which enables the extraction of the fireball temperature. As in the combined measurement of 0-40% centrality of figure 6.1, the same coarse-grained UrQMD simulation is used to predict the thermal dielectron yield for each centrality and both collision energies. In general, the description of the model aligns well for the most central collisions, i.e. 0-10% and to a certain extent, 10-20% centrality. However, with decreasing centrality, the model predictions appear to underpredict the actually measured yields. This systematic deviation indicates potential limitations of the current implementation of the model and motivates further differential investigations. In this case, the centrality selection inside the simulation is based on fixed values of the impact parameter b . In contrast, as discussed in section 3.3.2, the centrality selection in the experiment is based on the multiplicity of the overall event. This, in turn, leads to an overlap of the impact parameter distributions between the various centrality classes, as visible in figure 3.3. Because the yield depends non-linearly on the centrality, it serves as one possible explanation for at least part of the discrepancy between model predictions and data in the more peripheral centralities.

Beyond the comparison with the model calculation, the behaviour of the purely experimental measurements in dependence of the centrality can be studied directly. As summarised in the left panel of figure 6.4, the extracted temperatures show no significant dependence on centrality and, consequently, on the number of participating nucleons $\langle N_{\text{part}} \rangle$. Slightly higher temperatures are found for the energy of $\sqrt{s_{NN}} = 2.55$ GeV. In addition, the values for all centrality classes remain consistent with those extracted from the inclusive 0–40% selection. This apparent centrality independence is noteworthy, particularly when placed into context with the integrated excess yield N^{excess} as defined in equation 6.2. The right panel of figure 6.4 shows N^{excess} as a function of the mean number of participating nucleons for each centrality class. In contrast to the temperature, a clear increase of the excess yield with centrality is observed for both collision energies. To quantify this dependence, the distribution is fitted with a power law characterised by a scaling parameter α :

$$N^{\text{excess}} \propto \langle N_{\text{part}} \rangle^\alpha \quad (6.4)$$

This fit reveals a nonlinear increase of the thermal excess yield with the number of participating nucleons. The extracted scaling parameters are:

$$\begin{aligned} \alpha_{\text{Ag}2.55\text{Ag}} &= 1.39 \pm 0.04_{\text{stat}} \pm 0.13_{\text{sys}} \\ \alpha_{\text{Ag}2.42\text{Ag}} &= 1.33 \pm 0.14_{\text{stat}} \pm 0.15_{\text{sys}} \end{aligned}$$

Based on the estimation given in equation 6.3, this trend may be attributed to variations in the temperature T , system volume V , or lifetime τ of the hot and dense fireball. By construction of the centrality classes, the system volume is expected to scale approximately linearly with the number of participating nucleons. Since the temperature shows no significant dependence on centrality, the observed nonlinear scaling of N^{excess} suggests that the effective lifetime of the system increases with the number of participants.

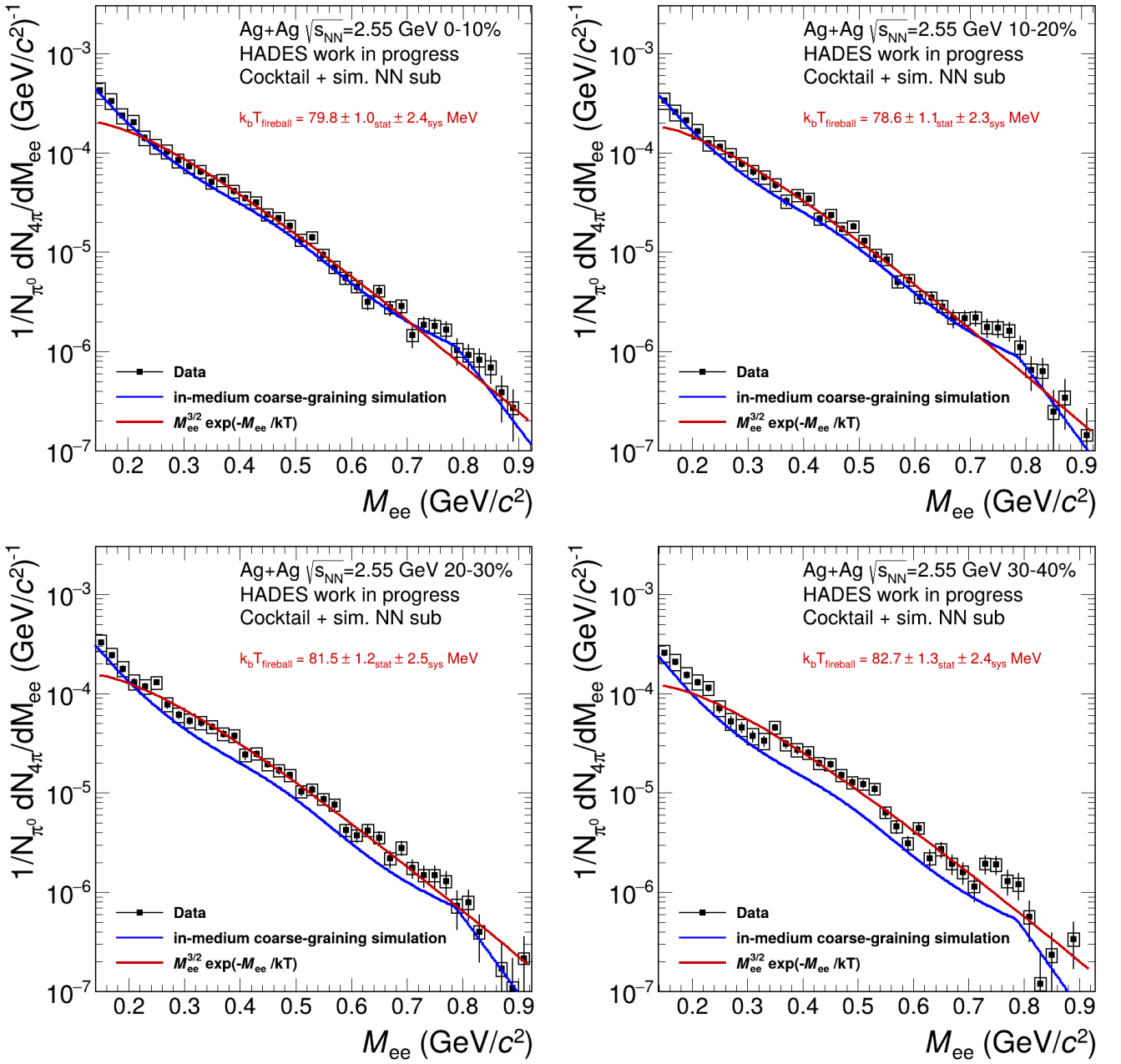


Figure 6.2: Thermal dielectron excess in dependence of the invariant mass for Ag+Ag collisions at $\sqrt{s_{NN}} = 2.55$ GeV in 10% centrality bins. Vertical lines represent statistical uncertainties. Boxes represent systematic uncertainties. The red line shows the Boltzmann fit and resulting estimated fireball temperature. The blue line shows the predicted thermal dielectron excess from coarse-grained UrQMD.

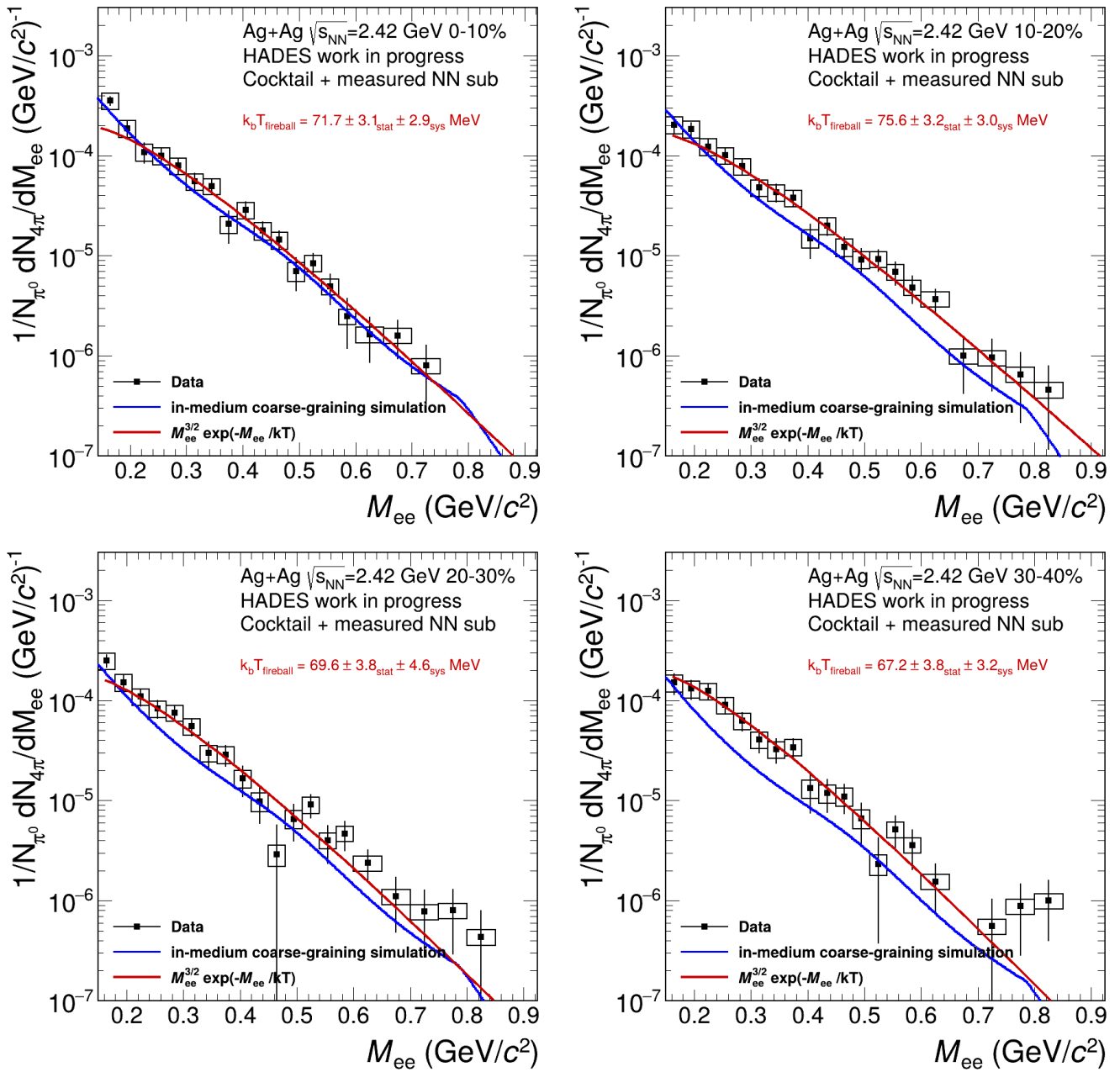


Figure 6.3: Thermal dielectron excess in dependence of the invariant mass for Ag+Ag collisions at $\sqrt{s_{\text{NN}}} = 2.42$ GeV in 10% centrality bins. Vertical lines represent statistical uncertainties. Boxes represent systematic uncertainties. The red line shows the Boltzmann fit and resulting estimated fireball temperature. The blue line shows the predicted thermal dielectron excess from coarse-grained UrQMD.

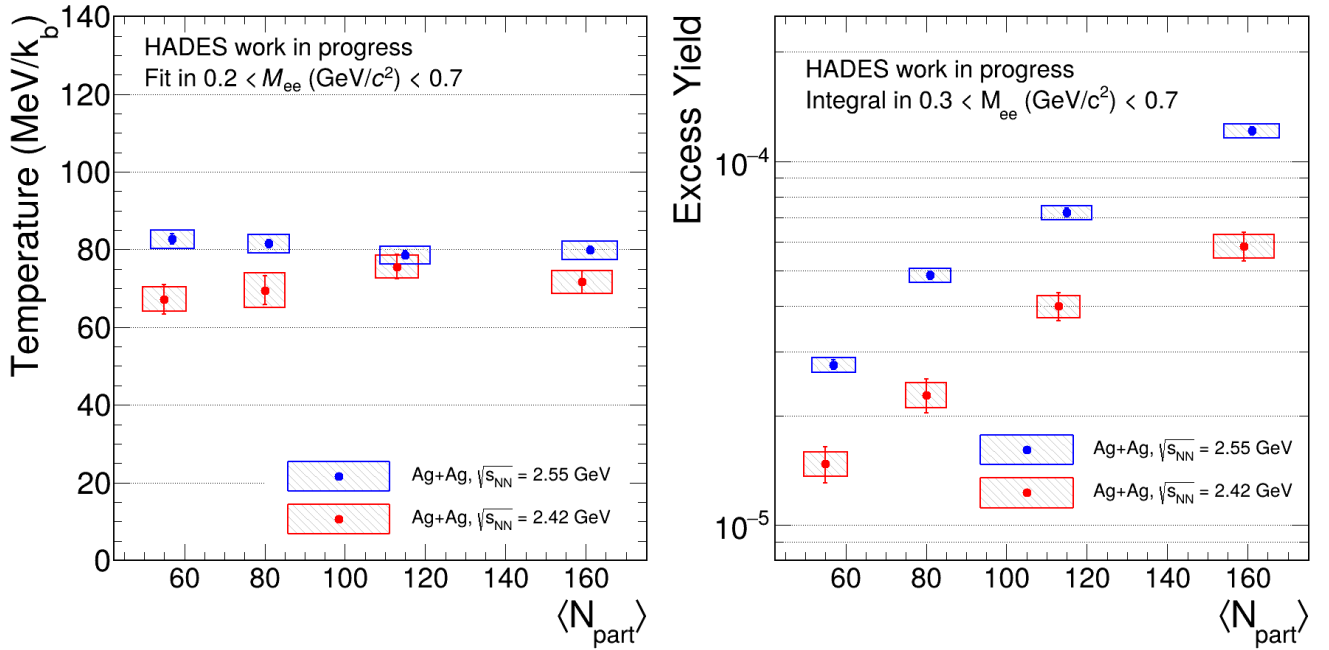


Figure 6.4: Thermal integrated excess yield (right panel) and fireball temperature (left panel) in dependence of the number of participants $\langle N_{\text{part}} \rangle$ for Ag+Ag collisions at $\sqrt{s_{NN}} = 2.55\text{ GeV}$ and 2.42 GeV . Vertical lines represent statistical uncertainties. Boxes represent systematic uncertainties.

The comparison of the excess spectrum between the two energies allows for additional insights into the properties of the hot and dense medium. Generally, a marked increase in the excess yield, approximately a factor of two, is observed for collisions at $\sqrt{s_{NN}} = 2.55\text{ GeV}$, compared to the lower energy collisions at $\sqrt{s_{NN}} = 2.42\text{ GeV}$. For one, this is related to the higher temperatures reached in the higher energy collisions. For another, it could indicate changes in the time evolution of the system, including its expansion dynamics and possibly its lifetime.

To further elucidate these effects, additional measurements across a broader range of collision energies and systems will be essential. Such data will aid in disentangling the various contributing factors and provide a more comprehensive understanding of the underlying dynamics of the system. For this purpose, normalising the excess yield by the number of produced pions may allow for easier comparisons across different collision systems and centralities. This is shown in figure 6.5. Because the number of pions is somewhat sensitive to the system's temperature and scales linearly with $\langle N_{\text{part}} \rangle$, see section 4.4, this representation helps to identify differences due to changes in the time evolution and lifetime of the hot and dense system.

These findings underscore the need for further studies that incorporate a wider range of collision systems as well as energies. Section 6.4 and chapter 7 discusses potential avenues for future measurements, as well as the importance of more detailed comparisons with theoretical models to fully characterise the dynamic evolution of the hot and dense medium.

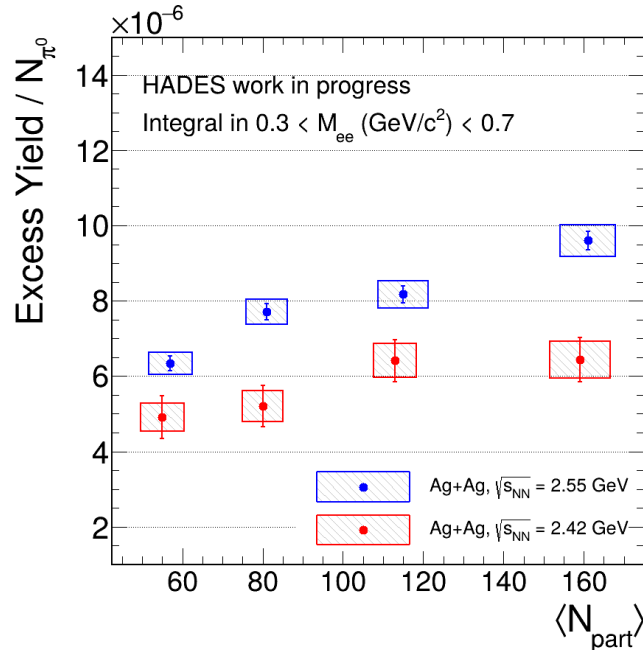


Figure 6.5: Thermal integrated excess yield, normalised by the number of pions, in dependence of the number of participants $\langle N_{\text{part}} \rangle$ for Ag+Ag collisions at $\sqrt{s_{\text{NN}}} = 2.55$ GeV and 2.42 GeV. Vertical lines represent statistical uncertainties. Boxes represent systematic uncertainties.

6.2 Integrated DiElectron Flow Coefficients

The next focus of this work is the measurement of the azimuthal anisotropy as experienced by dielectrons. Based on the procedures described in chapter 5, the resulting flow coefficients are presented. At this stage, they represent the integrated signal from all dielectron sources. All previously described corrections have been applied, including the Ag+C removal discussed in section 3.5.2, the global and event-by-event efficiency corrections from section 5.3 and 5.4, as well as the correction for the event plane resolution presented in section 3.4.1.

Directed Flow: Figure 6.6 shows the integrated directed flow v_1 as a function of the center-of-mass rapidity $y - y_{\text{cm}}$ for the two energies of $\sqrt{s_{\text{NN}}} = 2.55$ GeV and $\sqrt{s_{\text{NN}}} = 2.42$ GeV, as well as for the two collision systems of Ag+Ag and Au+Au. The Au+Au data is taken from the reanalysis described in section 5.7. It can be noted how they are subject to significant statistical and systematic uncertainties which complicates the interpretation and further evaluation of these results. In contrast, the Ag+Ag data shows a more coherent trend.

In every case, the directed flow is consistent with zero at midrapidity $y - y_{\text{cm}} = 0$, as expected for a symmetric collision system. One can also observe a positive slope, transitioning from negative values at backward rapidities to positive values at forward rapidities. For the Ag+Ag measurement of $\sqrt{s_{\text{NN}}} = 2.42$ GeV, the data point at around $y - y_{\text{cm}} = 0.5$ appears to deviate from this behaviour. However, given the uncertainties, this deviation is likely due to statistical fluctuations rather than a genuine physical effect. The smallest uncertainties are seen for the high-statistics Ag+Ag measurement at $\sqrt{s_{\text{NN}}} = 2.55$ GeV, where the directed flow measurement is dominated by systematic uncertainties. In this case, the slope of the

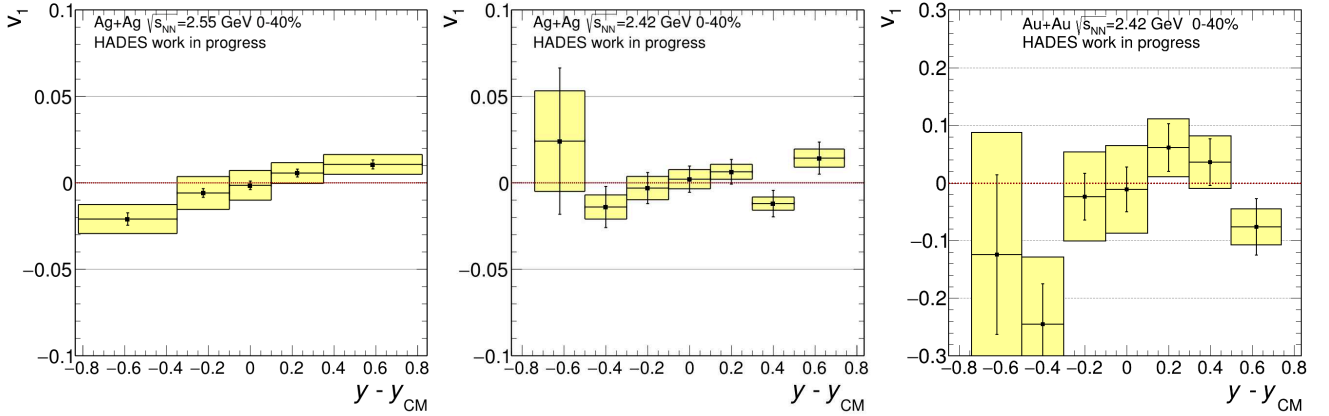


Figure 6.6: Integrated dielectron v_1 for two collision systems and two energies. Vertical lines represent statistical uncertainties. Boxes represent systematic uncertainties.

data can be quantified more precisely by applying a linear fit to the data. It yields a measurement of $(dv_1/dy|_{y=y_{cm}})_{\text{Ag}2.55\text{Ag}} = 0.027 \pm 0.0036_{\text{stat}} \pm 0.0058_{\text{sys}}$ for all dielectrons measured at 0-40% centrality.

This positive slope is qualitatively in agreement with available measurements of protons and light nuclei at these collision energies [46]. Quantitatively, however, the extracted $dv_1/dy|_{y=y_{cm}}$ from dielectrons is significantly smaller, by at least one order of magnitude, when compared to the values reported for protons in figure 1.9. A more appropriate quantitative comparison may be made with pions, as the dominant contribution to the dielectron signal in figure 6.6 arises from the π^0 Dalitz decay. When comparing the extracted slope with FOPI measurements of pion directed flow at similar energies [153], a much closer quantitative agreement is observed.

A more detailed understanding emerges when considering the centrality dependence. Figure 6.7 shows the integrated v_1 as a function of $y - y_{cm}$ for the high-statistics Ag+Ag measurement at $\sqrt{s_{NN}} = 2.55$ GeV, subdivided into 10% centrality classes. The slope of v_1 at midrapidity exhibits a clear centrality dependence. Namely, it is positive for the most central collisions and gradually decreases, becoming negative in the 30-40% peripheral class. The corresponding linear fit parameters are summarized in table 6.1, alongside preliminary results for charged pions. The pions show slopes of similar magnitude and a comparable transition from positive to negative values with increasing centrality. Assuming a comparable collective behaviour between charged and neutral pions, this observation is in-line with the assumption of the π^0 dominance in the dielectron cocktail. As such, it serves as a first explanation for the observed trend for the integrated v_1 .

However, despite these initial insights, a direct and precise comparison remains challenging and has to be treated with caution. The integrated directed flow measurement strongly depends on the underlying phase space coverage, which varies between different particle species. Notably, it is important to emphasize that this dielectron measurement is restricted to the phase space covered by the daughters of the dielectron pair (e^+/e^-) within HADES, as discussed in section 4.3.1. This corresponds to a specific phase space of the virtual photons, depending on the dilepton source and the composition of the cocktail that constitutes the integrated spectrum. Therefore, any comprehensive comparison with hadron measurements will require more detailed studies to account for these phase space effects.

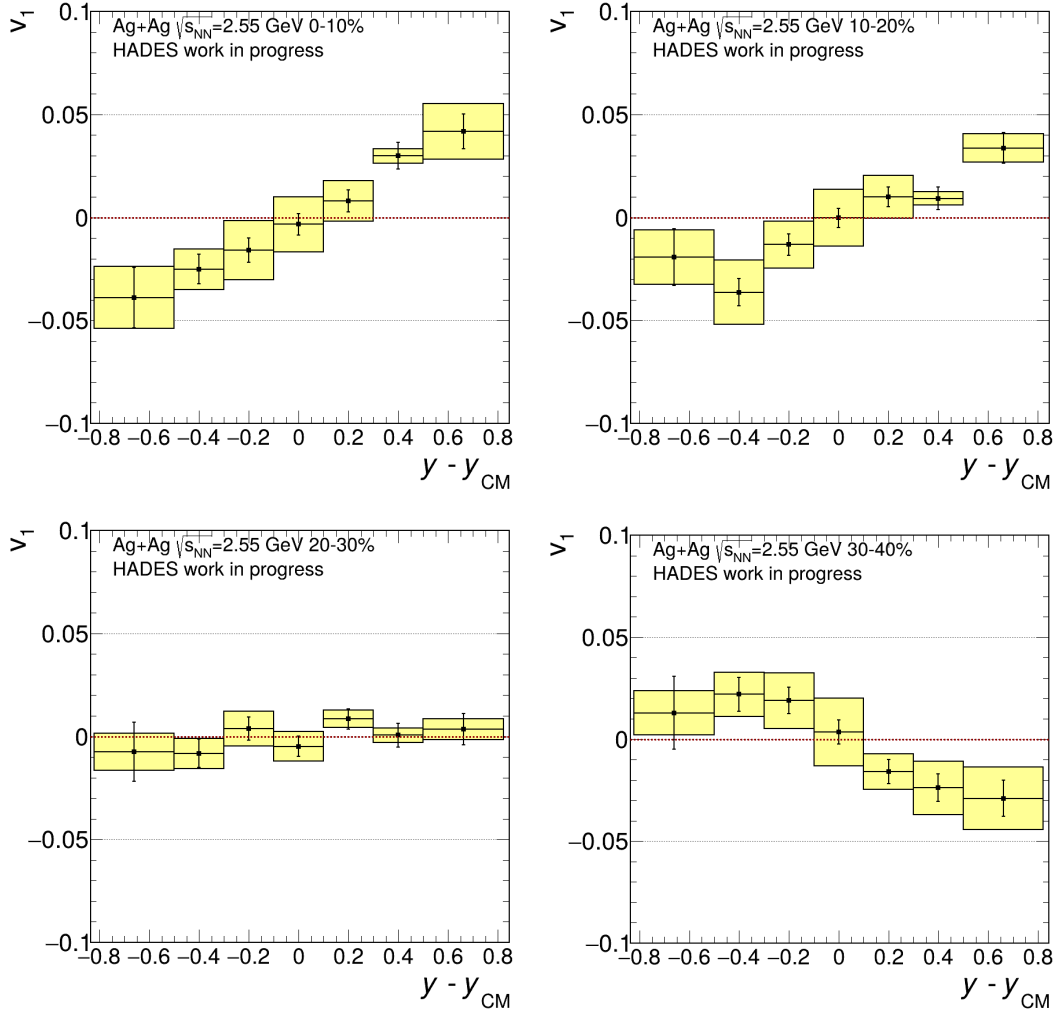


Figure 6.7: Directed flow v_1 in 10% centrality bins. Vertical lines represent statistical uncertainties. Boxes represent systematic uncertainties.

Centrality	$\left. \frac{dv_1}{dy} \right _{y=y_{cm}} \quad [\times 10^{-2}]$		
	DiElectrons	π^+ (Preliminary)	π^- (Preliminary)
0–10%	$6.0 \pm 0.76_{\text{stat}} \pm 0.71_{\text{sys}}$	$0.65 \pm 0.0175_{\text{stat}}$	$3.60 \pm 0.014_{\text{stat}}$
10–20%	$5.0 \pm 0.67_{\text{stat}} \pm 1.40_{\text{sys}}$	$-1.89 \pm 0.016_{\text{stat}}$	$2.092 \pm 0.013_{\text{stat}}$
20–30%	$0.9 \pm 0.70_{\text{stat}} \pm 0.50_{\text{sys}}$	$-7.50 \pm 0.017_{\text{stat}}$	$-3.387 \pm 0.014_{\text{stat}}$
30–40%	$-5.0 \pm 0.90_{\text{stat}} \pm 1.30_{\text{sys}}$	$-13.38 \pm 0.020_{\text{stat}}$	$-9.831 \pm 0.017_{\text{stat}}$

Table 6.1: Slope of directed flow dv_1/dy at midrapidity ($y = y_{cm}$), measured at HADES for Ag+Ag collisions at $\sqrt{s_{NN}} = 2.55$ GeV, of dielectrons and charged pions as a function of collision centrality. Values are given in units of 10^{-2} . The π^+ and π^- results are taken from [117] and serve as work-in-progress results.

Elliptic Flow: Figure 6.8 presents the integrated elliptic flow v_2 as a function of invariant mass for the same energies and collision systems. As with the directed flow v_1 , the Au+Au data are subject to the largest uncertainties. In general, the uncertainties increase with higher invariant masses due to the exponential decrease in the yield of dielectron pairs, which reduces the statistical precision of the measurements.

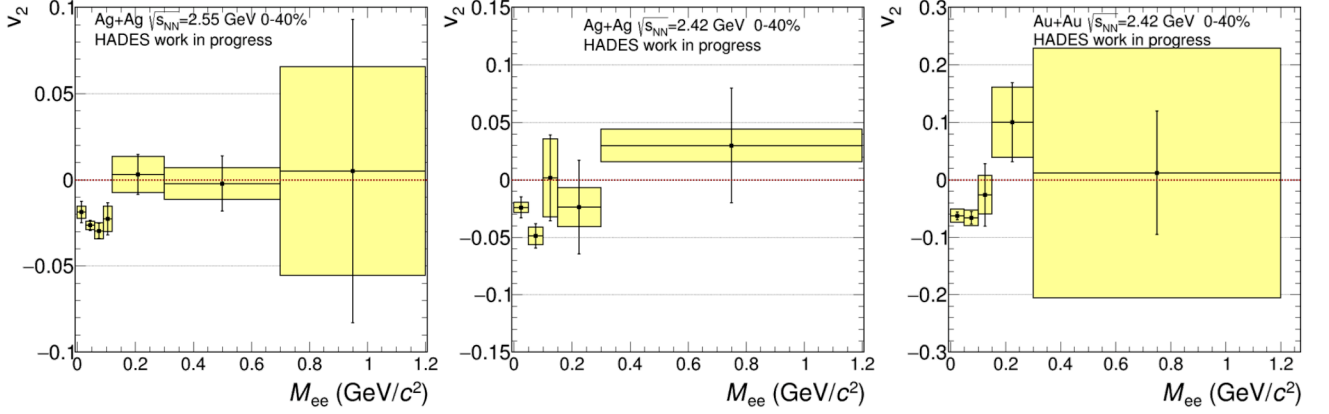


Figure 6.8: Integrated dielectron v_2 for two collision systems and two energies. Vertical lines represent statistical uncertainties. Boxes represent systematic uncertainties.

However, even within these statistical constraints, two distinct mass regions are evident in the data. For low invariant masses ($M_{ee} < 0.12$ GeV/c²), the flow is dominated by contributions from the π^0 Dalitz decay, which results in a negative elliptic flow for all investigated systems and energies. This is consistent with expectations from hadron measurements at these energies, where a negative v_2 is observed due to interplay with the spectators, see section 1.3. At higher invariant masses, the dielectron signal becomes increasingly dominated by thermal radiation. While the measurement at $\sqrt{s_{NN}} = 2.42$ GeV does not really allow for any conclusions due to the substantial uncertainties, the high statistics measurement of $\sqrt{s_{NN}} = 2.55$ GeV suggests a significant shift of the v_2 in this thermally dominated mass region, towards smaller or even positive values. This trend is consistent as a function of rapidity and p_t as well as across the two energies and systems. As such, it motivates further systematic studies discussed in the following section.

6.3 Isolation of the Thermal DiElectron Flow Coefficients

The flow coefficients shown in figures 6.6 and 6.8 represent fully inclusive dielectron azimuthal anisotropies and represent the superposition of all emission channels listed in table 1.3. Since each channel may be emitted at varying times of the collisions and experience different anisotropic responses to the collective expansion, a quantitative interpretation of the measurement requires a more precise understanding of the underlying sources. The focus of this work is on the thermal contribution emitted from the hot and dense fireball, which, in principle, may be isolated analogously to the procedure presented for the excess mass spectra in section 6.1. In his case, however, additional information is needed. While the relative yields are taken from the experimentally constrained cocktail, see section 4.4, the corresponding flow coefficients for each source must also be known. Unfortunately, as discussed in detail in section 5.5, precise experimental information are not available for most channels. For this reason, estimates from UrQMD

simulations provide guidance where necessary. In addition, the flow coefficients are calculated in large phase-space bins, which result in some channels, e.g. the ϕ or ω decays, to be negligible.

In general, a first indication of the importance of source separation is already visible in figure 6.8. As discussed, the overall behaviour suggests the dominance of two components. For one, the π^0 Dalitz decay, which largely inherits the strong elliptic flow of the freeze-out hadrons. For another, the thermal radiation emitted throughout the evolution of the fireball. These two contributions appear to exhibit notably different flow patterns, motivating a more differential investigation with the high-statistics Ag+Ag dataset at $\sqrt{s_{NN}} = 2.55$ GeV. Figure 6.9 shows the measured elliptic flow as a function of centrality, rapidity $y - y_{cm}$, and transverse momentum p_t separately for both mass regions. The data is compared with the UrQMD prediction for the virtual photon v_2 from π^0 Dalitz decays, see section 5.5. In every case, the agreement between the data and the UrQMD estimate is reasonably good in the low mass region, suggesting that the π^0 Dalitz decay indeed dominates this part of the spectrum, and that the UrQMD prediction follows the data. The small, yet systematic overshoot of the UrQMD curve may be attributed to the presence of a additional contributions even below $M_{ee} < 120$ MeV/ c^2 .

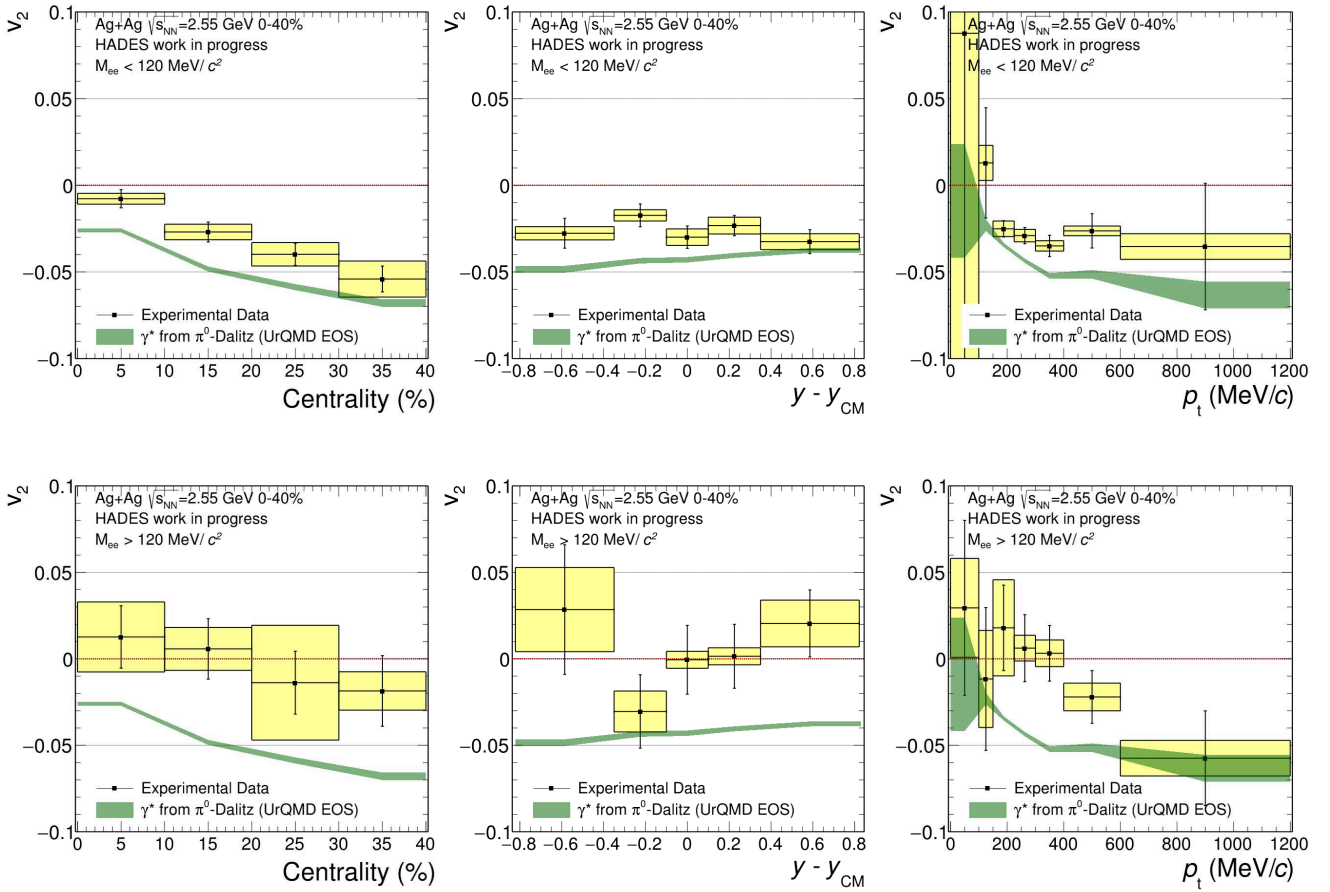


Figure 6.9: Measurement of the integrated dielectron v_2 over centrality (left panel), transverse momentum (middle panel) and rapidity (right panel). The top row shows the results within the mass region dominated by π^0 Dalitz decays. The bottom row shows results within the mass region dominated by thermal radiation. Vertical lines represent statistical uncertainties. Boxes represent systematic uncertainties.

In the higher-mass region, where the dielectron yield drops steeply and statistical uncertainties increase accordingly, a qualitative deviation from the π^0 trend is nevertheless visible. The data no longer follow the UrQMD π^0 prediction but instead generally show smaller magnitudes of v_2 . This behaviour is consistent with an increasing dominance of thermal radiation and agrees with the mass-integrated trends observed in figure 6.8.

This first differential comparison, however, faces two limitations. First, the low-mass region cannot be considered a pure π^0 sample, since the thermal continuum extends down to the π^0 mass and therefore inevitably contributes to the measured flow. In a similar vein, the high-mass region, although suppressing the π^0 contribution, still potentially contains non-thermal contributions, such as η Dalitz decays. Second, especially the higher invariant masses suffer from increased statistical uncertainties which limits interpretability. These considerations motivate a full cocktail-based subtraction in order to observe the thermal dielectron flow coefficients in the full mass range. While a fully multi-differential subtraction is not yet possible, due to limits in the available statistics and measurements of freeze-out hadrons flow coefficients, a first estimate to isolate the thermal elliptic flow is nevertheless attempted by utilising equation 5.2 to subtract non-thermal contributions. In every case, the experimental yields, discussed in section 4.4 and the UrQMD based flow coefficients, see section 5.5, serve as the combined inputs to estimate the hadronic freeze-out contributions. The resulting isolated v_2 is shown in figures 6.10 and 6.11 after subtraction of the π^0 and η contributions, evaluated as a function of invariant mass, transverse momentum, rapidity, and collision centrality.

Across all of these observables a consistent picture appears to emerge. The subtraction of the π^0 contribution shifts the residual anisotropy towards smaller magnitudes, and in several regions even allow for slightly positive v_2 values within the uncertainties. This is in agreement with the observation from figure 6.9 which relied purely on a source separation based on the invariant mass. Further subtraction of the η contribution in figure 6.11 results in only minor modifications of the residual anisotropies, which indicates that the remaining signal is already dominated by the thermal component. Moreover, figure 6.11 illustrates that the elliptic flow coefficient v_2 of the virtual photon originating from η decays is significantly reduced compared to that of the parent meson. This suppression results from the kinematics of the Dalitz decay, in which the virtual photon carries only a fraction of the original emission angle, as part of the momentum is taken by the accompanying real photon. While a similar effect is present for π^0 decays, the applied acceptance requirement of $p_{\gamma^*} > 100$ MeV/ c renders the corresponding angular smearing almost negligible in that case. It can also be noted that the thermal contribution, dominated by direct decays of vector mesons, see section 1.4.2, does not experience such an angular dilution. Therefore, it cannot account for the reduced v_2 magnitudes observed here. Instead, these first results point towards a time-dependent development of the azimuthal anisotropy in heavy-ion collisions. Recent transport-model studies [68] have shown that dielectrons can be sensitive to the elliptic flow during the hottest and densest stages of the reaction. In these models, the early overlap geometry leads to an initially positive v_2 and an in-plane emission pattern. As the system evolves, interactions with spectator matter and shadowing effects gradually diminish this in-plane preference, ultimately driving the sign change to the negative v_2 values and out-of-plane emission observed for hadronic probes at freeze-out.

The trends visible in figure 6.11 provide, for the first time, experimental indications consistent with this predicted temporal evolution and are qualitatively aligned with these theoretical expectations. Although the substantial statistical and systematic uncertainties in the present measurement preclude a more quantitative interpretation, the results clearly establish dielectron azimuthal anisotropy as a highly promising observable for future high-precision experiments. As discussed in [68], improved accuracy may ultimately enable a more direct constraint on the equation of state at densities of 2–3 times saturation.

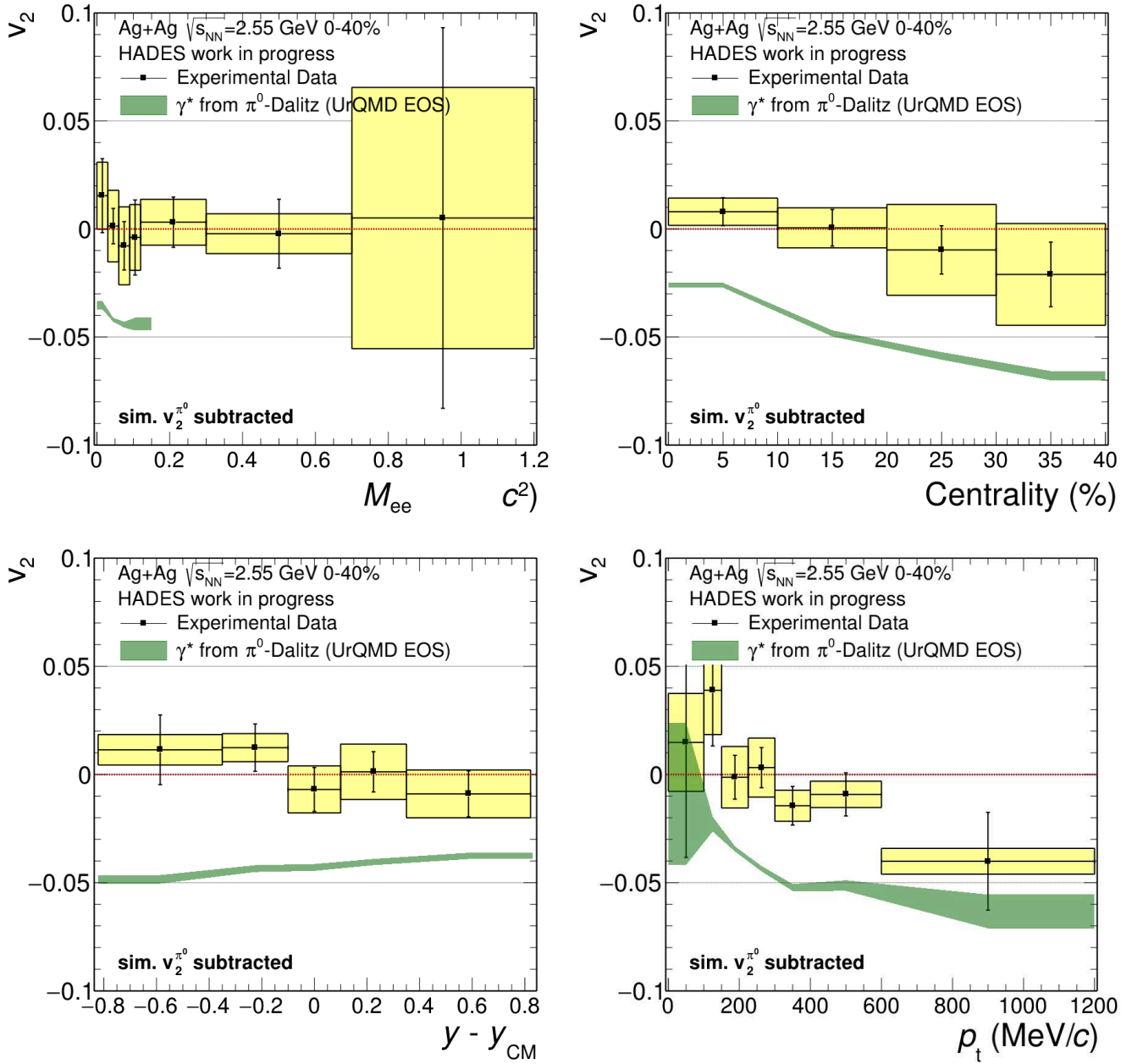


Figure 6.10: Estimated isolated dielectron v_2 after subtraction of the π^0 contribution. Vertical lines represent statistical uncertainties. Boxes represent systematic uncertainties.

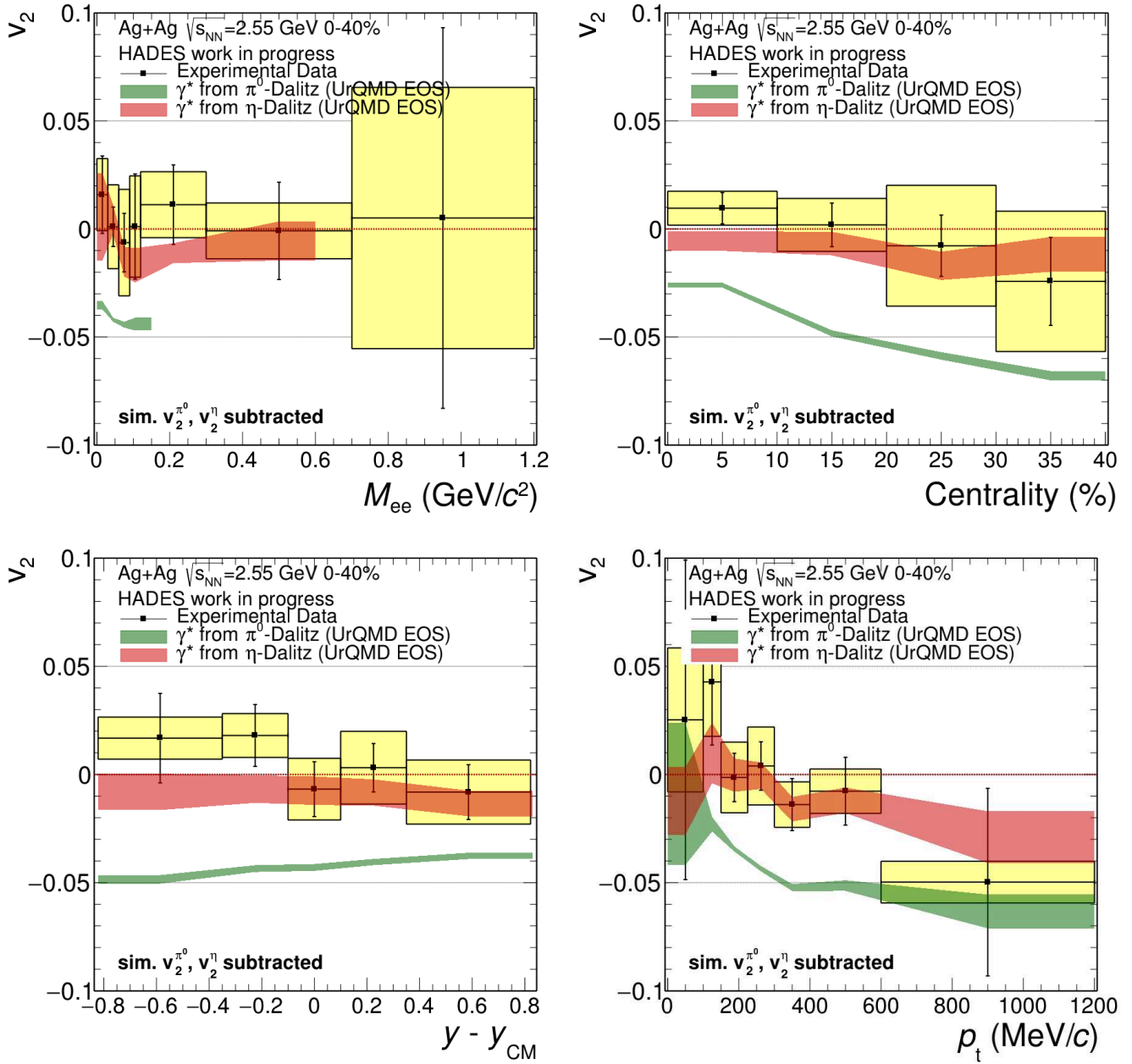


Figure 6.11: Estimated isolated dielectron v_2 after subtraction of the π^0 and η contribution. Vertical lines represent statistical uncertainties. Boxes represent systematic uncertainties.

6.4 Ongoing Perspectives with Multi-Differential Measurements

The results presented in the preceding sections contribute to the growing body of measurements demonstrating the penetrating nature of dielectrons as electromagnetic probes of the hot and dense medium, as initially motivated in section 1.4. The extraction of fireball temperatures and excess yields in Ag+Ag collisions at two beam energies, including their dependence on the number of participating nucleons, provides unique insights into the characteristics of the underlying fireball. In parallel, the first determination of the directed and elliptic flow of dielectrons, together with preliminary attempts to isolate the thermal contribution, demonstrates how such electromagnetic probes allow experimental access to the system's evolution over time.

These findings motivate further investigation. Ongoing work aims to not only extend these measurements to more collision systems as well as beam energies, but also to exploit the existing Ag+Ag dataset more comprehensively. Of particular interest are multi-differential measurements which provide more detailed insights into the conditions and evolution of the fireball. In addition, they offer important benchmarks for theory calculations, in particular the previously discussed coarse-grained UrQMD approach incorporating in-medium spectral functions.

Transverse Momentum Dependence: A first step towards such multi-differential analyses is the study of the transverse-momentum and transverse-mass dependence of the dielectron yield in narrow invariant-mass intervals. Figure 6.12 shows the fully corrected spectra, extrapolated to the full phase space.

The left panel displays the inclusive dielectron yield, which contains all sources contributing to the measured radiation. To isolate the thermal component, the freeze-out contributions from π^0 , η , and ω decays are subtracted, as shown in the right panel. Remaining hadronic contributions such as Bremsstrahlung and Δ Dalitz decays have not yet been removed. Their subtraction requires a corresponding multi-differential analysis of $p+p$ reference data in conjunction with GiBUU simulations for the specific (M, p_t) bins considered here. Work towards this goal is underway. Even at this intermediate stage, a comparison to the coarse-grained UrQMD calculations with in-medium spectral functions reveals a good level of agreement across most of the explored phase space. This is an important finding, as it strengthens the agreement seen in the integrated mass spectra of section 6.1. A fully quantitative assessment, however, will require a detailed evaluation of systematic uncertainties, which have not yet been performed for the multi-differential analysis.

In the end, the resulting transverse-momentum spectra of the thermal radiation provide valuable information on the temperature as well as radial flow, i.e. the collective expansion velocity, of the hot and dense medium [154]. Assuming locally thermalised emission, the spectral shape can be described by a Boltzmann-like distribution. After integrating over azimuthal angle and rapidity, one obtains:

$$\frac{1}{p_t} \frac{dN}{dp_t} \propto m_t K_1 \left(\frac{m_t c^2}{k_B T_{\text{eff}}} \right) \quad (6.5)$$

where $m_t = \sqrt{M^2 + p_t^2}$ and K_1 is the first order modified Bessel function of the second kind. In this case, T_{eff} serves as an effective temperature extracted from the fit. It encodes the true thermal temperature of the source, but is blue-shifted because of the expansion of the rapid expansion of the medium. The presence of radial flow leads to a characteristic dependence of the inverse-slope parameter on the invariant mass of the dilepton pair. In hydrodynamic and fireball descriptions of an expanding thermal source, this effect can

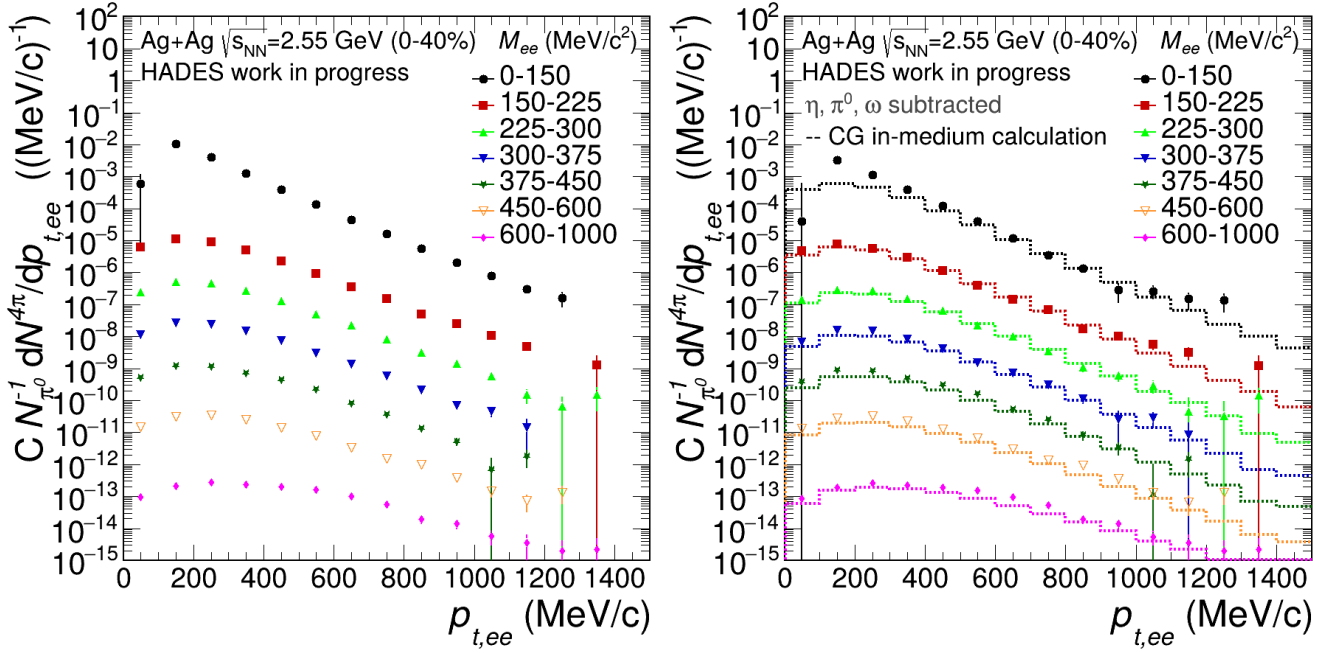


Figure 6.12: Dielectron spectrum as a function of transverse momentum p_t for various invariant-mass intervals in Ag+Ag collisions at $\sqrt{s_{\text{NN}}} = 2.55$ GeV. The left panel shows the integrated signal. The right panel displays the excess yield after subtraction of the freeze-out contributions from π^0 , η , and ω decays. Initial Bremsstrahlung and Δ Dalitz contributions are not yet subtracted. The results are compared to coarse-grained UrQMD calculations employing the in-medium spectral functions. Vertical lines represent statistical uncertainties. Each mass bin is scaled by an arbitrary factor C to make them visually distinct.

be understood as a consequence of the Lorentz boost of locally thermalised emitters. The resulting mass dependence of the effective temperature can be approximated by a linear scaling of the form [155]:

$$T_{\text{eff}}(M) \approx T + M \langle \beta_r \rangle^2 \quad (6.6)$$

where T denotes the true thermal temperature of the medium and $\langle \beta_r \rangle$ the average radial velocity at the time of emission. Heavier emitters experience a stronger blue-shift from the collective transverse expansion, causing their transverse-momentum spectra to appear harder.

Originally introduced to describe identified hadron transverse-momentum spectra using simple hydrodynamic-inspired parametrisations of the kinetic freeze-out temperature and collective expansion velocity, the blast-wave model has been widely used to fit the p_T spectra of pions, kaons, protons and other hadron species in order to extract a common freeze-out temperature and an average transverse expansion velocity $\langle \beta_T \rangle$ as a function of particle mass and collision centrality [156, 157]. Such fits exploit the characteristic mass dependence induced by the interplay of thermal motion and collective flow on the spectral slopes, providing a phenomenological handle on radial expansion dynamics. It should be noted, however, that this scaling may not hold precisely for dileptons, since their invariant mass reflects emission from different stages of the evolving medium rather than a single freeze-out condition. More recent work continues to refine this picture and explore alternatives to simple blast-wave parametrisation, e.g. by incorporating correlations and event-by-event fluctuations [158, 159]. Nevertheless, equation 6.6 motivates the application of a

similar strategy to dielectron radiation and may allow one to probe the interplay of thermal motion and radial expansion at different stages of the collision. Unlike hadrons, dielectrons are emitted continuously throughout the evolution of the fireball, which suggests that their mass-dependent slopes could reflect an earlier emission stage. Once the thermal component of the dielectron spectra is fully isolated, fitting the mass dependence of T_{eff} will provide quantitative constraints on both the medium temperature and the collective expansion velocity, potentially offering insight into the fireball's properties at earlier times than those accessible with hadronic observables.

Rapidity Dependence: In a similar vein, another important multi-differential measurement is the study of the invariant-mass spectra in bins of rapidity, as shown in figure 6.13. They are reconstructed analogously to the transverse momentum spectra with application of the necessary corrections and the extrapolation to the full phase space. The left panel displays the inclusive dielectron yield, whereas the right panel shows the excess after subtraction of freeze-out contributions from π^0 , η , and ω decays. A subtraction of initial sources will similarly require the NN reference in specific (M, y) bins. At this stage, a first comparison with the coarse-grained in-medium appears promising but can only be fully assessed once systematic uncertainties have been properly evaluated.

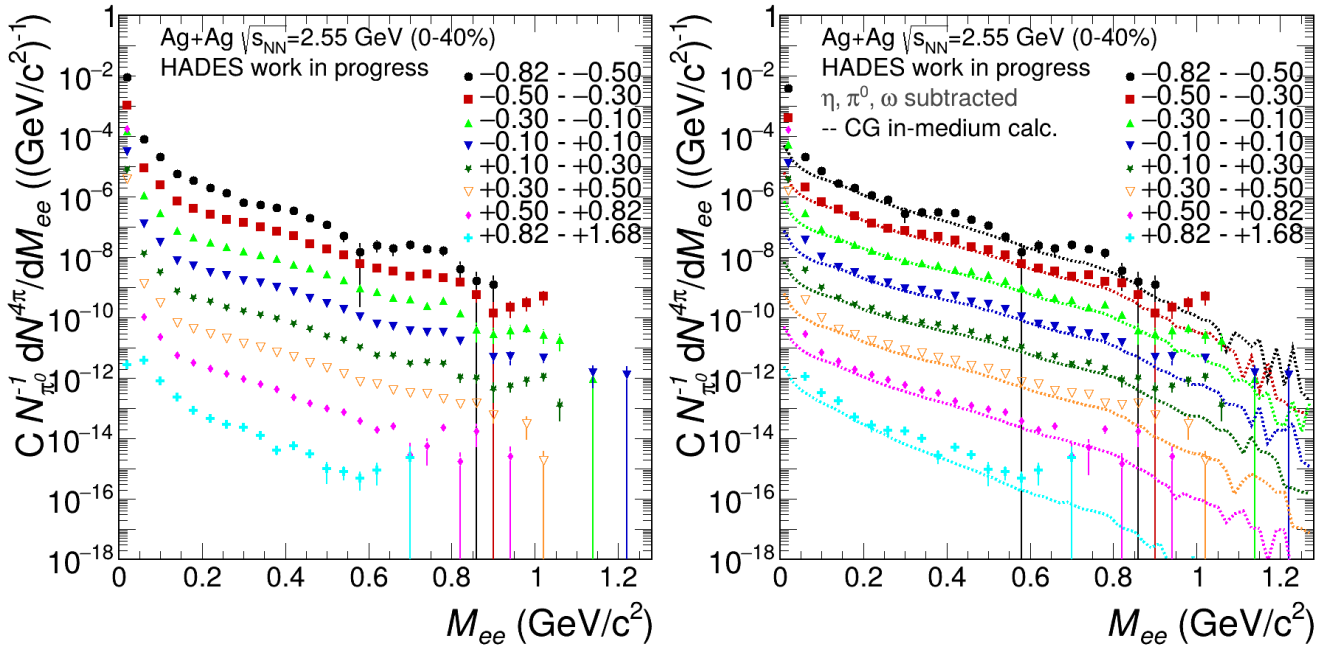


Figure 6.13: DiElectron spectrum in dependence of the invariant mass for various bins of rapidity for Ag+Ag collisions at $\sqrt{s_{\text{NN}}} = 2.55$ GeV. The left panel shows the integrated signal. The right panel shows the excess after subtraction of freeze-out contributions of π^0 , η and ω . Initial contributions from Bremsstrahlung are not yet subtracted. The results are compared to coarse-grained UrQMD calculations employing in-medium spectral function. Vertical lines represent statistical uncertainties. Each mass bin is scaled by an arbitrary factor C to make them visually distinct.

Beyond providing additional benchmarks for theoretical predictions, the rapidity dependence of the invariant-mass spectra offers complementary information on the longitudinal structure and dynamics of the fireball. Assuming a static thermal source, the temperature extracted from invariant-mass fits, based on equation 6.1, in each rapidity bin is expected to follow:

$$T_{\text{eff}}(y) \sim \frac{T}{\cosh(y - y_{cm})} \quad (6.7)$$

where T is the true thermal temperature of the source and y_{cm} the center-of-mass rapidity. Selecting dielectron pairs within a given rapidity bin effectively samples emission from source elements with different longitudinal velocities. As a result, the effective slope of the invariant-mass spectrum in each rapidity bin reflects not only the thermal motion of the source but also its longitudinal kinematics. Deviations from this scaling can therefore provide direct insight into longitudinal flow or possible non-equilibrium effects, helping to characterize the expansion dynamics along the beam axis.

Taken together, these multi-differential analyses provide complementary ways to test the hypothesis that dielectrons are emitted from a (locally) thermalised medium. In this work, the reconstruction has focused on the high-statistics Ag+Ag dataset at $\sqrt{s_{NN}} = 2.55$ GeV, which offers a unique opportunity to study dielectron spectra in multiple differential dimensions. Future and ongoing efforts aim to extend this approach to the 2.42 GeV dataset as well as to other collision systems, with the goal of exploiting the full potential of the available measurements and further constraining theoretical models of dielectron emission. By examining the effective slopes in different invariant-mass, p_t , and rapidity bins, one can in principle probe both the temperature and collective motion at different stages of the collision. As such, these studies will help to constrain the space–time evolution of the system and the relative contributions of early versus late emission, providing a more complete picture than single-differential measurements.

7 Summary and Outlook

This thesis set out to exploit the penetrating nature of dielectrons as probes of the hot and dense fireball created in heavy-ion collisions at SIS18 energies.

Two primary aspects formed the central focus of this work. First, the reconstruction of dielectron spectra from Ag+Ag collisions at $\sqrt{s_{NN}} = 2.42$ GeV and 2.55 GeV recorded by the HADES experiment. The latter served as an independent validation and finalisation of previous HADES results, while the former represents a new finalised analysis, enabling a more systematic comparison of the dielectron production at two closely spaced energies. The complete analysis chain has been carried out, including new advances in the event selection, particle identification, pair selection as well as efficiency and acceptance corrections as detailed in chapter 4. In the context of both analyses, an additional effort was made to develop a new machine learning model in order to identify and remove contamination from collisions with surrounding target material. As presented in chapter 3, the model achieved promising performance across all evaluation metrics, motivating its successful application within this work and beyond.

The thereby resulting excess spectrum has first been studied as a function of invariant mass, yielding a fireball temperature of $T_{\text{Ag}2.55\text{Ag}} = 82.2 \pm 0.8_{\text{stat}} \pm 2.9_{\text{sys}}$ MeV for Ag+Ag collisions at $\sqrt{s_{NN}} = 2.55$ GeV, and $T_{\text{Ag}2.42\text{Ag}} = 73.5 \pm 1.8_{\text{stat}} \pm 3.0_{\text{sys}}$ MeV at $\sqrt{s_{NN}} = 2.42$ GeV, both within 0-40% centrality. This is particularly interesting when put into perspective with the excess yield, which has been found to be $N_{\text{Ag}2.42\text{Ag}}^{\text{excess}} = (3.16 \pm 0.17_{\text{stat}} \pm 0.24_{\text{syst}}) \times 10^{-5}$ and $N_{\text{Ag}2.55\text{Ag}}^{\text{excess}} = (6.22 \pm 0.1_{\text{stat}} \pm 0.28_{\text{syst}}) \times 10^{-5}$ respectively. Further, this analysis has been extended to study the centrality dependence, through which a non-linear $\langle N_{\text{part}} \rangle$ scaling of $\alpha_{\text{Ag}2.55\text{Ag}} = 1.39 \pm 0.04_{\text{stat}} \pm 0.13_{\text{sys}}$ and $\alpha_{\text{Ag}2.42\text{Ag}} = 1.33 \pm 0.14_{\text{stat}} \pm 0.15_{\text{sys}}$ has been observed for the excess yield. It is the combination of these observations which allows to disentangle the fireball properties in terms of temperature, volume and lifetime. The multi-differential analysis has been further extended and include the analysis of transverse momentum as well as rapidity dependence in bins of invariant mass. This approach promises deeper insight into radial and longitudinal expansion of the medium, although further studies are required to isolate the thermal contributions and to robustly quantify systematic uncertainties. Future measurements of the same kind, but for varying energies and other collisions systems will aid significantly in that quest.

Second, this thesis has established a full analysis framework for extracting dielectron flow coefficients, motivated by recent theoretical predictions of the sensitivity of dielectrons to collective dynamics. A complete implementation of the reconstruction procedure, including necessary corrections, with detailed studies of the related systematic uncertainties, has been newly developed for this purpose. Details are given in chapter 5. This framework was applied to Au+Au and Ag+Ag collisions at $\sqrt{s_{NN}} = 2.42$ GeV and 2.55 GeV. In particular, the highest statistics measurement at 2.55 GeV indicates a smaller magnitude of the elliptic flow seen by thermal radiation, in comparison to what is observed for hadronic freeze-out sources. This is in-line with theory predictions [68] which emphasise how the thermal dielectrons are sensitive to the evolution of the systems collectivity over time.

This work thus establishes the methodological foundation for future dielectron flow measurements not only for SIS18 energy, but also future dilepton experiments such as CBM at FAIR, NA60+/DiCE at SPS, ALICE3 and LHCb-II at LHC. Today, it represents the first systematic study of dielectron azimuthal anisotropies in this energy regime.

Building on these results, several promising avenues for future research can be identified:

- **Additional Anisotropic Flow Observables:** This thesis has focused on the reaction-plane method to extract dielectron flow coefficients. Future studies could explore alternative observables that may provide higher sensitivity to the equation of state and better discrimination between hadronic and thermal dielectron sources. One suggested approach is the scalar-product method, which correlates dielectrons with hadron-tagged reference planes [69]. This method is proposed to reduce potential cancellation effects inherent to reaction-plane correlations and may allow a cleaner separation of the various dielectron contributions. Another avenue is event-by-event flow correlations [160], which have been shown to be highly sensitive to the nuclear equation of state in proton flow studies. Applying similar observables to dielectrons could provide new insights into the collective evolution and the EoS of the medium. Lastly, the use of global de-blurring techniques [161] could offer an alternative to the conventional Fourier-based description of collective flow, providing a more holistic representation of the system's anisotropic expansion. While statistical and systematic limitations of dielectron measurements must be carefully assessed, these approaches represent promising next steps to refine our understanding of anisotropic flow and medium properties.
- **Polarisation and Radial Flow:** Beyond anisotropic flow, additional observables related to collective dynamics could further enhance the understanding of the medium. Namely, this includes the polarisation, which can help in distinguishing the dielectron production channels, as well as the radial flow. As discussed in section 6.4, the latter is encoded in the transverse momentum spectra, motivating the finalisation of multi-differential studies of the available data. In the end, this could aid in a more comprehensive characterisation of the medium's kinematic properties, providing constraints on the fireball's pressure gradients and expansion dynamics.
- **Extension to Additional Systems and Energies:** The methodological framework developed here can be applied to other collision systems and energies, allowing systematic studies of dielectron production and flow. Newly recorded Au+Au data from HADES of 2024 and 2025 will provide novel measurements and enable a more detailed comparison between systems at varying energies. Such comparisons are essential to disentangle volume and lifetime contributions to the thermal excess yield. In general, the evaluation of excess spectra across multiple energies can shed light on the evolution of the fireball properties and help to benchmark theoretical models of hadronic and thermal contributions.
- **Improved DiElectron Cocktail Description:** A precise determination of the thermal dielectron contribution requires not only accurate measurements of the total dielectron yield but also detailed knowledge of the yields and flow coefficients of all known hadronic sources contributing to the dielectron cocktail. At present, limitations in the experimental access to these sources necessitated reliance on model simulations, such as UrQMD, to estimate their contributions and isolate the thermal flow coefficients. Future measurements that directly constrain both the yield and collective properties of key sources, such as π^0 and η , will substantially reduce model dependencies and allow for a more robust extraction of the thermal signal. The recent installation of an electromagnetic calorimeter (ECAL) covering all six HADES sectors provides a promising opportunity to reconstruct photons from π^0 and η decays, enabling improved measurements of their yields and flow characteristics. At HADES

and beyond, such developments may enhance the ability to subtract hadronic contributions with high precision and serve as a requisite for a model independent isolation of the thermal radiation.

- ***High-Statistics Multi-Differential Analyses at Future Facilities:*** Upcoming high-intensity experiments, particularly CBM at FAIR, will dramatically increase the available statistics for dielectron measurements. These facilities will allow extended multi-differential analyses of invariant mass, transverse momentum, rapidity and azimuthal distributions. Higher event rates and improved detector capabilities will enable systematic studies of thermal versus hadronic sources, providing access to rare channels and high-mass dielectron pairs that are currently statistically limited.

In conclusion, this thesis demonstrates the unique power of dielectrons as probes of the hot and dense medium created in heavy-ion collisions. Through the combination of established experimental measurements, advanced analysis techniques and dedicated methodological developments, new constraints on the thermodynamic and collective properties of the fireball have been established. The results presented here motivate further experimental and theoretical investigations that build upon the demonstrated sensitivity of dielectron observables. Ultimately, this work contributes to a deeper experimental understanding of strong interacting matter under extreme conditions.

Bibliography

- [1] Accessed: 2025-09-09. URL: <https://www.oxfordreference.com/display/10.1093/oi/authority.20110803100140545>.
- [2] Raymond A. Serway and John W. Jewett. *Physics for Scientists and Engineers with Modern Physics*. 7th. Student Edition. Belmont, CA: Brooks/Cole, 2008. ISBN: 978-0-495-11245-7.
- [3] Paul Langacker. *The Standard Model and Beyond*. Taylor & Francis, 2017. ISBN: 978-1-4987-6321-9. DOI: 10.1201/b22175.
- [4] Steven Weinberg. “The Making of the standard model”. In: *Eur. Phys. J. C* 34 (2004). Ed. by G. ’t Hooft, pp. 5–13. DOI: 10.1140/epjc/s2004-01761-1. arXiv: hep-ph/0401010.
- [5] Behruz Kardan. “Collective flow measurements in Gold-Gold collisions at 1.23 AGeV with HADES”. PhD thesis. Frankfurt U., Nov. 2022. DOI: 10.21248/gups.80958.
- [6] A. B. Arbuzov. “Quantum Field Theory and the Electroweak Standard Model”. In: (2017). Ed. by Martijn Mulders and Giulia Zanderighi, pp. 1–34. DOI: 10.23730/CYRSP-2017-004.1. arXiv: 1801.05670 [hep-ph].
- [7] https://en.wikipedia.org/wiki/Standard_Model. Accessed: 2025-09-09.
- [8] Peter W. Higgs. “Broken Symmetries and the Masses of Gauge Bosons”. In: *Phys. Rev. Lett.* 13 (1964). Ed. by J. C. Taylor, pp. 508–509. DOI: 10.1103/PhysRevLett.13.508.
- [9] Serguei Chatrchyan et al. “Observation of a New Boson at a Mass of 125 GeV with the CMS Experiment at the LHC”. In: *Phys. Lett. B* 716 (2012), pp. 30–61. DOI: 10.1016/j.physletb.2012.08.021. arXiv: 1207.7235 [hep-ex].
- [10] Georges Aad et al. “Observation of a new particle in the search for the Standard Model Higgs boson with the ATLAS detector at the LHC”. In: *Phys. Lett. B* 716 (2012), pp. 1–29. DOI: 10.1016/j.physletb.2012.08.020. arXiv: 1207.7214 [hep-ex].
- [11] Accessed: 2025-09-09. URL: <https://www.nobelprize.org/prizes/physics/2013/summary/>.
- [12] R. L. Workman et al. “Review of Particle Physics”. In: *PTEP* 2022 (2022), p. 083C01. DOI: 10.1093/ptep/ptac097.
- [13] Krishna Aryal et al. “The Effect of Charge, Isospin, and Strangeness in the QCD Phase Diagram Critical End Point”. In: *Universe* 7.11 (2021), p. 454. DOI: 10.3390/universe7110454. arXiv: 2109.14787 [nucl-th].
- [14] Jan M. Pawłowski. “The QCD phase diagram: Results and challenges”. In: *AIP Conf. Proc.* 1343 (2011). Ed. by F. J. Llanes-Estrada and J. R. Peláez, pp. 75–80. DOI: 10.1063/1.3574945. arXiv: 1012.5075 [hep-ph].

-
- [15] Lipei Du, Agnieszka Sorensen, and Mikhail Stephanov. “The QCD phase diagram and Beam Energy Scan physics: A theory overview”. In: *Int. J. Mod. Phys. E* 33.07 (2024), p. 2430008. doi: 10.1142/9789811294679_0007. arXiv: 2402.10183 [nucl-th].
- [16] Jana N. Guenther. “Overview of the QCD phase diagram: Recent progress from the lattice”. In: *Eur. Phys. J. A* 57.4 (2021), p. 136. doi: 10.1140/epja/s10050-021-00354-6. arXiv: 2010.15503 [hep-lat].
- [17] Bedangadas Mohanty. “Exploring the QCD phase diagram through relativistic heavy ion collisions”. In: *EPJ Web Conf.* 66 (2014). Ed. by Santo Lunardi et al., p. 04022. doi: 10.1051/epjconf/20146604022. arXiv: 1311.3722 [nucl-ex].
- [18] J. Adamczewski-Musch et al. “Probing dense baryon-rich matter with virtual photons”. In: *Nature Phys.* 15.10 (2019), pp. 1040–1045. doi: 10.1038/s41567-019-0583-8.
- [19] Y. Aoki et al. “The Order of the quantum chromodynamics transition predicted by the standard model of particle physics”. In: *Nature* 443 (2006), pp. 675–678. doi: 10.1038/nature05120. arXiv: hep-lat/0611014.
- [20] A. Bazavov et al. “The chiral and deconfinement aspects of the QCD transition”. In: *Phys. Rev. D* 85 (2012), p. 054503. doi: 10.1103/PhysRevD.85.054503. arXiv: 1111.1710 [hep-lat].
- [21] Peter Braun-Munzinger, Krzysztof Redlich, and Johanna Stachel. “Particle production in heavy ion collisions”. In: (Apr. 2003). Ed. by Rudolph C. Hwa and Xin-Nian Wang, pp. 491–599. doi: 10.1142/9789812795533_0008. arXiv: nucl-th/0304013.
- [22] Christof Wetterich. “Exact evolution equation for the effective potential”. In: *Phys. Lett. B* 301 (1993), pp. 90–94. doi: 10.1016/0370-2693(93)90726-X. arXiv: 1710.05815 [hep-th].
- [23] Maximilian Wiest. “Dileptons as probes of strongly interacting matter”. MA thesis. Darmstadt, Tech. U., 2021.
- [24] Mikhail Stephanov. “QCD critical point: Recent developments”. In: *EPJ Web Conf.* 314 (2024), p. 00042. doi: 10.1051/epjconf/202431400042. arXiv: 2410.02861 [nucl-th].
- [25] T. Abyazimov et al. “Challenges in QCD matter physics –The scientific programme of the Compressed Baryonic Matter experiment at FAIR”. In: *Eur. Phys. J. A* 53.3 (2017), p. 60. doi: 10.1140/epja/i2017-12248-y. arXiv: 1607.01487 [nucl-ex].
- [26] M. Durante et al. “All the fun of the FAIR: fundamental physics at the facility for antiproton and ion research”. In: *Phys. Scripta* 94.3 (2019), p. 033001. doi: 10.1088/1402-4896/aaf93f. arXiv: 1903.05693 [nucl-th].
- [27] S. Huth et al. “Constraining Neutron-Star Matter with Microscopic and Macroscopic Collisions”. In: *Nature* 606 (2022), pp. 276–280. doi: 10.1038/s41586-022-04750-w. arXiv: 2107.06229 [nucl-th].
- [28] H. Sazdjian. “Introduction to chiral symmetry in QCD”. In: *EPJ Web Conf.* 137 (2017). Ed. by Y. Foka, N. Brambilla, and V. Kovalenko, p. 02001. doi: 10.1051/epjconf/201713702001. arXiv: 1612.04078 [hep-ph].
- [29] K. Ackerstaff et al. “Measurement of the strong coupling constant $\alpha(s)$ and the vector and axial vector spectral functions in hadronic tau decays”. In: *Eur. Phys. J. C* 7 (1999), pp. 571–593. doi: 10.1007/s100529901061. arXiv: hep-ex/9808019.
- [30] Paul M. Hohler and R. Rapp. “Evaluating chiral symmetry restoration through the use of sum rules”. In: *EPJ Web Conf.* 36 (2012). Ed. by Angela Badala et al., p. 00012. doi: 10.1051/epjconf/20123600012. arXiv: 1209.1051 [hep-ph].

-
- [31] Patrick Sellheim. “Reconstruction of the low-mass dielectron signal in 1.23A GeV Au+Au collisions”. PhD thesis. Johann Wolfgang Goethe-Universität, 2017.
- [32] Volker Koch. “Introduction to chiral symmetry”. In: *3rd TAPS Workshop on Electromagnetic and Mesonic Probes of Nuclear Matter*. Dec. 1995. arXiv: nucl-th/9512029.
- [33] G. E. Brown and Mannque Rho. “Scaling effective Lagrangians in a dense medium”. In: *Phys. Rev. Lett.* 66 (1991), pp. 2720–2723. doi: 10.1103/PhysRevLett.66.2720.
- [34] R. Rapp and J. Wambach. “Chiral symmetry restoration and dileptons in relativistic heavy ion collisions”. In: *Adv. Nucl. Phys.* 25 (2000), p. 1. doi: 10.1007/0-306-47101-9_1. arXiv: hep-ph/9909229.
- [35] Paul M. Hohler and Ralf Rapp. “Is ρ -Meson Melting Compatible with Chiral Restoration?” In: *Phys. Lett. B* 731 (2014), pp. 103–109. doi: 10.1016/j.physletb.2014.02.021. arXiv: 1311.2921 [hep-ph].
- [36] Hans Georg Ritter and Reinhard Stock. “Collective Flow of QCD Matter: a Historical Introduction”. In: *J. Phys. G* 41 (2014), p. 124002. doi: 10.1088/0954-3899/41/12/124002. arXiv: 1408.4296 [nucl-ex].
- [37] Hans H. Gutbrod. “The Path to Heavy Ions at LHC and Beyond”. In: *Melting Hadrons, Boiling Quarks - From Hagedorn Temperature to Ultra-Relativistic Heavy-Ion Collisions at CERN. With a Tribute to Rolf Hagedorn*. Ed. by Johann Rafelski. 2016, pp. 97–106. doi: 10.1007/978-3-319-17545-4_13.
- [38] J. Adamczewski-Musch et al. “Centrality determination of Au + Au collisions at 1.23A GeV with HADES”. In: *Eur. Phys. J. A* 54.5 (2018), p. 85. doi: 10.1140/epja/i2018-12513-7. arXiv: 1712.07993 [nucl-ex].
- [39] S. Voloshin and Y. Zhang. “Flow study in relativistic nuclear collisions by Fourier expansion of Azimuthal particle distributions”. In: *Z. Phys. C* 70 (1996), pp. 665–672. doi: 10.1007/s002880050141. arXiv: hep-ph/9407282.
- [40] Sergei A. Voloshin, Arthur M. Poskanzer, and Raimond Snellings. “Collective phenomena in non-central nuclear collisions”. In: *Landolt-Bornstein* 23 (2010). Ed. by R. Stock, pp. 293–333. doi: 10.1007/978-3-642-01539-7_10. arXiv: 0809.2949 [nucl-ex].
- [41] Shreyasi Acharya et al. “Systematic studies of correlations between different order flow harmonics in Pb-Pb collisions at $\sqrt{s_{NN}} = 2.76$ TeV”. In: *Phys. Rev. C* 97.2 (2018), p. 024906. doi: 10.1103/PhysRevC.97.024906. arXiv: 1709.01127 [nucl-ex].
- [42] Shreyasi Acharya et al. “The ALICE experiment: a journey through QCD”. In: *Eur. Phys. J. C* 84.8 (2024), p. 813. doi: 10.1140/epjc/s10052-024-12935-y. arXiv: 2211.04384 [nucl-ex].
- [43] Joshua Vredevoogd and Scott Pratt. “Viscous Hydrodynamics and Relativistic Heavy Ion Collisions”. In: *Phys. Rev. C* 85 (2012), p. 044908. doi: 10.1103/PhysRevC.85.044908. arXiv: 1202.1509 [nucl-th].
- [44] P. Huovinen et al. “Radial and elliptic flow at RHIC: Further predictions”. In: *Phys. Lett. B* 503 (2001), pp. 58–64. doi: 10.1016/S0370-2693(01)00219-2. arXiv: hep-ph/0101136.
- [45] Yingxun Zhang et al. “Progress of quantum molecular dynamics model and its applications in heavy ion collisions”. In: *Front. Phys. (Beijing)* 15 (2020), p. 54301. doi: 10.1007/s11467-020-0961-9. arXiv: 2005.12877 [nucl-th].
-

-
- [46] J. Adamczewski-Musch et al. “Proton, deuteron and triton flow measurements in Au+Au collisions at $\sqrt{s_{NN}} = 2.4$ GeV”. In: *Eur. Phys. J. A* 59.4 (2023), p. 80. DOI: 10.1140/epja/s10050-023-00936-6. arXiv: 2208.02740 [nucl-ex].
- [47] Jaroslav Bielcik. “Dilepton spectroscopy with HADES”. PhD thesis. Technische Universität Darmstadt, 2008. DOI: 10.26083/tuprints-00000489.
- [48] G. Agakichiev et al. “Enhanced production of low mass electron pairs in 200-GeV/u S - Au collisions at the CERN SPS”. In: *Phys. Rev. Lett.* 75 (1995), pp. 1272–1275. DOI: 10.1103/PhysRevLett.75.1272.
- [49] D. Adamova et al. “Modification of the rho-meson detected by low-mass electron-positron pairs in central Pb-Au collisions at 158-A-GeV/c”. In: *Phys. Lett. B* 666 (2008), pp. 425–429. DOI: 10.1016/j.physletb.2008.07.104. arXiv: nucl-ex/0611022.
- [50] D. Adamova et al. “Enhanced production of low mass electron pairs in 40-AGeV Pb - Au collisions at the CERN SPS”. In: *Phys. Rev. Lett.* 91 (2003), p. 042301. DOI: 10.1103/PhysRevLett.91.042301. arXiv: nucl-ex/0209024.
- [51] Hans J. Specht. “Thermal Dileptons from Hot and Dense Strongly Interacting Matter”. In: *AIP Conf. Proc.* 1322.1 (2010). Ed. by Juan M. Nieves, Eulogio Oset, and Manuel J. Vicente Vacas, pp. 1–10. DOI: 10.1063/1.3541982. arXiv: 1011.0615 [nucl-ex].
- [52] Jorg Ruppert et al. “Low mass dimuons produced in relativistic nuclear collisions”. In: *Phys. Rev. Lett.* 100 (2008), p. 162301. DOI: 10.1103/PhysRevLett.100.162301. arXiv: 0706.1934 [hep-ph].
- [53] Hendrik van Hees and Ralf Rapp. “Dilepton Radiation at the CERN Super Proton Synchrotron”. In: *Nucl. Phys. A* 806 (2008), pp. 339–387. DOI: 10.1016/j.nuclphysa.2008.03.009. arXiv: 0711.3444 [hep-ph].
- [54] Kevin Dusling and Ismail Zahed. “Transverse momentum spectra of dileptons measured by the NA60 Collaboration in In+In collisions at 158 GeV/nucleon”. In: *Phys. Rev. C* 80 (2009), p. 014902. DOI: 10.1103/PhysRevC.80.014902. arXiv: hep-ph/0701253.
- [55] R. Arnaldi et al. “First measurement of the rho spectral function in high-energy nuclear collisions”. In: *Phys. Rev. Lett.* 96 (2006), p. 162302. DOI: 10.1103/PhysRevLett.96.162302. arXiv: nucl-ex/0605007.
- [56] R. Arnaldi et al. “NA60 results on thermal dimuons”. In: *Eur. Phys. J. C* 61 (2009), pp. 711–720. DOI: 10.1140/epjc/s10052-009-0878-5. arXiv: 0812.3053 [nucl-ex].
- [57] Hendrik van Hees and Ralf Rapp. “Comprehensive interpretation of thermal dileptons at the SPS”. In: *Phys. Rev. Lett.* 97 (2006), p. 102301. DOI: 10.1103/PhysRevLett.97.102301. arXiv: hep-ph/0603084.
- [58] Tetyana Galatyuk et al. “Thermal Dileptons from Coarse-Grained Transport as Fireball Probes at SIS Energies”. In: *Eur. Phys. J. A* 52.5 (2016), p. 131. DOI: 10.1140/epja/i2016-16131-1. arXiv: 1512.08688 [nucl-th].
- [59] Jean-François Paquet. “Electromagnetic probes in heavy-ion collisions: progress and open questions”. In: *PoS HardProbes2023* (2024), p. 009. DOI: 10.22323/1.438.0009. arXiv: 2307.09967 [nucl-th].
- [60] Chenliang Jin. “Dielectron measurements in Au+Au collisions at BES-II energies with the STAR experiment”. In: (May 2025). arXiv: 2505.06361 [nucl-ex].

-
- [61] Larry D. McLerran and T. Toimela. “Photon and Dilepton Emission from the Quark - Gluon Plasma: Some General Considerations”. In: *Phys. Rev. D* 31 (1985), p. 545. DOI: 10.1103/PhysRevD.31.545.
- [62] Ralf Rapp. “Dilepton Spectroscopy of QCD Matter at Collider Energies”. In: *Adv. High Energy Phys.* 2013 (2013), p. 148253. DOI: 10.1155/2013/148253. arXiv: 1304.2309 [hep-ph].
- [63] R. Abou Yassine et al. “First measurement of massive virtual photon emission from N^* baryon resonances”. In: (May 2022). arXiv: 2205.15914 [nucl-ex].
- [64] Stephan Endres et al. “Coarse-graining approach for dilepton production at energies available at the CERN Super Proton Synchrotron”. In: *Phys. Rev. C* 91.5 (2015), p. 054911. DOI: 10.1103/PhysRevC.91.054911. arXiv: 1412.1965 [nucl-th].
- [65] Gabriele Inghirami and Hannah Elfner. “The applicability of hydrodynamics in heavy ion collisions at $\sqrt{s_{NN}} = 2.4\text{--}7.7$ GeV”. In: *Eur. Phys. J. C* 82.9 (2022), p. 796. DOI: 10.1140/epjc/s10052-022-10718-x. arXiv: 2201.05934 [hep-ph].
- [66] Jan-Hendrik Otto. “Dielectron reconstruction in Ag+Ag collisions at $\sqrt{s_{NN}} = 2.55$ GeV with HADES”. PhD thesis. Justus-Liebig-Universität-Gießen, 2022. DOI: 10.22029/JLUPUB-7207.
- [67] Dominique Dittert. “Azimuthal Anisotropy of Virtual Photons in Au+Au Collisions at $\sqrt{s_{NN}} = 2.4$ GeV”. MA thesis. Darmstadt, Tech. U., 2019.
- [68] Tom Reichert et al. “Decoding the flow evolution in Au+Au reactions at 1.23A GeV using hadron flow correlations and dileptons”. In: *Phys. Lett. B* 841 (2023), p. 137947. DOI: 10.1016/j.physletb.2023.137947. arXiv: 2302.13919 [nucl-th].
- [69] Renan Góes-Hirayama and Hannah Elfner. “Distinguishing the sources of dielectron anisotropic flow at low beam energies”. In: *Phys. Rev. C* 110.6 (2024), p. 064903. DOI: 10.1103/PhysRevC.110.064903. arXiv: 2408.16603 [nucl-th].
- [70] J. Adamczewski-Musch et al. “Charged-pion production in Au + Au collisions at $\sqrt{s_{NN}} = 2.4$ GeV: HADES Collaboration”. In: *Eur. Phys. J. A* 56.10 (2020), p. 259. DOI: 10.1140/epja/s10050-020-00237-2. arXiv: 2005.08774 [nucl-ex].
- [71] G. Agakishiev et al. “Statistical hadronization model analysis of hadron yields in p + Nb and Ar + KCl at SIS18 energies”. In: *Eur. Phys. J. A* 52.6 (2016), p. 178. DOI: 10.1140/epja/i2016-16178-x. arXiv: 1512.07070 [nucl-ex].
- [72] J. Adamczewski-Musch et al. “Proton-number fluctuations in $\sqrt{s_{NN}} = 2.4$ GeV Au + Au collisions studied with the High-Acceptance DiElectron Spectrometer (HADES)”. In: *Phys. Rev. C* 102.2 (2020), p. 024914. DOI: 10.1103/PhysRevC.102.024914. arXiv: 2002.08701 [nucl-ex].
- [73] J. Adamczewski-Musch et al. “Sub-threshold production of K_s^0 mesons and Λ hyperons in Au+Au collisions at $\sqrt{s_{NN}} = 2.4$ GeV”. In: *Phys. Lett. B* 793 (2019), pp. 457–463. DOI: 10.1016/j.physletb.2019.03.065. arXiv: 1812.07304 [nucl-ex].
- [74] R. Schicker and Haralabos Tsertos. “Simulation studies of the HADES first level trigger. Part 1: Performance in heavy ion induced reactions”. In: (Sept. 1996). arXiv: nucl-ex/9610002.
- [75] J. Michel et al. “The upgraded HADES trigger and data acquisition system”. In: *JINST* 6 (2011), p. C12056. DOI: 10.1088/1748-0221/6/12/C12056.
- [76] L. Groening et al. *UNILAC Status Report*. Tech. rep. GSI-SR2013-FG-UNILAC-01. GSI Helmholtzzentrum für Schwerionenforschung, 2014. DOI: 10.15120/GR20141FGUNILAC01.
- [77] Birgit Kindler et al. “Targets for the electron-positron pair spectrometer HADES”. In: *Nucl. Instrum. Meth. A* 655.1 (2011), pp. 95–99. DOI: 10.1016/j.nima.2011.06.029.
-

- [78] J. Pietraszko et al. “Radiation damage in single crystal CVD diamond material investigated with a high current relativistic ^{197}Au beam”. In: *Nucl. Instrum. Meth. A* 763 (2014), pp. 1–5. DOI: 10.1016/j.nima.2014.06.006.
- [79] Rayane Abou Yassine. “Study of e^+e^- pair production in pp collisions at 4.5 GeV with HADES”. PhD thesis. universit  Paris-Saclay; Technische Universit t (Darmstadt, Allemagne), 2024.
- [80] J. Adamczewski-Musch et al. “Status of the CBM and HADES RICH projects at FAIR”. In: *Nucl. Instrum. Meth. A* 952 (2020), p. 161970. DOI: 10.1016/j.nima.2019.03.025.
- [81] Jochen Markert. “Untersuchung zum Ansprechverhalten der Vieldraht-Driftkammern niedriger Massenbelegung des HADES-Experimentes”. MA thesis. Feb. 2005.
- [82] G. Agakishiev et al. “The High-Acceptance Dielectron Spectrometer HADES”. In: *Eur. Phys. J. A* 41 (2009), pp. 243–277. DOI: 10.1140/epja/i2009-10807-5. arXiv: 0902.3478 [nucl-ex].
- [83] P. Salabura et al. “HADES: A High Acceptance DiElectron Spectrometer”. In: *Nucl. Phys. B Proc. Suppl.* 44 (1995). Ed. by E. Borchi et al., pp. 701–707. DOI: 10.1016/0920-5632(95)00605-2.
- [84] Georgy Kornakov Van. “New advances and developments on the RPC tof wall of the HADES experiment at GSI”. PhD thesis. U. Santiago de Compostela (main), 2013.
- [85] D. Belver et al. “The HADES RPC inner TOF wall”. In: *Nucl. Instrum. Meth. A* 602 (2009). Ed. by Naba K. Mondal, Sergio P. Ratti, and Rinaldo Santonico, pp. 687–690. DOI: 10.1016/j.nima.2008.12.090.
- [86] G. Kornakov et al. “Performance study and calibration strategy of the HADES scintillator TOF Wall with fast digital readout”. In: (Mar. 2021). arXiv: 2103.07416 [physics.ins-det].
- [87] O. Svoboda et al. “Electromagnetic calorimeter for the HADES@FAIR experiment”. In: *JINST* 9 (2014). Ed. by Pietro Govoni et al., p. C05002. DOI: 10.1088/1748-0221/9/05/C05002.
- [88] Adrian Rost. “Design, installation and commissioning of new read-out electronics for HADES ECAL and diamond detectors for T0-reconstruction and beam diagnostics”. PhD thesis. Darmstadt, Tech. U., 2020. DOI: 10.25534/tuprints-00012235.
- [89] R. Brun and F. Rademakers. “ROOT: An object oriented data analysis framework”. In: *Nucl. Instrum. Meth. A* 389 (1997). Ed. by M. Werlen and D. Perret-Gallix, pp. 81–86. DOI: 10.1016/S0168-9002(97)00048-X.
- [90] Szymon Harabasz. “Reconstruction of virtual photons from Au+Au collisions at 1.23 GeV/u”. PhD thesis. Darmstadt, Tech. Hochsch., 2017.
- [91] Wilhelm Kr ger. “Low Gain Avalanche Diodes for Beam Monitoring and Reaction Time Determination at High Rates in HADES”. PhD thesis. Darmstadt, Tech. U., 2025. DOI: 10.26083/tuprints-00029627.
- [92] J rg F rtsch. “Upgrade of the HADES RICH photon detector and first performance analyses”. PhD thesis. Wuppertal U., 2021. DOI: 10.25926/69gp-b484.
- [93] Simon Spies. “Strange hadron production in Ag+Ag collisions at 1.58A GeV”. PhD thesis. Frankfurt U., 2022. DOI: 10.21248/gups.68651.
- [94] Tom Reichert et al. “Comparison of heavy ion transport simulations: Ag + Ag collisions at $E_{lab} = 1.58\text{A GeV}$ ”. In: *J. Phys. G* 49.5 (2022), p. 055108. DOI: 10.1088/1361-6471/ac5dfe. arXiv: 2111.07652 [nucl-th].
- [95] S. A. Bass et al. “Microscopic models for ultrarelativistic heavy ion collisions”. In: *Prog. Part. Nucl. Phys.* 41 (1998), pp. 255–369. DOI: 10.1016/S0146-6410(98)00058-1. arXiv: nucl-th/9803035.

-
- [96] M. Bleicher et al. “Relativistic hadron hadron collisions in the ultrarelativistic quantum molecular dynamics model”. In: *J. Phys. G* 25 (1999), pp. 1859–1896. DOI: 10.1088/0954-3899/25/9/308. arXiv: hep-ph/9909407.
- [97] Agnieszka Wergieluk et al. *smash-transport/smash: SMASH-3.1*. Version SMASH-3.1. Feb. 2024. DOI: 10.5281/zenodo.10707746. URL: <https://doi.org/10.5281/zenodo.10707746>.
- [98] Justin Mohs, Simon Spies, and Hannah Elfner. “Constraints on the Equation of State of Nuclear Matter from Systematically Comparing SMASH Calculations to HADES Data”. In: (Sept. 2024). arXiv: 2409.16927 [nucl-th].
- [99] I. Fröhlich et al. “Pluto: A Monte Carlo Simulation Tool for Hadronic Physics”. In: *PoS ACAT* (2007), p. 076. DOI: 10.22323/1.050.0076. arXiv: 0708.2382 [nucl-ex].
- [100] R. Brun et al. “GEANT3”. In: (Sept. 1987).
- [101] Behruz Kardan. “Centrality Determination at 1.23 AGeV Gold-Gold collision and readout-electronics for the HADES electromagnetic calorimeter”. MA thesis. Frankfurt U., 2015.
- [102] Roy J. Glauber. “Quantum Optics and Heavy Ion Physics”. In: *Nucl. Phys. A* 774 (2006). Ed. by T. Csorgo et al., pp. 3–13. DOI: 10.1016/j.nuclphysa.2006.06.009. arXiv: nucl-th/0604021.
- [103] R. J. Glauber. “Cross-sections in deuterium at high-energies”. In: *Phys. Rev.* 100 (1955), pp. 242–248. DOI: 10.1103/PhysRev.100.242.
- [104] Betty Abelev et al. “Centrality determination of Pb-Pb collisions at $\sqrt{s_{NN}} = 2.76$ TeV with ALICE”. In: *Phys. Rev. C* 88.4 (2013), p. 044909. DOI: 10.1103/PhysRevC.88.044909. arXiv: 1301.4361 [nucl-ex].
- [105] Michael L. Miller et al. “Glauber modeling in high energy nuclear collisions”. In: *Ann. Rev. Nucl. Part. Sci.* 57 (2007), pp. 205–243. DOI: 10.1146/annurev.nucl.57.090506.123020. arXiv: nucl-ex/0701025.
- [106] Daniel Shiu, Chloë Hebborn, and Filomena M. Nunes. “Systematic study of the validity of the eikonal model including uncertainties”. In: (July 2025). arXiv: 2507.13291 [nucl-th].
- [107] H. Schopper, ed. *Nuclear Charge Radii*. Vol. 20. Landolt-Boernstein - Group I Elementary Particles, Nuclei and Atoms. Springer, 2004. ISBN: 978-3-540-45555-4. DOI: 10.1007/b87879.
- [108] J. Bystricky et al. “ENERGY DEPENDENCE OF NUCLEON-NUCLEON INELASTIC TOTAL CROSS-SECTIONS”. In: (Feb. 1987).
- [109] K. A. Olive et al. “Review of Particle Physics”. In: *Chin. Phys. C* 38 (2014), p. 090001. DOI: 10.1088/1674-1137/38/9/090001.
- [110] A. Bialas, M. Bleszynski, and W. Czyz. “Multiplicity Distributions in Nucleus-Nucleus Collisions at High-Energies”. In: *Nucl. Phys. B* 111 (1976), pp. 461–476. DOI: 10.1016/0550-3213(76)90329-1.
- [111] Arthur M. Poskanzer and S. A. Voloshin. “Methods for analyzing anisotropic flow in relativistic nuclear collisions”. In: *Phys. Rev. C* 58 (1998), pp. 1671–1678. DOI: 10.1103/PhysRevC.58.1671. arXiv: nucl-ex/9805001.
- [112] Jean-Yves Ollitrault. “Flow systematics from SIS to SPS energies”. In: *Nucl. Phys. A* 638 (1998). Ed. by T. Hatsuda et al., pp. 195–206. DOI: 10.1016/S0375-9474(98)00413-8. arXiv: nucl-ex/9802005.

-
- [113] Frédéric Julian Kornas. “Global polarization of Λ hyperons as a probe for vortical effects in A+A collisions at HADES”. PhD thesis. Dortmund U., 2021. DOI: 10.26083/tuprints-00019763.
- [114] J. Barrette et al. “Proton and pion production relative to the reaction plane in Au + Au collisions at AGS energies”. In: *Phys. Rev. C* 56 (1997), pp. 3254–3264. DOI: 10.1103/PhysRevC.56.3254. arXiv: nucl-ex/9707002.
- [115] Jean-Yves Ollitrault. “On the measurement of azimuthal anisotropies in nucleus-nucleus collisions”. In: (Nov. 1997). arXiv: nucl-ex/9711003.
- [116] Jean-Yves Ollitrault. “Determination of the reaction plane in ultrarelativistic nuclear collisions”. In: *Phys. Rev. D* 48 (1993), pp. 1132–1139. DOI: 10.1103/PhysRevD.48.1132. arXiv: hep-ph/9303247.
- [117] Marvin Nabroth. “Emission patterns of charged pions from Ag+Ag collisions at 1.58A GeV”. MA thesis. Frankfurt U., 2022.
- [118] Kai Zhou et al. “Exploring QCD matter in extreme conditions with Machine Learning”. In: *Prog. Part. Nucl. Phys.* 135 (2024), p. 104084. DOI: 10.1016/j.pnnp.2023.104084. arXiv: 2303.15136 [hep-ph].
- [119] Henrik Flörsheimer. “Electron Identification with machine learning in Ag+Ag collisions at 1.58A GeV”. MA thesis. Darmstadt, Tech. U., 2024.
- [120] Mateusz Wasiluk. “Implementation of machine learning algorithms in data analysis of the HADES experiment”. MA thesis. Warsaw University of Technology, 2021.
- [121] Mateusz Wasiluk. “Subtraction of Au+C contamination in Au+Au experiment with HADES using Machine Learning techniques”. GSI - Get Involved Report. Darmstadt, 2019. URL: <https://edms.cern.ch/document/2593148/1>.
- [122] Aleksander Glodkowski. “Analysis of Au+C contribution from reactions outside target in Au+Au run with HADES”. GSI - Summer Student Report. Darmstadt, 2019.
- [123] Niklas Schild. “System size and centrality dependence of thermal radiation measured by HADES”. MA thesis. Darmstadt, Tech. U., 2021.
- [124] Avrim Blum and Tom Mitchell. “Combining labeled and unlabeled data with co-training”. In: *COLT* 98 (1998), pp. 92–100. DOI: 10.1145/279943.279962. URL: <https://doi.org/10.1145/279943.279962>.
- [125] Yassine Ouali, Céline Hudelot, and Myriam Tami. “An Overview of Deep Semi-Supervised Learning”. In: (2020). arXiv: 2006.05278 [cs.LG]. URL: <https://arxiv.org/abs/2006.05278>.
- [126] Zhilu Zhang and Mert R. Sabuncu. “Generalized Cross Entropy Loss for Training Deep Neural Networks with Noisy Labels”. In: *CoRR* abs/1805.07836 (2018). arXiv: 1805.07836. URL: <http://arxiv.org/abs/1805.07836>.
- [127] Ian Goodfellow, Yoshua Bengio, and Aaron Courville. *Deep Learning*. <http://www.deeplearningbook.org>. MIT Press, 2016.
- [128] Diederik P Kingma and Jimmy Ba. “Adam: A method for stochastic optimization”. In: *International Conference on Learning Representations (ICLR)* (2015). arXiv: 1412.6980 [cs.LG].
- [129] E. Zherebtsova et al. “New Approach to Measure Centrality in the HADES Heavy-Ion Experiments”. In: *Phys. Part. Nucl.* 53.2 (2022), pp. 513–518. DOI: 10.1134/S1063779622020897.
- [130] M. Baznat et al. “Monte-Carlo Generator of Heavy Ion Collisions DCM-SMM”. In: *Phys. Part. Nucl. Lett.* 17.3 (2020), pp. 303–324. DOI: 10.1134/S1547477120030024. arXiv: 1912.09277 [nucl-th].

-
- [131] M. C. Abreu et al. “Dimuon and charm production in nucleus-nucleus collisions at the CERN SPS”. In: *Eur. Phys. J. C* 14 (2000), pp. 443–455. DOI: 10.1007/s100520000373.
- [132] A. Adare et al. “Detailed measurement of the e^+e^- pair continuum in $p + p$ and Au+Au collisions at $\sqrt{s_{NN}} = 200$ GeV and implications for direct photon production”. In: *Phys. Rev. C* 81 (2010), p. 034911. DOI: 10.1103/PhysRevC.81.034911. arXiv: 0912.0244 [nucl-ex].
- [133] Marek Gazdzicki and Mark I. Gorenstein. “Background subtraction from the dilepton spectra in nuclear collisions”. In: (Mar. 2000). arXiv: hep-ph/0003319.
- [134] L. Adamczyk et al. “Measurements of Dielectron Production in Au+Au Collisions at $\sqrt{s_{NN}} = 200$ GeV from the STAR Experiment”. In: *Phys. Rev. C* 92.2 (2015), p. 024912. DOI: 10.1103/PhysRevC.92.024912. arXiv: 1504.01317 [hep-ex].
- [135] M. K. Köhler. “Dielectron production in proton-proton collisions with ALICE”. PhD thesis. Darmstadt, Tech. Hochsch., 2014.
- [136] W. Ehehalt and W. Cassing. “Relativistic transport approach for nucleus nucleus collisions from SIS to SPS energies”. In: *Nucl. Phys. A* 602 (1996), pp. 449–486. DOI: 10.1016/0375-9474(96)00097-8.
- [137] Claudia Behnke. “Reconstruction of π^0 and η mesons via conversion in $^{197}\text{Au} + ^{197}\text{Au}$ at 1.23 GeV/u with the HADES Spectrometer”. PhD thesis. Goethe U., Frankfurt (main), 2016.
- [138] Alexandr Prozorov. “Neutral Meson Production in Ag+Ag Collisions at 1.58 A GeV with HADES Electromagnetic Calorimeter”. PhD thesis. Univerzita Karlova, Charles U., Prague (main), 2023.
- [139] R. Auerbeck et al. “Neutral pions and eta mesons as probes of the hadronic fireball in nucleus-nucleus collisions around 1-A-GeV”. In: *Phys. Rev. C* 67 (2003), p. 024903. DOI: 10.1103/PhysRevC.67.024903. arXiv: nucl-ex/0012007.
- [140] G. Agakishiev et al. “Dielectron production in Ar + KCl collisions at 1.76A GeV”. In: *Phys. Rev. C* 84 (1 July 2011), p. 014902. DOI: 10.1103/PhysRevC.84.014902. URL: <https://link.aps.org/doi/10.1103/PhysRevC.84.014902>.
- [141] J. Cleymans and K. Redlich. “Unified description of freezeout parameters in relativistic heavy ion collisions”. In: *Phys. Rev. Lett.* 81 (1998), pp. 5284–5286. DOI: 10.1103/PhysRevLett.81.5284. arXiv: nucl-th/9808030.
- [142] Marvin Kohls. “Production of K^\pm and ϕ -Mesons in Ag+Ag-Collisions at 1.58 A GeV”. PhD thesis. Goethe University Frankfurt, Frankfurt U., 2023.
- [143] G. Agakishiev et al. “Origin of the low-mass electron pair excess in light nucleus-nucleus collisions”. In: *Phys. Lett. B* 690 (2010), pp. 118–122. DOI: 10.1016/j.physletb.2010.05.010. arXiv: 0910.5875 [nucl-ex].
- [144] Karina Scharmman. *Dielectron analysis in p+p collisions at 1.58 GeV beam energy with HADES*. Poster presented at Quark Matter 2025. Frankfurt am Main, Germany, Apr. 2025. URL: <https://indico.cern.ch/event/1334113/contributions/6291939/>.
- [145] Lukáš Chlad. “Study of transverse flow of kaons in Au+Au collisions at 1.23A GeV”. PhD thesis. Charles U., Prague (main), Faculty of mathematics and physics Charles University Prague, Charles U., 2021.
- [146] A. Taranenko et al. “Azimuthal anisotropy of eta and pi0 mesons in heavy ion collisions at 2-A-GeV”. In: (Mar. 1999). arXiv: nucl-ex/9903008.
-

-
- [147] A. Taranenko et al. “Elliptic flow of eta and pi0 mesons in heavy ion collisions at 2/A-GeV”. In: *Czech. J. Phys.* 50S4 (2000). Ed. by A. Kugler, V. Wagner, and H. Lohner, pp. 139–166. DOI: 10.1007/s10582-000-0050-9. arXiv: nucl-ex/9910002.
- [148] Hannah Petersen et al. “A Fully Integrated Transport Approach to Heavy Ion Reactions with an Intermediate Hydrodynamic Stage”. In: *Phys. Rev. C* 78 (2008), p. 044901. DOI: 10.1103/PhysRevC.78.044901. arXiv: 0806.1695 [nucl-th].
- [149] Paula Hillmann, Jan Steinheimer, and Marcus Bleicher. “Directed, elliptic and triangular flow of protons in Au+Au reactions at 1.23 A GeV: a theoretical analysis of the recent HADES data”. In: *J. Phys. G* 45.8 (2018), p. 085101. DOI: 10.1088/1361-6471/aac96f. arXiv: 1802.01951 [nucl-th].
- [150] Jessica Ou Ya Vogel. “Combined Description of Thermal and Vacuum Contributions of Vector Mesons to the Dilepton Spectrum”. MA thesis. Darmstadt, Tech. U., 2025.
- [151] Mikhail Mamaev, Oleg Golosov, and Ilya Selyuzhenkov. “Estimating Non-Flow Effects in Measurements of Anisotropic Flow of Protons with the HADES Experiment at GSI”. In: *Phys. Part. Nucl.* 53.2 (2022), pp. 277–281. DOI: 10.1134/S1063779622020514. arXiv: 2012.04433 [nucl-ex].
- [152] Iuliana-Carina Udrea. *Low-mass, low-momentum virtual photon measurements with HADES*. Poster presented at Quark Matter 2025. Frankfurt am Main, Germany, Apr. 2025. URL: <https://indico.cern.ch/event/1334113/contributions/6291937/>.
- [153] W. Reisdorf et al. “Systematics of pion emission in heavy ion collisions in the 1A- GeV regime”. In: *Nucl. Phys. A* 781 (2007), pp. 459–508. DOI: 10.1016/j.nuclphysa.2006.10.085. arXiv: nucl-ex/0610025.
- [154] R. Arnaldi et al. “Evidence for radial flow of thermal dileptons in high-energy nuclear collisions”. In: *Phys. Rev. Lett.* 100 (2008), p. 022302. DOI: 10.1103/PhysRevLett.100.022302. arXiv: 0711.1816 [nucl-ex].
- [155] Tamás Csörgő and Gábor Kasza. “Scaling properties of spectra in new exact solutions of rotating, multi-component fireball hydrodynamics”. In: *Universe* 4.4 (2018). Ed. by Máté Csanád, Tamás Csörgő, and Tamás Novák, p. 58. DOI: 10.3390/universe4040058. arXiv: 1801.05716 [nucl-th].
- [156] Ekkard Schnedermann, Josef Sollfrank, and Ulrich W. Heinz. “Thermal phenomenology of hadrons from 200-A/GeV S+S collisions”. In: *Phys. Rev. C* 48 (1993), pp. 2462–2475. DOI: 10.1103/PhysRevC.48.2462. arXiv: nucl-th/9307020.
- [157] Zebo Tang et al. “Spectra and radial flow at RHIC with Tsallis statistics in a Blast-Wave description”. In: *Phys. Rev. C* 79 (2009), p. 051901. DOI: 10.1103/PhysRevC.79.051901. arXiv: 0812.1609 [nucl-ex].
- [158] Shreyasi Acharya et al. “Long-range transverse momentum correlations and radial flow in Pb–Pb collisions at the LHC”. In: (Apr. 2025). arXiv: 2504.04796 [nucl-ex].
- [159] Swati Saha, Ranbir Singh, and Bedangadas Mohanty. “pT-differential radial flow in a blast-wave model”. In: *Phys. Rev. C* 112.2 (2025), p. 024902. DOI: 10.1103/83zq-kdjg. arXiv: 2505.19697 [nucl-ex].
- [160] Tom Reichert et al. “Harmonic flow correlations in Au+Au reactions at 1.23 AGeV: a new testing ground for the equation-of-state and expansion geometry”. In: *Eur. Phys. J. C* 82.6 (2022), p. 510. DOI: 10.1140/epjc/s10052-022-10480-0. arXiv: 2203.15550 [nucl-th].

-
- [161] Pawel Danielewicz and Mizuki Kurata-Nishimura. “Deblurring for nuclei: 3D characteristics of heavy-ion collisions”. In: *Phys. Rev. C* 105.3 (2022), p. 034608. DOI: 10.1103/PhysRevC.105.034608. arXiv: 2109.02626 [nucl-th].
- [162] Renan Hirayama and Hannah Elfner. “Dilepton anisotropy at low beam energies in a transport approach”. In: *PoS HardProbes2023* (2024), p. 194. DOI: 10.22323/1.438.0194.
- [163] Ralf Rapp and Hendrik van Hees. “Thermal Dileptons as Fireball Thermometer and Chronometer”. In: *Phys. Lett. B* 753 (2016), pp. 586–590. DOI: 10.1016/j.physletb.2015.12.065. arXiv: 1411.4612 [hep-ph].
- [164] K. Piasecki and P. Piotrowski. “Systematics of yields of strange hadrons from heavy-ion collisions around threshold energies”. In: *Eur. Phys. J. A* 59.11 (2023), p. 272. DOI: 10.1140/epja/s10050-023-01182-6. arXiv: 2305.13760 [nucl-ex].
- [165] S.M. Harrison, J.S.H. Ross, and R.J. Riggs. “The HADES detector magnet—a large superconducting torus”. In: *IEEE Transactions on Applied Superconductivity* 9.2 (1999), pp. 860–862. DOI: 10.1109/77.783432.
- [166] C. Muntz et al. “The HADES tracking system”. In: *Nucl. Instrum. Meth. A* 535 (2004). Ed. by M. Jeitler et al., pp. 242–246. DOI: 10.1016/j.nima.2004.07.232. arXiv: physics/0404011.
- [167] O. V. Andreeva et al. “Forward scintillation hodoscope for nuclear fragment detection at the high acceptance dielectron spectrometer (HADES) setup”. In: *Instrum. Exp. Tech.* 57 (2014), pp. 103–119. DOI: 10.1134/S0020441214020146.
- [168] S. Agostinelli et al. “GEANT4 - A Simulation Toolkit”. In: *Nucl. Instrum. Meth. A* 506 (2003), pp. 250–303. DOI: 10.1016/S0168-9002(03)01368-8.
- [169] Bengt Friman et al., eds. *The CBM physics book: Compressed baryonic matter in laboratory experiments*. Vol. 814. 2011. DOI: 10.1007/978-3-642-13293-3.
- [170] Jerzy Bartke. *Introduction to relativistic heavy ion physics*. 2009.
- [171] David Griffiths. *Introduction to Elementary Particles*. 1987. ISBN: 978-0-471-60386-3.

Acknowledgements

For me, this thesis marks the culmination of four years as a PhD student and a whole decade of physics at university. Along this journey, I have learned a great deal and met many people who have accompanied me. To each of them, I am deeply grateful.

First and foremost, I want to express my gratitude to my supervisor, Tetyana Galatyuk. Your dedication, guidance, and trust in me have been invaluable. Thank you for your unwavering support, both directly and indirectly, and for always encouraging me to push my boundaries.

This extends to all current and former members of the ViP-QM working group. From Max to Carina, Willy to Vadym, Florian to Jessica, and everyone else, I always appreciate the fun we have and the support we give each other, whether for physics discussions or simply figuring out together how to properly fill out paperwork. I sincerely believe it is these small things that make or break everyday work.

A particular thanks needs to be given to Szymon, who not only taught me all I know about dielectrons but continues to support me, for example by proofreading this thesis. Thank you!

Beyond the Darmstadt group, I want to thank the whole HADES collaboration. Not only is it the reason the data in this thesis even exists, but it also entails many people I am grateful for. This includes all the knowledgeable seniors, Jurek, Manuel, Gosia, Christian, and many more, who are always approachable for advice. Gosia and Christian, thank you also for your organisational support in all things GSI. In addition, I would like to give a particular thank you to Joachim, who agreed to be my mentor at HGS HIRe, and to Claudia, who served as my second supervisor despite her many other obligations. I truly appreciate your extra efforts.

In the same vein, I want to thank the HADES young members, especially Karina, Carina, and of course Jana as fellow young members' representatives.

Experiencing such a large network during my PhD studies has been a huge blessing. For this reason, I also want to thank the ELEMENTS Cluster, which not only supported a large part of my PhD financially but also allowed me to meet and interact with more researchers in my field. Thank you all for this exchange. In particular, thank you, Owe Philipsen, for being part of my HGS HIRe committee, even though my topic is only indirectly related to your research.

Next, I want to thank my friends. Some of you I met through physics, and you have given me a lot of feedback and support for this thesis. In particular, thank you, Bea, for reading, and Fabian, for your advice. Some of you have nothing to do with physics, but honestly, your emotional support has been just as valuable. Thank you for being there in any case!

Finally, I want to thank my family. Thank you, Mom. Thank you, Dad. Your continuous help, encouragement, and belief in me have been my foundation throughout this journey.

Curriculum Vitae

Niklas Schild

January 2026

Education

Ph.D. Candidate	11/2021 – 02/2026
Technische Universität Darmstadt, Germany	
Thesis: <i>Characterising the hot and dense fireball with virtual photons at HADES</i>	
M.Sc. Physics	09/2018 – 08/2021
Technische Universität Darmstadt, Germany	
Thesis: <i>System size and centrality dependence of thermal radiation measured by HADES</i>	
Exchange Semester	09/2018 – 02/2019
University of British Columbia, Canada	
B.Sc. Physics	10/2015 – 09/2018
Technische Universität Darmstadt, Germany	
Thesis: <i>Reconstruction of e^+e^- in peripheral Au+Au collisions at $\sqrt{s_{NN}}=2.42$ GeV with HADES</i>	
Abitur	08/2013 – 07/2015
Taunusschule Bad Camberg, Germany	

List of Publications

- N. Schild (HADES Collaboration), *Studying properties of baryon-dominated matter with dileptons*, *EPJ Web of Conferences*, accepted (2025).
- N. Schild (HADES Collaboration), *Dilepton measurements with HADES as probes of hot and dense hadronic matter*, *Nucl.Phys.A* 1060 (2025) 123096.
- N. Schild (HADES Collaboration), *Characterising the hot and dense fireball with virtual photons at HADES*, *PoS HardProbes2023* (2024) 072.
- N. Schild (HADES Collaboration), *Characterising the hot and dense fireball with virtual photons at HADES*, *PoS FAIRness2022* (2023) 053.

List of Talks

INTERNATIONAL SCHOOL OF NUCLEAR PHYSICS, 46th Course <i>Characterising the hot and dense fireball with virtual photons at HADES</i>	18.09.2025
31th Conference on Ultra-relativistic Nucleus-Nucleus Collisions: Quark Matter 2025 <i>"Studying properties of baryon-dominated matter with dileptons"</i>	09.04.2025
DPG spring meeting of section Matter and Cosmos 2025 <i>"Characterising the hot and dense fireball with virtual photons at HADES"</i>	11.03.2025
14th International Conference on Nucleus-Nucleus Collisions: NN 2024 <i>"Dilepton Measurements with HADES as Probes of Hot and Dense Hadronic Matter"</i>	19.08.2024
DPG spring meeting of section Matter and Cosmos 2024 <i>"Characterising the hot and dense fireball with virtual photons at HADES"</i>	11.03.2024
Hard Probes 2023 <i>"Characterising the hot and dense fireball with virtual photons at HADES"</i>	30.03.2023
DPG spring meeting of section Matter and Cosmos 2023 <i>"Characterising the hot and dense fireball via virtual photons at HADES"</i>	23.03.2023
Workshop on Critical Point and Onset of Deconfinement (CPOD) 2022 <i>"Characterising the hot and dense fireball via dilepton polarization and flow in HADES"</i>	30.11.2022
FAIR next generation scientists – 7th Edition Workshop 2022 <i>"Characterising the hot and dense fireball via dilepton polarization and flow in HADES"</i>	22.05.2022
Virtual DPG meeting of section Matter and Cosmos 2021 <i>"Centrality and system size dependence of the thermal dilepton excess yield in HADES"</i>	24.08.2021

List of Posters

30th Conference on Ultra-relativistic Nucleus-Nucleus Collisions: Quark Matter 2023 <i>"Characterising collectivity with virtual photons at HADES"</i>	05.09.2023
786. WE-Heraeus-Seminar on QCD Phase Transition 2023 <i>"Characterising the hot and dense fireball with virtual photons at HADES"</i>	04.03.2023
29th Conference on Ultra-Relativistic Nucleus-Nucleus Collisions: Quark Matter 2022 <i>"Centrality and system size dependence of the thermal dilepton excess yield in HADES"</i>	04.04.2022

Scientific Honours and Awards

Giersch-Excellence-Award for outstanding scientific work in past year.	2024
PhD Award for Best Early Career Research Talk at ELEMENTS Conference	2023
Giersch-Excellence-Award for outstanding scientific work in past year	2022

Scientific Engagement

Representative of the HADES Young Members	2023 - 2025
Scientific Outreach	
Contribution in "Wissenschaft für Alle" public lecture series at GSI	17.12.2025
Participation in "Winterspaziergang durch das Universum" Twitch Stream	11.01.2024
Presentation of neutron star exhibit at the "Night Of Science" in Frankfurt	16.06.2023